278 ✓

JOURNAL OF THE Electrochemical Society

l. 112, No. 7 July 1965

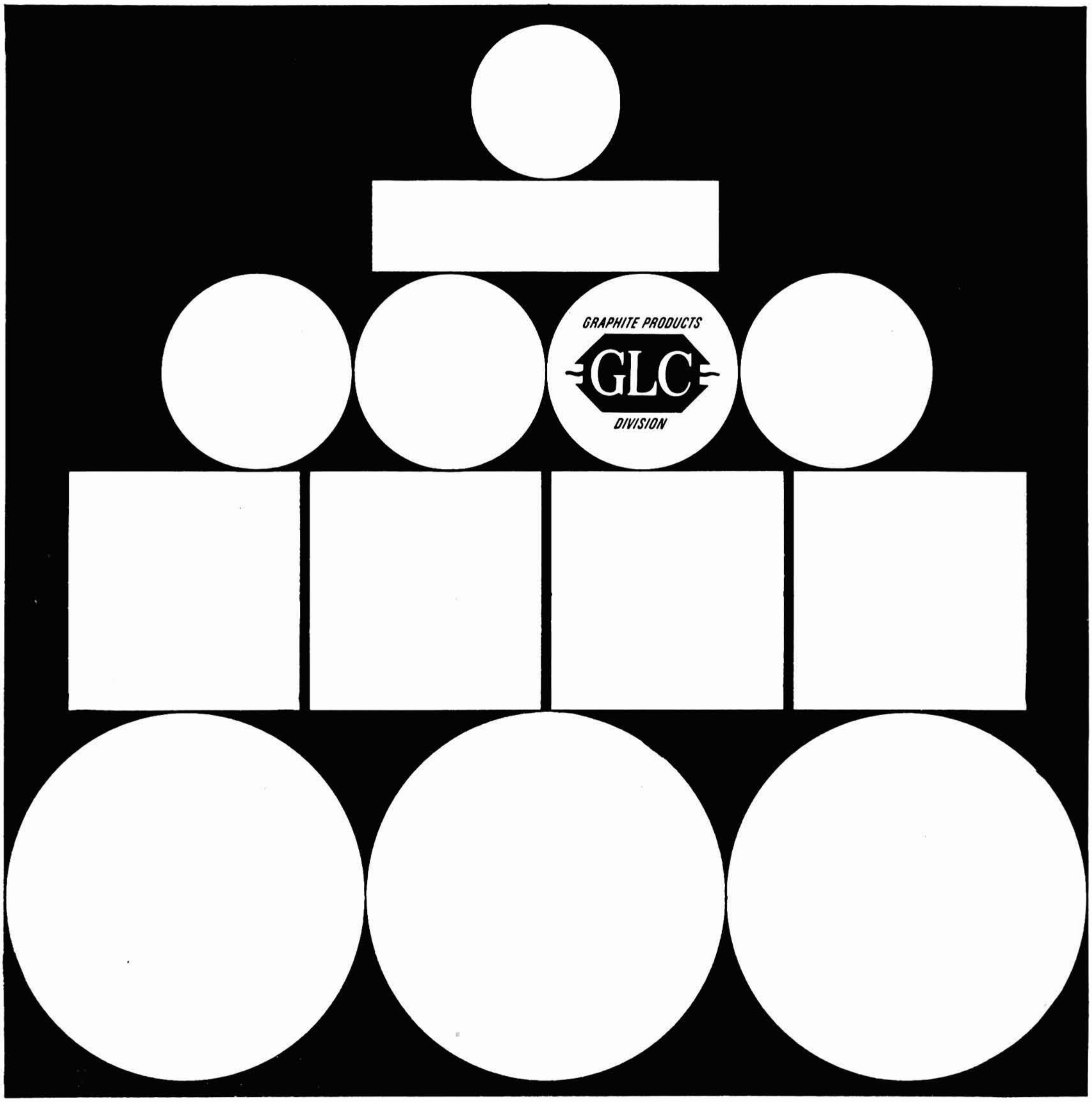
GRAPHITE PRODUCTS
GLC
DIVISION

A new concept in pH meters...

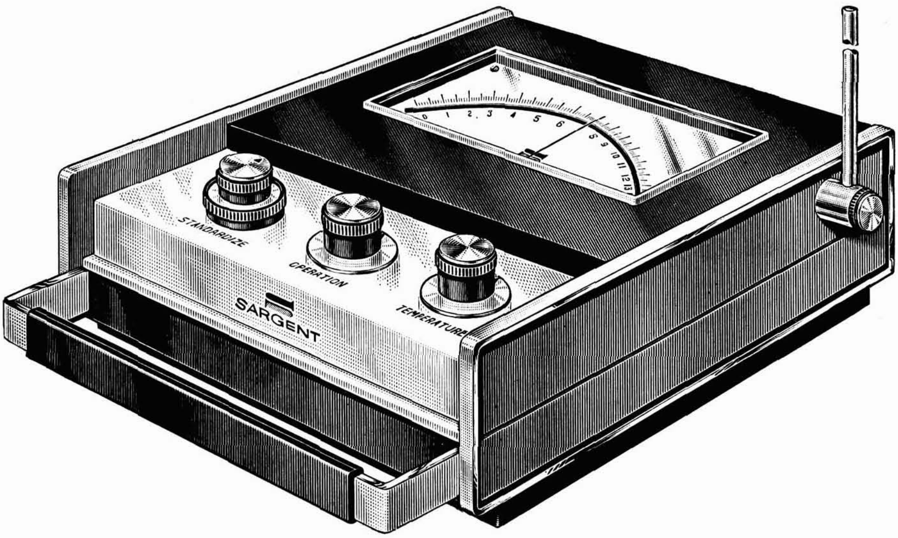

Interchangeable power supplies for laboratory and field.

Accuracy and stability found heretofore only in the highest-priced meters.

Rugged construction for use in any environment under field conditions.

SARGENT

MODEL PB—with modular mercury cell power source providing over 6 months of normal usage in the field.

MODEL PL—with modular Zener reference line power source for continuous use in the laboratory.

▪ **Relative Accuracy** ▪ for the most exacting purposes, readable to 0.02 pH, with meter accuracy of ±0.03 pH within 4 pH of the standardized point, and ±0.05 pH anywhere on the scale.

▪ **Stability** ▪ for long term use without need for readjustment, eminently suitable for recording, with circuit drift less than 0.02 pH per hour after short initial warm-up.

▪ **Rugged Construction** ▪ for use in any locale, any climate; moisture-proofed, transistorized circuitry, shock-proof case.

MODEL PB Cat. No. S-30007 with batteries, buffers and electrodes . . . $255.00
Cat. No. S-30007-10 with batteries only, for use with any electrodes . . . $215.00
MODEL PL Cat. No. S-30008 with line power source, buffers and electrodes . . . $295.00
Cat. No. S-30008-10 with line power source only, for use with any electrodes . . . $255.00
Power Supplies Cat. No. S-30007-15 Zener Line Source for substitution in Model PB meters. . . $60.00
Cat. No. S-30008-15 Mercury Cell Source for substitution in Model PL meters . . . $20.00

For complete information write for bulletin pHP.

SARGENT® SCIENTIFIC LABORATORY INSTRUMENTS • APPARATUS • SUPPLIES • CHEMICALS

E. H. SARGENT & CO., 4647 W. Foster Ave., Chicago, Ill. • Anaheim, Calif. • Birmingham • Dallas • Denver • Detroit • Springfield, N. J. • Toronto, Canada

JOURNAL OF THE

C. L. Faust, Chairman, Publication Committee
R. A. Kolbe, Manager of Publications

EDITORIAL STAFF

Cecil V. King, Editor
Norman Hackerman, Technical Editor
Ruth G. Sterns, Managing Editor
H. W. Salzberg, Book Review Editor
Daniel J. Immediato, Assistant Editor

DIVISIONAL EDITORS

W. C. Vosburgh, Battery
Paul C. Milner, Battery
G. A. Marsh, Corrosion
A. C. Makrides, Corrosion
Morris Cohen, Corrosion
Harry C. Gatos, Corrosion—Semiconductors
Newton Schwartz, Electric Insulation
Seymour Senderoff, Electrodeposition
Ephraim Banks, Electronics
Simon Larach, Electronics
Charles S. Peet, Jr., Electronics—Semiconductors
F. A. Trumbore, Electronics—Semiconductors
P. Wang, Electronics—Semiconductors
Sherlock Swann, Jr., Electro-Organic
Stanley Wawzonek, Electro-Organic
John M. Blocher, Jr., Electrothermics & Metallurgy
J. H. Westbrook, Electrothermics & Metallurgy
Scott Lynn, Industrial Electrolytic
C. W. Tobias, Theoretical Electrochemistry
A. J. deBethune, Theoretical Electrochemistry
R. M. Hurd, Theoretical Electrochemistry
M. W. Breiter, Theoretical Electrochemistry

ADVERTISING OFFICE
ECS

30 East 42 St., New York, N. Y., 10017

ECS OFFICERS

E. B. Yeager, President
Western Reserve University
Cleveland, Ohio

H. J. Read, Vice-President
Dept. of Metallurgy
Pennsylvania State University
University Park, Pa.

H. C. Gatos, Vice-President
Depts. of Met. & Electrical Eng.
Massachusetts Institute of Technology
Cambridge, Mass. 02139

Ivor E. Campbell, Vice-President
220 Gentry Rd.
Coraopolis, Pa.

Ralph H. Schaefer, Treasurer
The Electric Storage Battery Co.
Yardley, Pa.

R. F. Bechtold, Secretary
The Dow Chemical Co.
Midland, Mich.

Ernest G. Enck, Executive Secretary
National Headquarters, The ECS,
30 East 42 St., New York, N. Y., 10017

Robert A. Kolbe, Assistant Executive Secretary
The ECS, 30 East 42 St., New York, N. Y., 10017

JULY 1965

EDITORIAL

TECHNICAL PAPERS

ELECTROCHEMICAL SOCIETY

VOL. 112 • NO. 7

TECHNICAL NOTES

BRIEF COMMUNICATION

FEATURE SECTION

Manuscripts submitted to the Journal should be sent, in triplicate, to the Editorial Office at 30 East 42 St., New York, N. Y., 10017. They should conform to the revised Instructions to Authors published on pp. 366-45C of the Mar. issue. Manuscripts so submitted become the property of The Electrochemical Society and may not be published elsewhere, in whole or in part, unless permission is requested of and granted by the Editor.

The Electrochemical Society does not maintain a supply of reprints of papers appearing in its Journal. A photoprint copy of any particular paper, however, may be obtained by corresponding direct with the Engineering Societies Library, 345 E. 47 St., New York, N. Y., 10017.

Inquiries re positive microfilm copies of volumes should be addressed to University Microfilms, Inc., 313 N. First St., Ann Arbor, Mich.

Walter J. Johnson, Inc., 111 Fifth Ave., New York, N. Y., 10003, have reprint rights to out-of-print volumes of the Journal, and also have available for sale back volumes and single issues, with the exception of the current calendar year. Anyone interested in securing back copies should correspond direct with them.

Published monthly by The Electrochemical Society, Inc., at 215 Canal St., Manchester, N. H.; **Executive Offices, Editorial Office** and **Circulation Dept.**, and **Advertising Office** at 30 East 42 St., New York, N. Y., 10017, combining the JOURNAL and TRANSACTIONS OF THE ELECTROCHEMICAL SOCIETY. Statements and opinions given in articles and papers in the JOURNAL OF THE ELECTROCHEMICAL SOCIETY are those of the contributors, and The Electrochemical Society assumes no responsibility for them.

Claims for missing numbers will not be allowed if received more than 60 days from date of mailing plus time normally required for postal delivery of JOURNAL and claim. No claims allowed because of failure to notify the Circulation Dept., The Electrochemical Society, 30 East 42 St., New York, N. Y., 10017, of a change of address, or because copy is "missing from files." Subscription to members as part of membership service; subscription to nonmembers $24.00 plus $1.50 for postage outside U.S. and Canada. Single copies $1.70 to members, $2.25 to nonmembers. © 1965 by The Electrochemical Society, Inc. Entered as second-class matter at the Post Office at Manchester N. H., under the act of August 24, 1912. Postage paid at Manchester, N. H.

Editorial

Obsolescence

THE dynamic state of modern science and technology has created a situation in which obsolescence of people is a major problem of our times. While national attention has been given to this dilemma at the level of the nonskilled and semiskilled worker, obsolescence is an advancing threat among the scientists and the engineers—the very people in our society most responsible for these scientific and technological changes. The most pronounced symptom of this malady among scientists and engineers is the inability or reluctance to adapt to change—to make a rapid and effective attack on new problems and to develop or to adopt new approaches to existing problems. [This writer can not help noting that obsolescence among college and university teachers is a particularly severe malady—easily recognized even in its early stages by students and in its more advanced stages by fellow faculty members, particularly the younger ones, but rarely recognized by the faculty member inflicted with the disease.]

Resistance to obsolescence is an acquired characteristic which tends to decline with increasing age but at any age definite steps can be taken to enhance this resistance. The nature of these steps is the subject of this editorial.

First and foremost, the scientist and the engineer must recognize the importance of always remaining students in their outlook towards their work. Continuous study will be necessary throughout all of their professional careers. Such study takes various forms. For the researchers, keeping up with the scientific literature is an ever pressing problem which requires a distribution of study between broad general developments and highly specific developments. An extensive, readily accessible library is indispensible for this attack on the literature. Participation in courses and seminars given locally and at national meetings and conferences also is an important part of this continuous study. If the scientists in an industrial or governmental laboratory do not have access to such courses and seminars in a local college or university, then it is important that such courses and seminars be set up within the laboratory. In many instances, several laboratories in close proximity can profit by setting up such educational activities as a cooperative effort.

For many years the academic community has recognized the importance of the sabbatical leave as a period for study and the acquiring of new ideas and skills. This writer strongly recommends that the scientists of nonacademic laboratories also be given sabbatical leaves during which they return to the university campus for at least one and preferably two semesters of study and research at the postgraduate level. The mastery of just one new research approach can justify many-fold the financial cost to the employer.

Other types of preventative measures also are possible for warding off obsolescence. Scientists and engineers who undertake problems in new areas at reasonable intervals are like the fighter who keeps in trim by continuously fighting. Academic scientists find it is stimulating not only to make significant changes in the direction of their research from time to time, but also to teach at least one new course every two or three years.

(Continued on following page)

The "publish or perish" controversy rages on the university campus, but all things considered, publication based on research is a natural desire of scientists who continue to be productive and in itself helps to ward off obsolescence. The experience of having your work subjected to critical examination at technical meetings and during the course of publication is the fire which tempers the intellect of the scientist.

The industrial research scientist must usually spend most of his time on very practical problems often of limited scope. If his employer provides him with the opportunity to spend at least one third of his time on publishable research, the scientist is likely to be more productive even in his nonpublishable applied work and will be far more resistant to the malady of obsolescence.

Many of the recommendations just presented are not restricted to the scientist or engineer. At a time when the working force at the nontechnical level exceeds the demand, the prospect of a shorter working day is great. The additional time should not be given over to leisure, but rather to self-improvement through continuous study and training. Employers and unions would do well to consider using the extra time made available by automation for employer and/or union organized classes and training programs aimed at upgrading the skills of the worker and preventing obsolescence.

Ernest Yeager[1]
President—The Electrochemical Society 1965-1966

---

[1] Acting Chairman, Department of Chemistry, Western Reserve University, Cleveland, Ohio.

Design of Primary and Secondary Cells

II. An Equation Describing Battery Discharge

C. M. Shepherd

U. S. Naval Research Laboratory, Washington, D. C.

ABSTRACT

A discussion is given of the derivation and application of an equation which gives an excellent description of a wide variety of cell and battery discharges. This equation gives the cell potential during discharge as a function of discharge time, current density, and certain other factors. It makes possible a complete description of cell discharge characteristics, using a minimum of experimental data and at the same time pinpointing experimental errors. It can also be used to describe cell charges, capacities, power evolution, and to predict capacities. A description is given of a simple numerical method for fitting this equation to a particular set of battery discharge curves. A graphical method is described for comparing characteristics of various types of cells.

This paper is one of a series whose ultimate goal is to determine procedures for designing batteries having optimum properties such as minimum weight or minimum volume. In particular, the derivation and application of an equation describing cell discharge will be discussed. The equation can be used to locate variations in the discharge data due to experimental error, uncontrolled variables, etc., thus minimizing the amount of experimental data needed and cutting the costs of evaluation. A complete set of discharge curves can be described by a single equation, making it possible to present in less space a more detailed description of cell characteristics than has been customary in many battery papers.

Derivation and Determination of the Discharge Equation

The mathematical analysis given here is based on the assumption that the following conditions are applicable: (*A*). The anode and/or cathode have porous active materials. (*B*). The electrolyte resistance is constant throughout discharge. (*C*). The cell is discharged at a constant current. (*D*). The polarization is a linear function of the active material current density.

When ionic discharge is the slow or rate determining process, the relationship between steady-state current density and activation overpotential at an electrode in a constant concentration electrolyte is usually written as

$$i = i_o e^{\alpha \eta ZF/RT} - i_o e^{-(1-\alpha)\eta ZF/RT} \qquad [1]$$

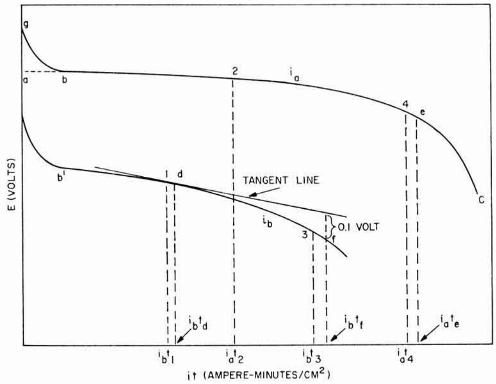

Fig. 1. Typical discharge curves used in equation fitting

where i is the apparent current density in amperes per square centimeter, i_o is the apparent exchange current density in amperes per square centimeter, α is the transfer coefficient ($0 \leq \alpha \leq 1$), Z is the number of electrons transferred in the rate-determining step, F is the Faraday, R is the gas constant, and T is the temperature in °K. The steady-state activation overpotential, η, is positive for the deposition of cations.

When the exponential terms are expanded as a series, powers greater than one can be neglected if η is sufficiently small and Eq. [1] becomes

$$\eta = \left(\frac{RT}{ZFi_o} \right) i \qquad [2]$$

thus establishing a linear relationship between η and i which is fairly accurate up to the values of η equal to approximately 0.03v. If Eq. [1] is applicable to a cell, the variation of η with change in i can be fitted by a straight line within approximately 0.02-0.04v up to values of η equal to about 0.2-0.4v. A potential drop of this magnitude would cover the major portion of the polarization that occurs during most battery discharges.

In Fig. 1, two solid curves, i_a and i_b, are shown which represent typical battery discharges. The potential in volts is plotted as a function of (it), the quantity of electricity that has been obtained from the battery at time t. It is assumed in the derivation that follows that the polarization is linear to the right of point b and b'. If all factors except polarization are ignored, then E_c, the cathode potential during discharge, is defined as

$$E_c = E_{sc} - K_c i_{am} \qquad [3]$$

where E_{sc} is a constant potential, K_c is the cathode coefficient of polarization per unit active material current density, and i_{am} is the active material current density. The successful use of Eq. [3] as a fundamental equation in the derivation that follows does not necessarily imply that the theoretical factors associated with Eq. [1] apply to most battery discharges even though both equations are linear.

In the case of a porous electrode the active material current density i_{am} is defined as being inversely proportional to the amount of unused active material and is also equal to i at the beginning of the discharge. Consequently

$$i_{am} = \left(\frac{Q_c}{Q_c - it} \right) i \qquad [4]$$

where t is the time at any point during the discharge and Q_c is the amount of available cathode active material expressed in units such as ampere hours per unit area.

When Eq. [4] is substituted in Eq. [3]

$$E_c = E_{sc} - K_c\left(\frac{Q_c}{Q_c - it}\right)i \qquad [5]$$

Similarly

$$E_a = E_{sa} - K_a\left(\frac{Q_a}{Q_a - it}\right)i \qquad [6]$$

where the subscripts a and c denote the anode and cathode values for the constants, respectively. A sign convention is used here which makes the value of the potential terms positive.

If Q_a is approximately equal to Q_c, as it generally is in a well designed cell, Eq. [5] and [6] can be summed to give

$$E = E_s - K\left(\frac{Q}{Q - it}\right)i \qquad [7]$$

where $E = E_a + E_c$ is the potential of the cell (neglecting the internal resistance) at any time t during the discharge; $E_s = E_{sa} + E_{sc}$ is a constant potential; $K = K_a + K_c$ is the polarization coefficient in ohm cm^2; and $Q = Q_a = Q_c$ is the available amount of active material in coulombs or similar units per unit area.

If Q_a is appreciably larger than Q_c, then the numerical increase in the value of the last term in Eq. [6] will be small compared to the numerical increase in the value of the last term of Eq. [5] as (it) approaches Q_c in value. Consequently, the second term of Eq. [6] can be considered to be approximately constant and the sum of Eq. [5] and [6] will still have approximately the form shown in Eq. [7]. Under these conditions the approximate values of K, Q and E_s will be $K = K_c$, $Q = Q_c$, and $E_s = E_{sa} + E_{sc} - K_a i$. If Q_c is appreciably larger than Q_a, then the approximate values of K, Q, and E_s will be $K = K_a$, $Q = Q_a$, and $E_s = E_{sa} + E_{sc} - K_c i$. Thus Q is determined by the amount of available active material on the controlling electrode which is the one that fails first. A similar argument will show that the same type of equation will be approximately true when several cells are connected in series to form a battery.

When the potential drop due to internal resistance is considered, Eq. [7] becomes

$$E = E_s - K\left(\frac{Q}{Q - it}\right)i - Ni \qquad [8]$$

where N, the internal resistance per unit area, is measured in ohm cm^2 or other suitable units.

When Eq. [8] is evaluated mathematically, a set of curves is obtained, one of which, plotted in Fig. 1, is a dotted line from a to b and a solid line from b to c. The initial drop in potential at the beginning of a cell discharge is not included in Eq. [8]. Consequently another term must be added to correct for the difference between the dotted line potential calculated from Eq. [8] and the solid line gb that represents the actual discharge potential. It has been found that the expression $A \exp(-BQ^{-1}it)$, where A and B are empirical constants, gives an excellent estimate of the initial potential drop in virtually every case. When this term is added to Eq. [8], the final equation

$$E = E_s - K\left(\frac{Q}{Q - it}\right)i - Ni + A\exp(-BQ^{-1}it) \qquad [9]$$

is obtained. In a number of cases the initial drop in potential was too rapid to be included in the observed experimental data and consequently, the value of $A \exp(-BQ^{-1}it)$, being negligible, could be ignored.

That portion of the discharge curve that lies to the right of point b in Fig. 1 could be predicted from Eq. [9] if the numerical values of E_s, K, Q, and N were known, providing the basic assumptions were true. However, the labor involved in determining these values would be so large that it probably would be easier, and certainly more accurate, to determine discharge curves experimentally. However, Eq. [9] can be fitted numerically to experimental discharge data, thus determining empirical values of E_s, K, Q, N, A, and B. Such a numerical equation gives an accurate description of the cell or battery discharge and can be used to describe energy evolution, cell capacity, and can be used in predicting cell capacities. Despite its successful applications, it must be considered to be an empirical equation since the numerical values of K, Q, and N that are determined in this manner will vary considerably at times from their true values as defined in the basic assumptions.

There are a number of methods that can be used to determine the numerical values of E_s, K, Q, N, A, and B in Eq. [9] from experimental discharge data, most of which are unsuitable. The least squares solution is particularly involved and time-consuming. The following approach is easily applied, rapid, reasonably accurate and is used in fitting Eq. [9] to discharge curves obtained at a number of current densities. In Fig. 1, four points, labeled 1, 2, 3, and 4 have been selected on two discharge curves which were obtained at the moderately low current density, i_a, and the moderately high current density, i_b. The values of E and (it) at points 1, 2, 3, and 4 are E_1, E_2, E_3, and E_4 and i_bt_1, i_at_2, i_bt_3, and i_at_4, respectively. These four points are chosen to the right of the initial potential drop. Thus the value of $A\exp(-BQ^{-1}it)$ is negligible and the potential at point 2 is found from Eq. [9] to be approximately

$$E_2 = E_s - K\left(\frac{Q}{Q - i_at_2}\right)i_a - Ni_a \qquad [10]$$

Similarly

$$E_4 = E_s - K\left(\frac{Q}{Q - i_at_4}\right)i_a - Ni_a \qquad [11]$$

Subtracting Eq. [11] from Eq. [10] gives

$$E_2 - E_4 = Ki_a\left(\frac{Q(i_at_4 - i_at_2)}{(Q - i_at_4)(Q - i_at_2)}\right) \qquad [12]$$

The equation for $E_1 - E_3$ is obtained in a similar manner and is divided into Eq. [12] to give

$$\frac{E_2 - E_4}{E_1 - E_3} = \frac{i_a}{i_b}\,\frac{(i_at_4 - i_at_2)}{(i_bt_3 - i_bt_1)}\,\frac{(Q - i_bt_3)(Q - i_bt_1)}{(Q - i_at_4)(Q - i_at_2)} \qquad [13]$$

When numerical values of E, i, and (it) are taken from the discharge data in Fig. 1 and substituted in Eq. [13], a quadratic equation in Q is obtained which is solved to give a numerical value of Q. This value of Q is substituted in Eq. [12] and solved to obtain a numerical value of K. When these values of Q and K are substituted in Eq. [10] and a similar equation for E_1, two simultaneous equations are obtained which may be solved to give numerical values for E_s and N. When these values of E_s, N, K, and Q are substituted in Eq. [9], E is obtained as a specific function of (it). The calculation of Q by use of Eq. [13] can generally be simplified by choosing point 2 in a manner such that i_at_2 equals either i_bt_3 or i_bt_1.

The two discharge curves, i_a and i_b, that are chosen as a basis for these calculations should be representative of the complete set of discharge curves and should show no obvious visual discrepancies that would indicate variations not present in the other curves. They are selected in the following manner. If (it) is held constant, Eq. [9] shows that the potential E to the right of point b in Fig. 1 may be stated as a linear function of the current density, i, in the form

$$E = E_s - B_1 i \qquad [14]$$

where B_1 is a constant equal to $K\left(\frac{Q}{Q - it}\right) + N$

A fairly good fit to Eq. [14] is shown in Fig. 2 where E has been plotted as a function of i for five values of

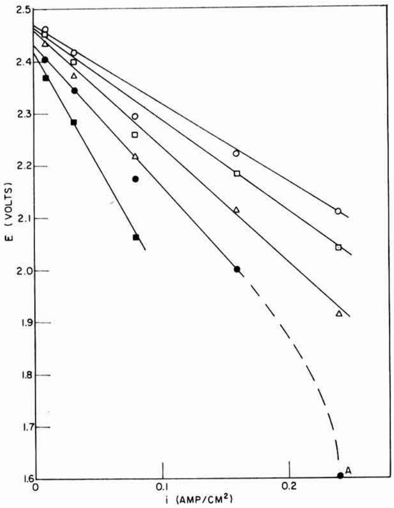

Fig. 2. Potential during cell discharge *vs.* current density for constant values of (*it*). The *it* values in amp-hr/cm²: ○, 0.00266; □, 0.00532; △, 0.00798; ●, 0.01063; ■, 0.01329.

(*it*) using the discharge data for the lead-zinc cell shown in Fig. 4g. The potentials, E at the current density, $i = 0.0798$ amp/cm², were considerably lower than the straight lines drawn through the corresponding values of (*it*), thus showing that this particular discharge was out of agreement with the remainder of the data. Variations this large were not observed as a rule. The remaining four values of i gave good straight line fits in Fig. 2. Either of the two low values of i could be used for i_a and either of the two high values could be used for i_b. As a rule a plot of E *vs.* i for each of two values of (*it*) will be sufficient to select satisfactory values of i_a and i_b. Points such as A which were taken past the knee of the discharge curve should not be used in making up these charts of E *vs* i. Very low values and very high values of i are avoided if feasible in selecting i_a and i_b since these extreme values have a tendency to be less accurate. With a little experience, i_a and i_b often can be selected on the basis of judgment without drawing up a chart such as that shown in Fig. 2.

If Eq. [9] is a perfect fit for the discharge data, then the plot of E *vs.* i as illustrated in Fig. 2 would consist of straight lines intersecting on the E axis at $E = E_s$. If the plot of E *vs.* i gives lines that do not intersect on the E axis or if they are curves, then Eq. [9] does not describe the discharge data perfectly. However, Eq. [9] is so adaptable that it can describe such cases with good accuracy and it has not been necessary to reject any data on this account. Discharge data were not accepted for study here whenever they were so erratic and full of error that a plot of E *vs.* i did not give some semblance of a smooth curve. It was found that all of the data that were acceptable on this basis could be fitted by Eq. [9]. Virtually all of the room temperature discharge data taken from the literature were found to be acceptable. At low temperatures the available data were more erratic and less acceptable.

The points 1, 2, 3, and 4 used to calculate the numerical values of the parameters K, Q, and N are selected in the manner illustrated in Fig. 1. A tangent is drawn to the high current density discharge curve at point d and point f is selected to be 0.1v below the tangent line. Point d is determined by eye by laying a transparent plastic straight edge tangent to the curve and adjusting the point of tangency until $i_b t_d$ equals 0.5 $i_b t_f$. This method is rapid and sufficiently accurate. Point e is located in a manner similar to f. The value of E for point 3 is approximately 0.03v greater than it is for point f. The value of E for point 4 is approximately 0.02v greater than it is for point e. Point 1 is chosen so $i_b t_1$ equals approximately 0.5 $i_b t_3$. If $i_b t_f / i_a t_e$ is less than 0.7, point 2 is chosen directly above point 3 so that $i_a t_2$ will equal $i_b t_3$. If $i_b t_f / i_a t_e$ is greater than 0.7, point 2 is chosen directly above point 1 so that $i_a t_2$ will equal $i_b t_1$. This procedure gives an approximate location of the points which supply the numerical data to substitute in Eq. [12] and [13], and make possible the calculation of numerical values of K, Q, N, and E_s which can be substituted in Eq. [9] along with values of A and B to give a fairly good numerical description of the discharge data. Values of E *vs.* (*it*) for different discharge rates can be calculated from this numerical equation and compared to the actual discharge data. If the agreement is not good enough, it can be improved by the method of successive approximations. A new calculation can be made using slightly different locations for one or more of the four points on the two discharge curves, i_a and i_b. If the calculated points were too far away from the measured results in the area to the left of some point such as 4, it could be corrected by selecting a new location for point 4 which would be slightly to the left of the old location and calculating a new numerical equation. The points calculated by this new equation to the right of point 4 would be a little farther away from the actual discharge data as a rough rule than those calculated from the first equation. A fairly good fit should be obtained with the first calculated equation. If it is at all possible, a very good fit will have been obtained by the third calculation. Each calculation should take less than one hour of time.

Table I. Values of ΔE in volts

	(*i t*)						
i	2	5	10	20	30	50	65
2	0.116	0.106	0.091	0.068	0.045	0.019	0.007
10	0.133	0.118	0.088	0.057	0.037	0.013	0.002
20	0.145	0.123	0.087	0.050	0.032	0.008	0.000
40	0.144	0.120	0.084	0.048	0.027	0.006	0.000
60	0.141	0.117	0.087	0.056	0.030	0.008	0.002
80	0.140	0.115	0.086	0.056	0.031	0.003	0.001
100	0.143	0.123	0.085	0.049	0.026	0.009	0.003
120	0.153	0.118	0.085	0.049	0.025	0.010	0.000
Avg.	0.139	0.118	0.087	0.054	0.032	0.0095	0.0018

The calculations thus far are sufficient to give a numerical evaluation of Eq. [8], which is plotted in Fig. 1 as a dotted line from a to b and a solid line from b to c. The difference in potential, ΔE, between this calculated dotted line of Eq. [9] and the true discharge potential shown by the solid line gb in Fig. 1 is approximated by the term $A \exp(-BQ^{-1}it)$ in Eq. [10]. In Table I values of ΔE *vs.* *it* are given for each discharge curve of the Edison cell shown in Fig. 4a. The average values of ΔE *vs.* (*it*) in Table I are plotted on semi log paper in Fig. 3 and fitted by a straight line

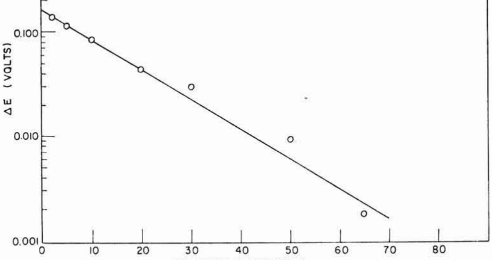

Fig. 3. Determination of ΔE from numerical data

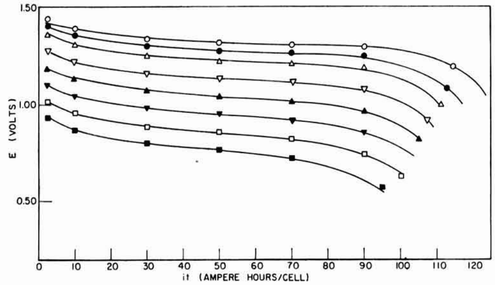

Fig. 4a-g. Comparison of points calculated from discharge equations with solid lines representing actual discharges at various current densities. a. Edison cell, NiOOH-Fe-KOH. Calculated points, amp/cell: ○, 2; ●, 10; △, 20; ▽, 40; ▲, 60; ▼, 80; □, 100; ■, 120.

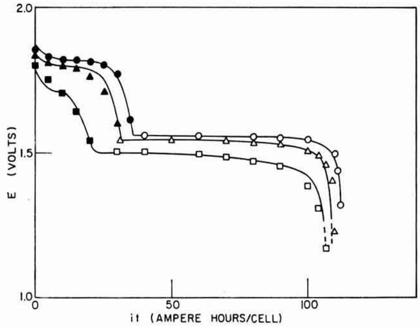

Fig. 4b. Silver cell, AgO-Zn-KOH. Calculated points, amp/cell: ●—○, 2.5; ▲-△, 10; ■-□, 60.

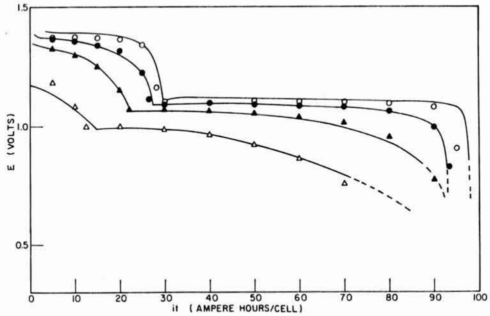

Fig. 4c. Silver cadmium cell, AgO-Cd-KOH. Calculated points, amp/cell: ○, 0.625; ●, 2.5; ▲, 10.0; △, 40.0.

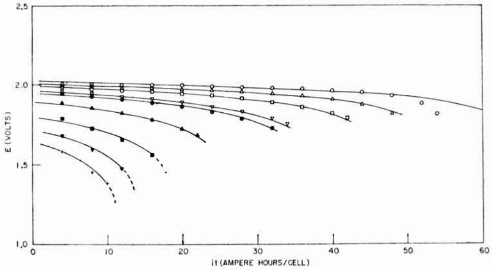

Fig. 4d. Lead acid cell, PbO_2-Pb-H_2SO_4. Calculated points, amp/cell: ○, 0.8; △, 2; □, 4; ▽, 8; ●, 10; ▲, 20; ■, 40; ▼, 60; +, 80.

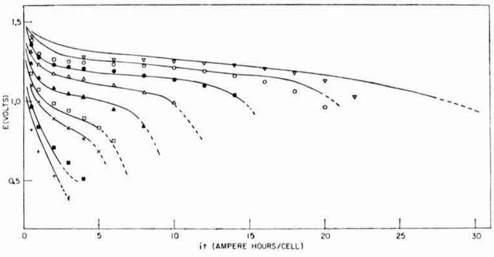

Fig. 4e. Dry cell. Calculated points, amp/cell: ▽, 0.125; ○, 0.25; ●, 0.5; △, 1.0; ▲, 2.0; □, 3.0; X, 4.0; ■, 6.0; +, 8.0.

whose equation is $\Delta E = A \exp(-BQ^{-1}it)$. The intercept on the ordinate gives the numerical value of A. The numerical value of B/Q can be calculated from the slope or from a single point taken on the straight line. In nearly all cells the value of ΔE is much less at high values of it/Q than in the example shown in Fig. 3 where $\Delta E = 0.006$v at it equals 50 or it/Q equals 0.433. In most cells ΔE would be less than 0.006v at a value of it/Q equal to 0.10 and would be close to zero in value at it/Q equals 0.15. If points 1 and 2 were chosen in Fig. 4a at $it = 50$ then a correction of $\Delta E =$ 0.006v should be subtracted from the values of E_1 and E_2 to be used in calculating the constants in Eq. [9]. This value of ΔE could not be estimated accurately until after the first calculation had been made.

Discussion of the Equation and its Applications

Experimental discharge data for a number of different types of batteries have been plotted as solid lines in Fig. 4 (1, 2, 3, 4, 5). The potential E is shown for various current densities, i, as a function of (it) which is expressed in ampere hours per square centimeter or ampere hours per cell where the area is not known. Equation [9] has been fitted numerically to each set of discharge data thus obtaining a different numerical equation for each chart in Fig. 4. The numerical values of the constants for each of these equations are shown in Table II and are dependent on the unit of time, t, and also on the unit of area used in defining the current density. Since the area is unknown in most cases, the area of the entire cell is

Table II. Values of the parameters in Eq. [9] for various types of cells

Type cell	Fig. No.	E_s, v	K, ohm cell*	Q, amp-hr/cell*	N, ohm cell*	A, v	B/Q Cell* (amp-hr)$^{-1}$	Temp, °C	Ref.
Edison	4a	1.3080	0.0003936	115.4	0.00390	0.165	0.06564	Room	1
Silver-zinc	$4b_1$	1.8310	0.005138	37.06	−0.00388	0.020	0.60	27	2
	$4b_2$	1.5567	0.00040	112.0	0.00067			27	2
Silver-cadmium	$4c_1$	1.3733	0.00831	28.68	−0.00543			27	
	$4c_2$	1.0990	0.00260	95.75	−0.000965			27	
Lead acid	4d	2.0030	0.0189	58.31	−0.0150			25	3
Dry cell	4e	1.2743	0.3343	25.61	−0.269	0.360	2.197	25	
Ni-Cd	4f	1.2021	0.001358	74.67	−0.000241	0.080	0.1386	−18	4
Lead-zinc	4g*	2.4607	0.9722	0.01737	0.3589			27	5

* The word cell is defined as the electrode area of the entire cell. It is replaced in 4g by cm^2. Since the area terms cancel out in Eq. [9], it is not necessary to know the numerical value of the area.

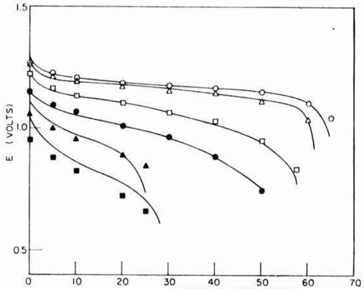

Fig. 4f. Sintered nickel cadmium cell, NiOOH-Cd-KOH, —18°C. Calculated points, amp/cell: ○, 15; △, 24; □, 65; ●, 120; ▲, 200; ■, 300.

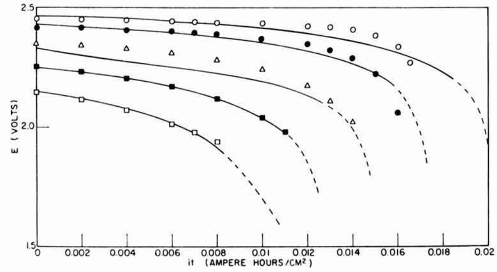

Fig. 4g. PbO_2-Zn-H_2SO_4 reserve cell. Calculated points, amp/cm^2: ○, 0.00957; ●, 0.0319; △, 0.0798; ■, 0.1595; □, 0.2393.

taken as the unit area and the current density is defined as the amperes per cell and is equal in value to the total discharge current. The points in Fig. 4 are calculated from these equations. It can be seen that the calculated points give good fits in every case to the solid lines that represent the actual discharge data. Thus the information in Table II is sufficient to give an excellent description of the discharge data in Fig. 4 at a considerable savings in space. Equation [9] was applied to a wide variety of discharge data from various types of physically constructed batteries for each of the common battery systems. The examples selected for Fig. 4 were in each case the one which covered the widest range of current densities. Equation [9] was also fitted successfully to discharge data from the following systems: PbO_2-Cd-H_2SO_4, HgO-In-KOH, air cell-air-Zn-KOH, AgCl-Zn-NaCl, PbO_2-Pb-$HClO_4$, CuO-Zn-NaOH, NiOOH-Zn-KOH, Cl_2-Zn-$ZnCl_2$, PbO_2-Sn-$HClO_4$, PbO_2-Pb-HBF_4, HgO-Zn-KOH. No individual curves were omitted in any case. The poorest fit obtained in all the cases studied was with the dry cell data which is shown in Fig. 4e. Most of the data was taken from the literature and was selected to cover as wide a range of current densities as possible. Unfortunately, the amount of low temperature discharge data was limited and some of it had to be rejected as erratic when tested by the method illustrated in Fig. 3.

In Fig. 4b and 4c the discharge took place in two steps and it was found that a separate equation could be fit to each step. The first step in each case is indicated by the subscript 1 on the figure number in Table II. For example, the equation for the silver cell in Fig. 4b would be

$$E = 1.8310 - 0.005138\left(\frac{37.06}{37.06 - it}\right) i + 0.00388\, i + 0.020 \exp\,(-0.60\, it)$$

or

$$E = 1.5567 - 0.0004\left(\frac{112}{112 - it}\right) i - 0.00067\, i$$

whichever is higher in value.

Whenever the calculated values of E_s, K, Q, and N are the true or defined values and are not affected by the choice of the four points, Eq. [9] fits that particular discharge data theoretically. Whenever the calculated values of E_s, K, Q and N are not the true or defined values and are affected by the choice of points 1 to 4, Eq. [9] is fitting that particular discharge data empirically. In this latter case, there are a number of specific combinations of numerical values of E_s, K, Q and N which will give good fits to a particular set of discharge curves. Among these combinations E_s and Q will be fairly constant while K and N may vary somewhat, N becoming smaller as K becomes larger. For example, two individuals fitting Eq. [9] to a particular set of discharge curves might get two different equations, each of which fit the data quite well even though they had appreciably different values for K and N.

As a very rough rule, a closer approach to a theoretical fit is generally found in the presence of one or more of the following conditions: the discharge data covers a narrow range of current densities, the potential drop due to polarization is low, the electrolyte does not change in composition during discharge, the slope of the discharge curves before the knee is relatively small, the ratio $(it)/Q$ is fairly large and covers a relatively narrow range of values of (it), and the calculated value of N is not negative. Most of these conditions can be observed in Fig. 4a.

In any case, Eq. [9] is so adaptable that wide variations in its constants, particularly K and N, enable it to be fitted with good accuracy to a very wide range of discharge data. A large increase in the numerical value of K will be accompanied by such a large decrease in the value of N that N will often be negative in value as can be seen in Table II. Since N is the internal resistance in the original derivation and theoretically cannot be negative in value, it is obvious that Eq. [9] must be considered to be empirical in most of its curve fitting applications and there is no reason to believe that it should have to describe fully the discharge of every type of battery.

In Fig. 2 the measured potential is low for the points at i equals 0.0798 amp/cm^2. In Fig. 4g the measured potential at this current density is appreciably lower than the calculated potential thus indicating the very strong likelihood of an error in this data. When there are only three discharge curves and two of them are correct, it is not possible to tell by this method which one of the three is in error without collecting more data. A fourth discharge made at a different current density will, if correct, determine which of the other three curves contains the error.

An examination of all of the data fitted by Eq. [9] shows that the differences between the calculated and the measured results are often larger at the highest current densities than they are at intermediate current densities. This larger variation can be attributed to the high relative dispersion of the data; the fact that the highly simplified calculation methods given here tend to give the poorest fit at high current densities; and the fact that the poorest fit is often obtained at the extreme limits when fitting equations to measured data. There is also a tendency for a very few of the calculated curves at the lowest current density to have less slope and a smaller capacity than the observed data. This condition is most noticeable in Fig. 4g and seems to be most generally associated with batteries whose electrolytes change appreciably in concentration during discharge. As a rough empirical approximation, it is assumed that the drop in potential in a battery is directly proportional to the change in electrolyte concentration during discharge, assuming all other factors are neglected. Equation (9) can then be written as

$$E = E_s - K\left(\frac{Q}{Q - it}\right) i - Ni + A \exp(-BQ^{-1}it) - Cit \qquad [15]$$

where C is a constant.

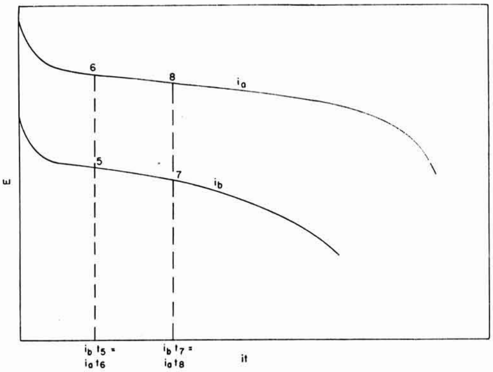

Fig. 5. Typical discharge curves to be used in numerical calculation of C.

To determine the numerical value of C select four points as shown in Fig. 5 which are far enough past the initial potential drop for the exponential term to be negligible. From Eq. [15]

$$E_5 = E_s - Ki_b \left(\frac{Q}{Q - i_b t_5}\right) - Ni_b - Ci_b t_5 \qquad [16]$$

and

$$E_7 = E_s - Ki_b \left(\frac{Q}{Q - i_b t_7}\right) - Ni_b - Ci_b t_7 \qquad [17]$$

Subtracting Eq. [17] from Eq. [16] gives

$$E_5 - E_7 = Ki_b \left[\left(\frac{Q}{Q - i_b t_7}\right) - \left(\frac{Q}{Q - ibt_5}\right)\right] + C(i_b t_7 - i_b t_5) \qquad [18]$$

Similarly

$$E_6 - E_8 = Ki_a \left[\left(\frac{Q}{Q - i_b t_7}\right) - \left(\frac{Q}{Q - ibt_5}\right)\right] + C(i_b t_7 - i_b t_5) \qquad [19]$$

From Eq. [18] and Eq. [19]

$$C = \frac{i_b(E_6 - E_8) - i_a(E_5 - E_7)}{(i_b - i_a)(i_b t_7 - i_b t_5)} \qquad [20]$$

Numerical values of C are calculated from Eq. [20] and substituted in Eq. [15].

Let $E' = E + Cit$.

Then $E_1' = E_1 + Ci_b t_1$, $E_2' = E_2 + Ci_a t_2$, $E_3' = E_3 + Ci_b t_3$, and $E_4' = E_4 + Ci_a t_4$. If E_1', E_2', E_3', and E_4' are substituted for E_1, E_2, E_3, E_4, respectively, in Eq. [10] to [13], they can be used to calculate numerical values of Q, K, N, and E_s in the manner previously described.

Numerical values of Eq. [15] were determined in this manner for the lead-zinc cell shown in Fig. 4g and found to be

$$E = 2.4775 - 0.9237 \left(\frac{0.0181}{0.0181 - it}\right) i - 0.4295\, i - 4.25\, it$$

Calculated points from this equation are shown in Fig. 6 to give a better fit to the experimental data than was obtained by the use of Eq. [9].

If the basic assumptions are assumed to be true during the charge of a cell, then the following equation would hold for the potential during charge

$$E = E_s + K \left(\frac{Q}{Q - it}\right) i + Ni - A \exp(-BQ^{-1}it) \qquad [21]$$

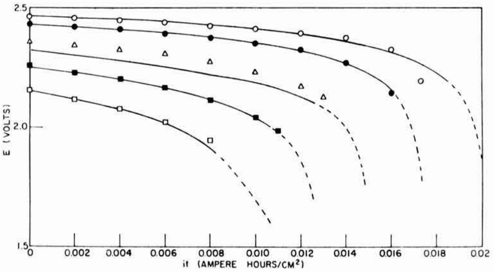

Fig. 6. Comparison of points calculated from the discharge equation with solid lines representing actual discharges at various current densities. PbO_2-Zn-H_2SO_4 reserve cell. Calculated points, amp/cm²: ○, 0.00957; ●, 0.0319; △, 0.0798; ■, 0.1595; □, 0.2393.

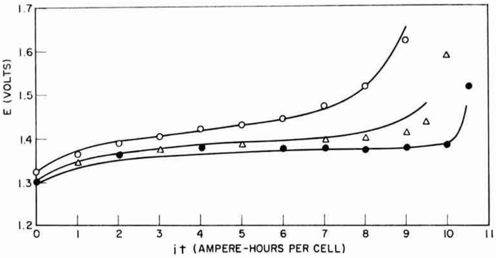

Fig. 7. Comparison of the charge data of a Ni-Cd cell with the calculated results for various current densities. Nickel cadmium cell, Ni-OOH-Cd-KOH. Calculated points, amp/cell: ○, 16.0; △, 2.5; ●, 0.16.

Equation [21] can be obtained from Eq. [9] by reversing the signs of the last three terms. Equation [21] has been fitted to the charge of a Ni-Cd cell in Fig. 7. The solid lines represent the actual data and the points are calculated from the equation

$$E = 1.379 + 0.0024 \left(\frac{1}{1 - 0.095\, it}\right) i - 0.00116\, i - 0.08 \exp(-0.693\, it)$$

The use of Eq. [21] in describing the charging of a cell has been tested on a very limited amount of data. Consequently, it is not yet certain to what extent it can be successfully applied.

The total energy W_t that has been evolved from the beginning of the discharge up to time t is defined by the equation

$$W_t = \int_o^t i\, E\, dt$$

Substituting Eq. [8]

$$W_t = \int_o^t \left[E_s i - K\left(\frac{Q}{Q - it}\right) i^2 - Ni^2 + Ai \exp(-BQ^{-1}it) \right] dt \qquad [22]$$

$$W_t = [E_s\, it + KQi \ln(Q - it) - Ni^2 t - AQ/B \exp(-BQ^{-1}it)]_o^t \qquad [23]$$

$$W_t = E_s it - KQi \ln(1 - it/Q)^{-1} - Ni^2 t + AQ/B(1 - \exp(-BQ^{-1}it)) \qquad [24]$$

The constants from an equation describing the discharge of a Ni-Cd cell at 27°C were substituted in Eq. [24] and the total energy evolved at time t was found to be

$$W_t = 1.25\, it - 0.0238\, i \ln(1 - 1.05\, it)^{-1} - 0.006\, i^2 t + 0.0248\, [1 - \exp(-3.83\, it)] \qquad [25]$$

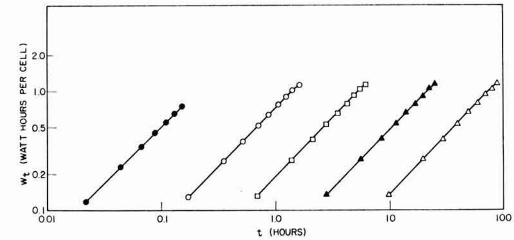

Fig. 8. Comparison of the energy evolved during the discharge of a Ni-Cd cell with the calculated results for various current densities. Sealed nickel cadmium cell, NiOOH-Cd-KOH, 27°C. Calculated points, amp/cell: ●, 4.5; ○, 0.56; □, 0.14; ▲, 0.035; △, 0.010.

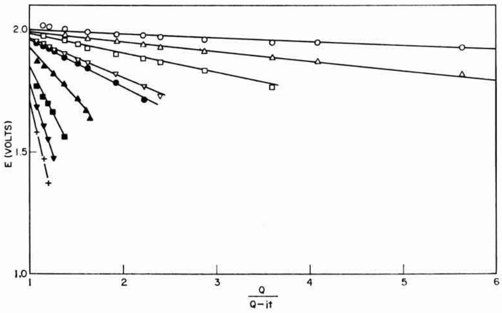

Fig. 9. Discharge curves showing the potential as a function of $Q/Q\text{-}it$ for various current densities. Lead acid cell, PbO_2-Pb-H_2SO_4. Current density, amp/cell: ○, 0.8; △, 2; □, 4; ▽, 8; ●, 10; ▲, 20; ■, 40; ▼, 60; +, 80.

In Fig. 8, W_t in watt hours per cell for a Ni-Cd battery has been plotted as a function of t in hours for various values of the cell current in amperes. The solid lines are obtained from calculations based on numerical integration of the actual discharge data. The points are calculated from Eq. [24]. The agreement between the calculated and the measured results in such cases depends entirely upon how well Eq. [9] can be fitted to the original discharge data.

Once the discharge is past the initial potential drop, the exponential term becomes negligible and Eq. [9] can be written as

$$E = E_s - Ni - \left(\frac{Q}{Q - it} \right) Ki \qquad [26]$$

which shows the potential E to be a linear function of $Q/(Q - it)$ with slope $-Ki$ for any given current density, i. Actual discharge potentials were taken from the lead acid battery discharge data in Fig. 4d and plotted in Fig. 9 against $Q/(Q - it)$ for each of nine current densities. Straight lines gave good fits to these plotted points. The average value of the K's, determined from the slopes of each of these nine lines was 0.0195 as compared to the calculated value of 0.0189 given in Table II.

In Fig. 9 the values of E for $Q/(Q - it)$ equals one can be seen from Eq. [26] to be

$$E = E_s - (N + K)i \qquad [27]$$

which shows E here to be a linear function of i with slope, $-(N + K)$, and intercept, E_s. Values of E for $Q/(Q - it)$ equals one were taken from Fig. 9 and plotted in Fig. 10 to give a straight line. The numerical values of E_s and N determined from this straight line were 1.998 and -0.0155 as compared to the calculated values of 2.003 and -0.0150 given in Table II. The values of E_s, K, and N determined by the two methods are virtually identical and show that the graphical method of Fig. 9 and 10 can be used in fitting Eq. [9] to discharge data whenever the value of Q is known. If the basic assumption holds true, then Q can be calculated from the amount of active material on the controlling electrode and the graphical method is applicable. In the more empirical applications, such as the lead acid battery just shown, the calculated value of Q will be somewhat less than the value determined from the amount of active material and the graphical method would not be accurate. Almost all of the available discharge data gave no information on the amount of active materials and consequently the feasibility of using this graphical method for fitting Eq. [9] to discharge data has not yet been determined.

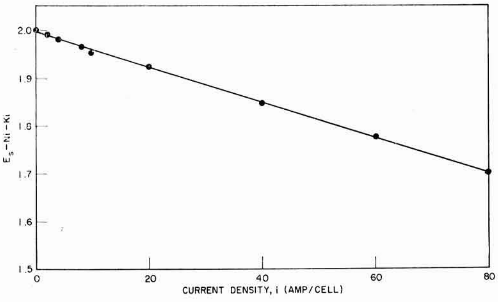

Fig. 10. E_s-Ni-Ki plotted as a function of current density

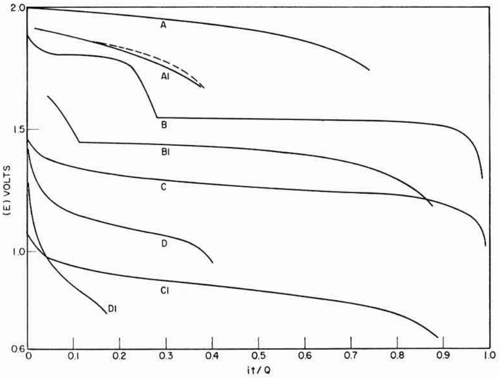

Fig. 11. Discharge curves showing the cell potential during discharge as a function of the fraction of active material used up at any given time.

	Rate	Q/i
A, Lead acid	**11 hr**	**14.6 hr**
A1, Lead acid	**1 hr**	**2.8 hr**
B, Silver zinc	**11 hr**	**11.2 hr**
B1, Silver zinc	**1 hr**	**1.14 hr**
C, Edison	**11 hr**	**11.3 hr**
C1, Edison	**1 hr**	**1.12 hr**
D, Dry cell	**11 hr**	**25.6 hr**
D1, Dry cell	**1 hr**	**6.4 hr**

Presentation of Discharge Data

A study of Eq. [9] suggests the possibility of plotting battery discharge data against dimensionless quantities in a manner that would make possible more direct comparisons between various types of cells. In Fig. 11 the potential during discharge is plotted as a function of it/Q where it/Q is the fraction of active material used up at time, t. Discharge data are shown here at the 1-hr and the 11-hr rate for four common types of cells. The value of it/Q at the end of the discharge is the efficiency of utilization of the active material. In each case, the discharge was assumed to be ended when E equalled $E_s - Ki - Ni - 0.25$v. Thus in Fig. 1, curve i_a, the end voltage would be 0.25v below the voltage at point a. A drop of more than 0.25v would have precluded the use of much of the available data. In Fig. 4 the discharge curves are shown as dotted lines wherever they extended past this assumed end point.

Here in Fig. 11 is a method of comparing at equal discharge times such factors as efficiencies, potentials, variations of potentials with time, potential drops due to internal resistance, etc., for various types of constructions of cells. The two curves at A1 represent two different sizes and constructions of lead acid cells. Although the difference in discharge characteristics is small between these two cells, it could, in many cases, be quite large and could be readily demonstrated on a chart of this type. Other things being equal, the cell size is not important here, since each cell is being discharged at a particular value of Q/i that is held constant with change in cell size, which is equivalent to saying n times the current would be drawn from a cell n times as large. The values of Q/i given in Fig. 11 represent the time each cell would have taken to discharge 100% of the active material on the controlling electrode at the particular current density, i. The discharge characteristics of the four cells in Fig. 11 could have been compared by plotting E *vs.* it/Q at a constant value of Q/i such as 10 hr, thus giving a slightly different graph. A number of other variations can be made of this chart. The vertical axis could be the ratio of the discharge potential to the theoretical potential. In this case the area under the curve would be the theoretical watt hour efficiency. If the vertical axis were the ratio of the discharge potential to the average charge voltage, E_c, the area under the curve would be the watt hour efficiency defined by the ratio of the output in watt hours to the input in watt hours. The equation for this latter curve can be obtained by dividing E_c into Eq. [9] to give

$$\left(\frac{E}{E_c}\right) = \left(\frac{E_s}{E_c}\right) - \left(\frac{K}{E_c}i\right)\left[\frac{1}{1-(it/Q)}\right] - \left(\frac{N}{E_c}i\right) + \left(\frac{A}{E_c}\right)[\exp(-BQ^{-1})(it)] \qquad [28]$$

where each quantity in brackets or parentheses is dimensionless. In Fig. 11 the values of it/Q were taken from Table II and are empirical to a certain extent. If Q had been calculated from the actual amounts of active material on the controlling electrode, its value would have been slightly larger and the discharge curves in Fig. 11 would be changed slightly. Values of (it) per unit weight of active material or per unit cell weight, or watt hour efficiencies could have been used in place of it/Q for the abscissa in Fig. 11. The important thing in each of these cases is that the use of some form of dimensionless quantity, or factor closely related thereto, as either or both of the coordinates enables a quantitative, visual study and comparison to be made of the characteristics of certain types of equivalent discharges, either for different types of cell systems, or different constructions of the same cell system, or both. As shown in Eq. [28], the equation for each of these cases can be obtained easily from Eq. [9].

Manuscript received Feb. 4, 1965. This paper was presented at the Boston Meeting, Sept. 16-20, 1962.

Any discussion of this paper will appear in a Discussion Section to be published in the June 1966 JOURNAL.

REFERENCES

1. C. F. Anderson, *This Journal*, **99**, 244C (1952).
2. C. P. Wales, NRL Rpt 5167, 11 Aug. 1958.
3. E. A. Hoxie, *Trans.*, AIEE, Part II Applications and Industry, **73**, 17 (1954).
4. G. B. Ellis, H. Mandel, and D. Linden, *This Journal*, **99**, 250C (1952).
5. W. J. Schlotter, *ibid.*, **99**, 205C (1952).

GLOSSARY

A	Numerical value of Δe at $(it) = 0$ (v)
α	Transfer coefficient (dimensionless)
B	Constant parameter (dimensionless)
C	Constant parameter (volt cm^2 amp^{-1} sec^{-1})
E	Cell potential during discharge (v)
E_a	Anode potential during discharge (v)
E_c	Cathode potential during discharge (v)
E_s	A constant potential parameter (v)
ΔE	Initial potential drop (v)
η	Steady-state activation overpotential (v)
F	Faraday (coulombs $equiv.^{-1}$)
i	Apparent current density (amp cm^{-2})
i_{am}	Active material current density (amp cm^{-2})
i_o	Apparent exchange current density (amp cm^{-2})
K	Coefficient of polarization (ohm cm^2)
K_a	Coefficient of polarization for anode (ohm cm^2)
K_c	Coefficient of polarization for cathode (ohm cm^2)
N	Internal resistance of cell (ohm cm^2)
Q	Amount of active material on controlling electrode as coulombs (coulombs cm^{-2})
Q_a	Amount of active material on anode as coulombs (coulombs cm^{-2})
Q_c	Amount of active material on cathode as (coulombs cm^{-2})
R	Gas constant (amp volt sec deg^{-1} $mole^{-1}$)
T	Temperature (deg)
t	Time (min or hr)
W_t	Energy evolved during cell discharge (amp volt sec cm^{-2})
Z	Number of electrons transferred in rate determining step (dimensionless)

The Electrode Potential of the Semiconductor CuS in Solutions of Copper Ions and Sulfide Ions

P. Ruetschi[1] **and R. F. Amlie**

The Carl F. Norberg Research Center, The Electric Storage Battery Company, Yardley, Pennsylvania

ABSTRACT

The electrode potential of cupric sulfide was measured in aqueous acidic solutions of cuprous chloride and cupric chloride, as well as in alkaline solutions of sulfur and sulfide ions. The redox couples Cu^{++}/Cu^{+} and S/S^{--} exhibit high reversibility on this electrode material. Nonstoichiometric excess sulfur in CuS behaves energetically like free elemental sulfur. The reason for the voltage increase observed when elemental sulfur is added to a cuprous chloride electrode is explained by the mechanism that the electrode reaction changes from $e^{+}CuCl \rightleftarrows Cu + Cl^{-}$ to a redox mechanism, $e + CuCl_2 \rightarrow CuCl + Cl^{-}$ at the $CuS^{=}$ solution interface, whereby cupric chloride is generated by the chemical reaction $2CuCl + S \rightleftarrows CuCl_2 + CuS$. The principle of coupling a chemical reaction with an electrochemical reaction in a closed cycle is shown to be of considerable advantage for the construction of certain types of battery electrodes.

As a result of the discovery that electrodes of cuprous chloride in magnesium chloride electrolyte show an increased electrode potential when the cuprous chloride is intimately mixed with elemental sulfur (1), an investigation was undertaken to elucidate the mechanism responsible for this phenomenon. It had been observed previously that cuprous chloride and sulfur mixtures, when suspended in a chloride electrolyte, reacted to form cupric sulfide. This reaction does not take place with mixtures of the dry materials in the absence of aqueous electrolytes, even when heated to the melting point of sulfur, but it proceeds when these mixtures are immersed in acidic aqueous magnesium chloride solutions according to

$$2\,CuCl + S \rightarrow CuS + CuCl_2 \text{ (dissolved)} \qquad [1]$$

The precipitation of CuS was confirmed experimentally by x-ray analysis, and the formation of $CuCl_2$ in solution by colorimetry. As early as 1889 Vortmann and Padberg (2) described this reaction qualitatively.

In view of reaction [1], it was considered desirable to determine the effect of cupric ion concentration on the potential of a cupric sulfide electrode. The present investigation also includes a study of the cupric sulfide electrode in solutions containing both cupric and cuprous ions, and further in solutions containing sulfide ions.

Electrochemical Properties of Metal Sulfides

An investigation of metal sulfide electrodes in aqueous solutions was carried out by Wrabetz, in collaboration with Noddack and Herbst (3-5). According to Wrabetz *et al.* the electrochemical behavior of heavy metal sulfide electrodes in aqueous solutions is influenced by the presence of nonstoichiometric excess sulfur in these materials. The sulfide electrodes differ from a normal electrode system of the first or second kind in that only a minute Faradaic current can flow without a complete exhaustion of the available excess sulfur and a corresponding alteration in the composition of the electrode surface. It was observed that many metal sulfide electrodes, in contact with solutions containing the corresponding cations, establish a reversible potential. It was also found that the metallic sulfides, in aqueous solutions containing the respective cation, have their own electrochemical potential series which is more noble than that of the respective parent metals. Many of the metal sulfides, studied in solutions containing different concentrations of the cation, showed the electrode potentials to be determined by the solute activity in accordance with the Nernst relationship. Only one measurement with a cupric sulfide electrode was described in the work of Wrabetz, and its potential was approximately 0.24v positive to that of copper in the cell system $Pt/CuS/CuSO_4$ (0.1m)/Cu. The potentials were unstable due to high resistance between the loose cupric sulfide powder and the platinum wire used for making contact.

Wrabetz *et al.* (3) were the first workers to systematically study the electrochemistry of metal sulfide electrodes in aqueous solutions; prior investigations lack quantitative data and are thus of limited value. However, a study by Trumpler (6) is pertinent since he measured the potentials of a series of metallic sulfide semiconductors in solutions containing the respective cations. He also studied metal sulfide electrodes in solutions containing sulfide ions and dissolved sulfur (*i.e.,* polysulfide ions), and came to the conclusion that sulfide electrodes exhibited the same potentials as an inert metallic electrode such as platinum.

Cupric sulfide is usually obtained as a lustrous, blue-black salt which is insoluble in water and cold dilute strong acids, although it dissolves readily in hot, moderately dilute nitric acid. Copper(II) sulfide is converted to Cu_2S at elevated temperature in the presence of air, and at lower temperatures in a hydrogen atmosphere. It is slowly oxidized by moist air. Copper(II) sulfide is a semiconductor showing an exceptionally high electronic conductivity, having a specific resistance in the order of 10^{-4} ohm-cm. Badecker (7) reports 1.25×10^{-4} ohm-cm and Fischbeck and Dorner (8) give 4×10^{-5} ohm-cm, which may be compared with 1.7×10^{-6} ohm-cm for copper metal. Cupric sulfide is reported as crystallizing in both the hexagonal and monoclinic systems (9). Remy describes the crystal structure as hexagonal with the lattice constants $a_o = 3.972Å$, $c_o = 16.344Å$.

Experimental

The electrochemical study of copper (II) sulfide in chloride solutions of copper ions, sulfide ions, or polysulfides was carried out by measuring electrode potentials both under equilibrium conditions and during current flow. The experiments were performed in Pyrex glass cells, one of which together with the electric circuit, is depicted in Fig. 1. All electrode potential measurements with chloride electrolytes were made by means of saturated calomel reference electrodes (0.241v *vs.* NHE), with the liquid junction established in the interconnecting capillary tube. In addition to the reference electrode capillary, the cell of Fig. 1 was also provided with a connection to the counter elec-

---

[1] Present address: LeClanche, S.A., Yverdon, Switzerland.

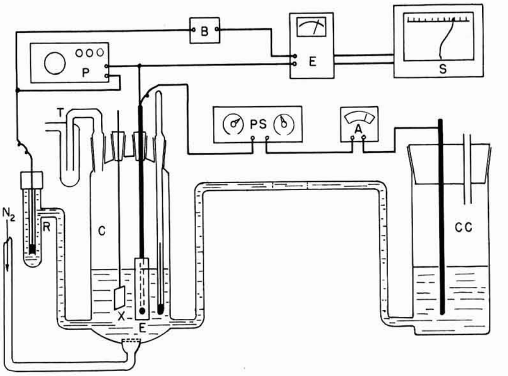

Fig. 1. Schematic of apparatus. C, Pyrex test cell: auxiliary Pt electrode; E, sample electrode; R, reference electrode; CC, counter electrode cell; P, potentiometer; B, bias box; E, electrometer-amplifier; S, strip chart recorder; PS, power supply; A, ammeter.

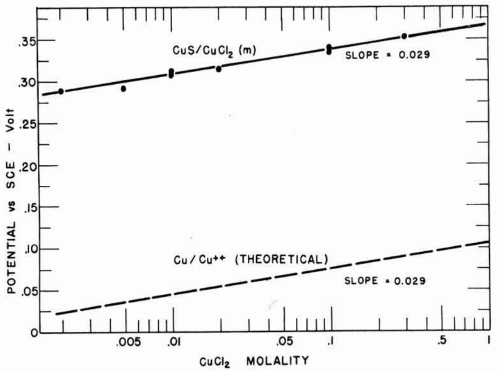

Fig. 3. Cupric sulfide potential as a function of $CuCl_2$ concentration. 1.0*M* HCl, 2*M* total (Cl^-). Theoretical Cu/Cu^{++} couple plot assumes $\gamma Cu^{++} = 1$.

trode compartment and with a gas inlet. Effective purging of dissolved oxygen was realized by the continuous introduction of a finely divided stream of prepurified nitrogen gas ($O_2 < 8$ ppm) introduced through a fritted-glass disk. The nitrogen was purified by passing it through a heated column of copper turnings. The counter electrode was a 0.6 cm diameter graphite rod in a separate compartment, which was connected to the test cell by an electrolyte bridge approximately 25 cm in length. A porous filter paper plug was inserted into the electrolyte bridge to reduce convection between compartments. The top section of the test cell was provided with four standard taper joints which held the sample electrode, the platinized platinum electrode, a gas exit bubble trap, and a thermometer. All experimental data were taken at 25°C.

Potentials were measured by means of both a Rubicon portable potentiometer (±0.0002v) and a General Radio type 1230-A DC Electrometer-Amplifier used to drive a Honeywell recorder. A bias box was included in the electrometer input to avoid switching of the electrometer polarity during discharge. A multirange constant current supply provided well regulated currents over the desired range.

Cupric sulfide electrode samples were retained in a 0.63 cm diameter cavity, drilled into a rectangular epoxy block as shown in Fig. 2. The epoxy block encapsulated a graphite rod of spectrographic purity, 0.63 cm in diameter, to provide contact with the electrode material in the cavity. The cupric sulfide was compacted into the cavity at pressures in the order of 3000 psi (150 lb total force) which was usually sufficient for cohesive compaction and could not be greatly exceeded due to the limited mechanical strength of the cast epoxy. Loosening of the pellet was only observed after prolonged immersion in acidic electrolytes, and this difficulty was eliminated by the addition of a few per cent of powdered Teflon to the CuS powder prior to compaction. Fisher Certified Reagent CuS used in this study was further purified by allowing it to remain in contact with a large quantity of 4% HNO_3 for 24 hr with intermittent shaking to achieve good dispersion. The acid solution acquired a faint blue color during this treatment due to the removal of copper. The sample was filtered, washed with distilled water, and dried at 100°C in air. Electrode potentials were measured during periods up to 3 days to insure that the stable equilibrium values had been obtained.

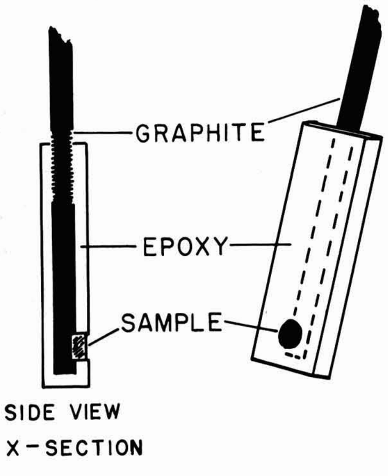

Fig. 2. Epoxy block sample holder

Results and Discussion

Effect of $CuCl_2$ *concentration on the* CuS *electrode potential.*—The dependence of the cupric sulfide potential (*vs.* saturated calomel) on the concentration of cupric chloride is shown in Fig. 3. In addition to the molal $CuCl_2$ concentration indicated, the solutions were 1*M* in HCl, with an addition of KCl adjusted to give a total chloride concentration of 2*M*. The *p*H values of the solutions were maintained essentially constant by this procedure, and the extent of complexing of cupric chloride ions was maintained constant (10). The cupric chloride concentration was varied by more than two orders of magnitude while the ionic strength changed only from 2.0 to 2.3. Under these conditions the mean activity coefficient of cupric chloride can be expected to remain nearly constant throughout the series of measurements. The results show that the CuS electrode in a $CuCl_2$ electrolyte obeys the theoretically expected relationship for a divalent ion. The electrode responds to the Cu^{++} activity in a reversible manner, and the potential-log concentration plot of Fig. 3 has a slope 0.029 which is in agreement with that predicted by the Nernst relationship

$$E = E_{o(CuS/CuCl_2)} + (2.3\,RT/2F)\log[CuCl_2] \qquad [2]$$

at 25°C. The theoretical behavior for the Cu/Cu^{++} electrode couple is also included in this graph for comparison, in order to illustrate that the sulfide electrode is about 0.260v more positive. This potential increase of the sulfide electrode can be explained by the supposition that the nonstoichiometric cupric sulfide, containing excess sulfur in the crystal lattice, can promote the following potential determining reaction

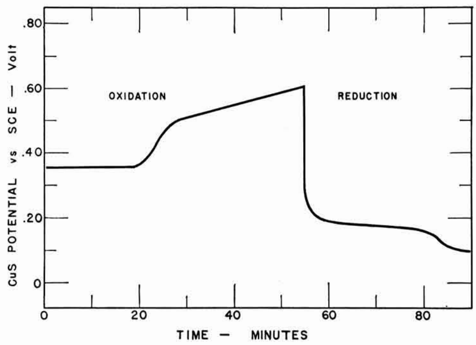

Fig. 4. Chronopotentiometric curve of CuS polarization during charge (oxidation) and discharge. 5 ma (16 ma/cm²); 0.1M $CuCl_2$, 1.0M HCl, 2M total (Cl^-).

$$2e^- + Cu^{++} + S_{(CuS)} \rightleftarrows CuS \qquad [3]$$

or

$$2e^- + Cu^{++} + \square_{(CuS)} \rightleftarrows CuS \qquad [4]$$

where $S_{(CuS)}$ represents excess sulfur and $\square_{(CuS)}$ is a copper ion deficiency in the CuS lattice. Subtracting from [3] or [4] the equation

$$2e^- + Cu^{++} \rightleftarrows Cu$$

one obtains

$$S_{(CuS)} + Cu \rightleftarrows CuS \qquad [5]$$

or

$$\square_{(CuS)} + Cu \rightleftarrows CuS \qquad [6]$$

The free energies of Eq. [5] and [6] determine the voltage difference between the CuS/Cu^{++} electrode and the Cu/Cu^{++} electrode. The experimental value of 0.26v, corresponding to a free energy increase of $\Delta G = -nFE = -11.9$ kcal, is very close to the free energy of formation of CuS from elemental copper and sulfur, namely —11.7 kcal (11). The excess sulfur in CuS is therefore shown to be essentially "free" sulfur.

Cupric sulfide can phenomenologically be considered as a "dilute copper metal," analogous to a metal amalgam. The "dissolved" Cu^{++} ions in CuS are able to equilibrate with Cu^{++} ions in solution and are able to support limited forward and backward electrochemical reactions. It is evident that deposition of Cu^{++} ions into the sulfide can only proceed as long as there is excess sulfur (or deficiency of copper) in the CuS structure. Dissolution of copper can proceed until the surface is so rich in sulfur that conductivity is impaired and strong polarization begins.

Polarization curves at constant current charge and discharge are illustrated in Fig. 4. The CuS/Cu^{++} couple is relatively easily polarized with slight current flow. No metallic copper is formed during cathodic polarization since (Cu^{++}) ions are discharged into the CuS crystal where they combine with excess sulfur or cation vacancies. During anodic polarization Cu^{++} ions are dissolved out of the CuS lattice, leaving excess sulfur or cation vacancies. On continued cathodic polarization, as the excess sulfur is depleted (or the Cu^{++} vacancies filled), the CuS electrode potential becomes polarized to more negative potentials and the reduction of cupric ions to cuprous ions becomes the predominant reaction. The corresponding reduction step is clearly indicated in Fig. 4.

The CuS *electrode in solutions of* Cu^+ *and* Cu^{++} *ions.*—A study was made on the behavior of the CuS electrode in solutions containing both Cu^+ and Cu^{++} ions. Figure 5 shows a plot of the potential (measured *vs.* a saturated calomel electrode) against the molal ratio of cupric chloride to cuprous chloride. The cupric chloride concentration was maintained at 0.1*M*, whereas the cuprous chloride concentration was varied between 0.003 and 0.30 moles per 1000g of water. These solutions also contained 1*M* HCl to maintain a constant *p*H and the requisite quantity of KCl to bring the total chloride concentration of the solutions up to 2*M* (12-15).

Cuprous chloride powder, dried at 100°C in an inert atmosphere, was added to the cell electrolyte after removal of dissolved oxygen, and a constant stream of purified nitrogen was maintained to prevent contact of the solution with air. Both the cupric sulfide electrode and a platinized platinum electrode reached the same stable potential after equilibration in a given solution. The results of the experiments shown in Fig. 5 demonstrate that the CuS electrode functions as the inert part of the redox electrode

$$e^- + Cu^{++} \rightarrow Cu^+ \qquad [7]$$

with

$$E = E_{o(CuCl_2/CuCl)} + (2.3\,RT/F)\log([CuCl_2]/[CuCl])$$

Anodic and cathodic polarization measurements showed that this redox reaction exhibited excellent reversibility at the solid CuS surface. High current densities could be supported in the forward and reverse directions with only small potential changes. To cite one example, in a solution 0.10*M* in both cuprous and cupric chloride, with an apparent current density of 3.2 ma/cm², the potential decreased 15 mv during reduction and increased 15 mv during oxidation, after 20 min. The corresponding polarizations for platinized Pt were about 380 mv and 60 mv, respectively. The reversibility of the redox reaction at the CuS electrodes was therefore better than that at the platinized platinum electrode. From Fig. 5 it is seen that the CuS electrode potential in solutions containing both monovalent and divalent copper ions is more negative than in solutions of cupric ions only, and that the potential is dominated by redox reaction [7]. The same potentials were realized with a platinized platinum electrode as with a CuS electrode which substantiates that the measured potentials were reversible redox values.

This important result provides a clear explanation of the mechanism of a cuprous chloride electrode, containing sulfur, in a water-activated battery (1). Wetting of the electrode initiates the reaction between cuprous chloride and sulfur, producing CuS and $CuCl_2$ according to reaction [1]. The cupric ions generated in this manner are reduced in a subsequent electrochemical step, according to Eq. [7], which has been shown to be very fast. The excellent reversibility of this redox reaction makes possible a relatively high discharge current and also dictates that the redox couple will determine the electrode potential. The reaction of cuprous ions with sulfur replenishes the cupric ion concentration and maintains the Cu^{++}/Cu^+ ratio essentially constant. In this manner, cuprous chloride and sulfur are consumed to form cupric sulfide and chloride ions as the end-products of the discharge reaction. CuS has been identified as the end-product in discharged electrodes by x-ray diffraction analysis. This mechanism explains how elemental sulfur appears to be readily reducible with little polarization, and how the high positive voltage level is attained. The $Cu/CuCl/Cl^-$ potential in 2*M* chloride solution at *p*H 0 is about —0.10v against the saturated calomel reference electrode. The $Cu^{++}/(Cu^+)$ redox potential, as measured by the CuS electrode at very low (Cu^+) concentrations, is in the vicinity of 0.35v (*vs.* SCE), as may be seen from Fig. 5. It is evident that a potential increase of about 0.45v can therefore be attained. This increase has actually been realized during activation and discharge of cuprous chloride-magnesium batteries by the addition of sulfur to the cuprous chloride active material (1). It is thus evident that the addition of sulfur can provide a substantial benefit by increasing the energy output of this battery system.

From a thermodynamic standpoint, the maximum available voltage increase is given by the difference in free enthalpy between the reactions

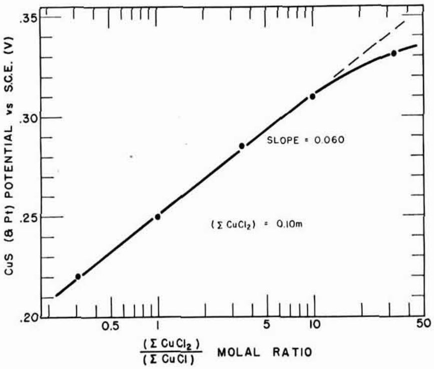

Fig. 5. Cupric sulfide (and platinized Pt) potential as a function of the $CuCl_2/CuCl$ molal ratio. 0.1*M* $CuCl_2$, 1.0*M* HCl, 2*M* total (Cl^-).

$$e^- + CuCl \rightleftarrows Cu^+ Cl^- \quad [8]$$

and

$$e^- + CuCl + S \rightleftarrows CuS + Cl^- \quad [9]$$

From the difference in free enthalpy one obtains $\Delta E = -\Delta G/nF = 11.7/23.06 = 0.506v$.

Experimental results given in reference (1) indicate that this theoretical upper limit can be approached rather closely. This would mean that the reaction of sulfur according to Eq. [1] proceeds to nearly the saturation concentration of $CuCl_2$ in solution, such as to render the free energy of reaction [1] equal to zero. According to Latimer, reaction [1] has a positive free energy of 2.7 kcal if all the reactants and products are in the crystalline state and does thus not proceed spontaneously. However, for dissolved $CuCl_2$ at 1*M* concentration the free energy is −2.5 kcal. Thus, the equilibrium cupric chloride concentration for reaction [1] is close to the saturation value of about 5.8*M*.

The potential of CuS was also briefly investigated in solutions containing only cuprous chloride, but no cupric chloride. Oxygen was removed carefully from these solutions to avoid oxidation and metallic, oxide-free copper powder was stirred into the solution to remove any cupric ions present by the reaction $Cu^{++} + Cu \rightarrow 2\ Cu^+$. The electrode potentials were erratic and not reproducible. This is apparently due to a lack of an exchange between cupric ions in solution and in the solid. The hypothetical reaction $e^- + Cu^+ + S_{(CuS)} \rightleftarrows CuS$ does not seem to proceed because the excess free sulfur $S_{(CuS)}$ reacts preferably with CuCl according to reaction [1], producing cupric ions which become potential determining according to reaction [7].

There is however one additional reaction which deserves attention in this connection. If an electrode of CuS is immersed in a solution of CuCl which is free of $CuCl_2$, the potential remains considerably higher than that of copper in a solution of CuCl. Solutions free of $CuCl_2$ are conveniently prepared by removal of oxygen and reacting the CuCl solutions with clean metallic copper powder. The reaction

$$Cu + CuCl_2 \rightarrow 2\ CuCl$$

removes all traces of divalent copper.

The electrode potential of CuS in CuCl solution is maintained at nearly the same level even after applying small currents in the cathodic direction. It was established experimentally that the following reaction proceeds

$$e^- + CuCl + CuS \rightarrow Cu_2S + Cl^- \quad [10]$$

The product Cu_2S was identified by x-ray analysis. Up to one third of the capacity of CuS could be utilized in this manner. In a 0.3*M* solution of CuCl (1*M* HCl + 1*M* KCl) the open circuit voltage of the electrode was +0.156v *vs.* Hg_2Cl_2, which is 0.271v above the potential of the Cu/CuCl couple. Theoretically, one calculates for the couple $CuS/Cu_2S/CuCl/Cl^-/CuCl/Cu$ a voltage of 0.385v.

Reaction [10] therefore constitutes a further reserve capacity of electrodes containing cuprous chloride and sulfur. After exhaustion of the sulfur according to reaction [1] and formation of CuS, the cuprous chloride can further react according to Eq. [10], at a slightly reduced voltage level.

Response of the CuS electrode to sulfide ions.—Sodium sulfide solutions varying in concentration between 0.001 and 0.5*M* were prepared with 0.5*M* sodium chloride as the supporting electrolyte, and the potential of the CuS electrode measured in these solutions, using a saturated calomel reference electrode. The *p*H values increased with increasing Na_2S concentration, attaining 13.1 in the 0.5*M* Na_2S + 0.5*M* NaCl solution. Sodium sulfide is extensively hydrolyzed in these solutions

$$Na_2S + H_2O \rightleftarrows NaHS + NaOH$$

with

$$HS^- \rightleftarrows H^+ + S^{--}; K = 10^{-14}$$

From this one calculates for the concentration of $[HS^-]$

$$[HS^-] \rightleftarrows [H^+]\ [S_t^{--}]/([H^+] + 10^{-14}) \quad [11]$$

where S_t^{--} is the total concentration of divalent sulfur present ($S^{--} + HS^-$). The electrode potentials of CuS in sulfide ion solutions are shown in Fig. 6. At very low sulfide ion concentrations the potential rises to a positive and constant value which must represent an adsorption potential by chloride ions.

The potential decreases sharply as the Na_2S concentration is increased above 0.003*M* and follows subsequently a straight line on the logarithmic plot, with a slope of about 30 mv.

If the reaction at the sulfide electrode is written in the form

$$2e^- + S_{(CuS)} + H_2O \rightleftarrows HS^- + OH^- \quad [12]$$

and at the mercurous chloride reference electrode as

$$2e^- + HgCl_2 \rightleftarrows 2Hg + 2Cl^- \quad [13]$$

the over-all reaction becomes

$$S_{(CuS)} + 2Hg + 2Cl^- + H_2O \rightleftarrows Hg_2Cl_2 + HS^- + OH^- \quad [14]$$

where $S_{(CuS)}$ is the excess sulfur in CuS. One would then expect the following potential dependence

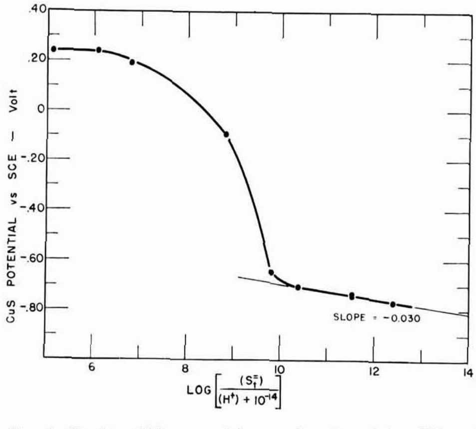

Fig. 6. Cupric sulfide potential as a function of log $[(S_t^{--})/(H^+ + 10^{-14})]$ where (S_t^{--}) = total Na_2S concentration. 0.5*M* NaCl.

$$E = E_{o(\mathrm{CuS/S_t^{--}})} - (2.3\,RT/2F)\log \{[\mathrm{S_t}^{--}]/([\mathrm{H}^+] + 10^{-14})\} \quad [15]$$

since (Cl^-) concentration was maintained constant. This would predict a slope of —0.029v, when the potential is plotted against the logarithmic term. The experimental results of Fig. 6 agree well with this prediction.

The deviation between the experimental and theoretical slope is due to a dissolution of sulfur and the presence of polysulfides in the more concentrated sulfide solutions, as shown below in greater detail.

The standard potential of the couple

$$2e^- + \mathrm{S} \rightleftarrows \mathrm{S}^{--}$$

at *p*H 14 is —0.72v *vs.* calomel according to Latimer.

This value checks well with the experimentally measured value extrapolated with the help of reference (15), from the data of Fig. 6, to a concentration of 1*M* at *p*H 14, which is another indication that the excess sulfur in CuS is essentially "free."

It has been pointed out that sulfur readily dissolves in alkaline solutions. Hickling (16) has studied the behavior of solutions containing both dissolved sulfur and sodium sulfide, on inert electrodes. He found that the dissolved sulfur species were able to support a reversible redox potential and high currents in the forward and backward direction. Also Gerischer (17) reports that the electrochemical oxidation of sulfide to sulfur can proceed with high efficiencies. It was of interest to measure the redox couple

$$2e^- + \mathrm{S_{(dissolved)}} + \mathrm{H_2O} \rightleftarrows \mathrm{HS}^- + \mathrm{OH}^- \quad [16]$$

on CuS electrodes.

Solutions containing sulfur and sulfide in varying concentrations were prepared, and the voltage of CuS in these solutions measured against a calomel reference electrode. The potentials showed extreme reversibility and were established with ease. Forward and backward electrochemical reactions could be maintained with very small polarization. It was discovered that on CuS the redox couple was even more reversible than on platinized platinum.

According to Eq. [16] one obtains for the potential

$$E = E_{o(\mathrm{S/SH^-})} - (2.3\,RT/2F)\log [[\mathrm{S_t}^{--}]/\{[\mathrm{S}]([\mathrm{H}^+] + 10^{-14}\})] \quad [17]$$

Figure 7 confirms this behavior; the slope checks excellently with the theoretical value. These results are in agreement with the data reported by Hickling and, moreover show that Eq. [17] can be applied to solutions of different *p*H values.

Conclusions

1. Cuprous chloride reacts with sulfur in acidic aqueous chloride solution to produce cupric sulfide and dissolved cupric chloride; the latter reaches an equilibrium concentration close to saturation.

2. The increase in voltage observed when sulfur is added to a cuprous chloride electrode in acidic magnesium chloride solution is caused by the fact that the electrode mechanism changes from

$$e^- + \mathrm{CuCl} \rightarrow \mathrm{Cu} + \mathrm{Cl}^-$$

to

$$e^- + \mathrm{CuCl_2} \rightarrow \mathrm{CuCl} + \mathrm{Cl}^-$$

where the cupric chloride is generated by chemical reaction between cuprous chloride and sulfur:

$$2\mathrm{CuCl} + \mathrm{S} \rightarrow \mathrm{CuCl_2} + \mathrm{CuS}$$

If the cupric chloride reaches the equilibrium concentration, the total free energy of formation of CuS (11.7 kcal) can be utilized as electrical energy and the over-all process can be written in the form

$$e^- + \mathrm{CuCl} + \mathrm{S} \rightarrow \mathrm{CuS} + \mathrm{Cl}^-$$

resulting in a theoretical voltage increase of 0.506v. Further capacity could be delivered by the electrode through the reaction

$$e^- + \mathrm{CuCl} + \mathrm{CuS} \rightarrow \mathrm{Cu_2S} + \mathrm{Cl}^-$$

with a theoretical electrode potential increase of 0.38v.

3. The discovery of this phenomenon is of practical importance to the technology of cuprous chloride-magnesium batteries.

4. Potential measurements of CuS in solutions containing either cupric ions or sulfide ions indicate that the nonstoichiometric excess sulfur in CuS acts essentially as "free" sulfur.

5. In solutions containing both dissolved sulfur and sulfides, CuS exhibits the characteristics of a very reversible redox electrode

$$2e^- + \mathrm{S\ (dissolved)} \rightarrow \mathrm{S}^{--}$$

$$\mathrm{S}^{--} + \mathrm{H}^+ \rightleftarrows \mathrm{HS}^-$$

6. While Wrabetz (3) showed that nonstoichiometric micro-quantities of excess sulfur in metal sulfides are responsible for the high electrode potential of these materials in solutions of their cations, the present investigation showed that similar over-all effects can be achieved with stoichiometric macro-quantities of elemental free sulfur, mechanically admixed with cuprous chloride to form the electrodes, whereby the sulfur regenerates continuously the higher oxidation state of the electrode couple from the lower oxidation state and large current outputs at an increased voltage become possible.

7. The utilization of a purely chemical step in the production of electrical energy according to the scheme

$$\underbrace{\underset{\uparrow}{\mathrm{A}} + \mathrm{B} \xrightarrow[\text{reaction}]{\text{chemical}} \mathrm{C}\,|}_{\text{electrochemical reaction}} + \mathrm{D}$$

may have considerable merit in the construction of various types of battery electrodes.

Manuscript received Nov. 30, 1964.

Any discussion of this paper will appear in a Discussion Section to be published in the June 1966 JOURNAL.

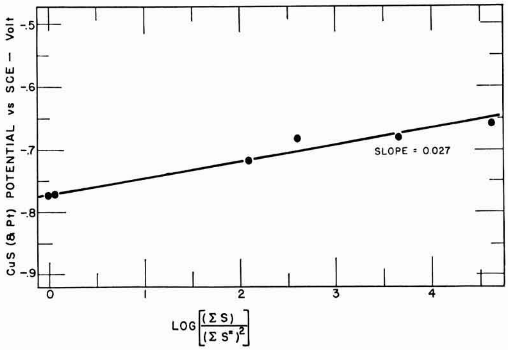

Fig. 7. Cupric sulfide (and platinized Pt) potential as a function of log $(\Sigma \mathrm{S})/(\Sigma \mathrm{S}^=)^2$ Total sulfide concentration, $(\Sigma \mathrm{S}^=)$, corrected hydrolysis by $[\mathrm{H}^+]\,[\mathrm{S}^=]/[\mathrm{HS}^-] = 10^{-14}$; 0.5*M* NaCl.

REFERENCES

1. H. N. Honer, R. F. Amlie, and P. Ruetschi, To be published.
2. G. Vortmann and C. Padberg, *Chem. Ber.*, **22**, 2642 (1889).
3. W. Noddack and K. Wrabetz, *Z. Electrochem.*, **59**, 96 (1955).
4. W. Noddack, K. Wrabetz, and W. Herbst, *ibid.*, **59**, 752 (1955).

5. K. E. Wrabetz, *ibid.*, **60**, 722 (1956).
6. G. Trümpler, *Z. Physik. Chem.*, **99**, 9, (1921).
7. K. Badeker, *Ann. Phys.*, (4) **22**, 749 (1907).
8. K. Fischbeck and O. Dorner, *Z. anorg. allgem.. Chem.*, **181**, 372 (1929).
9. H. Remy, "Treatise on Inorganic Chemistry," Vol. II, p. 390, Elsevier Publishing Co., New York (1956).
10. D. F. C. Morris and E. L. Short, *J. Chem. Soc.*, 2672 (1962).
11. W. M. Latimer, "Oxidation Potentials," p. 184, Prentice Hall Inc., New York (1952).
12. A. A. Noyes and M. Chow, *J. Am. Chem. Soc.*, **40**, 739 (1918).
13. F. Fenwick, *ibid.*, **48**, 860 (1926).
14. O. Gatty and E. C. R. Spooner, "The Electrode Potential Behavior of Corroding Metals in Aqueous Solutions," Oxford University Press (1938).
15. Tor Hurlen, Special Scientific Report No. 3, Jan. 1961, Central Institute for Industrial Research, Blindern, Oslo, Norway, ASTIA AD-252811.
16. P. L. Allen and A. Hickling, *Trans. Faraday Soc.*, **53**, 1626 (1957).
17. H. Gerischer, *Z. Elektrochem.*, **54**, 540 (1950).

Effect of Surface Treatment on the Corrosion of Stainless Steels in High-Temperature Water and Steam

M. Warzee, J. Hennaut, M. Maurice, C. Sonnen, and J. Waty

Société d'Etudes, de Recherches et d'Applications pour l'Industrie "S.E.R.A.I.", Bruxelles, Belgium

and Ph. Berge

EURATOM, Bruxelles, Belgique

ABSTRACT

The corrosion behavior of AISI 304 and 410 steels as well as 23.5 Cr-21.5 Ni steels in superheated steam at temperatures between 400° and 600°C was found to be influenced markedly by preliminary surface treatments: electrolytic polishing, mechanical polishing, milling, lathe-turning, grinding. The treatments accompanied by cold-working reduced the corrosion rate, the effect being retained for long times (at least 2000 hr for AISI 304 steel at 450°C). This enhanced corrosion resistance is attributed to the presence of cold-worked surface layers which were detected by measurement of x-ray line broadening. Electron microprobe analyses of the oxide layers and of the underlying metal showed that the oxide is enriched and the metal depleted in chromium and manganese. These elements thus seem to diffuse through the cold-worked layer toward the oxide. In water, at 300°C and below, the phenomena are more complex and not yet fully understood.

The corrosion of stainless steels in water and steam at high temperature has been studied extensively in recent years in connection with nuclear reactor construction (1). One of the factors liable to modify the corrosion rate is the initial surface treatment of the metal. The studies carried out previously, however, scarcely enable the importance of this corrosion factor to be evaluated and, above all, to be understood.

Fowler, Douglas, and Zyzes (2) consider that the initial surface treatment does not have an important effect on the corrosion of stainless steels in pressurized water between 250° and 320°C. On the other hand, Friend (3) thinks that roughness is disadvantageous, and Roebuck, Breden, and Greenberg (4) recommend actual machine finishing or pickling in order to obtain good corrosion resistance under these conditions. Nevertheless, they consider that the favorable effect of these treatments diminishes greatly during long-term tests. Videm and Aas (5) show that the surface treatment of stainless steels has considerable influence on their behavior in water at high temperature, but do not give details of the favorable treatments. Tolstaya *et al.* (6) show that electrolytic polishing decreases the corrosion rate by a factor of 2, while Rockwell and Cohen (7) put the factor at about 10. On the other hand, Ruther and Greenberg (8) found that electrolytic polishing had a disastrous influence on the behavior of stainless steels in steam at 650°C. Stiefel (9) indicates that a finely machined surface behaves much better in steam at 650°C than a nonmachined surface, but does not specify the type of machining.

In order to try to evaluate and understand the role played by the surface treatment, we endeavored to distinguish the three characteristics of the surface of a metal, as defined by Jacquet (10):

1. Microgeometric characteristics (roughness).
2. Chemical characteristics. Pollution and, particularly, the presence of an oxide film are the most important.
3. Physical or structural characteristics. Disturbances in the metallic lattice, either at the microscopic, submicroscopic, or atomic levels, caused by the surface treatments. Hardness changes and internal stresses in the surface layers are possible consequences of these structural disturbances.

One of the aims of this study was to see which of these characteristics could have an influence on the corrosion of stainless steels in water and steam over a fairly wide temperature range.

Preliminary Experiments and Objectives

The first part of the study, published elsewhere (11), concerned AISI 304 stainless steel. The curves in Fig. 1 reproduce the results obtained in autoclaves in pressurized water at 300°C and in steam at 400°C and 200 atm pressure with specimens which have been subjected to various mechanical surface treatments or to

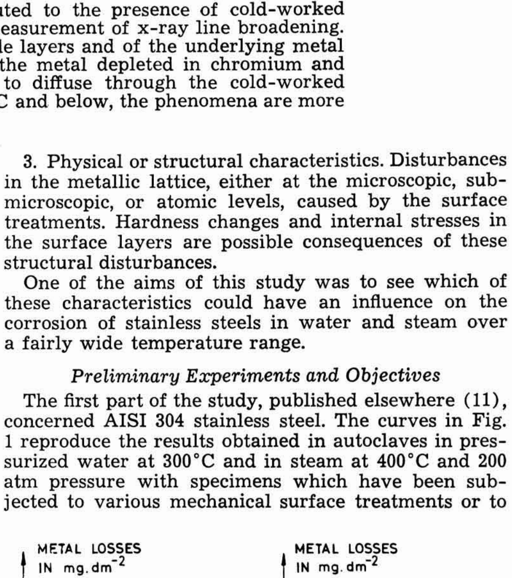

Fig. 1. Corrosion of AISI 304 in autoclaves: (a) (left), water at 300°C; (b) (right), steam at 400°C, 200 kg/cm^2.

electrolytic polishing. Details of these treatments are given in the experimental section of this paper. The values reported are averages over many tests, each involving a large number of specimens which made it possible to study statistically the significance of the results. It was found that electrolytic polishing appreciably improved the corrosion behavior in water at 300°C as compared with the three mechanically treated states. In steam at 400°C, the mechanically treated samples behaved better than in water at 300°C and became better than the electrolytically polished specimens.

The preliminary studies suggested that the following areas should be investigated: (*a*) to discern if the differences observed in water at 300°C and in steam at 400°C were due to a change in the physical state of the water or to the rise in temperature; (*b*) to cover a wider temperature range; (*c*) to investigate whether the surface treatment affected only the initial phase of oxidation or whether this effect persisted to longer times. The very slight corrosion of stainless steels under these conditions did not make it possible to study by autoclave tests the corrosion rate after 1000 hr with sufficient accuracy; (*d*) to ascertain whether other stainless steels behave similarly; (*e*) to discern what surface state characteristic is responsible for the observed effects.

Experimental

Specimen preparation.—The material used for this investigation was mainly AISI 304 stainless steel. Some additional tests were made using AISI 410 steel and also with a steel containing 23.5% Cr and 21.5% Ni.

Prior to the corrosion tests, the surface of the specimens was treated in a standardized manner. Three different mechanical treatments were used: (i) mechanical polishing through 600 grit paper, (ii) machine grinding with carborundum (grain size 80), and (iii) milling. A fourth type of treatment was electrolytical polishing in a perchloric-acetic acid bath. These treatments were followed by a chemical conditioning of the resulting surfaces. The standard method was immersion for 2 min in boiling water. Occasionally, conditioning techniques were tried in order to check if this step in the preparation of the specimens might alter the corrosion behavior. Alternate treatments were as follows: (*a*) exposure during 8 days in an air-conditioned room at 20°C and 50% humidity; (*b*) immersion for 2 min in nitric acid of density 1.33 at 20°C; (*c*) pickling during 25 min in a bath composed of 10% HNO_3, 3% HF, and 87% H_2O at 30°C (a layer of 6μ was dissolved by this treatment). Some of the mechanically treated specimens were heated under H_2, A, or in vacuum at 1050°C followed by quenching. The specimens were then chemically conditioned by the standard method (2 min in boiling water).

The surface of the treated specimens was examined by various methods: the roughness of the surface was measured with a profilograph Talysurf model 3 (Taylor-Hobson); the results are expressed in terms of the "central line average," henceforth designated as C.L.A. which is defined as the mean absolute deviation of the profile from the center line. Results of these measurements are given in Table I.

The oxide films formed on stainless steel in various media were compared by coulometric reduction in sulfuric acid. This method, as described previously (12), makes it possible to evaluate the number of coulombs required to reduce the passivation oxides of stainless steels as well as the exchange current, expressing slow oxidation in sulfuric acid (13). This last value may therefore indicate the protection conferred by the oxide independently of its thickness. The exchange current values obtained with these different chemical treatments vary greatly (13).

Table I. Effect of surface treatment on roughness values of AISI 304 steels

Surface treatment	C.L.A. in microns Parallel*	 Perpendicular*
Milling	11	11
Grinding	3	5.2
Mechanical polishing	1	8
Electrolytic polishing	1.6	1.6

* The roughness profiles were measured parallel and perpendicular to the direction of mechanical surface treatment.

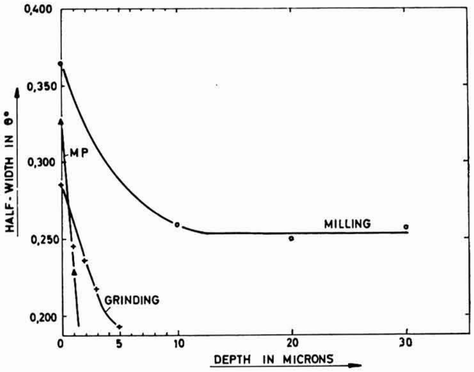

Fig. 2. Measure of the surface cold work of AISI 304 using the half-width of the (111) austenite line. Depth for which the ray profile is similar to that of the electrolytic polished state; grinding, 5-6μ; mechanical polishing, 1-2μ.

In order to evaluate the thickness of the layers affected by the various mechanical treatments, the broadening of the (111) austenite line in the x-ray diffraction pattern of the specimen was measured. For this purpose, the method for the study of surface layers by grazing emergence of the diffracted beam, described by Legrand (14), was adapted to an asymmetrically mounted focusing camera. The Kα line of copper, obtained from a bent quartz crystal monochrometer was used. Figure 2 shows the variation in the half-peak width of the (111) line measured on the photometric recordings. It can be seen that the depths of the cold-worked layer depend greatly on the mechanical treatment. The method reveals no further surface cold-work for specimens polished through 600 grit paper, after 2μ have been dissolved, whereas 6μ are to be removed from ground specimens, and milled specimens are still thoroughly cold-worked at a depth of 30μ.

Autoclave tests.—This technique has been described previously (15). The water used in all of the experiments was extremely pure (resistivity reading 20 Mohm-cm and oxygen content below 15 x 10^{-6} g/liter).

Measurement of the diffused hydrogen.—When a metal is oxidized in oxygen-free water, hydrogen is produced. If the specimen under study is in the shape of a small capsule containing water or steam, the hydrogen formed diffuses through the walls. Bloom *et al.* (16) have shown that it is possible to plot the corrosion-*vs.*-time curve by measurement of the quantity of evolved hydrogen. A longitudinal section through the capsules used is shown in Fig. 3. They are small cylinders of 20 mm diameter and 38 mm length. After annealing, all inside surfaces are subjected to the specified treatments. Bottom and top are then sealed by electron beam welding. The required quantity of water is added through the filling tube which is then pinched off and sealed by spot welding. The sealed capsules are placed in a gas collecting rig, a flow sheet of which is shown in Fig. 4. The rig is made of Pyrex glass and can hold ten capsules which are placed in ten gas collecting chambers heated individually by electric furnaces. The gas accumulated in each collecting chamber is periodically swept into a gas chromatograph for measurement. Because of the high precision

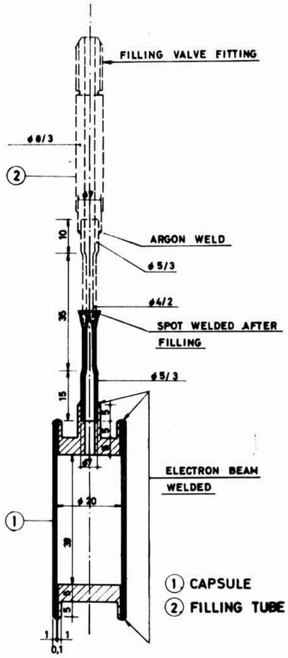

Fig. 3. Hydrogen diffusion test capsule

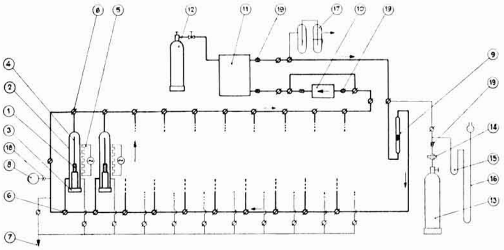

Fig. 4. Flow sheet of experimental rig for hydrogen diffusion measurements: 1, test capsule; 2, gas collecting chamber; 3, bottom closure of chamber; 4, thermometer; 5, electric furnace; 6, three-way stopcocks; 7, to vacuum line; 8, Penning vacuum gauge; 9, flow meter; 10, sealed circulating pump; 11, gas chromatograph; 12, bottle for calibration gas mixture; 13, argon bottle; 14, high-purity pressure reducer; 15, liquid air trap; 16, mercury manometer; 17, exit gas bubble counter with no return safety device; 18, conical ground joint; 19, glass to metal seals.

of hydrogen determination by gas chromatography, this method makes it possible to measure accurately the low corrosion rate of AISI 304 steel at 300°C after 1000 hr. This was not possible with autoclave measurements.

Results and Discussion

The corrosion was evaluated after reduction of the oxide layer in a stream of pure hydrogen at 800°C. It was always assumed that the metal to oxygen ratio was that of magnetite. However, for high corrosion rates, i.e., for electrolytically polished specimens at temperatures above 450°C, the results are given by simple measurement of the weight gain, as reduction in hydrogen and descaling have proved unsatisfactory. The values obtained are thus slightly below the real total corrosion values since the metal lost as detached scale in the autoclave is not taken into account.

In order to examine the oxide layers microscopically, polished cross sections were prepared after protecting the oxide by a layer of cobalt deposited electrolytically.

Variations in composition of the oxide and the underlying metal were determined with the electron microprobe. Specimens oxidized in steam for 1000 hr were used for these measurements.

Table II shows the total corrosion values from 1000-hr experiments in autoclaves at different temperatures in pressurized water and superheated steam for the electropolished and mechanically treated states. As the three mechanically treated states give very close corrosion values, the corrosion results for the milled and the electropolished specimens only are indicated. The corrosion rate at 500°C is sufficiently high for the autoclave measurements to indicate the oxidation

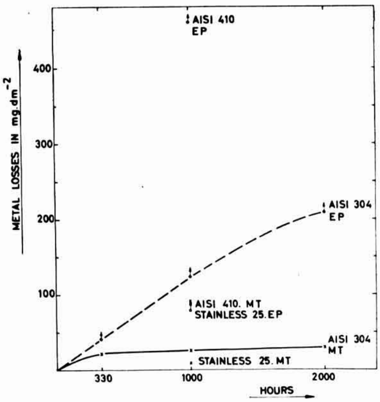

Fig. 5. Corrosion of stainless steels in superheated steam at 500°C, 70 kg/cm^{-2} (autoclaves).

Table II. Total corrosion values in mg dm^{-2} after 1000 hr in autoclaves

		Water				Superheated steam					
		Temperature, °C				Temperature and pressure					
						250°C	350°C	400°C	450°C	500°C	600°C
Stainless Steel Compositions, %	Surface treatment	200	250	300	350	15 kg/cm^2	35 kg/cm^2	70 kg/cm^2	70 kg/cm^2	70 kg/cm^2	70 kg/cm^2
AISI 304 C 0.04 Si 0.5 Ni 11.0 Mn 1.1 Cr 18.8	Milled	12.4	13.4	12.9	5.1	3.0	4.5	7.5	27.2	34.2	18.7
	Electro-polished	6.9	4.7	3.4	3.3	3.1	4.5	11.4	78	>160	>1100
Stainless 25 (Uddeholm) C <0.075 Si <2.0 Ni 21.5 Mn <2.0 Cr 23.5 P <0.03 S <0.025	Milled	—	—	3.3	—	—	—	3.8	—	8.4	—
	Electro-polished	—	—	>7.5	—	—	—	>5	—	>79	—
AISI 410 C 0.07 Cr 13.4 Mn 0.38 Si 0.32 P 0.021 S 0.006	Milled	—	—	30.5	—	—	—	6.8	—	83	—
	Electro-polished	—	—	30.1	—	—	—	55	—	>460	—

Table III. Corrosion rates of AISI 304 steel in mg dm^{-2} hr^{-1} measured by hydrogen diffusion

Measured at time, hr	Treatment	Corrosion rates* Water, 300°C	Corrosion rates* Superheated steam, 300°C 50 kg/cm^2	Corrosion rates* Superheated steam, 450°C 70 kg/cm^2
1000	Electropolished	0.003	0.003	0.045
	Lathe-turned	0.008	0.003	0.005
2000	Electropolished	—	—	0.040
	Lathe-turned	—	—	0.003

* For the calculation of the corrosion rates, the metal to oxygen ratio was assumed to be that of magnetite.

kinetics, even after 1000 hr (Fig. 5). This is not so at 300°C.

The corrosion rates of AISI 304 steel measured by hydrogen diffusion are shown in Table III.

These results show that:

1. The adverse influence of a mechanical surface treatment noted for AISI 304 in water at 300°C did not occur in superheated steam at the same temperature. In saturated steam, however, the results were similar to those obtained in water. Below the critical temperature, the physical state of water must thus be considered as an essential factor of the behavior. Between 250° and 350°C, the corrosion in superheated steam was independent of the surface state and was generally lower than in water.

The fact that the corrosion of electropolished specimens in water was higher at 200° than at 250°C and 300°C is due to the larger quantity of metal in solution in the water at 200°C. It is probable that the transformation of more soluble ferrous hydroxide into magnetite is slower at 200° than at 300°C (1, 17).

2. The curves in Fig. 6 summarize the results of AISI 304 corrosion after 1000 hr in superheated steam at various temperatures. The corrosion in this medium, which was independent of the surface state up to 350°C, was dependent on this factor above 400°C. A mechanical surface treatment improved the behavior of the specimens above that temperature; this improvement increased with temperature. At 600°C, the total corrosion rate of electropolished specimens in 1000 hr was more than 50 times greater than that of mechanically treated specimens.

3. The hydrogen diffusion data (Fig. 7 and 8) and also the 500°C autoclave curves (Fig. 5) clearly demonstrate that the effect of the surface treatment is not a short-term effect; under the conditions employed in our experiments, the oxidation kinetics in steam from 400°C upwards and for exposure times up to 2000 hr are considerably altered by mechanical treatment. The favorable effect of electrolytic polishing on corrosion in water at 300°C was retained after 1000 hr.

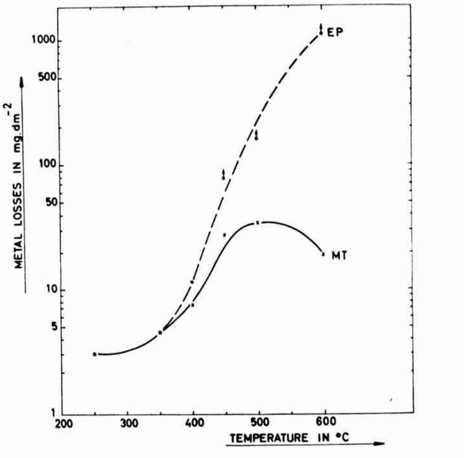

Fig. 6. Total corrosion of AISI 304 in 1000 hr in superheated steam (autoclaves).

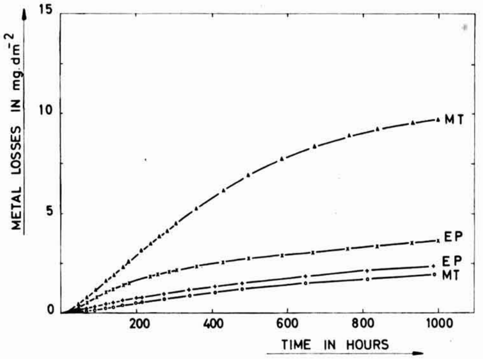

Fig. 7. Total corrosion of AISI 304 at 300°C measured by hydrogen evolution. △, X, Water 300°C; +, ○, superheated steam at 300°C.

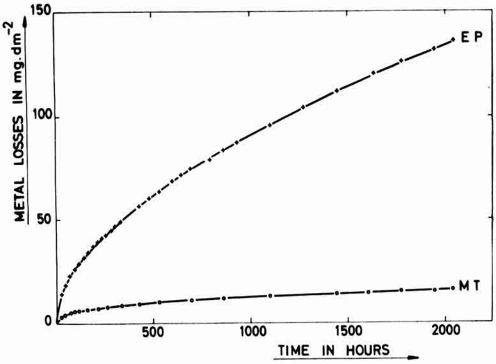

Fig. 8. Total corrosion of AISI 304 in superheated steam at 450°, 70 kg/cm^2, measured by hydrogen evolution.

4. The favorable effect of a mechanical surface treatment on corrosion in steam at high temperature is the same for AISI 410 and 23.5 Cr-21.5 Ni steels as for AISI 304 steel. On the other hand, electrolytic polishing imparts no noticeable improvement on these steels in water at 300°C.

5. The various roughness values obtained by the different mechanical treatments do not alter appreciably the corrosion behavior of AISI 304 steels in water and steam. Furthermore, the different methods of chemical conditioning of the surface did not bring about noticeable effects. The pickling of a previously electropolished specimen also did not change the corrosion behavior of the surface in water and steam at high temperature. It is thus impossible to relate the behavior of electrolytically polished specimens in this medium to the presence of an oxide film formed during polishing as was the case in the corrosion of iron-chromium alloys oxidized in oxygen (18).

The influence of cold-work on the corrosion behavior was shown by the specimens which had been pickled in the nitric-hydrofluoric acid bath after the four surface treatments. Only the milled specimen which had been cold-worked to a depth greater than 6μ, maintained a low corrosion rate at 500°C after pickling, whereas the three other surface treatments produced corrosion rates similar to that of the electropolished specimen. All the specimens which were quenched from 1050°C behaved similarly in steam at 500°C to the electropolished specimens.

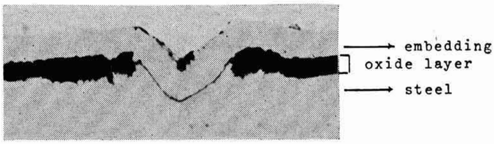

Fig. 9. Section of an AISI 304 sample marked with a diamond point and oxidized for 1000 hr in steam at 500°C.

Figure 9 shows a section of an electropolished specimen of AISI 304 steel on which a mark was scribed with a diamond point under constant load. The specimen was oxidized during 1000 hr in steam at 500°C. It can be seen that the oxide layer on the area cold-worked by the diamond point is distinctly thinner than on the remainder of the surface. These results show that the improvement in the behavior in steam at high temperature observed after mechanical treatment is due to the presence of a cold-worked layer several microns thick.

The electron microprobe analysis of cross sections of mechanically treated specimens was not possible because after 1000 hr at 500°C in steam the oxide films are too thin (0.4μ). However, surface analysis of a specimen was carried out, the depth of penetration of the beam being about 3μ. The results obtained were therefore only qualitative, but a very marked enrichment of the oxide layer in chromium and in manganese was observed. This is shown in Table IV.

The microscopic study of oxides formed on electropolished specimens has shown that they consist of two layers separated by the initial surface of the metal. The outside layer is highly crystallized magnetite, free of chromium and nickel, whereas the inside layer probably resulted from an internal oxidation of chromium in a nickel-rich austenite matrix (19). The chromium content of the metal under the oxide layer is given in Table V.

It may be ascertained that no chromium concentration gradient is formed in the metal of the electropolished sample, whereas with the mechanically treated samples a depletion of the chromium content is found in the neighborhood of the oxide, which itself is rich in chromium. It is therefore probable that the diffusion rate of the chromium is higher in the layer affected by the mechanical treatments because of the increased number of dislocations in the crystal lattice.

The film initially formed on the cold-worked surfaces would be greatly enriched in chromium as a result of this diffusion and might thus afford a greater degree of protection against later oxidation of the iron. A similar mechanism has been suggested by Poulignier *et al.* (20) to explain the favorable effect of superficial cold-work on the oxidization of Cr-Ni-Co-Mo alloys in air.

Table IV. Electron microprobe analysis of a milled specimen of AISI 304 steel oxidized for 1000 hr in steam at 500°C

	Concentrations in %				
Analyzed layer	Fe	Cr	Ni	Mn	Si
Original metal	69	18	11	1.5	0.9
Oxide	59.6	23.6	10	6.2	0.6

Table V. Chromium content of the metal under the oxide layer of AISI 304 steel specimens oxidized for 1000 hr at 500°C

Thickness of the metal consumed by corrosion	Milled 0.4μ	Ground 0.4μ	Electro-polished Approx. 2μ
Depth under oxide layer, μ	Chromium contents in %		
2	17.3	17.3	18.0
5	17.4	17.6	18.0
10	17.7	17.9	18.0
20	17.7	18.1	18.0
30	18.1	18.1	18.0
200	18.1	18.1	18.0

Conclusions

The corrosion rate of stainless steel in superheated steam at high temperature is greatly affected by the initial surface treatment of the metal. The essential factor was found to be cold-work which reduces considerably the corrosion rates. Definition of the surface state in terms of its roughness is totally inadequate. Pickling or electrolytic polishing are also insufficient to define a surface state, because the cold-worked surface layers may not have totally disappeared.

In water at 300°C and below, more complex phenomena seem to be involved in which the physical state of the water, the temperature, and the surface state of the metal as well as its composition contribute in a manner which is not yet fully understood. The investigation of these mechanisms is more difficult because of the low corrosion values obtained.

It should be possible to make use in nuclear power plants of the considerable improvement in corrosion behavior in superheated steam produced by suitable surface treatments.

Acknowledgment

This work was supported by the Commission of the European Atomic Energy Community. The authors thank for the permission to publish this paper. Thanks also due to Mr. Hochmann, Director of Research of the Company "Ateliers et Forges de la Loire," for his kindness to permit the electron microprobe analyses to be carried out in his laboratories.

Manuscript received Oct. 2, 1964. This paper was presented at the Washington Meeting, Oct. 11-15, 1964.

Any discussion of this paper will appear in a Discussion Section to be published in the June 1966 JOURNAL.

REFERENCES

1. Corrosion and Wear Handbook for Water Cooled Reactors," D. J. De Paul, Editor (1957).
2. R. Fowler, D. L. Douglas, and F. C. Zyzes, KAPL-1248 (1954).
3. W. Z. Friend, *Proc. Amer. Power Conf.*, **18**, 613 (1956).
4. A. N. Roebuck, C. R. Breden, and S. Greenberg, *Corrosion*, **13**, 87 (1957).
5. K. Videm and S. Aas, Kjeller Report, No. 39 (1963).
6. M. A. Tolstaya, G. N. Gradusov, and S. V. Bogatyreva, AEC-tr-4698 (1960).
7. T. Rockwell and P. Cohen, *Prog. Nuclear Energy*, Series IV, **1**, p. 281 (1956).
8. W. E. Ruther and S. Greenberg, *This Journal*, **111**, 1116 (1964).
9. W. Stiefel, *Rev. Tech. Sulzer*, No. 3, 21 (1961).
10. P. A. Jacquet, *Met. Rev.*, **1**, 157 (1956).
11. M. Warzee, Ph. Berge, M. Maurice, and J. Waty, *Compte rend. Acad. Sc. Paris*, **256**, 5566 (1963).
12. Ph. Berge, *Compte rend.*, **245**, 1239 (1957).
13. M. Cunha Belo, Ph. Berge, J. Montuelle, and G. Chaudron, *Corrosion et Anticorrosion*, **12**, 297 (1964).
14. C. Legrand, *Bull. Soc. Franç. Minéral. Crist.*, **74**, 20 (1951).
15. M. Warzee, M. Maurice, C. Sonnen, J. Waty, and Ph. Berge, *Rev. Met.*, **61**, 593 (1964).
16. M. C. Bloom, M. Krulfeld, W. A. Fraser, and P. N. Vlannes, *Corrosion*, **13**, 297 (1957).
17. U. R. Evans, "The Corrosion and Oxidation of Metals," p. 438, Edward Arnold, London (1960).
18. D. Caplan, A. Harvey, and M. Cohen, *This Journal*, **108**, 134 (1961).
19. M. Warzee, J. Hennaut, M. Maurice, and Ph. Berge, *Mém. Sci. Rev. Mét.*, **62**, 239 (1965).
20. J. Poulignier and P. A. Jacquet, *Rev. Mét.*, **49**, 541 (1952); J. Poulignier, *Corrosion et Anticorrosion*, **11**, 466 (1963).

The Migration of Metal and Oxygen during Anodic Film Formation

J. A. Davies, B. Domeij, J. P. S. Pringle, and F. Brown

Research Chemistry Branch, Chalk River Nuclear Laboratories,

Atomic Energy of Canada Limited, Chalk River, Ontario, Canada

ABSTRACT

Beta-ray spectroscopy and radiotracer techniques have been used to study the transport of metal and oxygen during anodic oxidation. Both species are mobile during oxide film growth on Al, Nb, Ta, and W, but in Zr and Hf only oxygen transport is observed. Radiotracer measurements showed that the amount of metal dissolving in the electrolyte was usually less than 1% of the total oxidized, but that for Al it could be as high as 40%, depending on the current density and electrolyte used.

Although the anodic oxidation of metals has been studied extensively in recent years, the nature of the mobile species within the growing oxide film has not been clearly established. Experimental evidence has been presented in Al, for example, to suggest that anodic oxidation proceeds by metal ion migration (1, 2), by oxygen ion migration (3), or by a combination of both processes (4, 5).

To resolve such discrepancies, a "transport number" experiment is required in which a thin surface layer is tagged with a completely immobile marker atom, whose position is then followed during the subsequent anodic oxidation. If the metal ions alone are mobile, new oxide will be formed at the oxide/electrolyte interface on top of the tagged layer, and so the marker will become buried. On the other hand, if oxygen ions are the only mobile species, the new oxide forms at the metal/oxide interface underneath the tagged layer, and so the marker remains close to the outer surface throughout the oxidation.

The ideal marker atoms for such a transport experiment should be (i) uncharged, so that they do not migrate under the influence of the applied electric field; (ii) large in size, so that they do not diffuse significantly within the oxide lattice; (iii) present in trace amount, so that the macroscopic properties of the tagged oxide remain unaltered; and (iv) such that their depth beneath the surface can be determined *in situ,* without damaging or destroying the oxide layer. Previous investigations (1, 6) have not fulfilled these criteria.

Radioactive isotopes of the heavier inert gases should approximate the ideal marker closely. Of all the possible atomic markers, the inert gases are the most likely to remain uncharged within the oxide lattice. The heavier gases are much bigger than either metal or oxygen ions and, if radioactive, can be used in trace amounts. Furthermore, the radioisotopes Xe^{125} and Rn^{222} decay with the emission of monoenergetic conversion electrons and α particles respectively, and so their depth beneath the surface of a solid can be measured *in situ* by means of high precision nuclear spectroscopy (7, 8).

Our earlier experiments on the anodic oxidation of Al and Ta in aqueous solution (3) showed that the Xe^{125} markers in anodic Al_2O_3 remained very close to the outer surface. We also noted that an appreciable amount of aluminum went into solution during anodizing, which suggested that aluminum ions might be mobile but were not building oxide at the outer surface. Subsequent experiments (4,5) showed that the final location of the marker atoms within the aluminum oxide layer depended markedly on the current density used and also on the nature of the electrolyte. At higher current density we observed an appreciable burying, which shows that metal transport is responsible, at least in part, for oxide growth. We have now found that the amount of aluminum going into solution during anodizing also varies with the current density; obviously, this loss must be considered in assessing the relative importance of cation mobility in the growing oxide.

Consequently, it was decided to carry out a more detailed radiochemical investigation of the anodizing behavior of Al and Ta. Two types of experiments have been used: (i) transport number experiments using Xe^{125} marker atoms as in the previous work (3, 5); and (ii) experiments with neutron-activated metals in order to determine the amount of metal ion dissolving during the anodic oxidation. The effect of current density was studied in both sets of experiments, and for Al the nature of the electrolyte was varied. In addition, the anodic behavior of zirconium, niobium, hafnium, and tungsten was studied.

Experimental Procedure

Xe^{125} *depth measurements.*—In these experiments, trace amounts of Xe^{125} were incorporated in a thin anodic oxide layer on the surface of a metal foil. After measuring the mean depth of the Xe^{125} atoms, the foil was anodized further to produce a thick oxide film, and the mean depth of the Xe^{125} atoms was again determined. The difference in the Xe^{125} depths, divided by the thickness increment of the oxide, gave the fraction of the anodic oxide formed outside the Xe^{125} layer.

A previous paper from this laboratory (9) has described the use of an isotope separator for injecting Xe^{125} into solid targets. The Xe^{125} ions strike one tenth of the area of the target, 3.5 x 1.0 cm, as a line 3.5 cm long and 0.1 cm wide; the total number of Xe^{125} was always less than $10^{12}/cm^2$, and so the atomic concentration of Xe^{125} in the tagged layer did not exceed 20 ppm. A relatively low injection energy, either 3 or 5 kev, was used to keep the depth of the tagged layer small. The Xe^{125} could have been injected directly into the oxide layer, and a very narrow Xe^{125} depth distribution would have resulted (10). Because of the possibility that radiation damage to the oxide might affect its anodizing behavior, we preferred to put the Xe^{125} into the metal, and then anodize to convert the surrounding metal to oxide. As the distribution of embedded Xe is known for Al (9) and W (11), it is possible to calculate the anodizing voltage required to oxidize just this depth, and suitable voltages for the other metals could be inferred. This procedure does not eliminate the possibility that radiation damage in the metal may affect the anodic oxidation, but it has previously been shown that this is negligible for Al (12).

With the Xe^{125} atoms in a very thin layer of oxide, the target was inserted into the source chamber of the Chalk River $\pi\sqrt{2}$ β-spectrometer and the shapes of the

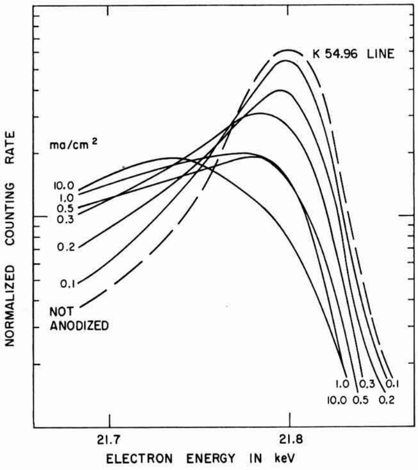

Fig. 1. The K54.96 conversion electron spectra from Xe^{125} atoms in anodic Al_2O_3; 3 kev Xe^{125} in Al subsequently anodized to 125v. The effect of current density is shown.

21.79 and 155.2 kev electron peaks, arising from K conversion of the 54.96 and 188.4 kev nuclear transitions, respectively, were measured. The target was then removed, anodized under the desired conditions, replaced in the spectrometer, and the peaks remeasured. Further anodizing and peak measurements were carried out as needed. The depth of the Xe^{125} layer after anodizing was found from the conversion electron spectra by comparing the observed attenuation of the 21.79 kev peak with that produced by absorbers of known thickness (7). The 155.2 kev peak is not significantly attenuated by the absorber thicknesses involved in the present work; it was measured to provide a normalizing factor for eliminating variations in source strength, geometrical efficiency, etc., in the spectrometer. Sample K54.96 spectra are shown in Fig. 1 for the anodization of Al in aqueous citrate.

A detailed description of this β-spectroscopic method for measuring small penetration depths has been given elsewhere (7). In the article, the method had been calibrated against known thicknesses of Al and Au absorbers; it was necessary for the present purpose to extend these calibrations to anodic oxides. Accordingly, anodized Al and W targets were bombarded with monoenergetic Xe^{125} ions of 1, 40, and 160 kev energy, and the Xe^{125} conversion electron spectra measured. The mean penetration depth, $\overline{R}$, of Xe^{125} in anodic Al_2O_3 and WO_3 is known accurately as a function of incident energy from the work of Domeij *et al.* (10), and the targets were anodized sufficiently (70v for W, 125v for Al) to ensure that essentially all the Xe^{125} was stopped in the oxide layer. Comparison of $\overline{R}$ against the normalized K54.96 peak height, N, in Fig 2 shows that N decreases exponentially with $\overline{R}$ as observed previously for Al and Au. Strictly, the mean "exponential" depth, $\overline{x}$, defined in the previous article (7) should be used for comparison with N, but the discrepancy between $\overline{R}$ and $\overline{x}$ is small provided that the thickness of the Xe^{125} layer is also small, as is the case in these oxides.

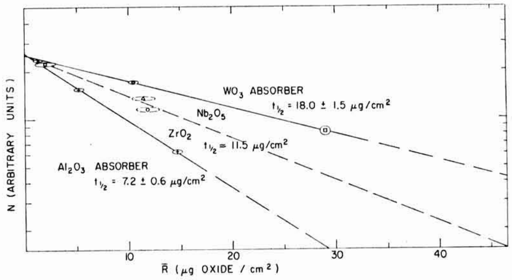

Fig. 2. Calibration of N, the normalized counting rate at the natural peak position of the K54.96 line, against the mean depth, $\overline{R}$, of the Xe^{125} atoms in anodic oxides.

Xenon penetration depths are not known experimentally for the other anodic oxides; it was assumed that the electron stopping powers of HfO_2 and Ta_2O_5 were the same as that of WO_3. To provide a calibration for ZrO_2 and Nb_2O_5, the mean penetration depths of 80 kev Xe^{125} ions in these oxides were calculated from the theory of Lindhard (13) and used with the experimentally observed K54.96 peak height to construct the calibration shown in Fig. 2. These theoretical penetration depths, 11.9 $\mu g/cm^2$ for ZrO_2 and 11.5 $\mu g/cm^2$ for Nb_2O_5 are estimated to have an error of about 10%; it was assumed that the calibration for these two oxides was the same.

Dissolution of metal during anodizing.—A neutron activation technique was used to measure the extremely small amounts of metal ion that dissolve during anodic oxidation. Metal targets identical to those used above were irradiated in the NRX reactor at a flux of 2 x 10^{13} n cm^2/sec until a specific activity of ~10 mc/g was attained. No suitable radioisotope of Nb is produced by neutron activation, and the short half life of Al^{28} makes it necessary to start with a much higher specific activity (approximately 1000 mc/g) in order to have sufficient time to carry out the anodic oxidation. The irradiated targets were anodized at constant current to various voltages, and the amount of metal dissolved was determined by comparing with a standard. The latter was prepared by dissolving a known weight of the irradiated metal in an identical volume of etching solution.

Target preparation.—The targets were high-purity metal foils of dimensions 3.5 x 1.0 x 0.02 cm. Apart from W, all targets were polished either chemically or electrochemically in order to remove the mechanically damaged surface region using the following reagents:

(*a*) For Nb and Ta: chemically polished with a 5:2:2 mixture of concentrated H_2SO_4:HNO_3:HF acids.

b) For Zr and Hf: chemically polished in a 45:4:51 mixture of concentrated HNO_3:concentrated HF:H_2O.

(*c*) For Al: electrochemically polished in perchloric acid-acetic anhydride.

(*d*) For W: not polished; the same material was used as in ref. (11).

Immediately prior to use, targets of Al and W were given a final pre-anodizing treatment, which consisted of the successive formation and dissolution of several anodic oxide layers approximately 1000Å thick. Unfortunately, no suitable reagent for dissolving the anodic oxides of Zr, Nb, Hf, and Ta without attacking the underlying metal is known to us, and so this pre-anodizing treatment could not be applied.

Anodizing procedure.—The anodic oxidations were all carried out at constant current, using the following electrolytic solutions:

(*a*) For Nb and Ta: 0.1M Na_2SO_4 in water.

(*b*) For Zr, Hf, and W: 0.4M KNO_3 + 0.04M HNO_3 in water.

(*c*) For Al: (i) Vermilyea's solution A (6), *i.e.*, sodium tetraborate (50 g/l) in 95% ethylene glycol—5% water; (ii) ammonium dihydrogen citrate (30 g/l) in water. The electrolyte temperature was always 25°C.

Results

Mobility of metal and oxygen.—Before discussing the behavior of individual metals, it is necessary to establish the significance of the experimental results. For

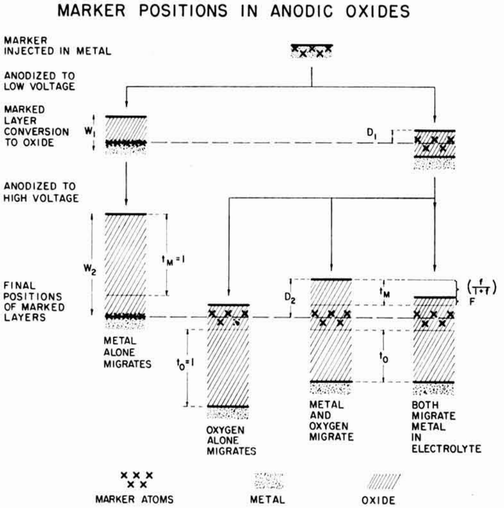

Fig. 3. Effect of metal and oxygen migration on the final position of an inert marker in an oxide film.

this purpose, the oxide is assumed to grow on a plane surface, to be of effectively uniform thickness at all times, and to be free of flaws; it is also assumed that the marker is present in negligible concentration and is truly immobile. There are then three possibilities for oxide growth; either the metal alone moves, or the oxygen alone, or they both move. The effect of metal and oxygen mobility on the final marker position is illustrated in Fig. 3.

If metal ion migration is solely responsible for film growth, the fresh oxide layers will be formed at the oxide/electrolyte interface on top of the marked layer. The situation is complicated, however, by the fact that the metal layers consumed during the oxidation must be replaced by oxide if the film is to remain in contact with the metal. Since the oxygen is, by definition, immobile, the oxide film must adjust itself to the metal surface by some process of plastic flow deformation; under these circumstances, the marker atoms will be trapped at the oxide/metal interface. Such markers would, therefore, appear buried by the full depth of the oxide film, but no practical example of this has yet been found.

If the oxide grows entirely by the inward movement of oxygen ions, migrating either directly through the oxide or by a series of replacement events, then the fresh oxide layers will be formed at the metal/oxide interface underneath the marked layer. The latter will, therefore, remain close to the oxide/electrolyte interface, and no burying of the marker will be observed.

If both metal and oxygen move, the marker atoms will be found somewhere in the middle of the film, the exact position depending on the relative mobilities of the metal and oxygen. Since all the metal ions migrating across the marked layer give rise to oxide above it, and all the oxygen ions migrating inward to oxide below, it is evident that the final position of the marked layer within the oxide can be used as a measure of the ionic transport fractions of metal and oxygen. Denoting these fractions by t_m and t_o, such that $t_m + t_o = 1$, it follows that t_m is equal to F, the fractional burying of the marked layer.

So far, it has been assumed that fresh oxide is formed only at the surfaces of the existing oxide. This is where it must occur if either the metal or the oxygen is the sole mobile species. If, however, both are mobile, the possibility arises that fresh oxide can be formed at points within the existing oxide, as suggested by Cheseldine (14). Growth of new oxide within the existing oxide does not appear to occur under the conditions of the present experiments, for if it did the Xe^{125} distribution would tend to broaden; the experiments with Rn^{222} show that no significant broadening takes place (4).

For the practical determination of t_m, account must be taken of the finite depth of the Xe^{125} markers in the initial oxide film. Accordingly, differential experiments were carried out in which the Xe^{125} depth, D_1, was measured in the low voltage oxide of thickness W_1. After anodizing to high voltage to produce an oxide film of thickness W_2, the depth, D_2, of the Xe^{125} was again measured. The fraction F was then obtained from

$$F = \frac{D_2 - D_1}{W_2 - W_1}$$

The cationic transport fraction, t_m, is equal to F only if no metal dissolves in the electrolyte; if metal does dissolve, say a fraction, f, of that giving rise to oxide, then

$$t_m = \frac{F + f}{1 + f}$$

Niobium, tantalum, and tungsten (*Fig.* 4).—After bombardment with Xe^{125}, samples of these three metals were anodized to low voltage in order to incorporate the Xe^{125} in the oxide layer, and then reanodized to a much higher voltage. No Xe^{125} was lost from any of these oxides during the oxidation process, and only trace amounts of metal were found in the electrolyte; less than 0.1% for Ta, and less than 0.5% for W. No information could be obtained for Nb as no suitable radioisotope was available. Oxide thicknesses were extracted from the appropriate information in Young's book (15). The increase in the Xe^{125} depth divided by the increase in the total oxide thickness gave the fractional burying, F, of the Xe^{125}; with such a small loss of metal to the solution, F approximates the cationic transport fraction t_m very closely.

As can be seen from Table I, t_m is close to 0.30 for all three metals, and so the oxygen mobility is about twice that of the metal. The error in each determination is probably about ±0.03, due to uncertainties in the Xe^{125} depth; variations in the individual errors quoted for the latter are due to differing counting rates in the samples measured. The Xe^{125} depths in Nb_2O_5 are less reliable because of the larger uncertainty in the calibration; Ta_2O_5 has been assumed to have the same

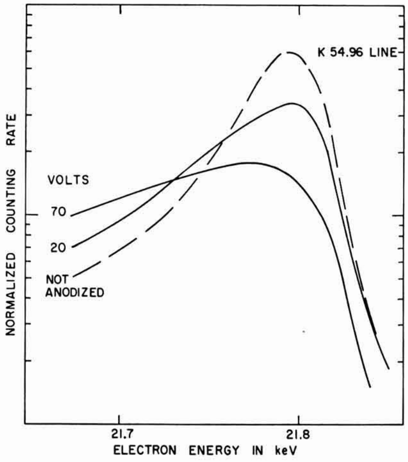

Fig. 4. The K54.96 conversion electron spectra from Xe^{125} atoms in anodic WO_3; 5 kev Xe^{125} in W subsequently anodized at 0.1 ma/cm^2.

Table I. Niobium, tungsten, and tantalum

Current density, ma/cm^2	Final voltage, v	Total oxide formed, μg/cm^2	Xe^{125} depth, μg/cm^2	Change in oxide thickness, μg/cm^2	Change in Xe^{125} depth, μg/cm^2	Fractional burying, $F = t_m$
Niobium						
0.1	10	11.3	5.7 ± 1.0			
0.1	125	141	34 ± 6	130	28	0.22
1.0	10	10.5	4.5 ± 1.0			
1.0	60	63	18.5 ± 3	52.5	14	0.27
10.0	10	8.8	(5)			
10.0	125	110	38 ± 4	101	33	0.33
Tantalum						
0.1	10	13.4	3.5 ± 1.5			
0.1	60	82.8	21.5 ± 1.0	69	18	0.26
1.0	10	12.9	6.0 ± 1.0			
1.0	60	77.4	25.7 ± 1.5	64.5	20	0.31
10.0	10	12.1	7.7 ± 1.0			
10.0	125	151	48 ± 2	139	40	0.29
Tungsten						
0.1	20	26.8	16.8 ± 1.0			
0.1	70	93.8	37 ± 3	67	20	0.30
1.0	10	12.3	13.5 ± 1.0			
1.0	60	73.8	36.5 ± 1.5	61.5	23	0.37

calibration as WO_3. No value for the Xe^{125} depth in Nb anodized at 10 ma/cm^2 to 10v was measured, and so a value of 5 μg/cm^2 was chosen. In the light of these errors, no significant variation of t_m with current density or oxide thickness is observed in these metals.

Zirconium and hafnium (Fig. 5).—As can be seen from Table II, the fractional burying, F, of the Xe^{125} in these metals was very small at all the current densities used. Substantial amounts of Xe^{125} were lost during the anodizing process, together with a small loss of metal; we have no data for Hf, but about 0.6% of the Zr appeared in the electrolyte. As is well known, the anodizing behavior of these two metals is much more variable than that of the metals already discussed; there is a marked tendency to evolve oxygen, with resulting lower current efficiency for the formation of oxide. Accordingly, the oxide thicknesses were calculated from a fixed rate of 20 Å/v (15), using a density of 5.5 g/cm^3 for ZrO_2 and 9.7 g/cm^3 for HfO_2 (16); the errors in these thicknesses could easily reach 25%.

The amount of metal appearing in solution corresponds to approximately 1.0 μg/cm^2 of oxide, and this loss is nearly sufficient to account for the magnitude of the Xe losses. If the Xe^{125} tagged layers nearest the surface are removed, the depth distribution of the remaining Xe^{125} will change in such a way that the measured mean depth increases. This effect could account for at least part of the apparent burying; certainly t_m is not greater than 0.05. Accordingly, the thickening of the anodic oxide in these metals must proceed almost entirely by oxygen migration.

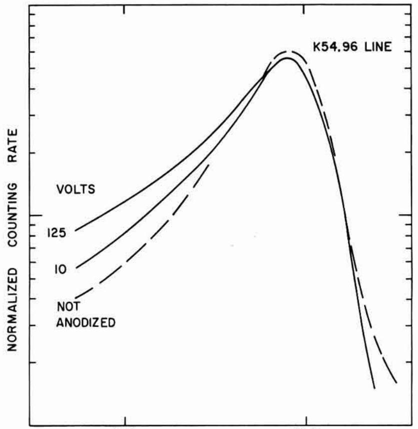

Fig. 5. The K54.96 conversion electron spectra from Xe^{125} atoms in anodic ZrO_2; 3 kev Xe^{125} in Zr subsequently anodized at 1.0 ma/cm^2.

Table II. Zirconium and hafnium

Current density, ma/cm^2	Final voltage, v	Oxide formed, μg/cm^2	Xe^{125} depth, μg/cm^2	Xe^{125} retained, %	Change in oxide thickness, μg/cm^2	Change in Xe^{125} depth, μg/cm^2	Fractional burying, $F = t_m$
Zirconium							
1.0	10	11	3.4 ± 1.0	82			
1.0	125	138	3.2 ± 1.0	69	127	−0.2	0
4.0	10	11	(3)				
	125	138	8 ± 1.5	64	127	5	0.04
10.0	10	11	(3)	81			
	113	124	8 ± 1.5	59	113	5	0.05
Hafnium							
1.0	10	19	3.7 ± 1.0	93			
1.0	57	110	8.5 ± 1.0	86	91	5	0.05

Aluminum.—In solution A.—The results obtained on anodizing Al to 125v in solution A (50 g/l sodium tetraborate in 95% ethylene glycol, 5% water) are given in Table III. The Xe^{125} is completely retained in the oxide at all current densities and occurs at the same depths, 31 μg/cm^2, within the experimental error of 3 μg/cm^2. Some 2% of the metal appears in the electrolyte, the amount decreasing with increasing current density. The mean value of t_m calculated from these results is 0.58 ± 0.04; the error in the individual results is greater than this at 0.06, arising largely from uncertainty in the Xe depth.

In these experiments with Al, the preliminary anodization to low voltage was omitted, and t_m was calculated by a different method. The mean range, $\overline{R}$, of 3 kev Xe^{125} projectiles in polycrystalline Al foil is known to be 2.9 μg/cm^2 (9), which corresponds to 5.5 μg/cm^2 of Al_2O_3. This value was then substituted for D_1 and W_1 in the formula already given for F. Oxide thicknesses were calculated from the weight gains recorded by Bernard and Cook (17) at constant current in an ammonium pentaborate/glycol electrolyte; reasonable agreement with a constant voltage calibration made in solution A is observed.

In ammonium citrate (Fig. 1).—The results obtained on anodizing Al to 125v in 3% aqueous ammonium citrate are shown in Table IV, and are substantially different from those obtained in solution A. In order to relate t_m to the observed Xe^{125} depth in the oxide, two other factors must be taken into account; the first is the dissolution of the Al in the electrolyte, and the second is the loss of Xe^{125}.

Although the amount of Al appearing in the electrolyte decreases with increasing current density as in solution A, the fraction f is nearly twenty times as great at the same current density. It was observed that this dissolution occurs only during anodizing; if the oxide is immersed in the electrolyte without an applied field for a time comparable to the anodizing time, the dissolution is negligible. Similarly, if the applied voltage (100v) was less than that used to form the oxide (125v), no dissolution occurred either. These results confirm Hoar and Mott's hypothesis (18) that the dissolution of the Al is field assisted.

The Xe^{125} is all retained in the oxide except at very low current densities, where for 0.2 ma/cm^2, the loss of 8% is insufficient to affect the mean Xe^{125} depth very much. The 69.5% loss at 0.1 ma/cm^2, however is in a very different category, because the observed Xe^{125} depth is then a measure of the Xe^{125} remaining, which may have a very different depth distribution from the original. Two extreme possibilities can be considered. The Xe^{125} layer can be removed completely from 69.5% of the surface, the remaining 30.5% being untouched and thus retaining its original depth distribution. Under these circumstances, the measured depth corresponds to that measured at other current densities, although the significance of the resultant t_m is open to question. Alternatively, the Xe^{125} layer may

Table III. Aluminum

Aluminum anodized to 125v	In solution A				
Experimental results					
Current density (ma/cm^2)	0.1	0.3	0.5	1.0	10
Observed Xe^{125} depth (μg/cm^2)	30.0 ± 3	30.5 ± 3	33.5 ± 3	32.0 ± 3	29.5 ± 3
Observed Xe^{125} retention (%)	100	100	100	100	100
Al fraction in electrolyte, F*	[0.03]	0.02_3	[0.02]	0.01_6	0.00_8
Calculations					
(i) Oxide formed (μg/cm^2)	46.9	45.6	45.1	44.2	42.4
(ii) Oxide equivalent in electrolyte (i) × F (μg/cm^2)	1.4	1.0	0.9	0.7	0.3
(iii) Corrected Xe^{125} depth Observed + (ii) − 5.5 (μg/cm^2)	25.9	26.0	28.9	27.2	24.2
(iv) corrected oxide thickness (i) + (ii) − 5.5 (μg/cm^2)	48.3	46.6	46.0	44.9	42.7
(v) Cationic transport fraction t_m = (iii)/(iv)	0.54	0.56	0.63	0.60	0.57

* Values of F in brackets have been interpolated for the purpose of calculation.

be removed uniformly across the surface, leaving 30.5% of the Xe^{125} behind at all points. In polycrystalline Al, 30.5% of the 3 kev Xe^{125} projectiles penetrate more than 2.8 μg/cm^2, which corresponds to 5.3 μg/cm^2 of Al_2O_3. The net burial of the Xe^{125} atoms is then 5.5-5.3 μg/cm^2 or 0.2 μg/cm^2, not 5.2 μg/cm^2 as observed. Both values have been used in the calculations for Table I to give the possible range for t_m.

The oxide film thickness was calculated from data available in the literature, as no experimental calibrations were available for the constant current conditions used here. For aqueous borate electrolytes, Young (15) has given an equation relating the current density to the field strength across the oxide, from which angstrom per volt increments can be obtained for any current density. Young, however, measured his oxide thicknesses by a method which included the charge to form the films as a parameter and apparently assumed 100% current efficiency for oxide formation. This is not so; as with aqueous citrate, substantial amounts of Al pass into the borate electrolyte. If Young's values are corrected for the loss of Al to solution, they become very similar to those obtained by Bernard and Cook (17) in ammonium pentaborate/glycol; the latter have therefore been used to compute the oxide thicknesses in aqueous citrate as well as in solution A.

Calculations of Table IV show that in aqueous citrate, t_m does vary with current density, from about 0.37 at 0.1 ma/cm^2 to 0.72 at 10 ma/cm^2. The experimental error in each value is about 10%, arising both from uncertainty in the Xe^{125} depth and in the fraction of Al going into solution; errors in the total oxide thickness have relatively little effect, except at high current density. The value of 0.72 recorded at 10 ma/cm^2 may not therefore be significantly greater than 0.58, but the variation of t_m with current density in aqueous citrate definitely is significant.

Although there does not appear to be any chemical difference between the oxides formed in aqueous and nonaqueous electrolytes (15, 17), it has long been known that Al tends to give duplex films in the former. The outer layer, that next to the electrolyte, has a low resistance to the passage of ionic current and is porous (19), whereas the inner "barrier" layer is continuous and has a high resistance. It is questionable whether the films produced here contain pores, as pore formation has only been observed, for neutral electrolytes like ammonium citrate, on prolonged anodizing at about 0.01 ma/cm^2 (19, 20), which is one tenth of the lowest current density used here. The agreement between the oxide thicknesses formed in aqueous and nonaqueous electrolytes is additional evidence against the presence of a porous layer. Nevertheless, these citrate films do show similarities to porous films, particularly as regards the solution of Al in the electrolyte.

No direct measure of the Al dissolving in the electrolyte appears to have been made under conditions in which the anodic films are known to be porous, but values of f can be calculated from data on the amount of Al remaining in the oxide (21, 22). Thus on anodizing in 15% H_2SO_4 at 21.1°C for 30 min, the fraction f ranges from 0.57 at 13 ma/cm^2 to 0.44 for 78 ma/cm^2. This variation is qualitatively similar to that observed in the citrate electrolyte, but the f values are somewhat greater. It seems possible, therefore, that the variation in t_m is related to the onset of porous oxide formation.

Discussion

The differing results reported in the literature for oxygen and metal mobility in these oxides stem from incomplete interpretation of the experimental data. This arises first from a belief that either the metal or the oxygen can move, but not both (2), and second from a tacit assumption that the foreign atoms used as

Table IV. Aluminum

Aluminum anodized to 125v	In 3% aqueous ammonium citrate					
Experimental results						
Current density (ma/cm^2)	0.1	0.2	0.3	0.5	1.0	10
Observed Xe^{125} depth (μg/cm^2)	5.2 ± 1.5	9.6 ± 1.0	13.0 ± 2	22.5 ± 2	21.0 ± 3	30.0 ± 4
Observed Xe^{125} retention (%)	30.5	92	100	100	100	100
Al fraction in electrolyte, F*	0.43 ± 0.02	[0.41]	0.40 ± 0.02	[0.35]	0.31 ± 0.02	0.19 ± 0.01
Calculations						
(i) Oxide formed (μg/cm^2)	46.9	46.0	45.6	45.2	44.2	42.4
(ii) Oxide equivalent in electrolyte (i) × F (μg/cm^2)	20.2	18.9	18.2	15.8	13.7	8.1
(iii) Corrected Xe^{125} depth Observed + (ii) − 5.5 (μg/cm^2)	20.4-25.4†	23.0	25.7	32.8	29.2	32.6
(iv) Corrected oxide thickness (i) + (ii) − 5.5 (μg/cm^2)	61.6	59.4	58.3	55.4	52.4	45.0
(v) Cationic transport fraction t_m = (iii)/(iv)	0.33-0.41	0.39	0.44	0.59	0.56	0.72

* Values of F in brackets have been interpolated for the purpose of calculation.
† See text for correction applied.

markers are themselves immobile. To illustrate, the work of Lewis and Plumb (1) will be discussed.

These workers anodized aluminum at 50v in 3% ammonium tartrate and then briefly at 52v in radioactive 0.1% $H_2S^{35}O_4$ electrolyte; analysis of the oxide by slow dissolution in 5% H_3PO_4-2% CrO_3 at 50°C showed that almost all the radioactivity was removed in the first 4 min. The reverse experiment, 15v in the $S^{35}O_4^{--}$ electrolyte first followed by 50v in tartrate, was also performed, whereupon the bulk of the radioactivity dissolved between the eighth and fourteenth minutes in the stripping solution. Lewis and Plumb concluded that the oxide applied first was removed last and, hence, that fresh oxide was being formed at the oxide-electrolyte interface. However, these workers had apparently no means of knowing when their oxide was completely dissolved, and consequently, in the reverse experiment, they had no means of knowing whether any oxide was being formed underneath the radioactive layer due to oxygen migration. Furthermore their interpretation rests on the assumption that the $S^{35}O_4^{--}$ is a truly immobile marker. Were the sulfate ion mobile, it would, from its charge, tend to move in toward the metal-oxide interface, and these experiments could then be interpreted solely on the basis of oxygen migration.

Similar experiments have been performed with tantalum, using the film formed in concentrated sulfuric acid as the marker layer. Such films dissolve much more rapidly in HF than do films formed in dilute aqueous electrolytes, and this property has been used to analyze the duplex films. Vermilyea (6) anodized first in dilute aqueous sulfate, and then in concentrated sulfuric acid, and found that the faster dissolving layer was on the outside of the final oxide film. Like Lewis and Plumb, he concluded that metal was the mobile species. Franklin, as reported by Young (15), carried out the reverse experiment, using concentrated sulfuric acid first and dilute acid second, and found that the faster dissolving layer was in the middle of the final oxide. Very recently, Cheseldine (14) has repeated this last experiment almost exactly, forming his marker layer in formic acid rather than concentrated sulfuric. His observations were the same as Franklin's, and he concluded that both the metal and the oxygen were mobile. His value for t_m, 0.48, is however rather larger than that reported here.

It is quite clear that in these experiments on Ta, the marked layer has different properties from the rest of the oxide, and the same may be true of the $S^{35}O_4^{--}$ experiments on Al. In an effort to avoid the complications of chemically different layers, Amsel and Samuel (2) have used O^{18} as the tracer during the anodization of Al, and determined its position in the final oxide by means of nuclear spectroscopy. The introduction of a marker that is part of the oxidation system in principle increases the information that may be obtained from the experiment, for the final depth distribution of the O^{18} is a function not only of the oxygen mobility, but of the method by which it moves. Difficulty in determining the O^{18} distribution with sufficient accuracy, however, limits the information that can be obtained by this nuclear method.

Amsel and Samuel found that a thin O^{18} layer put on first remained essentially in contact with the metal/oxide interface during subsequent anodization to high voltage in an O^{16} electrolyte. They therefore concluded that either the oxygen was immobile, or that it moved in single jumps from one lattice plane to the next, so that the order of the oxygen atoms in the oxide was conserved. The mixing of the O^{16}/O^{18} layers predicted on the basis of the second assumption was not observed, but even with 100% oxygen transport, it would only have been three times the experimental limit of detection. Amsel and Samuel's results are not therefore in conflict with the present observation of about equal metal and oxygen transport in Al.

The results obtained from previous experiments are not therefore in conflict with those reported here, provided that the usual assumption is made; that the Xe^{125} markers are immobile. The Xe^{125} could move in these oxides for one of two reasons; it could diffuse, or it could move under the influence of the applied field because it has a net charge. Since no experimental evidence can be presented on the second point, it will be assumed, for the purposes of the present paper, that the Xe is not charged.

The absence of Xe^{125} diffusion in these oxides is well established. Except for injection energies below 5 kev, all the Xe^{125} striking the surface of anodic Al_2O_3 and WO_3 remains in the oxide (10). This behavior exactly parallels that of the corresponding metals, where the low sticking factor at low bombardment energies was ascribed to failure of the ions to penetrate to a sufficient depth in their initial impact (12). Furthermore, experiments in this laboratory by Kelly have shown that on heating anodic Al_2O_3, no Xe^{125} is released below 600°C, even when the Xe^{125} is injected directly into the oxide at such low energy, 1 kev, that it must be very close to the surface. And finally, the range and the range straggling of injected Xe^{125} ions in anodic Al_2O_3 and WO_3 agrees well with that expected from the theory (13) of Lindhard *et al.* on the range of energetic particles in amorphous solids.

Although the Xe^{125} does not diffuse appreciably in the static oxide, there remains the possibility that it could diffuse in the growing oxide. If so, the distribution of the Xe^{125} markers in the oxide should broaden. The β-ray spectrometry method used here provides no information on the depth distribution of the Xe^{125}, but in a similar experiment using the closely related isotope Rn^{222}, it was shown, by α-particle spectrometry, that no appreciable broadening of the distribution occurs (4).

Manuscript received Dec. 21, 1964.

Any discussion of this paper will appear in a Discussion Section to be published in the June 1966 JOURNAL.

REFERENCES

1. J. E. Lewis and R. C. Plumb, *This Journal*, **105**, 496 (1958).
2. G. Amsel and D. Samuel, *J. Phys. Chem. Solids*, **23**, 1707 (1962).
3. J. A. Davies, J. P. S. Pringle, R. L. Graham, and F. Brown, *This Journal*, **109**, 999 (1962).
4. J. A. Davies and B. Domeij, *ibid.*, **110**, 849 (1963).
5. J. P. S. Pringle and J. A. Davies, Paper presented at the Pittsburgh Meeting of the Society, April 1963, Abstract No. 167.
6. D. A. Vermilyea, *Acta Met.*, **2**, 482 (1954).
7. R. L. Graham, F. Brown, J. A. Davies, and J. P. S. Pringle, *Can. J. Phys.*, **41**, 1686 (1963).
8. B. Domeij, I. Bergström, J. A. Davies, and J. Uhler, *Arkiv fysik*, **24**, 399 (1963).
9. J. A. Davies, F. Brown, and M. McCargo, *Can. J. Phys.*, **41**, 829 (1963).
10. B. Domeij, F. Brown, J. A. Davies, and M. McCargo, *ibid.*, **42**, 1624 (1964).
11. M. McCargo, J. A. Davies, and F. Brown, *ibid.*, **41**, 1231 (1963).
12. F. Brown and J. A. Davies, *ibid.*, **41**, 844 (1963).
13. J. Lindhard, M. Scharff, and H. E. Schiøtt, *Kgl. Danske Videnskab. Selskab., Mat.-Fys. Medd.*, **33**, 1 (1963).
14. D. M. Cheseldine, *This Journal*, **111**, 1128 (1964).
15. L. Young, "Anodic Oxide Films," Academic Press, New York (1961).
16. Handbook of Chemistry and Physics, Chemical Rubber Publishing Co., 43rd ed., (1961-2).
17. W. J. Bernard and J. W. Cook, *This Journal*, **106**, 643 (1959).
18. T. P. Hoar and N. F. Mott, *J. Phys. Chem. Solids*, **9**, 97 (1959).
19. M. S. Hunter and P. F. Towner, *This Journal*, **108**, 139 (1961).
20. T. A. Renshaw, *ibid.*, **108**, 185 (1961).
21. R. B. Mason and P. E. Fowle, *ibid.*, **101**, 53 (1954).
22. R. B. Mason, *ibid.*, **102**, 671 (1955).

Magnetic Properties and Corrosion Behavior of Thin Electroless Co-P Deposits

J. S. Judge, J. R. Morrison, D. E. Speliotis, and G. Bate

Systems Development Division, International Business Machines Corporation, Poughkeepsie, New York

ABSTRACT

Thin magnetic films of Co-P were prepared in two somewhat different electroless cobalt solutions. The magnetic properties and the corrosion behavior of these films as a function of thickness was studied. The films exhibited high coercivities with a maximum of about 1000 oe at a thickness of 600Å. The magnetic moment of these films was found to decrease on exposure to high humidity and moderate temperatures (40°-70°C); this was used as a means of studying the extent of corrosion. The extent of corrosion was found to vary as the 2/3 power of the thickness of the film.

Advances in information storage have created an increasing demand on the capacity of the storage media. For very high density applications, the thinness of the recording surface is of the utmost importance. A thin recording medium not only facilitates the writing of sharper transition regions by the recording transducer, but is also better able to resist demagnetization. Metallic surfaces of chemically deposited Co-P have been investigated as recording media (1, 2). However, the thickness region below 4000Å, which is of far greater importance for high density recording, has not been investigated. It is primarily this region that is the subject of our study.

Two thickness series, produced in somewhat different solutions, were examined. The structural and magnetic properties of these deposits were investigated. Furthermore, the magnetic moment of the deposits was found to decrease on exposure to relatively mild conditions of humidity and temperature. This phenomenon was utilized to study the corrosion behavior of the deposits.

Preparation

The films were deposited on Mylar substrates which were presensitized with the usual $SnCl_2$-$PdCl_2$ treatments (3). Prior to this, the Mylar substrate had been rendered hydrophilic by a two-step process involving immersion first into a hot chromic-sulfuric acid solution, and then into a hot sodium hydroxide solution.

Two somewhat different electroless cobalt solutions were used, a sulfate and a chloride solution. The composition and conditions of the plating solutions were:

Sulfate		Chloride	
$CoSO_4$	0.11M	$CoCl_2$	0.13M
NaH_2PO_2	0.19M		
$(NH_4)_2SO_4$	0.50M	$NH_4H_2PO_2$	0.18M
Na_3(citrate)	0.12M	$(NH_4)_2H$(citrate)	0.155M

Temp.: 80°C; pH: 8.7 at 50°C (pH adjusted with NH_4OH); no agitation.

Thickness, Composition, and Structure

Figure 1 shows the dependence of the weight of the deposit on plating time for the two solutions. From the slope of these curves, the plating rates were measured to be 1.35 μg/cm²/sec for the deposits from the sulfate solution, and 1.12 μg/cm²/sec for the deposits from the chloride solution. These weights were determined by x-ray fluorescence measurements.

The weight of phosphorus deposited was also determined in this way. The dependence of the weight of phosphorus deposited on the total weight of the deposits is shown for the deposits from both solutions in Fig. 2. It can be seen from this plot that there is no apparent change in per cent phosphorus (within the precision of the data) over this thickness range. The average phosphorus content obtained from the slope of the plots of Fig. 2 is 5.8 ± 0.35% and 5.0 ± 0.2% for the deposits from the sulfate and chloride solutions, respectively.

Assuming a density similar to bulk cobalt of 8.9 g/cm³, these films cover a thickness range from 200 to 5000Å.

The structure of the films was examined by x-ray diffraction, and was found to be hcp, with crystallite

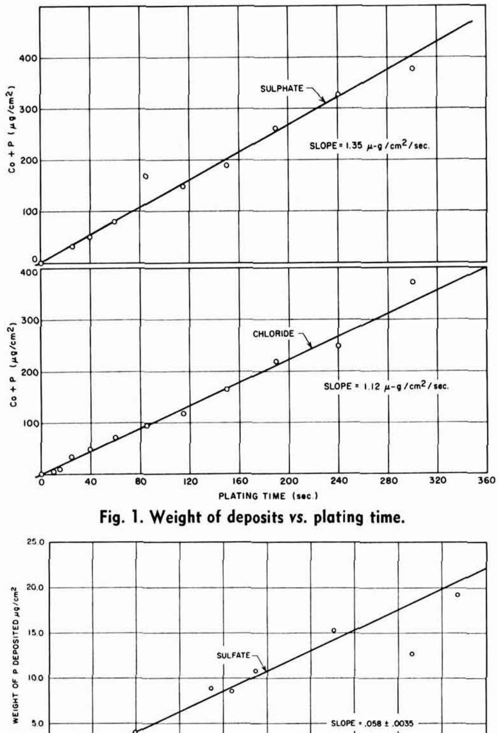

Fig. 1. Weight of deposits vs. plating time.

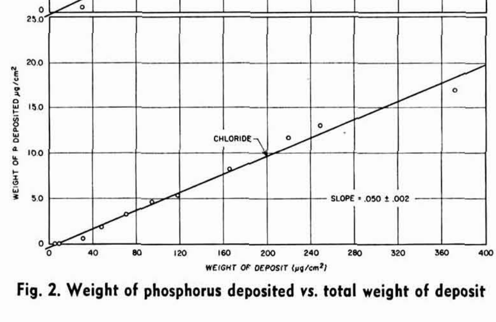

Fig. 2. Weight of phosphorus deposited vs. total weight of deposit

size ranging from 200 to 700Å. This technique gave no evidence of the whereabouts of the phosphorus.

The films had a residual compressive stress of ~20,000 psi. This stress was estimated from the curvature of a sample with plating on only one side (4).

Magnetic Properties

Magnetic measurements were performed using a vibrating sample magnetometer and a very sensitive torsion balance magnetometer (5). The variation of coercivity with thickness is shown in Fig. 3; both curves rise quickly from zero to a maximum coercivity at a thickness of 600-700Å, and then decrease more gradually, tending to a constant coercivity of approximately 400 oe at very large thicknesses. Referring to Fig. 3, we distinguish three different regions of the dependence of coercivity on thickness. Region a (less than 200Å) is dominated by a large number of superparamagnetic regions, resulting in coercivities increasing rapidly with increasing particle size. Region b (300-1000Å) is characterized mostly by a single domain region with very high coercivity. It is interesting to note that this thickness range corresponds to the size of the crystallites. Finally, region c (>1000Å) corresponds to the growth of multidomain regions. Further support to this interpretation can be derived from Fig. 4, where the ratio of remanent to saturation moments is plotted as a function of the thickness of the deposit. In region a, one would expect very low squareness due to the presence of superparamagnetic regions. Region b is characteristic of individual single domain regions with increasing interactions. Finally, region c, with relatively high squareness, is characteristic of strongly coupled and multidomain areas.

The magnetic moment density of the deposits was found to be 111 emu/g for samples prepared in the sulfate bath, and 116 emu/g for samples prepared in the chloride bath, and independent of the thickness of the deposit. The calculated magnetic moment densities, assuming the phosphorus to exist in the films as the nonferromagnetic Co_2P, were 120 emu/g and 125 emu/g for the films from the sulfate and chloride baths, respectively. The discrepancy between the measured and calculated values of the magnetic moment of the deposits may be attributed to the presence of some cobalt oxide or an amorphous cobalt phase (6).

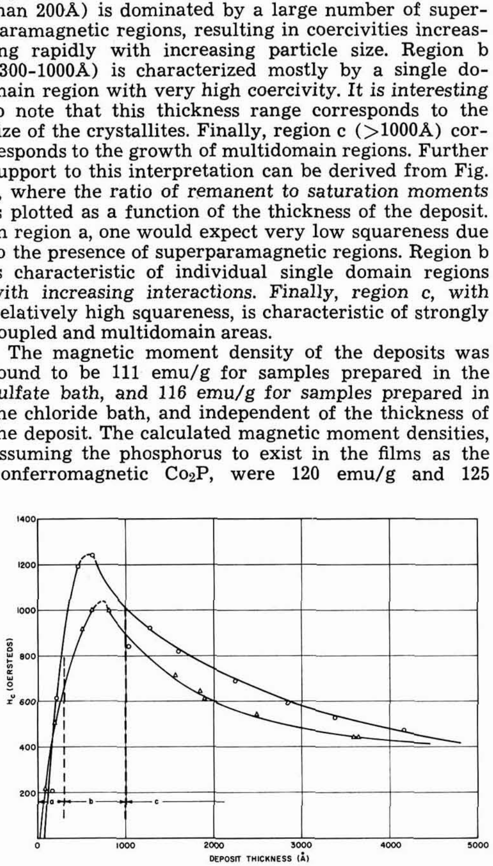

Fig. 3. Coercivity *vs.* thickness; △, chloride; ○, sulfate

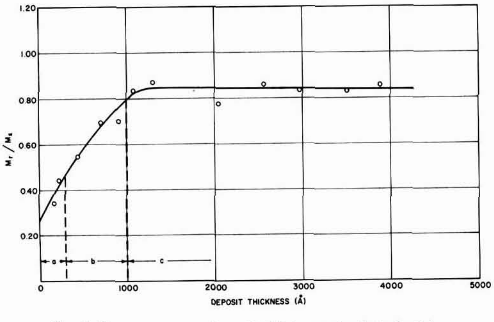

Fig. 4. Squareness *vs.* deposit thickness (sulfate bath)

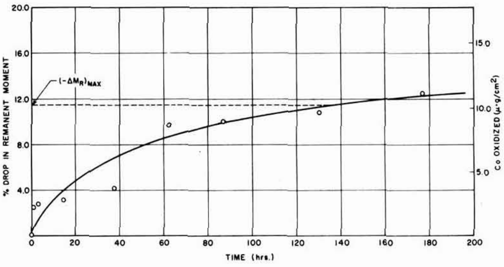

Fig. 5. Per cent decrease in remanence with time due to corrosion

Corrosion Behavior

The corrosion behavior of these deposits was followed by periodically measuring their magnetic moments as they were exposed to high humidity and temperature. Apparently, because of the thinness of these films, and their consequently high surface to volume ratio, relatively large percentage changes in their magnetic moments occurred

A torsion balance magnetometer (5) was used in these studies This instrument had the necessary sensitivity for measurements of small changes in remanent moment. Sensitive measurements of saturation moments were too time consuming to obtain and since there was no apparent change in squareness with corrosion and since the greater sensitivity of the torsion balance was necessary, all the corrosion data are based on changes in remanent moments

The sample used was a disk of 1 cm diameter. These disks were placed in a constant temperature-humidity cabinet and periodically removed for measurements of M_r.

Ten samples plated in an identical manner to a nominal thickness of 1000Å were subjected to this test at 43.5° ± 1.5°C and 80 ± 5% relative humidity. A typical curve of per cent drop in remanent moment *vs.* time is shown in Fig. 5.

The remanent moment, M_r, is related to the amount of ferromagnetic (unoxidized cobalt) by the following relationship

$$M_r = Sq.\, M_s$$

where M_s is the saturation moment of the sample and $Sq.$ the squareness of the sample.

$$M_s = \sigma_s \left(\frac{W}{A}\right) A = \sigma_s XA$$

where W is the weight of unoxidized cobalt, A the

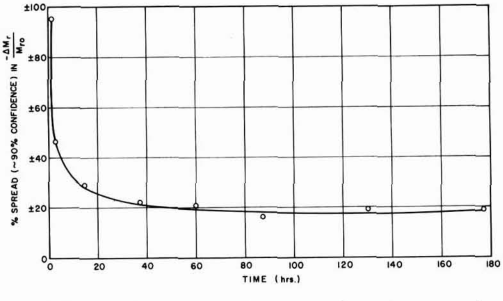

Fig. 6. Per cent deviation from the average change in ten samples

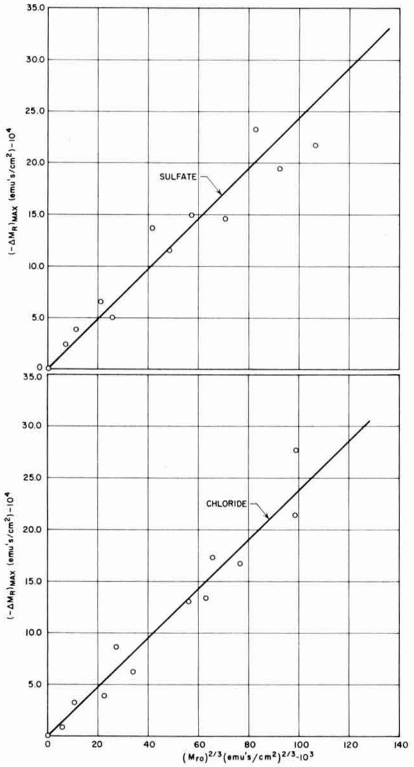

Fig. 7. Dependence of extent of corrosion on initial moment

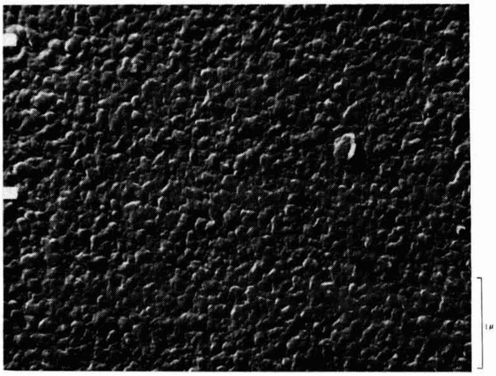

Fig. 8. Electron micrograph of electroless cobalt on Mylar

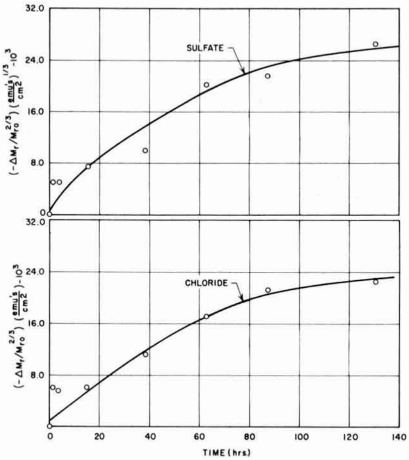

Fig. 9. Corrosion vs. time; temperature, 43.5°C; relative humidity, 80%.

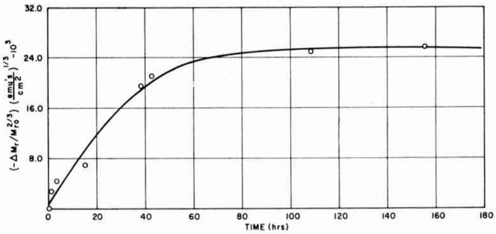

Fig. 10. Corrosion vs. time; temperature, 65°C relative humidity, 80%.

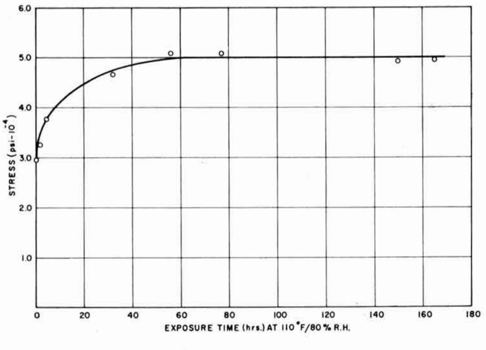

Fig. 11. Deposit stress vs. corrosion time

area of the sample, $X = W/A$, σ_s the saturation moment per gram

$$M_r = Sq.\, \sigma_s XA$$

$$\text{or the fraction of cobalt oxidized} = \frac{-\Delta X}{X_o} = -\Delta M_r/M_{ro}$$

then $-\Delta X = -\Delta M_r X_o/M_{ro}$ = weight per unit area of cobalt oxidized. The weight per unit area of oxidized cobalt for the 1000Å film has been indicated on the right hand ordinate of Fig. 5.

The reproducibility was evaluated by plotting the per cent spread (90% confidence level) in the value of the percentage corrosion as a function of time. This is plotted in Fig. 6; it shows that "identical" samples level out to within ±20% of the same final value of corrosion. The necessity of considering the average behavior of a number of samples is apparent.

When the two thickness series previously described were subjected to these conditions (43.5°C, 80% R.H.), it was found that the change in remanent moment increased with increasing thickness. This effect is particularly apparent, considering only the maximum drop in remanent moment after sufficiently long exposure (*i.e.*, a value at times greater than 100 hr; for these purposes $(-\Delta M_r)_{\text{Max}}$ is $-\Delta M_r$ after 140 hr exposure, see Fig. 5). The dependence of $(-\Delta M_r)_{\text{Max}}$ on sample thickness was found to best fit an $M_{ro}{}^{2/3}$ dependence. This dependence is shown in Fig. 7 for samples from both solutions. This dependence would result if the film were composed of hemispherical clumps the surface area of which increased as the 2/3 power of their thickness. Electron micrographs of similar samples lend support to this interpretation (see Fig. 8).

As a consequence of this thickness dependence, the average value of the thickness independent quantity $-\Delta M_r/M_{ro}^{2/3}$ has been plotted against time for these samples in Fig. 9. These curves show a parabolic or logarithmic (the data does not enable one to distinguish) dependence typical of the formation of a protective oxidation product. It is interesting that despite the difference in early environment (*i.e.,* the plating solution), magnetic properties, and composition of the samples from the sulfate solution and the chloride solution, they exhibit almost identical corrosion behavior. The behavior for both series at 65.5°C and 80% relative humidity is shown in Fig. 10. In this case, the curve levels out at the same value of $-\Delta M_r/M_{ro}^{2/3}$ but rises to this value in about half of the time.

The residual compressive stress of the deposits increased in a manner similar to that of the decrease in remanent moment. The average stress (estimated by the bent strip method) as a function of exposure time at 43.5°C, 80% R. H. is shown in Fig. 11. This result indicates the formation of a corrosion layer of greater specific volume than the metal, again indicative of a protective product (6).

Reflection electron diffraction indicates that the corroded surface is mainly Co_3O_4. Furthermore, an estimate of the thickness of the corrosion film from electron diffraction data agrees fairly well with the 12% measured from the magnetic data for the 1000Å film.

Assuming the product is completely Co_3O_4, the parabolic rate constant in terms of oxygen pick-up can be estimated. This yields the following results for a 1000Å film

	43.5°C	65.5°C
K (g/cm²)²/sec	$3.6 \cdot 10^{-17}$	$4.7 \cdot 10^{-17}$

Conclusion

The magnetic properties of electroless cobalt deposits of variable thickness prepared in different solutions (a sulfate and a chloride solution) were found to be very similar. Furthermore, the variations of the magnetic properties with thickness are related to the crystallite size growth of the deposits. Magnetic moment measurements were used successfully as a very sensitive means of studying the corrosion of magnetic deposits. The amount of corrosion increased with increasing thickness, indicating that the deposits became rougher at increased thickness, *i.e.,* their surface area increased. The advantages of very thin metallic films for magnetic recording must be contrasted with the danger of significant atmospheric corrosion when their surface to volume ratio becomes large. In addition, magnetic and recording studies of such materials must be undertaken with precautions lest significant corrosion occurs during the sometimes extended period of investigation of specific samples.

Manuscript received Sept. 22, 1964; revised manuscript received March 12, 1965.

Any discussion of this paper will appear in a Discussion Section to be published in the June 1966 JOURNAL.

REFERENCES

1. R. D. Fisher and W. H. Chilton, *This Journal,* **109,** 485 (1962).
2. L. D. Ransom and V. Zentner, *ibid.,* **111,** 1423 (1964).
3. E. A. Bergstrom, U. S. Pat. No. 2,702,253.
4. L. Serota, *Metal Finishing,* p. 77, May (1961).
5. G. Bate, D. Schofield, and W. Sucksmith, *Phil. Mag.,* **46,** 621 (1965).
6. J. S. Sallo and J. M. Carr, *J. Appl. Phys.,* **34,** 1309 (1963).
7. N. B. Pilling and R. E. Bedworth, *J. Inst. Met.,* **29,** 529 (1923).

Rotating Disk Study of the Dissolution of Zirconium in HF-HNO_3

R. E. Meyer

Chemistry Division, Oak Ridge National Laboratory, Oak Ridge, Tennessee

ABSTRACT

The rotating disk electrode system was used to determine the rate constants of the reaction of zirconium with HF in solutions of HNO_3 and HF. The reaction was found to be first order with respect to HF, and the rate constants decreased slightly as the potential became more anodic. Possible mechanisms explaining the role of HF in the dissolution reaction are discussed.

When zirconium dissolves in aqueous solutions containing HF, the over-all rate of the reaction is controlled by the rate of mass transfer of undissociated HF molecules to the surface of the electrode (1, 2). An investigation in detail of the kinetics of this reaction requires that the concentration of HF be precisely controlled and determined at the reaction interface. A rotating disk electrode was therefore selected to study this system; for, as Levich (3) has emphasized, this system provides a uniformly accessible surface, *i.e.,* it provides a uniform, determinable concentration of the migrating species along the surface of the electrode. If this condition of uniform accessibility were not met, as would be the case if ordinary methods of stirring were employed, the overpotential would vary across the surface, and complicated current-voltage behavior would be observed.

The dissolution of zirconium in solutions containing HF appears to be complicated in that in some, and perhaps in all cases the reaction proceeds by the continuous formation and dissolution of a film (2). The study of the over-all reaction, therefore, involves the study of both the dissolution and film formation reactions. Some aspects of the kinetics of the film formation reaction were reported previously (2), but the dissolution reaction could not be studied until the mass-transfer conditions were better defined. In the work described here, the rotating disk was used to determine the rate constants of this surface reaction and the dependence of this rate constant on the potential and concentration. All measurements were carried out at potentials sufficiently anodic so that the rate of the hydrogen evolution reaction was negligible.

The derivations of the equations describing the rotating disk electrode system have been summarized by Levich (3). In this reference, it is shown that the flux of a neutral particle is given to within a few per cent by the expression

$$j = 0.62\, D^{2/3}\nu^{-1/6}\omega^{1/2}(C_B - C_i) \qquad [1]$$

where j is the flux, D is the diffusion coefficient, ν is the kinematic viscosity, ω is the angular velocity in radians per second, C_B is the concentration in the bulk of the solution, and C_i is the concentration of the reactant at the interface. If the migrating species is neutral, or if the species is charged and there is a large excess of inert electrolyte (at least 100 to 1), then the current will be given by

$$I = 0.62\, nFSD^{2/3}\nu^{-1/6}\omega^{1/2}(C_B - C_i) \qquad [2]$$

where nF is the charge that is transferred per mole of the migrating species, and S is the area of the electrode.

In many cases of interest, the rate of the surface reaction is comparable to the rate of mass transfer. The reaction rate at the surface may be expressed by the equation

$$I = n'FkSC_i^m \qquad [3]$$

where k is the rate constant, C_i is the concentration of the reactant at the interface, and m is the order.[1] In the steady state

$$I = nFAS(C_B - C_i)\,\omega^{1/2} = n'FkSC_i^m \qquad [4]$$

where $A = 0.62\ D^{2/3}\nu^{-1/6}$. If $m = 1$, these equations may be solved with the elimination of C_i to give

$$\frac{1}{I} = \frac{1}{n'FkSC_B} + \frac{1}{nFASC_B\omega^{1/2}} \qquad [5]$$

A plot of I^{-1} *vs.* $\omega^{-1/2}$ should therefore be linear for a first order reaction, and the rate constant can be determined by extrapolation of the line to infinite frequency of rotation ($\omega^{-1/2} \rightarrow 0$). From the slope of the line, the expression nFA can be calculated, and n can be determined if the value of D is known (or D can be determined if n is known). If the order is not unity, the determinations of the order and the constants are less straightforward, but various techniques have been devised for treating the data (3, 4).

If the rate constant k is large so that the rate of the surface reaction is fast compared to the rate of mass transfer, then C_B will be much greater than C_i in Eq. [2] and the limiting current will be given by

$$I = nFASC_B\omega^{1/2} \qquad [6]$$

and a plot of I^{-1} *vs.* $\omega^{-1/2}$ will go through the origin.

In this work, a series of determinations were made of the current as a function of angular velocity, potential, and solution composition at several potentials anodic to the open-circuit potential. The rate constant k was determined, and n was calculated using estimates of the value of D.

Experimental

In the design of the experiment, the conditions assumed in the solution of the convective-diffusion equation must be maintained. The flow of the solution over the surface of the electrode must be laminar, and the dimensions of the electrode must be large compared to the diffusion and hydrodynamic boundary layers and small compared to the dimensions of the cell (3, 5, 6). In practice, the correct conditions are best determined empirically by varying the pertinent dimensions of the cell until reasonable results are obtained. The conditions depend on the degree of precision desired. If it is desired to determine diffusion coefficients, great care must be taken, for the slopes of plots of Eq. [5] are quite sensitive to the hydrodynamic conditions. If rate constants of surface reactions are desired, then the requirements are relaxed slightly as long as reasonable extrapolations can be carried out.

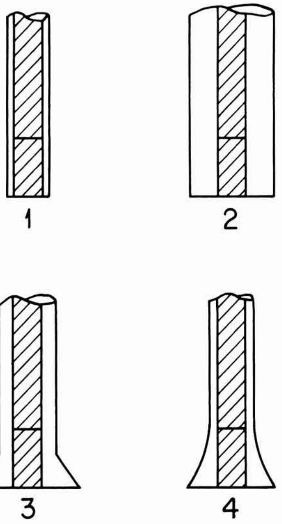

Fig. 1. Electrode shapes used in rotating disk experiments. The outer sections are Teflon.

The electrode shapes shown in Fig. 1 were tried. In each of these configurations, the working surface was the end of a cylindrical electrode ¼ in. in diameter, which was carefully machined perpendicular to the axis of rotation. The electrode was then threaded to a holder which was mounted so that the eccentricity of rotation was less than 0.0015 in. The cylindrical surfaces of the electrode were insulated with a lacquer, and Teflon sleeves of various shapes were fitted about the electrode. All of these configurations gave the same results, and most of the experiments were conducted with No. 1 and 4 of Fig. 1. The cell was made of Teflon with an outer steel liner for reinforcement, and it had an internal diameter of 2¾ in. and a depth of 4 in. Varying the depth of the solution and varying the position of the electrode did not affect the results. Gas inlets and exits were made by leading ⅛ in. diameter Teflon "spaghetti" tubing through holes in the Teflon cell just large enough to insure a tight fit. The saturated calomel reference electrode was also bridged into the solution with the Teflon spaghetti tubing. Varying the position of the tip of the tubing did not affect the results. The solutions contained the required amount of HF plus 1.2M HNO$_3$. The nitric acid served to minimize IR drop, to act as an inert electrolyte, and to suppress ionization of HF.

Speed control was effected by a General Radio 1701-AK Variac speed control driving a 1/15 hp d-c motor. This unit gave excellent regulation from about 100 rpm to 4000 rpm. The angular velocity was determined with a General Radio Strobotac.

During the experiments, the electrodes were held at constant potential with a potentiostat. Currents were recorded by measuring the potential drops across precision resistance with a Hewlett-Packard 425 AR DC Microvolt-Ammeter coupled to a Brown recorder. In some of the experiments, temperatures were maintained at 25°C with a water bath, but since the temperature coefficient of the reaction was quite small, many of the experiments were conducted at 25° ± 1°C with the room thermostat.

Results

The experimental apparatus was tested by investigating the reduction of oxygen on platinum in the limiting current region where Eq. [6] should be valid. For this purpose, a platinum disk electrode whose exposed surface area was identical to that of the zirco-

---

[1] In Eq. [3], the n is primed because it does not necessarily have the same value as the n in Eq. [2]. In the mass transfer expression, Eq. [2], n refers to the number of Faradays transported for every mole of HF that reacts with the zirconium at the surface. This number would therefore depend on the ratio of zirconium to HF in the complex that forms at the surface. The n' in Eq. [3] is the number of Faradays transported across the interface for every mole of zirconium that reacts and would therefore normally have a value of four.

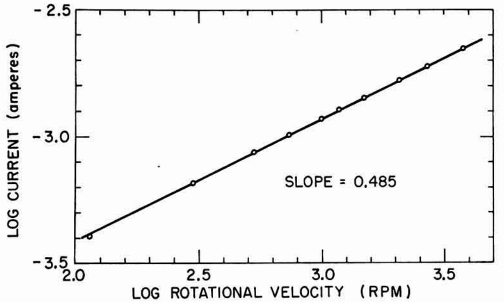

Fig. 2. Reduction of oxygen on rotating platinum disk electrode 0.1M Na_2SO_4, O_2-saturated, electrode area = 0.316 cm^2.

nium electrodes was used. Figure 2 shows a plot of log *I* vs. log ω for this system. The slope of the line is 0.485, which is very close to the theoretical 0.5. A few additional experiments were performed in which a large glass beaker was substituted for the Teflon container, and crystals of $KMnO_4$ were placed in the bottom. The flow pattern characteristic of rotating disks (3) was observed as the $KMnO_4$ dissolved.

Plots of I^{-1} *vs.* $\omega^{-1/2}$ are shown in Fig. 3 and 4 for two separate runs. According to Eq. [5], the extrapolations of these lines determine the fraction $1/n'FkSC_B$, *i.e.*, the reciprocal current at infinite frequency of rotation. The rate constant, *k*, was then calculated for each experiment, and values of the rate constant are recorded in Table I.

If the reaction were precisely first order with respect to the concentration of HF, the values of *k* would be independent of concentration. Instead they tend to decrease slightly as the concentration is reduced to 0.005*N* HF, and then they decrease more sharply as the concentration is reduced to 0.001*N*. Possible explanations for this effect are discussed below. The deviations from first order in an individual run did not appear to be large enough to affect the validity of the extrapolation to infinite frequency, for, as shown in Fig. 2 and 3, the deviations from linearity are not apparent.

The tendency for the apparent order to be slightly greater than unity can also be shown by calculating the concentration at the interface by using the following equation, obtained from Eq. [4]

$$C_i = C_B - \frac{I}{nFAS\omega^{1/2}} \qquad [7]$$

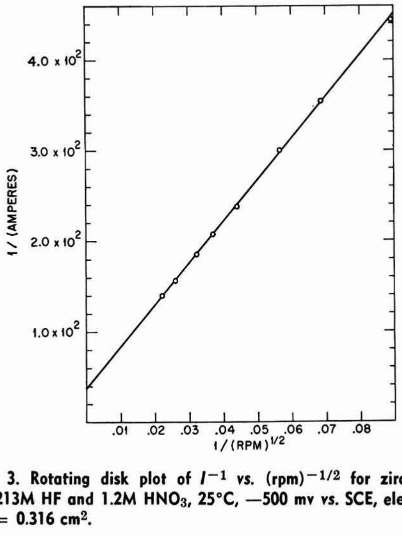

Fig. 3. Rotating disk plot of I^{-1} vs. $(rpm)^{-1/2}$ for zirconium in 0.0213M HF and 1.2M HNO_3, 25°C, —500 mv vs. SCE, electrode area = 0.316 cm^2.

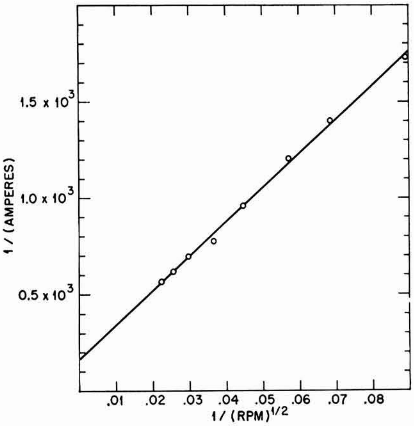

Fig. 4. Rotating disk plot of I^{-1} vs. $(rpm)^{-1/2}$ for zirconium in 0.00535M HF and 1.2M HNO_3, 25°C, —500 mv vs. SCE, electrode area = 0.316 cm^2.

The numerical or effective order can be determined from a plot of log *I* vs. log C_i, since the slope of this plot is numerically equal to the order. The quantity *nFA* was obtained from the slope of the plots of $1/I$ *vs.* $1/\omega^{1/2}$ (Eq. [5]) for each run. The average value of *nFA* for all of the runs in 1.2M HNO_3 is 32.5. In this computation, the units of concentration were moles per cubic centimeter and the units of ω were rpm. An example of a plot of log *I* vs. log C_i is shown in Fig. 5 where an order of 1.17 was found. For most of the runs, the orders found were slightly above unity; values between 1.1 and 1.2 were most common.

The value of the quantity *nFA* was checked by another method of evaluation which took advantage of the fact that as the stirring rate tends to zero, the concentration at the interface also tends to zero. Therefore, if a plot of *I* vs. $\omega^{1/2}$ is extended to the origin, the slope of the tangent drawn to the line at the origin will be given by Eq. [8] [cf. ref. (4)].

$$\frac{dI}{d\omega^{1/2}} = nFASC_B \qquad [8]$$

This method is illustrated in Fig. 6 where it is estimated that *nFA* equals 33.7. This value agrees well with the values found above.

The value of *n* in the product *nFA* can be determined if the diffusion coefficient and the viscosity are known, as shown by Eq. [1]. The viscosity will be given to a

Table I. First order rate constants for zirconium dissolving in 1.2M HNO_3 and varying concentrations of HF

Concentration of HF, mole/liter	*k* in cm sec^{-1}			
	−600 mv	−500 mv	−400 mv	−300 mv
0.0426	0.0197	0.0110	0.0195	—
0.0426	—	0.0146	0.0176	0.0126
0.0213	0.0104	0.0105	0.00961	0.00826
0.0200	0.0101	0.00940	0.00886	0.00855
0.0200	0.0104	0.00948	0.00868	0.00826
0.0100	0.00977	0.00870	0.00806	0.00785
0.0100	0.00948	0.00914	0.00863	0.00762
0.00532	0.0108	0.00958	0.00800	0.00658
0.00532	0.00943	0.00834	0.00697	0.00640
0.00500	0.00914	0.00720	0.00642	0.00596
0.00500	0.00806	0.00684	0.00627	0.00598
0.00500	0.00876	0.00782	0.00787	—
0.00213	0.00526	0.00495	0.00456	0.00417
0.00213	0.00376	0.00358	0.00329	0.00409
0.001065	0.00324	0.00290	0.00267	0.00242
0.00100	0.00321	0.00298	0.00311	0.00275
0.00100	0.00313	0.00332	—	0.00254
0.001065*	0.00471	0.00438	0.00399	0.00368
0.001065**	0.00414	0.00376	0.00339	0.00316
0.001065**	0.00391	0.00386	0.00347	0.00342

* 0.12M HNO_3.
** 0.12M HNO_3 + 1.1M $NaNO_3$.

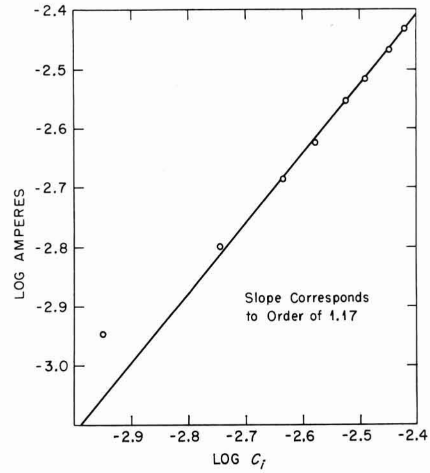

Fig. 5. Determination of order of reaction for zirconium in 0.010M HF, 1.2M HNO$_3$, 25°C, —300 mv vs. SCE, electrode area = 0.316 cm^2.

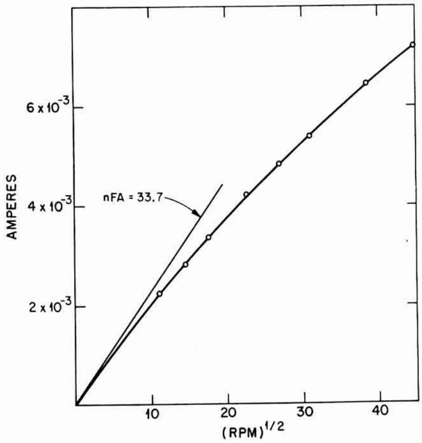

Fig. 6. Rotating disk plot of I vs. (rpm)$^{1/2}$ for zirconium in 0.0213M HF, 1.2M HNO$_3$, 25°C, —500 mv vs. SCE, electrode area = 0.316 cm^2.

good approximation by the viscosity of the appropriate concentration of HNO$_3$. Since the viscosity enters as the 1/6 power, it need not be known precisely. To the author's knowledge, the diffusion coefficient of HF has not been determined experimentally. Further, it is difficult to make a reliable estimate of D because the degree of the interaction of HF with the water is unknown. However, because all known values of D in aqueous solutions are of the order of magnitude of 10^{-5} cm^2/sec, such a value would be expected. From the known values of nFA, the product $nD^{2/3}$ is calculated to be 7.6 x 10^{-4}. Therefore, if D is 2 x 10^{-5}, n is about 1, and if D is 10^{-5}, n is 1.65. If n would be 4, D would be 2.6 x 10^{-6}, a value that is probably too low. A value of D between 10^{-5} and 2 x 10^{-5} seems reasonable for HF and would be consistent with a complex containing from 2.5 to 4 fluoride ions per zirconium ion. The charge on the zirconium ion is assumed to be four.

Discussion

The essential results may be summarized as follows: (A) The reaction rate constant, k, is almost potential independent. (B) The reaction at the surface is first order with respect to HF. (C) The over-all reaction occurring at or very near the surface is $Zr + bHF \rightarrow ZrF_b^{4-b} + bH^+ + 4e^-$ where b probably has a value from 2.5 to 4. (D) There is an effect which tends to decrease the rate constants as the concentration of HF is reduced.

If the dissolution reaction were a simple electrochemical reaction with a normal potential dependence, then the rate constant, k, should increase as the potential becomes more anodic. Furthermore, if normal values of the Tafel slope are assumed, the current would increase by at least two orders of magnitude in the 300 mv potential region that was investigated. Instead, values tended to decrease slightly as the potential became more anodic. This effect is understandable if the potential at the film solution interface where the dissolution takes place remains essentially unchanged as the over-all potential between the metal and the solution is changed. The potential change would then occur primarily across the film or the film-metal interface. This would be in accord with a model, previously proposed (2), in which the dissolution reaction occurs by the continuous dissolution and formation of the film. In this model, the zirconium is oxidized to form a film of oxide on the surface, and the dissolution proceeds by the action of HF on the zirconium ions at the interface between the film and the solution. This is also similar to the case of passive iron (7) where it is observed that the rate of dissolution of the film is potential independent over a wide potential range. In the case of iron, it was assumed that the potential at the interface stays constant and is determined by the equilibrium $2H^+ + O^{=}_{\text{lattice}} \rightleftharpoons H_2O$. A similar equilibrium might also be proposed for the case of zirconium.

The following scheme seems reasonable for the reaction mechanism at the interface between the film and the solution

$$Zr^{+4}{}_{\text{lattice}} + HF \rightarrow ZrF^{+3} + H^+$$
$$ZrF^{+3} + HF \rightarrow ZrF_2{}^{+2} + H^+$$
$$- - - - - - - - - - - - - -$$
$$Zr_{b-1}{}^{4-(b-1)} + HF \rightarrow ZrF_b{}^{4-b} + H^+$$

The intermediate complexes may either be solution complexes at or near the surface, or they may be surface complexes in that they are bonded to the film. If the first reaction is rate-determining, then the rate of the reaction will be given by the expression

$$r = k_1(HF) \qquad [9]$$

where k_1 is the rate constant for the first reaction. If the succeeding complexing reactions occur rapidly in the solution at or very near the interface, a value of n in agreement with the results could be obtained. The complexing reactions must occur in a distance small compared to the width of the diffusion boundary layer so that the complexing affects the value of the concentration of HF at the interface. If the complexing reactions occurred in the bulk of the solution, then the value of n found experimentally would be four, because four units of charge (the Zr^{+4} ion) would be removed from the interface for every reacting HF molecule. The actual value of n is probably from 1 to 1.65 as shown above. Therefore, Eq. [9] could represent the correct mechanism if the complexing occurs at or near the interface.

A similar kinetic equation would result if some or all of the complexing reactions occurred with surface atoms as in the following scheme

$$Zr^{+4}{}_{\text{lattice}} + HF \rightarrow ZrF^{+3}{}_{\text{lattice}} + H^+$$
$$ZrF^{+3}{}_{\text{lattice}} + HF \rightarrow ZrF_2{}^{+2}{}_{\text{lattice}} + H^+$$
$$- - - - - - - - - - - - -$$
$$ZrF_{b-1}{}^{4-(b-1)}{}_{\text{lattice}} + HF \rightarrow ZrF_b{}^{4-b} + H^+$$

In this scheme, all but the last complex is formed on the surface of the film. The expressions for the rates of these reactions are

$$r_1 = k_1(HF)\left(1 - \sum_{n=1}^{b-1} \theta_n\right) \qquad [10]$$

$$r_2 = k_2\,(\mathrm{HF})\,\theta_1 \qquad [11]$$

- - - - - - - - -

$$r_b = k_b\,(\mathrm{HF})\,\theta_{b-1} \qquad [12]$$

In these equations, the θ's represent the coverages of the various complexes on the surface.

In the steady state, the r's are equal and

$$k_1(\mathrm{HF})\left(1-\sum_{n=1}^{b-1}\theta_n\right)=k_2(\mathrm{HF})\,\theta_1=\ldots=k_b(\mathrm{HF})\,\theta_{b-1} \qquad [13]$$

or

$$k_1\left(1-\sum_{n=1}^{b-1}\theta_n\right)=k_2\,\theta_1=\ldots k_b\,\theta_{b-1} \qquad [14]$$

Since there are $(b-1)$ equations in $(b-1)$ unknowns (the values of θ_n), this set of equations may be solved to give any of the values of θ_n in terms of the rate constants. Therefore, the resulting current expression will have the form

$$I = nFKS(\mathrm{HF}) \qquad [15]$$

where K is a combination of rate constants.[2] This has the same form as Eq. [9], and unfortunately, there seems to be no way of distinguishing between these two possibilities.

As noted above, the reaction is not exactly first order, but the effective order is slightly greater than unity. According to the above mechanisms, one would expect an exact first order. A possible clue to this behavior is provided by the experiments in 0.12M HNO_3. Although the concentration of HF is essentially unchanged, the rates are greater than the rates at the same concentration of HF and 1.2M HNO_3. It may be that the nitrate ion, which is present in large relative quantities, competes with the HF molecules at the interface. At high ratios of HNO_3 to HF, the reaction may be slightly inhibited. The ratio of HNO_3 to HF is decreased as the stirring rate is increased, and the rate would then increase faster than if a normal first order mechanism were operating.

Another possibility is that at the lower concentrations of HF, a thicker film may be formed on the surface [cf. ref. (2)]. Relatively thick films may be more resistant to the action of HF as compared to the very thin films formed in the more concentrated solutions. Therefore, as the HF concentration at the interface is changed by varying the rotational velocity, the film may vary in thickness, and, if the thicker films are more resistant, the effect would be to increase the order slightly above first order. This effect would also explain the slight decrease in rate at constant concentration as the potential is made more anodic, for at the more anodic potentials, thicker films are formed (2).

It is also possible that the above systems of equations do not describe this system correctly, and that a more complex mechanism leading to an order of 1.2 occurs. However, the mechanisms described above seem to be the simplest that will describe the data.

Manuscript received Nov. 19, 1964; revised manuscript received Feb. 23, 1964. This paper was presented at the Washington Meeting, Oct. 11-15, 1964. The research was sponsored by the United States Atomic Energy Commission under contract with Union Carbide Corporation.

Any discussion of this paper will appear in a Discussion Section to be published in the June 1966 JOURNAL.

REFERENCES

1. T. Smith and G. R. Hill, *This Journal*, **105**, 117 (1958).
2. R. E. Meyer, *ibid.*, **111**, 147 (1964).
3. V. G. Levich, "Physico-Chemical Hydrodynamics," pp. 72-78, Prentice-Hall, Englewood Cliffs, N. J. (1962).
4. A. N. Frumkin and G. Tedoradse, *Z. Elektrochem.*, **62**, 251 (1958).
5. D. Jahn and W. Vielstich, *This Journal*, **109**, 849 (1962).
6. D. P. Gregory and A. C. Riddiford, *J. Chem. Soc.*, 3756 (1956).
7. K. J. Vetter, *Z. Elektrochem.*, **58**, 230 (1954).

---

[2] If, for example, b equals three, then $K = (k_1k_2k_3)/(k_1k_2 + k_1k_3 + k_2k_3)$.

Electronic Paramagnetic Resonance Study of the Thermal Decomposition of Dibasic Calcium Orthophosphate

J. A. Parodi, R. L. Hickok, W. G. Segelken, and J. R. Cooper

Lighting Research Laboratory, Lamp Division, General Electric Company, Cleveland, Ohio

ABSTRACT

Electronic paramagnetic resonance (EPR) spectra of trace quantities of Mn^{+2} in solid solution in $CaHPO_4\cdot 2H_2O$, $CaHPO_4$, γ-$Ca_2P_2O_7$, β-$Ca_2P_2O_7$, and α-$Ca_2P_2O_7$ are given. The utility of EPR in following phase changes is demonstrated. The transition from β-$Ca_2P_2O_7$ to α-$Ca_2P_2O_7$ is established as occurring within the temperature range, 1171°-1179°. The results of hydrothermal experiments indicate that γ-$Ca_2P_2O_7$ is a metastable phase. It is established by EPR that the amorphous gel formed as an intermediate in the dehydration-recrystallization of $CaHPO_4\cdot 2H_2O$ is in dynamic equilibrium with the solution phase.

Although electronic paramagnetic resonance (EPR) has been used extensively in physics research and free radical chemistry (1, 2) since it was discovered by Zavoyskiy (3) in 1944, it has had rather limited use in the study of solid-state chemical reactions. It has been used to study the effect of pressure (4) and also of impurities (5) on the hexagonal to cubic phase transformation of ZnS, and to follow the course of the synthesis of calcium fluorophosphate (6). Phase changes were followed by observing the EPR spectrum of manganous ion introduced in solid solution in the concentration range of 0.005-0.05% by weight.

In the following paper the EPR of Mn^{+2} is used to follow the thermal decomposition of dibasic calcium orthophosphate dihydrate, beginning with the dehydration to $CaHPO_4$ and followed by pyrolysis to γ-$Ca_2P_2O_7$ with subsequent inversions to β-$Ca_2P_2O_7$ and α-$Ca_2P_2O_7$.

The mechanism of dehydration of $CaHPO_4\cdot 2H_2O$, which has been studied by Vol'fkovich and Urusov (7), Boullé and Dupont (8-10), and Rabatin, Gale, and Newkirk (11), is dependent on the partial pressure of water vapor in contact with the salt and on the method of preparation. Dehydration is favored by high humidity; indeed the recrystallization of $CaHPO_4 \cdot 2H_2O$ to $CaHPO_4$ goes to completion very readily above 75° in water (10). Chiola and Vanderpool (12) state that $CaHPO_4$ is formed by the dehydration of $CaHPO_4 \cdot 2H_2O$ in aqueous medium over the temperature range 65°-104°. The question of whether or not there is an exchange with the solution during recrystallization is taken up in this paper.

The thermal decomposition of dibasic calcium orthophosphate to γ-$Ca_2P_2O_7$ is apt to be rather complex depending on whether $CaHPO_4 \cdot 2H_2O$ or crystalline $CaHPO_4$ is the starting material and whether the ambient atmosphere is dry or humid (8-11). The highest reported temperature at which γ-$Ca_2P_2O_7$ is formed is about 475° (11). When γ-$Ca_2P_2O_7$ is fired at a somewhat higher temperature β-$Ca_2P_2O_7$ is produced. Temperatures reported for this phase transition are 555° (13), 700°-750° (14), and 850° (15). The transition temperature for the inversion of β-$Ca_2P_2O_7$ to α-$Ca_2P_2O_7$ is given as 1140° (16), 1270° (17), 1130° (18), and 1220° (15). The latter two inversions (γ to β and β to α) appear to be straightforward and will be used to illustrate the utility of the EPR method in following phase transformations.

Experimental

Preparation of materials.—The refractive indices and x-ray diffraction patterns of all preparations described below were in agreement with the literature.

1. $CaHPO_4 \cdot 2H_2O$, brushite

Dibasic calcium orthophosphate dihydrate was prepared by two methods. The first of these procedures, described by St. Pierre (19), produces high-purity crystals. It was not possible to introduce manganese into solid solution by this method, but incorporation of manganese was achieved by the second procedure described below.

A solution containing 0.4M $Ca(NO_3)_2$, 0.4M H_3PO_4, and 0.004M $Mn(NO_3)_2$ was slowly neutralized with dilute NH_4OH at 53°. The product was washed with 10^{-3}M H_3PO_4 to insure that no adsorbed Mn would remain. Although it is desirable to carry out this precipitation at low temperature in order to minimize hydrolysis, it was possible to incorporate manganese only at 53° and above.

2. $CaHPO_4$, monetite

Anhydrous dibasic calcium orthophosphate containing trace concentrations of divalent manganese was prepared in two ways: (*a*) by the dehydration-recrystallization of $CaHPO_4 \cdot 2H_2O$ (10, 12) and (*b*) by a homogeneous precipitation procedure (20, 21) in which a solution of the cation salts and phosphoric acid is very slowly neutralized by ammonia liberated during the hydrolysis of urea. The preparative details for the former method are given further on in this paper. Typical conditions for some of the preparations made by the latter method are given in Table I.

Chemical analysis of the recrystallized $CaHPO_4$ gave a Ca/PO_4 mole ratio of 1.023 and an ignition loss of 7.54%, indicating the presence of minor amounts of basic hydrolysis products. On the other hand chemical analysis of homogeneously precipitated $CaHPO_4$ (*e.g.*, $Ca/PO_4 = 0.983$ and ignition loss = 7.25%) suggests contamination with a small quantity of a more acidic phosphate, even though microscopic examination showed the crystals to be free of included impurity phases.

Table I. Homogeneous precipitation of $CaHPO_4$

Concentrations of chemicals used to make solution, and other conditions of preparation

Preparation No.	1 and 2	3	4
$Ca(NO_3)_2$	1.2M		
$CaCO_3$		0.1M	0.2M
$Mn(NO_3)_2$	2×10^{-3}M	10^{-4}M	2×10^{-4}M
H_3PO_4	1.5M	1.0M*	1.0M*
Urea	1.5M	0.4M	0.6M
Temperature	83°	85°-90°	85°-90°
Time	5 days	8 hr	1 hr
*p*H at end of precipitation	2.5	<3.0	2.3

* Actual hydrogen ion concentration is somewhat less than indicated, because acid was used to neutralize $CaCO_3$.

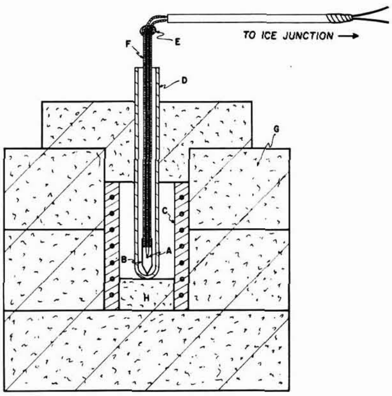

Fig. 1. Furnace for phase transition experiments. A, Pt, Pt-10% Rh thermocouple; B, Pt sample tube; C, heating element; D, mullite tube; E, epoxy cement; F, alumina thermocouple tube; G, alumina fire brick; H, alumina fire brick plug.

3. Calcium Pyrophosphate $Ca_2P_2O_7$

All of the calcium pyrophosphates were obtained from the pyrolysis of monetite or brushite. Gamma calcium pyrophosphate was obtained both by prolonged heating in a vacuum (*e.g.*, 8 days at 275°) and by firing for 4 hr at 500°. β-$Ca_2P_2O_7$ was prepared by firing at 1050° for 1 hr or by hydrothermal treatment: 4 hr at 450° and 30,000 psi. Alpha calcium pyrophosphate was prepared by ignition at 1250° for 1 hr. In addition to using dibasic orthophosphates containing manganese in solid solution, traces of manganese were incorporated in the beta and alpha polymorphs by slurrying the material to be ignited in acetone containing a manganous salt, drying, and firing.

Temperature of the phase transitions, γ-$Ca_2P_2O_7 \rightarrow \beta$-$Ca_2P_2O_7$ *and* β-$Ca_2P_2O_7 \rightarrow \alpha$-$Ca_2P_2O_7$.—The temperatures of the indicated phase transitions were determined by inserting a thermocouple directly into the center of the sample as shown in Fig. 1. The weight of the sample was about 0.2g. The thermocouple was calibrated both before and after the experiments against a standard thermocouple certified by the National Bureau of Standards. There was no change in calibration with use. The output of the thermocouple was read from a precision potentiometer.

Samples were fired from 16 to 20 hr, and the resulting structures were determined by x-ray diffraction and EPR (Mn^{+2} present in the approximate concentration, $Mn/Ca = 10^{-3}$).

Electronic paramagnetic resonance.—Electronic paramagnetic resonance of the polycrystalline calcium phosphate was measured on a Varian Associates V-4500 EPR spectrometer with a resonant frequency of 9480 Mc/s and a modulation frequency of 200 cps. Approximately ¾ in. of sample at one end of a fused quartz sample tube 4 mm OD x 3 mm ID x 4 in. or more in length was used. The EPR spectra reproduced in this paper are potentiometric recorder tracings of the first derivative of absorption of microwave energy versus the magnetic field, which increases from left to right in the figures.

Results and Discussion

EPR spectra of divalent manganese in $CaHPO_4 \cdot 2H_2O$, $CaHPO_4$, γ-$Ca_2P_2O_7$, β-$Ca_2P_2O_7$, and α-$Ca_2P_2O_7$ are presented in Fig. 2. All EPR spectra of a given compound, irrespective of method of preparation, are identical. This indicates that the local symmetry of the

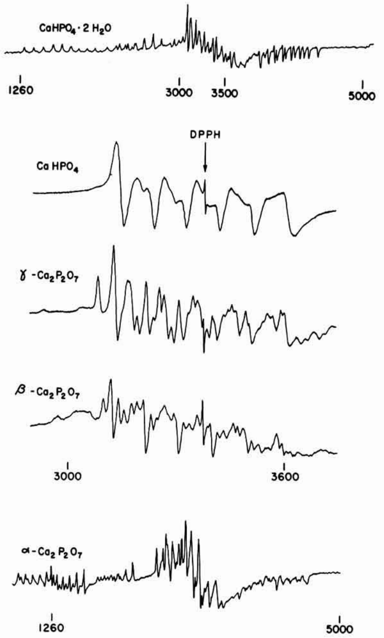

Fig. 2. EPR spectra of Mn^{++} in solid solution in the indicated dibasic orthophosphates and pyrophosphates of calcium. The field marker diphenyl picryl hydrazyl, g = 2.0036, is indicated by DPPH.

crystalline field about the manganous ion (assumed to substitute for Ca^{+2} in these structures) is not affected by minor deviations from stoichiometry which may exist (22, 23).

The high-temperature polymorph, α-$Ca_2P_2O_7$:Mn, has an EPR spectrum which, although unique, is similar to that of $CaHPO_4 \cdot 2H_2O$:Mn in broad outline. Further, both extend over a wide range of magnetic field, about 4100 gauss for the former and 3300 gauss for the latter. The crystalline field interaction with Mn^{+2} is, thus, quite intense for these two structures. On the other hand the effect of the crystalline field on Mn^{+2} in $CaHPO_4$, γ-$Ca_2P_2O_7$, and β-$Ca_2P_2O_7$ appears to be much less, because the range of all three spectra is only about 600 gauss. In the case of powdered samples, however, one cannot discount the possibility that the angular dependence of the spectral lines is such that lines which would appear at large separation in spectra of single crystals are washed out in spectra of powders, and therefore that the fine structure splitting constant is actually larger than it appears to be.

Recrystallization of $CaHPO_4 \cdot 2H_2O$

During the dehydration-recrystallization of $CaHPO_4 \cdot 2H_2O$ in an aqueous slurry the formation of an amorphous gel intermediate was observed. Nucleation and growth of the $CaHPO_4$ crystals occurs in and from this intermediate. One of the questions arising from this observation was whether equilibrium was established between this intermediate phase and the ions in solution. To answer this question experiments were conducted in which EPR measurements were used to follow the course of Mn^{+2} during the transformation.

$CaHPO_4 \cdot 2H_2O$, both with and without incorporated Mn^{+2}, was slurried at 82°C in water and in 0.01M H_3PO_4. For the latter starting material the solutions were also 1.44 x 10^{-4}M in $Mn(NO_3)_2$. In every case EPR showed that Mn^{+2} was incorporated in the recrystallized $CaHPO_4$.

To eliminate the possibility that incorporation of Mn^{+2} in $CaHPO_4$ had occurred after crystallization, $CaHPO_4$ was equilibrated in 0.01M $Mn(NO_3)_2$ at 90°-100°C for two weeks. EPR showed no trace of Mn^{+2} incorporation.

Table II. Determination of transition temperature, β-$Ca_2P_2O_7 \rightarrow \alpha$-$Ca_2P_2O_7$

Firing range, °C	Firing time, hr	EPR result	X-ray result
1170.1-1171.2	22	β	β
1172.8-1173.6	17½	α + small amt. β	α + small amt. of some other phase
1174.3-1175.4	17½	α + trace β	α
1177.3-1179.0	15½	α	α

The β-$Ca_2P_2O_7$:2 × 10^{-3} Mn used for this experiment was made by firing $CaHPO_4 \cdot 2H_2O$ plus manganous acetate at 1050° for 90 min. The $CaHPO_4 \cdot 2H_2O$ was made by the procedure described by St. Pierre (19).

The conclusion reached from these experiments is that the amorphous gel formed as an intermediate in the dehydration-recrystallization of $CaHPO_4 \cdot 2H_2O$ is in dynamic equilibrium with the solution phase. Exchange of ions appears to be rapid.

It is interesting that β-$Ca_2P_2O_7$ and not γ-$Ca_2P_2O_7$ is the result when dibasic calcium orthophosphate undergoes pyrolysis at 450° and 30,000 psi. This temperature is well below that reported for the transition of γ-$Ca_2P_2O_7$ to β-$Ca_2P_2O_7$. As a matter of fact the purpose of carrying out the original hydrothermal pyrolysis at 450° was to prepare well crystallized γ-$Ca_2P_2O_7$. Subsequent experiments in which $CaHPO_4$ was fired overnight or longer at 30,000 psi water pressure and at various temperatures over the range 300°-450° yielded only the starting material, $CaHPO_4$, or β-$Ca_2P_2O_7$. Products were identified by EPR and x-ray diffraction. Temperature and pressure were quenched simultaneously at the conclusion of each experiment. The transition from $CaHPO_4$ to β-$Ca_2P_2O_7$ occurred at 410° ± 15°. When β-$Ca_2P_2O_7$ was similarly treated at 398° and 376° the reverse reaction did not proceed. From these experiments it is concluded that γ-$Ca_2P_2O_7$ is a metastable phase. Mesmer and Irani (15) have shown that the transition from γ- to β-$Ca_2P_2O_7$ is exothermic and therefore also have concluded that the γ-phase must be metastable.

Temperature of the Phase Transition, β-$Ca_2P_2O_7$ *to* α-$Ca_2P_2O_7$

The transition from beta calcium pyrophosphate to alpha calcium pyrophosphate occurs over a narrow range of no greater than 8°. As is seen by reference to Table II the transition begins at a temperature of 1171° or greater. The upper limit of the transition is, according to x-ray results, 1175°; whereas according to EPR it is between 1175° and 1179°. The EPR interpretation is based on a small difference in relative intensity of three pairs of lines. Referring to Fig. 3, the line intensity ratios, A/B, C/D, and E/F, increase on going from the beta to the alpha pyrophosphate. In all samples ignited at 1179° and above the corresponding intensity ratios are the same, whereas for the sample fired at 1174°-1175° the ratios are all a little less than the respective ratios in the former samples. This indicates that perfection of the α-$Ca_2P_2O_7$ structure is not quite complete at 1175° and that at some temperature in the interval, 1175°-1179°, the transformation is complete. It should be emphasized that the temperatures given here are those of the thermocouple at a point within the sample and that there is bound to be some temperature variation along the ¾ in. length of the sample, which might account for the observed temperature range for the phase transition.

The data in Table II were obtained from a sample of β-$Ca_2P_2O_7$:2 x 10^{-3} Mn prepared by firing $CaHPO_4 \cdot 2H_2O$ to which manganous acetate was added prior to ignition. The same results were obtained with β-$Ca_2P_2O_7$:Mn prepared by the pyrolysis of $CaHPO_4$:Mn precipitated from homogeneous solution. This indicates that the transition is independent of the history of the

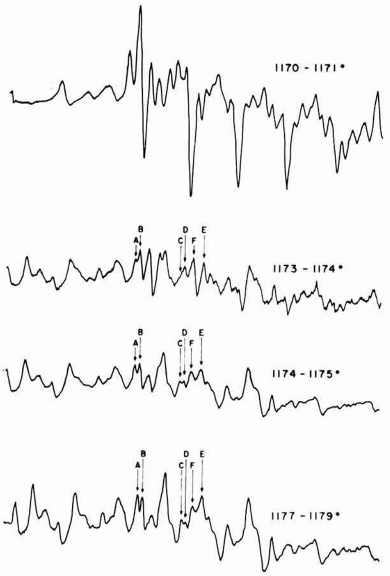

Fig. 3. EPR spectra of $Ca_2P_2O_7$:2 x 10^{-3} Mn fired overnight at indicated temperatures. A progressive change from the beta to the alpha polymorph is evident as the firing temperature increases.

starting material. Furthermore, inasmuch as the method of St. Pierre (19), which was used to prepare the brushite, is known to give very high-purity material, the results also indicate that the quantity and kind of impurities present in the homogeneously precipitated monetite have a negligible effect on the phase transition.

The transition temperature of 1175° ± 4° given here for the above materials is intermediate between the temperatures reported by Hill, Faust, and Reynolds (16) and Mesmer and Irani (15), 1140° and 1220°, respectively.

A point that perhaps should be brought up is the irreversibility of the above structure transformation under normal conditions of preparation for relatively pure material. If the structure change were reversible, quenching would have been necessary to preserve the high-temperature form. The phase transition is so irreversible, as a matter of fact, that α-$Ca_2P_2O_7$ has been prepared by firing at 1250° and annealing overnight in the range 1150° ± 20°, which it is seen is just below the transition range.

Temperature of the Phase Transition, γ-$Ca_2P_2O_7$ to β-$Ca_2P_2O_7$

The transition from γ-$Ca_2P_2O_7$ to β-$Ca_2P_2O_7$ is rather sluggish and poorly defined. Roughly, the temperature range in which the phase change occurs lies between 680° and 740°, in approximate agreement with McIntosh and Jablonski (14), but this appears to be partially dependent on the history of the sample. Results are summarized in Table III.

It is seen that for one starting material, A, there is practically a one to one correspondence between EPR and x-ray diffractometer results. The one exception is for the sample fired at 729°-730°: EPR indicates that conversion to β-$Ca_2P_2O_7$ is not quite complete whereas x-ray results indicate that the conversion is complete. The EPR interpretation is based on the disappearance of a line due only to γ-$Ca_2P_2O_7$:Mn and the appearance and subsequent growth of a line due only to β-$Ca_2P_2O_7$:Mn. As seen in Fig. 4, at 729°-730° there is still a trace of the γ-$Ca_2P_2O_7$:Mn line showing in the EPR spectrum.

Table III. Determination of transition range, γ-$Ca_2P_2O_7$ → β-$Ca_2P_2O_7$

Starting material	Run No.	Firing range, °C	Firing time, hr	EPR result	X-ray result*
A	1	689	16	γ	γ
	2	696	17½	γ + trace β	progressive change toward β ↓
	3	701-702	16	γ + small amt. β	
	4	721	18	β + small amt. γ	
	5	729-730	19	β + trace γ	β
	6	737-739	17	β	β
B	7	685-687	7	γ + trace β	
	8	697-700	17	$\gamma + \beta$	
	9	704-705	21	β + small amt. γ	
	10	706	19	β + small amt. γ	
	11	711	19	β + trace γ	
C	12	686-687	17½		γ
	13	691-692	16½		$\gamma + \beta$
	14	700-704	15½		$\gamma + \beta$
	15	707-708	15½		β

Note: The EPR spectrum of Run No. 7 was identical to that of No. 2 and the EPR of No. 11 was the same as that of No. 5. Thus by comparison with starting material A, the estimated maximum transition range of B is 680°-720°. Starting materials: A, prepared by firing $CaHPO_4$:Mn 1 hr at 500°; B, prepared by firing $CaHPO_4$:Mn 18 hr at 500°; C, prepared by firing $CaHPO_4 \cdot 2H_2O$ 2-3 hr at 600°. $CaHPO_4 \cdot 2H_2O$ prepared by addition of calcium sucrate solution to a dilute solution of phosphoric acid (*19*).

* For group A the x-ray diffractometer was used; for group C the x-ray powder camera was used.

Summary

The thermal decomposition of dibasic calcium orthophosphate was studied by electron paramagnetic resonance (EPR) and x-ray diffraction. EPR spectra of trace amounts of manganous ion in solid solution in $CaHPO_4 \cdot 2H_2O$, $CaHPO_4$, γ-$Ca_2P_2O_7$, β-$Ca_2P_2O_7$, and α-$Ca_2P_2O_7$ are presented. The utility of EPR in following phase changes is demonstrated. The investigations of the phase transitions, γ-$Ca_2P_2O_7$ to β-$Ca_2P_2O_7$ and β-$Ca_2P_2O_7$ to α-$Ca_2P_2O_7$, delineate the fact that EPR is often more sensitive than x-ray diffraction in detecting phase changes.

Some results of the above study which are of possible interest to lamp phosphor technology are given below.

1. It is established by EPR that the amorphous gel formed as an intermediate in the dehydration-recrys-

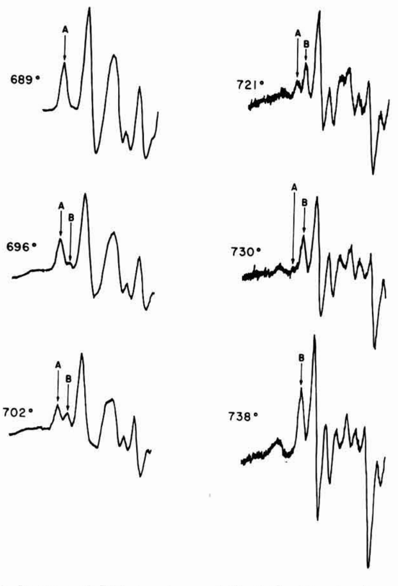

Fig. 4. Portion of EPR spectrum of $Ca_2P_2O_7$:Mn showing change from γ- to β-$Ca_2P_2O_7$:Mn as the firing temperature is increased. Peak A is due to γ-$Ca_2P_2O_7$:Mn and peak B is due to β-$Ca_2P_2O_7$:Mn.

tallization of $CaHPO_4 \cdot 2H_2O$ is in dynamic equilibrium with the solution phase.

2. The transition from β-$Ca_2P_2O_7$ occurs within the temperature range 1171°-1179°.

3. The phase change from γ-$Ca_2P_2O_7$ to β-$Ca_2P_2O_7$ is very sluggish and poorly defined, proceeding roughly between 680° and 740°.

4. When $CaHPO_4$ is heated over the temperature range, 300°-450°, under 30,000 psi water pressure only $CaHPO_4$ or β-$Ca_2P_2O_7$ is produced, the transition occurring at 410° ± 15°. This indicates that γ-$Ca_2P_2O_7$, which under normal atmospheric pressure is the product of the pyrolysis of $CaHPO_4$ in the approximate temperature range of 300°-700°, is a metastable phase.

Acknowledgment

The authors are greatly indebted to Dr. J. F. Sarver for his help in both the implementation and interpretation of the hydrothermal experiments.

Manuscript received Oct. 14, 1964; revised manuscript received March 9, 1965.

Any discussion of this paper will appear in a Discussion Section to be published in the June 1966 JOURNAL.

REFERENCES

1. S. A. Al'tshuler and B. M. Kozyrev, "Electron Paramagnetic Resonance," C. P. Poole, Jr., Translation Editor, Academic Press, New York (1964).
2. D. J. E. Ingram, "Free Radicals as Studied by Electron Spin Resonance," Academic Press, New York (1958).
3. Ye. K. Zavoyskiy, Doctor's Dissertation, Moscow, FIAN, 1944; *J. Phys. USSR*, **9**, 245 (1945).
4. J. S. van Wieringen, *Physica, s'Grav.*, **19**, 397 (1953).
5. M. Aven and J. A. Parodi, *J. Phys. Chem. Solids*, **13**, 56 (1960).
6. P. H. Kasai, *J. Phys. Chem.*, **66**, 674 (1962).
7. S. I. Vol'fkovich and V. V. Urusov, *Izvest. Akad. Nauk S.S.S.R., Otdel. Khim. Nauk*, **4**, 341 (1951).
8. A. Boullé, *Compt. rend.*, **226**, 1617 (1948).
9. A. Boullé and M. Dupont, *ibid.*, **240**, 860 (1955).
10. A. Boullé and M. Dupont, *ibid.*, **241**, 42 (1955).
11. J. G. Rabatin, R. H. Gale, and A. E. Newkirk, *J. Phys. Chem.*, **64**, 491 (1960).
12. V. Chiola and C. D. Vanderpool, Canadian Pat. No. 673, 681, Nov. 5, 1963.
13. E. J. Fox and K. G. Clark, *Ind. Eng. Chem.*, **35**, 1264 (1943).
14. A. O. McIntosh and W. L. Jablonski, *Anal. Chem.*, **28**, 1424 (1956).
15. R. E. Mesmer and R. R. Irani, *J. Chem. Engr. Data*, **8**, 530 (1963).
16. W. L. Hill, G. T. Faust, and D. S. Reynolds, *Am. J. Sci.*, **242**, 457 (1944).
17. W. F. Bale, J. F. Bonner, H. C. Hodge, H. Adler, A. R. Wreath, and R. Bell, *Ind. Eng. Chem., Anal. Ed.*, **17**, 491 (1945).
18. G. Trömel, H. J. Harkort, and W. Hotop, *Z. anorg. Chem.*, **256**, 253 (1948).
19. P. D. S. St. Pierre, *J. Am. Chem. Soc.*, **77**, 2197 (1955).
20. L. Gordon, M. L. Salutsky, and H. H. Willard, "Precipitation from Homogeneous Solution," John Wiley & Sons, Inc., New York (1959).
21. R. W. Mooney and M. A. Aia, *Chem. Revs.*, **61**, 433 (1961).
22. B. Bleaney and K. W. H. Stevens, *Rept. Progr. Phys.*, **16**, 108 (1953).
23. K. D. Bowers and J. Owen, *ibid.*, **18**, 305 (1955).

APPENDIX

The following x-ray diffraction powder pattern was obtained for gamma calcium pyrophosphate made by the pyrolysis of both $CaHPO_4 \cdot 2H_2O$ and $CaHPO_4$ preparations described earlier. It is compared here with the earlier determination of McIntosh and Jablonski (14). It is seen that the two patterns are essentially in agreement, but that there are minor differences. The differences are probably accounted for, however, by the techniques used. The present data were taken on a modern goniometer with larger dispersion and better resolution than the film technique of McIntosh and Jablonski.

X-ray powder pattern of gamma calcium pyrophosphate

This paper*		M. and J.		This paper*		M. and J.	
dÅ	I/I_1	dÅ	I/I_1	dÅ	I/I_1	dÅ	I/I_1
4.51	5	4.55	7	1.951	5	1.96	8
		4.19	5	1.880	<5	1.88	5
3.35	30	3.35	42	1.859	5	1.86	11
3.23	10	3.25	13	1.830	<5		
3.092	65	3.11	65	1.810	10	1.82	35
3.050	45	3.06	35	1.776	5	1.79	27
2.978	5			1.737	<5	1.74	9
2.924	100	2.94	100			1.70	5
2.820	5			1.661	<5	1.67	17
2.788	5	2.78	7	1.638	<5		
2.758	10			1.620	<5		
		2.70	17	1.606	<5		
2.688	5			1.592	<5		
2.544	5	2.56	9	1.567	<5	1.57	13
2.402	<5	2.42	7	1.504	<5	1.51	13
2.359	<5			1.489	<5		
				1.465	<5	1.47	11
2.336	<5	2.34	7			1.40	5
2.268	<5			1.375	<5	1.38	5
2.247	<5			1.336	<5	1.34	5
2.218	15	2.24	35	1.305	<5	1.31	7
2.161	5	2.18	27			1.28	5
2.135	<5	2.15	7			1.27	5
2.113	<5					1.22	4
2.090	15	2.10	23			1.20	4
2.027	<5	2.02	7			1.12	5
1.999	<5					1.09	5
1.979	<5						

* Data taken on G.E. goniometer using copper radiation through nickel filters.

Erratum

The Brief Communication "Recrystallization of Thin Films of Germanium and Silicon" which was published on pages 534 and 535 of the May 1965 issue of the JOURNAL has two authors J. D. Filby and S. Nielsen. Mr. Filby's name was omitted in error.

The Solidification of PbTe-SnTe Alloys under the Influence of Ultrasonic Agitation

H. E. Bates and Martin Weinstein

Tyco Laboratories, Incorporated, Waltham, Massachusetts

ABSTRACT

The previously described technique for the solidification of thermoelectric materials by ultrasonic agitation of a freezing melt has been applied to the solid solution 0.7 PbTe-0.3 SnTe. The material prepared by this technique is fine-grained, dense, and chemically homogeneous. The thermoelectric properties of lead telluride-tin telluride have been measured as a function of temperature. The room temperature figure of merit is approximately $0.6 \times 10^{-3}/°K$. Compressive-flow strength and ductility are improved by ultrasonic agitation; 0.7 PbTe-0.3 SnTe prepared in this study showed 35% reduction in length at an ultimate compressive stress of over 16,000 psi, compared to an ultimate compressive strength of 7,500 psi and 10% reduction in length for unagitated material. Precipitation in the PbTe-SnTe system is discussed. In particular the effects of ultrasonic irradiation on the precipitation phenomenon are described in detail.

Interest in the use of thermoelectric materials for power generation and refrigeration has led to important research into the fundamental nature of thermoelectric phenomena and the means of optimizing thermoelectric properties by alloying and doping (1). Of equal or greater importance to the designer of practical thermoelectric devices are what Klein (2) terms "the auxiliary properties": melting point, vapor pressure, coefficient of expansion, mechanical strength, etc. While the first three properties are quite insensitive to any manipulation of the material other than appreciable changes in composition, which may be incompatible with the desired thermoelectric properties, the possibility does exist of improving the mechanical properties without affecting the composition.

Because of the predominantly covalent nature of most thermoelectric materials, they tend to be highly susceptible to cleavage and brittle failure. The simplest way to decrease brittle fracture in any material is to decrease the grain size, that is, to interpose as many barriers (grain boundaries) as possible to the propagation of micro- and gross cracks. The irradiation of solidifying ingots with ultrasound as a means of producing a fine-grained, equiaxed structure has been studied extensively in the USSR and to a lesser extent in this country (3, 4). An entirely satisfactory mechanism for the refinement of grain structure by ultrasonic vibration has yet to be advanced, but there is general agreement that refinement is caused through decreasing the critical nucleus size by increasing the pressure at certain points in the liquid (3, 5) and/or disrupting the advancing solid-liquid interface by cavitation (4, 6).

The application of ultrasonic irradiation to PbTe-SnTe alloys can be expected to yield several benefits: a fine grained, equiaxed structure with good mechanical strength, free of inclusions and porosity; a chemically homogeneous material free of the gross and microsegregation which occurs under normal freezing conditions. Because of the tendency of doping elements to segregate during normal freezing, most commercial thermoelectric materials have been prepared by cold pressing and sintering or extrusion. The purpose of this investigation was to prepare crystalline, homogeneous alloys with satisfactory thermoelectric properties and mechanical properties superior to those of materials prepared by other techniques.

Experimental

The experimental equipment and procedures here outlined have been described in detail elsewhere (1). Figure 1 shows the assembly used to solidify a melt under ultrasonic agitation. A charge of 50-75g was sealed under vacuum in the quartz tube. A Pt-wound resistance furnace was lowered over the tube and heated until the charge melted, as indicated by a thermocouple attached at the base of the tube. At this point the piezoelectric transducer, epoxied to the base of the quartz pedestal, was energized. Shortly after agitation began, the furnace was raised by a motorized hoist so that solidification proceeded from the bottom of the ingot upward at a rate defined by the rate of removal of the furnace. As the freezing interface moved upward, the input frequency to the PZT crystal was varied to maintain a resonant condition. The input power was also increased gradually to compensate for attenuation of the ultrasonic waves in the solidified portion of the ingot.

Ingots of 0.7 PbTe-0.3 SnTe were solidified under agitation of 19-21 kc at approximately 50w nominal input power and 33-35 kc at 35w. Directional solidification was begun with the base of the melt at approximately 910°C. Growth rate in both cases was about 1.1 in./hr. Faster growth rates tended to diminish grain refinement.

A calorimetric technique was devised to measure the ultrasonic energy input to the melt. The heat capacity of a gallium melt of the same volume as an ordinary ingot was measured in the agitation assembly (Fig. 1), using a thermocouple and a small resistance heater immersed in the melt. The gallium melt was then agitated at various levels and frequencies. The energy absorbed by the melt during agitation was calculated from the known heat capacity and the temperature increase during the application of the ultrasound. The results of these measurements are shown in Fig. 2; the nominal power input refers to the electrical input to the transducer. It can be seen from Fig. 2 that the efficiency of the system is highest when operation takes place in the vicinity of the natural frequency of the transducer (36 kc). Efficiencies of over 35% were achieved at the 34.4 kc resonance. Inputs producing more than 10 w/cm^2 fractured the quartz tube at the tube-pedestal joint.

Results

Employing the process variables noted above, ingots of 0.7 PbTe-0.3 SnTe were produced 0.7 in. in diameter and over 1 in. long which were fine-grained, dense, and chemically homogeneous.

Microstructure.—The solidification of 0.7 PbTe-0.3 SnTe under the influence of ultrasonic agitation resulted in a microstructure (Fig. 3) free of inclusions, porosity, columnar grains, and the segregation asso-

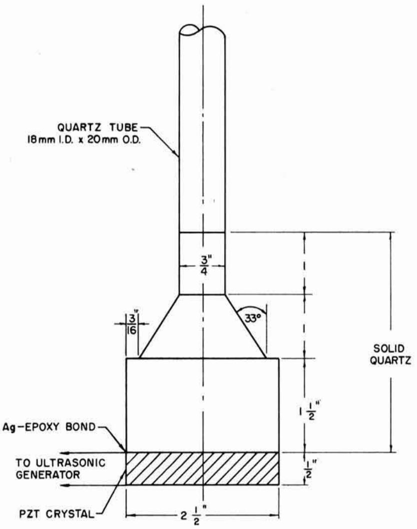

Fig. 1. Piezoelectric transducer, quartz concentrator, and crucible assembly.

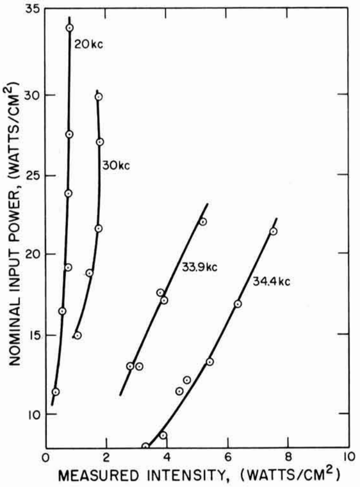

Fig. 2. Ultrasonic energy conversion efficiency for four resonant frequencies.

ciated with normal freezing. Directionally solidified ingots ordinarily consist of five or six columnar grains running the length of the ingot. The surfaces of unagitated ingots usually show considerable porosity and roughness, a feature which is eliminated by the ultrasonic agitation. The microstructure of a water-quenched 0.7 PbTe-0.3 SnTe ingot, with dendritic structure and extensive microsegregation characteristic of this treatment, is shown in Fig. 4. Annealing of this structure below the melting point for 2 hr produced spheroidization of the intergranular segregated phase with little accompanying recrystallization and grain growth. Evidence for the chemical homogeneity produced by ultrasonic agitation is shown in Fig. 5, where the room temperature resistance of p-type 0.7 PbTe-0.3 SnTe is plotted as a function of distance for an agitated and an unagitated ingot. Variations of this sort are even more pronounced in doped alloys where segregation of the dopant produces a quite abrupt variation in properties in the final portion of the ingot to freeze.

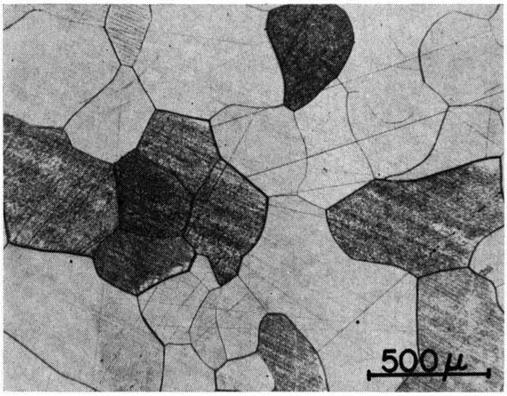

Fig. 3. Microstructure of 0.7 PbTe-0.3 SnTe ingot solidified under ultrasonic agitation. Magnification approximately 42X.

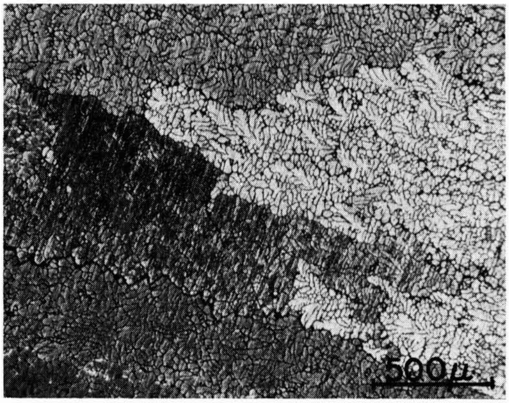

Fig. 4. Microstructure of water-quenched 0.7 PbTe-0.3 SnTe ingot. Magnification approximately 42X.

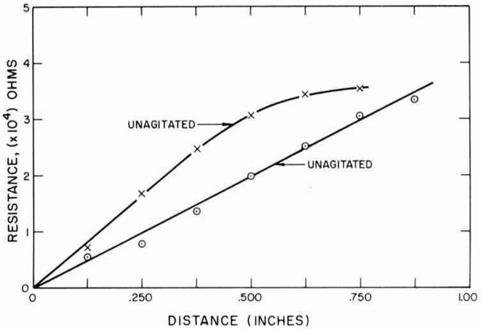

Fig. 5. Room temperature resistance as a function of distance along agitated and unagitated 0.7 PbTe-0.3 SnTe ingots.

Thermoelectric properties.—The figure of merit $Z = \alpha^2/K\rho$ provides a means of comparing the efficiencies of different thermoelectric materials. In the above expression α is the Seebeck coefficient in volts per °C, K is the thermal conductivity in watts/cm/°C, and ρ the electrical resistivity in ohm-centimeters. The Seebeck coefficient and resistivity of cast, directionally solidified, and ultrasonically agitated 0.7 PbTe-0.3 SnTe ingots were measured as a function of temperature.

1. Seebeck Coefficient.—The variation of Seebeck coefficient with temperature is shown in Fig. 6. The ultrasonically agitated material contained a slight excess (0.3 at. %) of Te. The recent investigation by

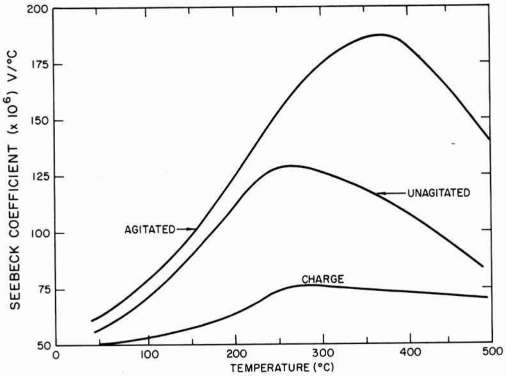

Fig. 6. Seebeck coefficient as a function of temperature of 0.7 PbTe-0.3 SnTe.

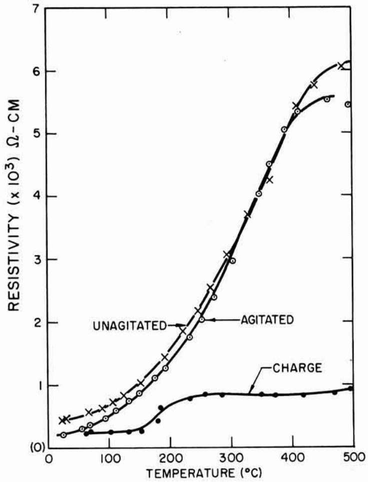

Fig. 7. Resistivity as a function of temperature of 0.7 PbTe-0.3 SnTe.

Machonis and Cadoff (7) which employed cation-rich single crystals of nominal composition 0.7 PbTe-0.3 SnTe showed a slightly different Seebeck behavior, giving a maximum Seebeck coefficient of 190 μv/°C at 180°C. Both the Te-rich and cation-rich specimens are p-type. The low value of the Seebeck coefficient for the directionally solidified material is probably due to segregation and inhomogeneities of the kind discussed by Cosgrove *et al.* (8). The directionally solidified, unagitated ingot also contained 0.3 a/o (atom %) excess Te. Metallographic examination of the cast material showed that the peculiar behavior of the Seebeck coefficient, and of the resistivity, was caused by melting of the interdendritic phase, probably Pb-Sn eutectic (eutectic temperature $\approx$ 185°C). Melting was evidenced by spheroidization of the phase in the preexistant segregation pattern.

2. Resistivity.—The variation of resistivity with temperature is shown in Fig. 7. The difference between agitated and unagitated ingots is negligible. The resistivity as a function of temperature given by Machonis and Cadoff (7) for cation-rich 0.7 PbTe-0.3 SnTe varied from 0.9 x 10^{-3} ohm-cm at room temperature to 10 x 10^{-3} ohm-cm at 500°C.

3. Electrical Efficiency.—The electrical efficiency factor α^2/ρ is shown in Fig. 8 as a function of temperature. The low values of the directionally solidified material are due to lowering of the Seebeck coefficient by inhomogeneous distribution of excess constituents.

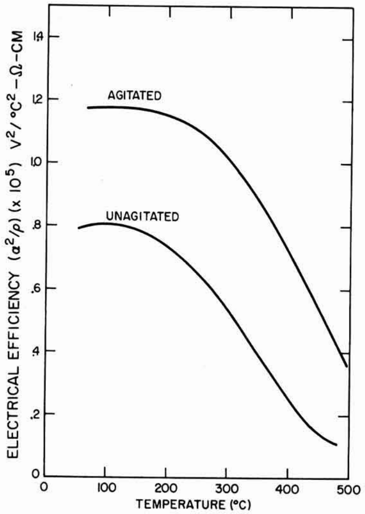

Fig. 8. Electrical efficiency factor as a function of temperature of 0.7 PbTe-0.3 SnTe.

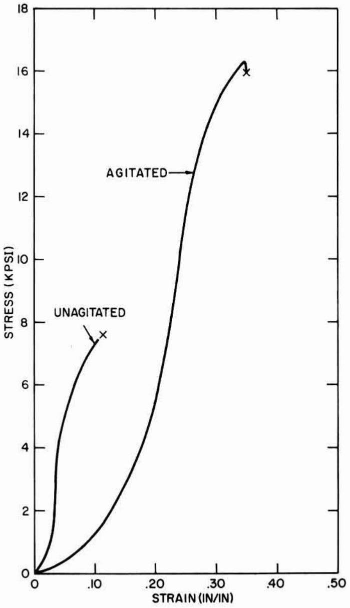

Fig. 9. Stress-strain behavior in compression of 0.7 PbTe- 0.3 SnTe prepared by directional solidification, and directional solidification with ultrasonic agitation.

The total thermal conductivity of 0.7 PbTe-0.3 SnTe has been estimated, in the absence of any measurements, as 0.02 w/cm °K at room temperature. It is probably actually lower, the data of Machonis and Cadoff indicate $k_T \approx$ 0.015 w/cm °K at 300°K; however, using 0.02 w/cm °K the room temperature figure of merit, *Z*, of ultrasonically prepared 0.7 PbTe-0.3 SnTe is approximately 0.6 x 10^{-3}/°K.

Mechanical properties.—The stress-strain characteristics in compression of 0.7 PbTe-0.3 SnTe prepared by directional solidification, with and without ultrasonic agitation, were measured. Rectangular specimens about 0.4 in. square by 0.3 in. long were compressed in a Hounsfield Tensometer, Type W. Strain rate was

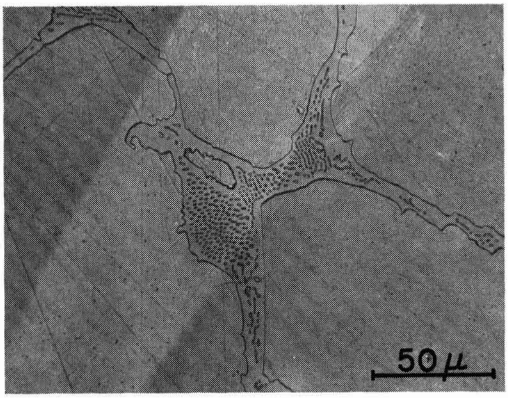

Fig. 10. Sn-Pb eutectic in grain boundaries of stoichiometric 0.7 PbTe-0.3 SnTe ingot. Magnification approximately 420X.

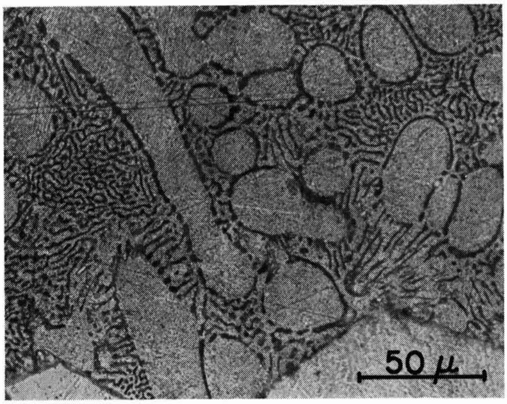

Fig. 11. Eutectic structure in last portion to freeze of unagitated ingot of 0.7 PbTe-0.3 SnTe +0.3 a/o Te. Magnification approximately 420X.

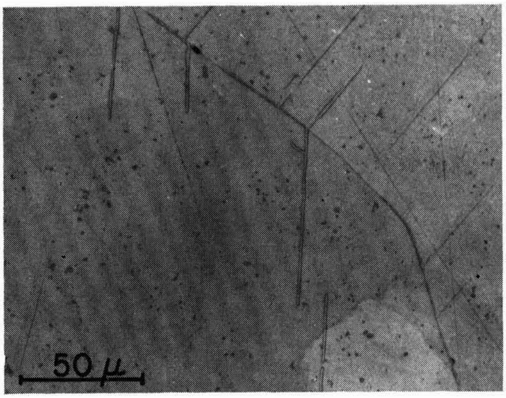

Fig. 12. Precipitation of excess Sn as stringers and spheroids in ultrasonically agitated 0.7 PbTe-0.3 SnTe. Magnification approximately 420X.

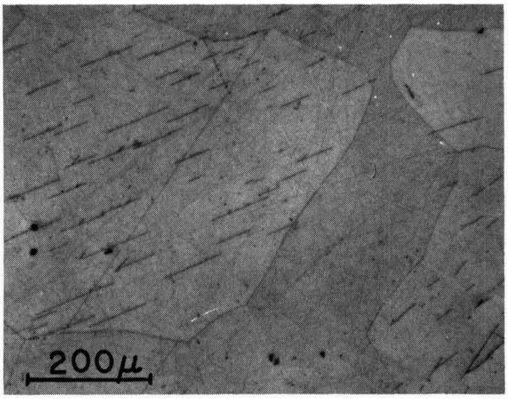

Fig. 13. Precipitation of excess Sn on slip lines in grains of ultrasonically agitated 0.7 PbTe-0.3 SnTe. Magnification approximately 85X.

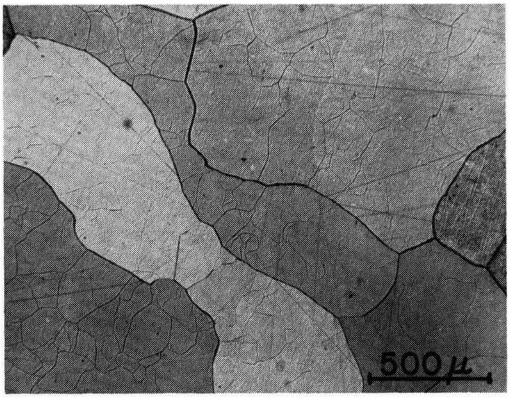

Fig. 14. Extensive subgrain array in bottom portion of ultrasonically agitated ingot of 0.7 PbTe-0.3 SnTe. Magnification approximately 42X.

approximately 5 %/min. Results of these measurements are presented in Fig. 9. Compression was parallel to the direction of solidification in both cases. The unagitated material showed 30-40% lower strength when compressed perpendicular to the growth axis, while the agitated ingots were isotropic. The considerable improvement in strength and ductility of the agitated material can be attributed, as in the case of PbTe in the previous study (1), to the production of a fine-grained, equiaxed structure free of inclusions and porosity. It is interesting to note that in both systems, PbTe and 0.7 PbTe-0.3 SnTe, the agitated material has twice the ultimate strength and three times the ductility of the unagitated.

Precipitation phenomena.—Some interesting observations of second phase precipitation were made during this investigation. Some ingots of 0.7 PbTe-0.3 SnTe when agitated with fairly high sound intensities (8-10 w/cm^2 at 35 kc) showed extensive intergranular porosity in the bottom third of the ingot. In the solid portion of the ingot there was an almost continuous network of eutectic phase (Fig. 10). These ingots were made with the stoichiometric amounts of Sn and Te. Due to the deviation from stoichiometry in SnTe (9, 10), a stoichiometric melt will contain an excess of Sn on solidification. It is felt that this eutectic is of Sn-Pb, which, because of its low $(\approx 185°C)$ melting point appeared in the grain boundaries as liquid and was then forced out by the ultrasonic irradiation and concentrated in the top of the ingot. To eliminate this problem, ingots were prepared with excess Te and the intensity of the ultrasound was slightly reduced. Addition of 0.3 a/o excess Te effectively eliminated precipitation of Sn. In the unagitated ingot a small amount of eutectic which is thought to be Te-PbTe was found in the last portion to freeze (Fig. 11). The interesting aspect of the precipitation of excess Sn in stoichiometric ingots was that moderate intensities of ultrasound resulted in a regular array of parallel stringers and tiny, random spheroids of Sn in the bulk of the grains, with very little precipitation in the grain boundaries. Figure 12 shows the intersection of the needle-like Sn with a grain boundary. Figure 13 shows the regularity of this structure and the virtual absence of Sn precipitated at the grain boundaries. It is felt that these precipitates occur on slip lines in the grains; the regularity of the array, the change in orientation from one grain to the next, the appearance of competing orientations intersecting the predominant one, (Fig. 13) and particularly the observation of subgrain formation in agitated ingots (Fig. 14) indicate deformation of the grains by the ultrasonic process. Lane, Cunningham, and Tiller (11) also observed decoration of slip lines by carbide precipitates in an Fe-Mn-Cr alloy with ultrasonic agitation of the solidifying ingot.

Silverstein *et al.* (12) found evidence of increased stress in the grain boundaries of ultrasonically agitated weldments in Ta, but in the present investigation the evidence from precipitation of excess Sn indicates that although the grain boundaries remain regions of high strain, the ultrasonic irradiation has effected a redistribution of the strain in the aggregate such that precipitation is now favored in the bulk.

Conclusions

1. Fine-grained, homogeneous p-type 0.7 PbTe-0.3 SnTe has been prepared by ultrasonic agitation of directionally solidified ingots.
2. The ultrasonic irradiation of solidifying 0.7 PbTe-0.3 SnTe produced material with twice the compressive strength and three times the ductility of directionally solidified 0.7 PbTe-0.3 SnTe.
3. The thermoelectric properties and efficiency of p-type 0.7 PbTe-0.3 SnTe (Te-rich) prepared by ultrasonic agitation are superior to those of directionally solidified unagitated material.
4. Ultrasonic agitation promotes the precipitation of excess Sn from 0.7 PbTe-0.3 SnTe in the bulk of the grains along slip planes, rather than at the grain boundaries.

Acknowledgments

The authors wish to thank Mr. E. J. Sherwin for aid in the experimental segment of the program. The financial support of the Bureau of Ships, Department of the Navy, under contract No. NObs-86015 is gratefully acknowledged.

Manuscript received Dec. 1, 1964; revised manuscript received March 10, 1965. This paper was presented at the Washington Meeting, Oct. 11-15, 1964.

Any discussion of this paper will appear in a Discussion Section to be published in the June 1966 JOURNAL.

REFERENCES

1. M. Weinstein, *Trans. AIME,* **230,** 321 (1964).
2. P. H. Klein, in "Thermoelectric Materials and Devices," p. 56, I. B. Cadoff and E. Miller, Editor, Reinhold Publishing Co., New York (1960).
3. J. R. Wallace, *J. Metals,* **15,** 5372 (1963).
4. J. G. Kura and H. W. Mishler, Defense Metals Information Center, Battelle Memorial Institute, AD Report No. 410538, Air Force Contract No. AF 33(616)-7747, May 1963.
5. R. G. Garlick and J. F. Wallace, *AFS Trans.,* **67,** 366 (1959).
6. I. G. Polotskii and G. I. Levin, *Sb. Nauchn. Rabot. Inst. Metallofiz. Akad. Nauk UKrSSR,* **13,** 176 (1961).
7. A. A. Machonis and I. B. Cadoff, *Trans. Met. Soc. AIME,* **230,** 333 (1964).
8. G. J. Cosgrove, J. P. McHugh, and W. A. Tiller, *J. Appl. Phys.,* **32,** 621 (1961).
9. J. Umeda, M. Jeong, and T. Okada, *Japan. J. Appl. Phys.,* **1,** 277 (1962).
10. R. F. Brebrick, *J. Phys. Chem. Solids,* **24,** 27 (1963).
11. D. H. Lane, J. W. Cunningham, and W. A. Tiller, *Trans. Met. Soc. AIME,* **218,** 985 (1960).
12. S. M. Silverstein, J. N. Antonvich, R. P. Sopher, and P. J. Rieppel, *Metal Prog.,* **80,** 6 (1960).

Donor Diffusion into GaAs from Group VI Compounds

R. G. Frieser

Bell Telephone Laboratories, Incorporated, Murray Hill, New Jersey

ABSTRACT

A simple and reproducible technique is presented for diffusing donors into p-type GaAs using binary sulfides, selenides, or tellurides as donor sources. Using compound sources, the effective vapor pressure of the donor impurity is reduced, thereby limiting troublesome surface erosion of the wafers during diffusion. Either a sealed or a "closed box" system is suitable. With Al_2S_3 as a doping source, observed junction depth in zinc or in cadmium doped GaAs varied linearly with the square root of time. The diffusion coefficient of sulfur is given by $D = 2.6 \times 10^{-5} \exp(-1.86/kT)$ in Zn doped GaAs. Anomalous results were obtained in Cd doped substrates at higher temperatures where higher values of the effective diffusion coefficients were observed.

Donors such as S, Se, Te, or Sn have been diffused into GaAs by several investigators (1-4). In all reported cases the donor sources were the elements themselves. Reported difficulties with this technique were alloying and formation of sulfides during diffusion which produced severe surface erosion. At diffusion temperatures both donor elements and arsenic are not only quite reactive, but volatilize to an appreciable extent (5, 6). Furthermore, in the presence of sulfur the transport problem of arsenic and gallium from the surface of the GaAs wafers is enhanced, presumably by the formation of volatile compounds (5).

The present work was directed toward employing group VI compounds (sulfides, selenides, or tellurides) as donor sources, thus reducing the vapor pressure of donor elements during diffusion. This report describes a simple and reproducible technique, using compounds as donor sources for diffusion into GaAs. The effective diffusion coefficient of sulfur has been determined and will be discussed.

Experimental

Exploratory work indicated that a practical and useful donor diffusion system for GaAs should incorporate the following features: (*a*) a minimum temperature gradient across the diffusion system to prevent surface erosion caused by transport and redeposition of material elsewhere in the system; (*b*) an oxygen-free source of arsenic to satisfy the equilibrium arsenic pressure in the system; and (*c*) a source providing a constant and low concentration of donor atoms.

These conditions were approximated in the following manner. Sealed quartz tubes were used for the major portion of this work; however, equally good results were obtained with a "closed box" system for the diffusions (7). The temperature gradient across the sealed diffusion tube was 3°C or less during the diffusion, thereby reducing surface erosion. Crushed undoped GaAs was placed in the system to limit arsenic as well as gallium loss from the slice to be diffused (5). Sulfides were chosen as donors since the concentration of donors over these compounds in a closed system is constant and only a function of the dissociation pressure, which is uniquely determined by the temperature. A wide range of surface concentrations and junction depth is therefore possible by merely choosing a sulfide with an appropriately low vapor pressure of sulfur and a suitable diffusion temperature and time. The same argument applies to selenides and tellurides as well. One limitation on the choice of source is that the second component of the source should not form a stable arsenide at diffusion conditions.

Materials.—Table I lists the properties of the GaAs used in this work as supplied by the manufacturer on the basis of Hall and resistivity measurements. All crystals were cut into slices perpendicular to their growth direction, <111> within 5°, and ~0.38 mm thick. The slices were lapped and then chemically polished (8) on the arsenic-rich side prior to diffusion. All donor compounds came from commercial sources and were used without further treatment.

To provide the partial vapor pressure of arsenic in the diffusion system, crushed undoped GaAs (B18) (Table I) was acid washed [70 ml H_2SO_4 (95%), 15 ml H_2O_2 (30%), 15 ml H_2O] (9), rinsed with deionized water, acetone, and dried. Table II is a list of all the compounds examined on an exploratory basis as donor sources. Diffusion temperature was 900°C except for those compounds in Table II marked with an asterisk for which it was 800°C. Diffusion time was 2 hr.

Primarily because of their melting points and because little surface erosion and good junctions were obtained, the following compounds were chosen for more detailed consideration as donor sources: As_2S_3, GeS, Ga_2S_3, and Al_2S_3. Aluminum sulfide provided the bulk of the data of this work.

Procedure.—Quartz tubes (9 mm ID, 1 mm wall) were thoroughly cleaned (HF, NH_4OH, DI water) and dried at 100°C in an oven. Precisely weighed amounts of crushed GaAs (1000-4000 μg), the donor source (100-1000 μg) and one or two wafers (of different zinc concentration) were placed into the bottom of a tube. The weight of the wafers ranged from 10,000 to 80,000 μg. This tube was evacuated to ~1 Torr, heated for about 5 min at 300°C to remove any moisture, oxygen, or free sulfur, if present, and sealed while still under vacuum and hot. For donor sources other than Al_2S_3 the temperature was 150°C. Diffusions were carried out in a high-temperature furnace operated in the range of 800° to 1100° for ½ to 16 hr. The sealed diffusion tubes were placed in a heavy stainless steel jacket. Temperature gradients of 3° ± 0.5°C or less in a 12 cm temperature zone were observed during diffusions. To prevent surface deterioration after diffusion and during cooling the following procedure was found to be best. The steel jacket with the tube inside was removed from the furnace and ~¼ in. of the tube was exposed to room air for ~1 min until the steel jacket reached ~750°C (cherry red). The ampoule was then completely withdrawn from the steel jacket and the end opposite the wafer was quenched.

Table I. GaAs substrate

GaAs crystals		Impurity conc per cm^3	Resistivity ohm-cm
Designation	Impurity		
M15	Zn	8.1×10^{16}	3.2×10^{-1}
M16	Zn	5.6×10^{17}	5.8×10^{-2}
M10	Zn	4.2×10^{18}	1.2×10^{-2}
M21	Cd	5.6×10^{17}	5.8×10^{-2}
B10	Cd	9.2×10^{17}	5.6×10^{-2}
B25	Cd	2.8×10^{17}	6.5×10^{-2}
B18	Undoped	—	—

Table II. Donor sources investigated at 900°C in crystal B25

Junctions were obtained with the following compounds

Al_2S_3
Al_2Se_3
Al_2Te_3
As_2S_2
As_2S_3
As_2Se_3
As_2Se_5
Ga_2S_3
GeS
GeS_2
In_2S_3*
MoS_3
$MoSe_2$
PtS*
P_2S_5*
SnS
NH_4SCN
NH_2CSNH_2*

No junctions were obtained with the following compounds

HgS*
MoS_2
$MoTe_2$
P_4S_3
SnS_2
Tl_2S
WS_2
ZnS

Evaluation.—The diffused wafers were examined microscopically (37x — 235x) for etch pits and other signs of erosion. Also, each GaAs slice was checked for weight loss following each diffusion run. Most Zn doped and many of the Cd doped wafers exhibited blemish-free surfaces after diffusion. Pitting in spots was occasionally observed. Wafers which showed weight loss in excess of 0.3% were discarded.

Films that deposited occasionally on GaAs during the quenching operation were removed by boiling the wafers in CS_2 followed by boiling in dilute (1:1) HCl, (etch rate ~100 Å/min.).

The diffused wafers were angle lapped and stained. The staining solution[1] when applied to a junction under illumination darkens the p-region with respect to the n-region or decorates the n-region preferentially with copper, depending on the conductivity difference between the two sides of the junction. Junction depths were obtained by both the standard technique (10) and by interference microscopy (11) with a general accuracy of $\pm 0.3\mu$.

Results

Table III indicates that higher concentrations of sulfur can be obtained with the lower melting sulfides employed in this study. Junctions were obtained in low resistivity GaAs using As_2S_3 as a donor source while Al_2S_3 produced a junction only at higher temperatures in the same material. The highest melting donor sources did not produce a junction at 900°C in the high conductivity GaAs.

Using Al_2S_3 as the donor source the presence of either elemental arsenic or crushed GaAs resulted in the same junction depth. This observation is in contrast with Vieland's results (2). He found that the junction depth of sulfur in GaAs depended on the arsenic pressure below 1 atm. The equilibrium pressure in the present system was presumably satisfied from the lapped side of the GaAs, since only one side of the wafer was polished. That this contention is justified is supported by the following observation. In some cases the wafers exhibited weight losses (2%) without any structural changes on the polished side of the GaAs wafer. Presumably the material was lost from the lapped rather than the polished side.

Zinc out-diffusion appeared not to have been very significant in this study, although it cannot be completely ruled out. A series of experiments was performed at 900°, 1000°, and 1100°C for 2- and 4-hr

Table III. Comparison of junction depth as a function of mp and bp of sulfides

Wafer acceptor conc, cm^{-3}	Diffusion		Junction depth, μ	Source material	Source	
	Time, hr	Temp, °C			MP, °C	BP, °C
Zn 8.1×10^{16}	2	900	None	Ga_2S_3	1225	—
Zn 8.1×10^{16}	2	900	1.6	Al_2S_3	1100	1550
Zn 4.2×10^{18}	1	1100	1.6	Al_2S_3	1100	1550
Zn 4.2×10^{18}	1	900	None	Al_2S_3	1100	1550
Zn 4.2×10^{18}	1.5	900	0.2	As_2S_3	300	700

---

[1] Staining solution: solution A: 10g $CuSO_4 \cdot 5H_2O$ + 50 ml H_2O; solution B (8, 9): 35 ml conc. H_2SO_4 + 5 ml H_2O + 5 ml H_2O_2 (30%); stain: 1 ml of solution B + 50 ml solution A.

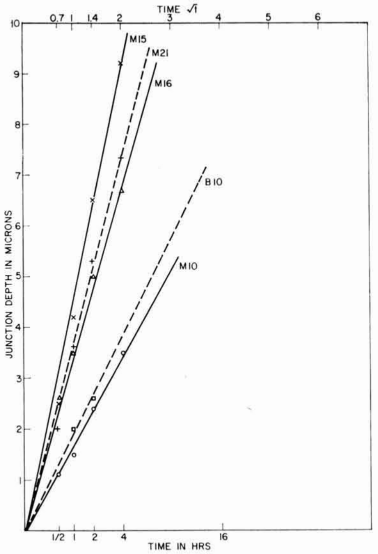

Fig. 1. Sulfur diffusion into GaAs at 1100°C

M15 x——x Zn 8.1×10^{16} M16 △——△ Zn 5.6×10^{17}
M10 ○——○ Zn 4.2×10^{18} M21 +——+ Cd 5.6×10^{17}
B10 □——□ Cd 9.2×10^{17}

diffusions into zinc-doped GaAs samples of two different acceptor concentrations within the same ampoule. The observed junction depths were found to be independent of the number of wafers in the diffusion capsule and the presence of wafers of other acceptor concentrations. Even though crushed undoped GaAs was present in all capsules, noticeable differences in the junction depth might have been expected if outdiffusion had been significant. Comparable experiments were not performed using the Cd doped series.

Figures 1-3 are plots of the average junction depth in microns as a function of the square root of diffusion time for the various wafers using Al_2S_3 as the donor source. It is assumed, since no junction was observed for sample M10, that the maximum concentration of electrically active sulfur was $<4 \times 10^{18}$ cm^{-3} at 900°C. Because erosion problems were encountered in the Cd runs, the precision of these data is not as high as that of the Zn runs. For that reason the Cd data will be discussed separately. Figure 4 shows photomicrographs (90X) of representative junctions obtained in M15 (900°C, 16 hr) using Al_2S_3 as a donor source and in two samples of M15 (1100°C, 1 hr) using GeS and As_2S_3.

Estimation of apparent diffusion coefficients.—Although neither the surface concentration nor the dis-

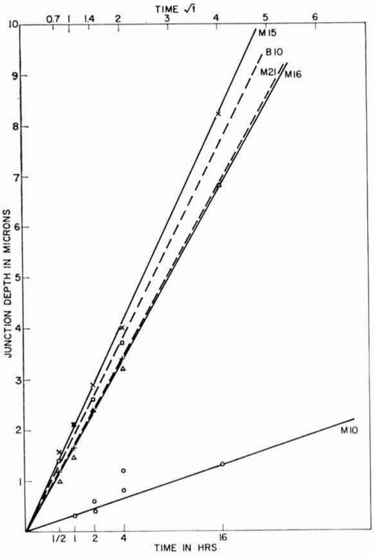

Fig. 2. Sulfur diffusion into GaAs at 1000°C

M15 x——x Zn 8.1×10^{16} M16 △——△ Zn 5.6×10^{17}
M10 ○——○ Zn 4.2×10^{18} M21 +——+ Cd 5.6×10^{17}
B10 □——□ Cd 9.2×10^{17}

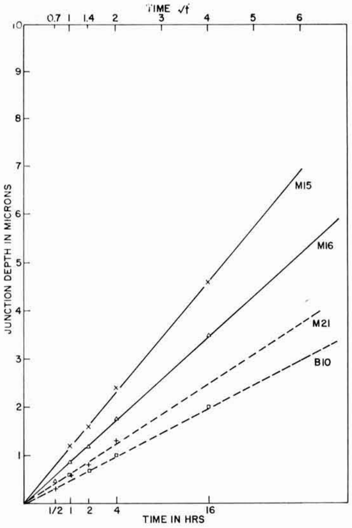

Fig. 3. Sulfur diffusion into GaAs at 900°C

M15 x——x Zn 8.1×10^{16} M16 △——△ Zn 5.6×10^{17}
M21 +——+ Cd 5.6×10^{17} B10 □——□ Cd 9.2×10^{17}

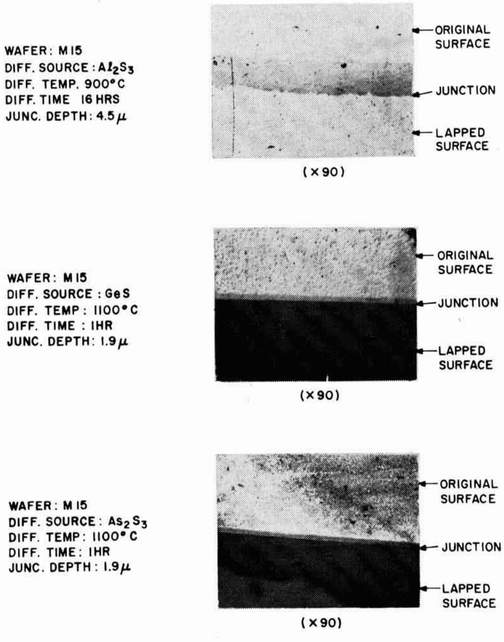

Fig. 4. Representative n on p junctions in GaAs

Table IV. Calculated diffusion coefficients in cm²/sec

Wafer pairs		GaAs—1100°C 2 hr	4 hr
(a)	M15	3.9×10^{-12}	3.9×10^{-12}
	M10	4.2×10^{-12}	3.2×10^{-12}
(b)	M15	4.0×10^{-12}	4.1×10^{-12}
	M16	3.8×10^{-12}	3.9×10^{-12}
(c)	M10	3.8×10^{-12}	4.0×10^{-12}
	M16	3.8×10^{-12}	3.9×10^{-12}

$D_{1100} = 3.9 \pm 0.2 \times 10^{-12}$; $D_{1000} = 1.1 \pm 0.2 \times 10^{-12}$; $D_{900} = 2.9 \pm 0.2 \times 10^{-13}$.

tribution profile of sulfur in these wafers was known, effective diffusion coefficients were estimated, using a modification of a method employed by Fuller (12). The following assumptions had to be made:

1. At a given temperature the same effective donor concentration exists above Al_2S_3 in all capsules.
2. All wafers have the same surface concentration of donors, under the same diffusion conditions.
3. The diffusion coefficient is independent of the donor and the acceptor concentration (a frequent, although not necessarily correct assumption).
4. The supply of donors is essentially unlimited in the diffusion system.
5. Sulfur diffusion in GaAs follows a complementary error function distribution.

On the basis of these assumptions, the surface concentrations are the same for a given temperature and the following equation is applicable

$$\frac{N_1}{N_2} = \frac{\text{Erfc } (X_1/2\sqrt{Dt})}{\text{Erfc } (X_2/2\sqrt{Dt})} \qquad [1]$$

X is the junction depth in cm, D the diffusion coefficient in cm²/sec, t the diffusion time in seconds, and N_1 and N_2 are the Zn concentrations in the two crystals chosen (Table I). Using paired values of the observed junction depth in GaAs samples of different acceptor concentrations the diffusion coefficients of sulfur were calculated by a technique of successive approximations (curve fitting) (12). Table IV shows the values obtained by this technique for Zn doped wafers at 1100°C as well as the averages for 1000° and 900°C. These values are plotted in Fig. 5 and, within experimental error, lie on a straight line. The activation energy for sulfur diffusing into GaAs computed from these data is 1.86 ± 0.01 ev. The diffusion coefficient can be thus described by the equation $D = 2.6 \times 10^{-5} \exp(-1.86/kT)$.

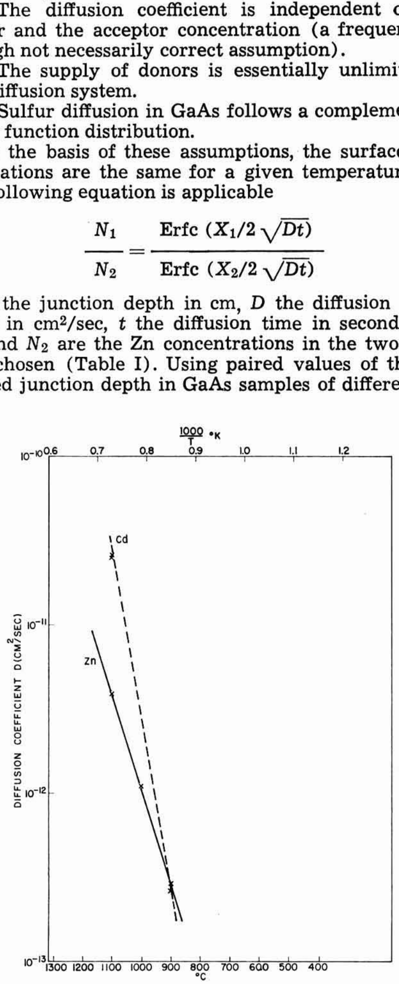

Fig. 5. Diffusion constants of sulfur in GaAs. The variation of the calculated D with $1/T$ for the Zn and Cd experiments is attributed partially to the effects of out diffusion. The Zn data (solid line) are considered more reliable (see text).

Zn doped
$D_{900} = 2.9 \pm 2.0 \times 10^{-13}$
$D_{1000} = 1.1 \pm 0.2 \times 10^{-12}$
$D_{1100} = 3.9 \pm 0.2 \times 10^{-12}$
$D = 2.6 \times 10^{-5}\, e^{-1.86/KT}$

Cd doped
$D_{900} = 3.6 \times 10^{-13}$
$D_{1100} = 2.6 \times 10^{-11}$
$D = 4.4\, e^{-3.06/KT}$

Discussion

The straight line relationship between the junction depth and (time)$^{1/2}$ indicates that Fick's law is obeyed in these experiments. Out-diffusion of zinc was found to be small, if not negligible, on the basis of special experiments. The activation energy obtained in this study agrees closely with that reported by Vieland (2) who based his value on junction migration studies. The present value is about one half that reported by Goldstein (1) from his radiotracer studies. Table V summarizes the literature values and those of this study.

Fane and Goss, studying the diffusion of Sn and Se in GaAs (3), have observed that junction depths are consistently less than penetration depth when determined by radiotracer techniques. Tannenbaum had observed that the phosphorous concentration in silicon determined by radiotracer techniques was larger than that determined by electrical measurements (13) and concluded that not all impurity atoms in a semiconductor contribute to the conductivity.

It may be appropriate to consider the Cd data plotted as dashed lines on Fig. 1-3. Even though these data were not as reliable as the Zn data the points which could be determined lie on straight lines passing through the origin and, therefore, deserve consideration. The diffusion coefficients could only be calculated at 900° and 1100°C which yielded values of $D_{900} = 3.6 \pm 0.1 \times 10^{-13}$ and $D_{1100} = 2.6 \pm 0.1 \times 10^{-11}$. This is equivalent to an effective activation energy of 3.06 ev and a $D_o = 4.4$. As discussed previously, out-diffusion did not appear to play an important role in the zinc experiments. Unfortunately, even less is known about the out-diffusion of Cd. While it is possible that the effects observed here are due to some extent to Cd out-diffusion, this cannot be resolved on the basis of the present work. However, it is possible that the difference is due partially to another effect. Certain anomalies exist in the data as plotted in Fig. 1-3. Sulfur diffusion into Zn or Cd doped GaAs of the same acceptor concentration might be expected to yield data giving comparable slopes. This is observed for diffusions at 1100° and 1000°C, but not at 900°C (Fig. 1-3, M16 and M21). The relative position of the lines with respect to each other should be the same at each diffusion temperature. This is found to be the case for Zn doped GaAs. For Cd doped GaAs a reversal of this order takes place at 1000°C. While there is a large uncertainty in the precision of the Cd points, it appears that the general relationship of these lines to each other is real.

There appears to be a correlation between the relative position of these lines and the intrinsic temperature. GaAs is extrinsic at the indicated temperatures if the impurity concentration exceeds the values shown in Table VI. With the data of this table applied to the experimental findings, the following picture emerges.

Table V. Sulfur diffusions into GaAs

	E, ev	D_o, cm²/sec*	$D_{1100°C}$, cm²/sec
This work	1.86 ± 0.01	2.6×10^{-5}	3.9×10^{-12}
Vieland (2)	1.8 ± 0.8	—	—
Goldstein (1)	4.04	4×10^{3}	6.0×10^{-12}

$*D_T = D_o \exp - E/kT$.

Table VI. Intrinsic-extrinsic conditions of GaAs at diffusion temperatures

Intrinsic carrier concentration (14)

WAFERS			Condition at diff. temp.		
			1100°C	1000°C	900°C
Designation	Type	Acceptor conc, cm^{-3}	1.7×10^{18}	7×10^{17}	3×10^{17}
M10	Zn	4.2×10^{18}	ex.	ex.	ex.
M15	Zn	8.1×10^{16}	int.	int.	int.
M16	Zn	5.6×10^{17}	int.	int.	ex.
M21	Cd	5.6×10^{17}	int.	int.	ex.
B10	Cd	9.2×10^{17}	int.	ex.	ex.

Table VI shows that M21, M16, and B10 are intrinsic at 1100° and extrinsic at 900°C. Figures 1 and 3 show that at these temperatures the slope of these respective lines increases regularly as the acceptor concentration of the wafer to be diffused decreases. Differences in the slope of M21 and M16 may reflect out-diffusion at these temperatures. At 1000°C (Fig. 2) the slope of B10 is steeper than that of M21 and M16. At this temperature, however, B10 is extrinsic whereas both M21 and M16 are intrinsic (Table VI). This may suggest an influence of the electric field on donor diffusions into GaAs and the possibility that the activation energy for the diffusion of sulfur into GaAs is dependent not only on the presence but on the type of acceptor (*i.e.*, Zn or Cd) as well. Further work to investigate these anomalies is required before definite conclusions can be drawn.

It should be pointed out, too, that defects in the crystal structure, which are known to affect the diffusion coefficient (4) were not taken into account in this study.

Summary

A simple and reproducible technique is described for the donor diffusion into GaAs using group VI compounds as sources. This technique limits surface erosion and permits control over the donor concentration. Junction migration studies have provided values for the effective activation energies for the diffusion of S in Zn-doped GaAs comparable to those in the literature. Discrepancies observed in Cd doped wafers could partially be attributed to out-diffusion. It is, however, suggested that the sulfur diffusion into GaAs may also be affected by the presence or absence of an electric gradient in the GaAs during the diffusion. This effect if present, appears to be impurity dependent.

Acknowledgment

The author wishes to thank C. S. Fuller, J. M. Whelan, J. Klerer, and Mrs. E. Handelman for their helpful discussions and advice, and L. J. Boccia for technical assistance.

Manuscript received Jan. 19, 1965. This paper was presented at the Toronto Meeting, May 3-7, 1964.

Any discussion of this paper will appear in a Discussion Section to be published in the June 1966 JOURNAL.

REFERENCES

1. B. Goldstein, *Phys. Rev.*, **121**, 1305 (1961).
2. L. J. Vieland, *J. Phys. Chem. Solids*, **21**, 318 (1961).
3. R. W. Fane and A. J. Goss, *Solid-State Electronics*, **6**, 383 (1963).
4. L. R. Weisberg, *Trans. Met. Soc. AIME*, **230**, 291 (1964).
5. L. R. Weisberg, Editor, Scientific Rep. No. 7, High Temp. Semicon. Res. (RCA), April-June 1961, p. 34.
6. J. van Den Boomgaard and K. Schol, *Philips Research Repts.*, **12**, 127 (1957).
7. L. A. D'Asaro, *Solid-State-Electronics*, **1**, 3 (1960).
8. M. V. Sullivan and G. A. Kolb, *This Journal*, **110**, 585 (1963).
9. T. A. Cunnel, J. T. Edmond, and W. R. Harding, *Solid-State Electronics*, **1**, 97 (1960).
10. C. S. Fuller and J. A. Ditzenberger, *J. Appl. Phys.*, **27**, 544 (1956).
11. N. L. Bond and F. M. Smits, *Bell System Tech. J.*, **35**, 1209 (1956).
12. C. S. Fuller, *Phys. Rev.*, **86**, 136 (1952).
13. E. Tannenbaum, *Solid-State-Electronics*, **2**, 123 (1961).
14. Scientific Rep. No. 7A, Application of Tunneling to Active Diode (GE), January 1962, Fig. 10.

Photovoltaic Effects at Rectifying Junctions to Deposited CdS Films

M. Bujatti[1] and R. S. Muller

College of Engineering, University of California, Berkeley, California

ABSTRACT

The photovoltaic response of blocking contacts to deposited CdS films has been measured in the wavelength range 0.3-1.3μ. Film properties as deduced from these measurements are compared with inferences drawn from photoconductivity behavior and with information on film treatment. Although evidence for photoemission of electrons from the rectifying contacts was sought, none was found. An interesting interference phenomenon was observed in thicker films. The phenomenon can be traced to standing-wave patterns in the films.

The photovoltaic effect at rectifying contacts made to vapor deposited CdS thin films has been studied. The CdS films were deposited using the technique described by Zuleeg and Senkovits (1). The quality of the CdS films deposited was found to depend critically on the temperature of the substrate with respect to the temperature of the source; films deposited on a cold substrate were dark orange or black and conductive, while those deposited on a properly heated substrate were lemon yellow and highly resistive. These characteristics are believed to be related to differing amounts of excess Cd present in the films.

The metals used to make contacts to the CdS films were Al, Cu, Te, and Au. Of these, only Al formed an ohmic contact; Cu, Te, and Au formed rectifying contacts. The photovoltaic effect at the junction was detected as a function of light intensity and wavelength. The dependence on light intensity was found to be linear. The dependence on wavelength varied slightly with the metal involved. Some common features were observed:

1. The photovoltage *vs.* wavelength plots achieved a maximum value beginning at a wavelength which varied with the metal involved and ending at approximately 0.5μ (which corresponds energetically to the CdS band gap).
2. The lower wavelength limits corresponded to photon energies varying linearly with the work function of the metal forming the junction.
3. In addition to the main response these photovoltage plots consistently exhibited a weak maximum (between 10^{-1} to 10^{-2} times weaker than the main peak) at a wavelength of 850 mμ. At this wavelength value a peak was observed both in the absorption and in the photoconductivity measurements on the CdS films. The peak at 850 mμ is therefore attributed to a transition internal to the CdS.
4. No evidence of photoemission from the metal was found. No simple relation holds between the response in the long wavelength region and the thickness of the metal layer or the metallic work function. The weak response which was detected at long wavelengths was probably due to the presence of impurity states in the CdS band gap.

Fabrication of the Samples

The structure of the diodes used in the experiments is shown in Fig. 1. The three differing geometries shown in Fig. 1 were adopted to determine if anisotropy in the properties of the films might affect photovoltage measurements. In fact, all diode structures behaved in substantially the same way. Two sources provided the CdS which was used to make the diodes: (*a*) CdS powder (mat 33-C-291) from RCA Laboratories;[2] (*b*) CdS powder of an ultra-high purity grade from Eagle Picher Company. The resistivity of the material was measured by compressing the powder in a ceramic cylinder between a copper plate and a screw tightened to the cylinder. The value of the resistivity as obtained from this measurement was of the order of 10^7 ohm-cm. The over-all electrical results obtained with either material (*a*) or material (*b*) were substantially the same.

The films were deposited on glass substrates which were heated to temperatures ranging from 150° to 350°C. A source similar to that described by Zuleeg and Senkovits (1) was used. The color of the films deposited ranged from a dark orange for substrate temperatures near 150°C to yellow for the higher temperatures. The resistivity varied correspondingly from 1 ohm-cm to approximately 10^4 ohm-cm in the dark. The films evaporated on warm substrates were all photosensitive to some degree, with the sensitivity depend-

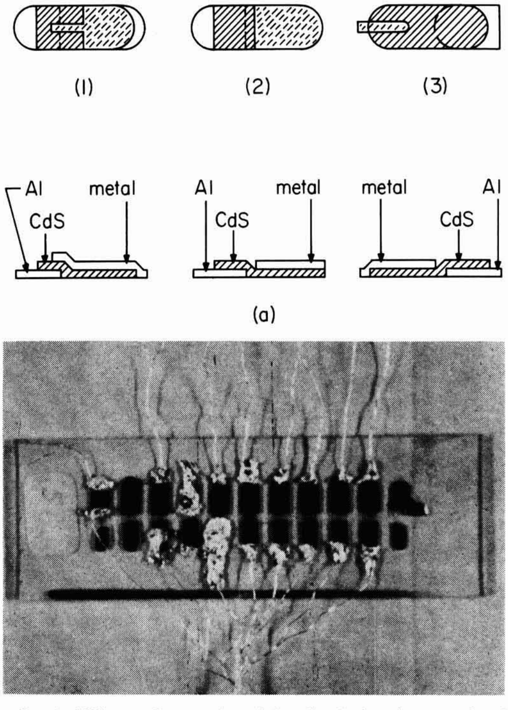

Fig. 1. Different shapes adopted for the diodes. An example of type I is shown in (b) (bottom) in actual size.

---

[1] Present address: Facoleta di Ingegneria, Universita di Roma, Italy.

[2] Kindly supplied by Dr. P. K. Weimer of the RCA Laboratories, Princeton, New Jersey.

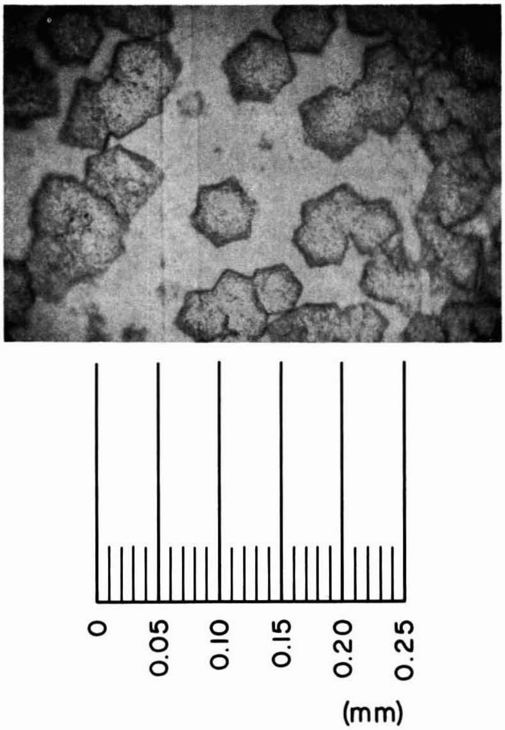

Fig. 2. Etch patterns on a CdS film deposited on a substrate warmed at 150°C.

ing on the temperature of the substrate. Ratios of dark to room-light resistivities of 2:1 or 3:1 were typical. When the temperature of the substrate reached or exceeded 300°-350°C, the deposition became slow and re-evaporation was observed. An optimum substrate temperature seems to be about 200°C when the source temperature is around 750°-800°C. The composition of the films also varied with the thickness of the deposit; thinner films showed higher conductivity than thicker ones for the same temperature of evaporation.

The crystallographic structure of the CdS films was studied via x-ray examination. Diffraction patterns from the films contained only one strong line corresponding to the (002) direction of the hexagonal structure. The line corresponding to the (101) direction (the strongest line for randomly oriented powders) was much weaker in the pattern from the films and was of the same order as the line corresponding to the (004) direction (*i.e.*, the second-order diffraction in the direction of the principal hexagonal axis). The intensity ratio between the (002) and (101) lines was approximately 10^4, while a randomly oriented sample would give a ratio 59/100 for these lines. Two weak lines corresponding to CdO were detected on the x-ray pattern from a sample deposited on a cold substrate and baked in air at 350°C.

Some of the samples were etched by exposure to warm vapors of concentrated HCl. Under microscopic examination at 200 magnification, no crystalline pattern was detectable on the samples evaporated on a cold substrate, postbaked or not. On films deposited on a warm substrate, hexagonal patterns ranging in size up to 40-50μ were observed (Fig. 2). These patterns may either be $CdCl_2$ precipitates or else actual etch pits. Recent work on this question will soon be published. The Al and CdS layers were deposited in a two-step evaporation, without opening the bell jar in order to avoid oxidation of the Al layer. The counter electrode (Cu, Au, or Te) was then deposited in a straight-forward manner. The metal-CdS diode cells fabricated in this laboratory and discussed in this paper belong to five sets of samples. Table I summarizes the fabrication data for these samples.

Table I. Sample fabrication properties

Slide No.	Structure	Evaporation pressure,* Torr	Temp. substr, °C	Temp. source, °C	Thickness of CdS, μ**	Dark resistivity, ohm-cm
51	Al-CdS-Au	1.9×10^{-7}	300	780	0.098	4.9×10^3
54	Al-CdS-Te	3×10^{-7}	250	780	0.243	5.8×10^2
55	Al-CdS-Cu	3×10^{-7}	275	770	0.164	6.6×10^3
56	Al-CdS-Cu	3.5×10^{-7}	250	760	0.115	2.3×10^3
59	Al-CdS-Au	1.2×10^{-7}	285	780	0.140	3.1×10^3

* The pressure was measured at the throat of the chamber just before the evaporation started; during evaporation, the pressure typically reached 2 or 3 × 10^{-6} Torr.

** The thickness was measured by using a Normarski-type interferometer.

Experimental Results

No appreciable bulk photovoltage was detected across CdS films deposited on warm substrates, the connections being made through In-soldered ohmic contacts. (In a few cases photovoltages which never exceeded a few microvolts were obtained at such junctions under very concentrated visible illumination.[3]) Somewhat larger bulk photovoltages were obtained on some CdS samples deposited on substrates at lower temperatures. The maximum value of the bulk photocurrent detected was 0.2 nA (1 Mohm meter resistance). This was measured on a 1μ thick sample having a resistivity of 2.75 ohm-cm. The bulk-generated photocurrent varied quite irregularly when a concentrated beam of light was moved along test samples which consisted of ohmic contacts made to the opposite edges of films 1.2 cm in length. This photocurrent probably stemmed from a nonuniform distribution of impurity states in the film, which gave rise to a nonuniform conductivity. Potential barriers at the microcrystal boundaries could also be responsible for the detected photoeffect. In all cases, however, and particularly in the case of the films deposited on warm substrates, the bulk photovoltage was negligible in magnitude when compared to the photovoltages measured at metal blocking contacts to the CdS films.

A Bausch and Lomb monochromator with a coil-filament tungsten bulb was used as a light source. Photovoltaic response was measured in a range of wavelengths extending from 0.325 to 1.6μ, obtained by using two different diffraction gratings (0.325-0.800μ and 0.700-1.600μ). The intensity of illumination at each

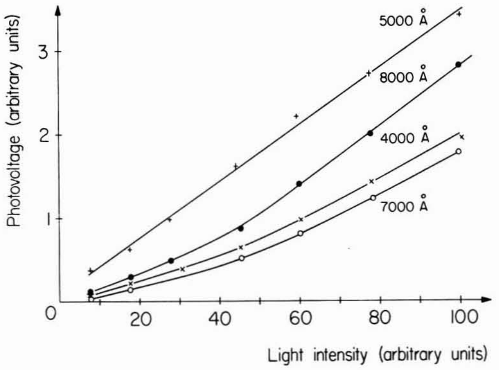

Fig. 3. Photovoltage *vs.* light intensity for an Al-CdS-Te diode (unit 54.3) at five different wavelengths. The polarity of the photovoltage was such as to make the blocking contact positive.

---

[3] G. O. Müller has reported measurements of ohmic-contact photovoltage responses. *Phys. Stat Solidi*, **3**, 523 (1963).

wavelength was varied by adjusting the monochromator supply voltage with a variac. The measured photovoltage depended linearly on the intensity, and was of a polarity to make the blocking contact positive. A typical curve of photovoltage *vs.* light intensity for an Al-CdS-Te sample is shown in Fig. 3.

Figure 4 shows typical curves of the measured photovoltage versus wavelength for three different metal-CdS rectifying contacts. Several features common to all three curves are easily understood.

1. The measured photovoltage drops in each case all three curves are easily understood.
ev, this energy is near to values reported for the CdS band gap at room temperatures (2).

2. In each case the photovoltage becomes appreciable at a short wavelength which varies with the metal used to make the blocking contact.

3. A much smaller peak is detectable for a wavelength of about 850 mμ.

In order to investigate further the nature of the peaks detected in the photovoltaic response, both the photoconductive response and the absorption spectrum of the CdS films were also measured. Curves obtained from these measurements are shown in Fig. 5 and 6. Finally, the photovoltage measurements obtained on the diodes fabricated in this laboratory were compared with the measurements made on samples supplied by R. Zuleeg of the Hughes Microelectronics Division, Newport Beach, California. Measurements on the Hughes units are plotted in Fig. 7 for a typical cell. The Hughes samples were Au-CdS diodes with different thicknesses of the Au-layer, deposited in the structure described by Zuleeg (1). The CdS powder used by Zuleeg was supplied by Harshaw Chemical Company.

Discussion of Results

It is found that evaporation in a vacuum of roughly 10^{-6} Torr leads to dark-colored low-resistivity films when the substrate temperature is roughly 150°C or less (with a temperature of about 850°C for the source). At temperatures below 150°C the vapor pressure of free Cd is less than 10^{-5} Torr, and hence free Cd condensation is likely. Free S has a vapor pressure more than four orders of magnitude higher than free Cd in this range of temperatures, so that excess S is not likely to be present in the evaporated films. The dark color and low resistivity can thus be plausibly connected with the presence of Cd excess, either by virtue of S vacancies in the lattice, or else because of interstitial Cd atoms. Recent work with radioactive tracers by Woodbury (3) has indicated that interstitial Cd is very unlikely in CdS crystals.

It was possible to alter the resistivity of the films, which were deposited on a cold substrate by baking them in an open tube under a H_2 atmosphere for roughly 30 min at 350°C. During this heat-treatment, the films changed color from dark orange to pale yel-

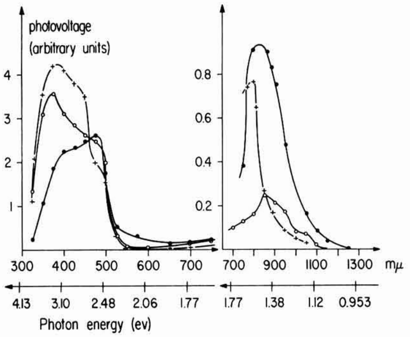

Fig. 4. Photovoltage *vs.* wavelength for three CdS diodes: +, Al-CdS-Te; ●, Al-CdS-Cu; ○, Al-CdS-Au.

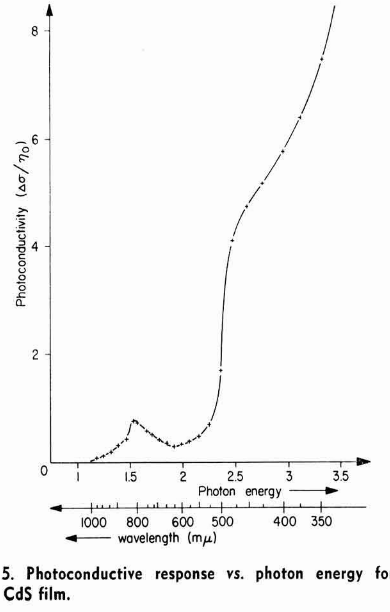

Fig. 5. Photoconductive response *vs.* photon energy for a deposited CdS film.

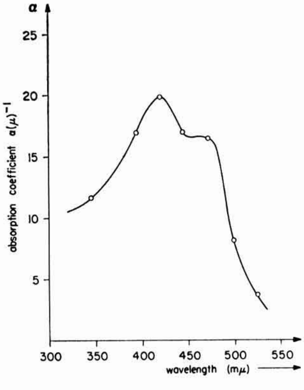

Fig. 6. Absorption spectrum for a deposited CdS film

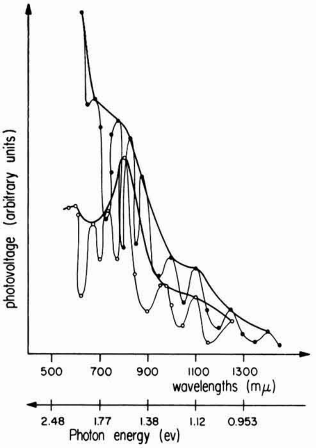

Fig. 7. Photovoltage *vs.* wavelength for two Al-CdS-Au diodes showing interference phenomena: ○, thinner Au layer (a); ●, thicker Au layer (b).

low and simultaneously increased in resistivity by as many as six orders of magnitude from their as-deposited condition. By contrast, it was found that air-baking in an open tube of samples for times comparable to the hydrogen bake resulted in a much smaller resistivity change while preserving the striking color change. The increased resistivity is thought to stem from the elimination of the excess Cd at the crystallite surfaces. The comparative ineffectiveness of air baking may be a result of the oxidation of the Cd at the material surface; which may act to inhibit further Cd diffusion. (CdO was observed in the x-ray spectrum of air-baked samples.) Berger *et al.* (4) have explained measurements on CdS films which were heat treated in vacuum by postulating the presence of two competing processes. The first is the diffusion of excess Cd to the surface where it is vaporized, and the second is the creation of sulfur vacancies near to the crystal surface owing to CdS dissociation. The increase in resistivity and color changes which we have observed suggest that the elimination of excess Cd predominates at low temperatures outside of vacuum. Somorjai and Jepsen (5) argue that the relatively fast diffusion which adjusts the resistivity of annealed CdS films is due to sulfur-vacancy migration from the Cd-rich interior to the surface. The diffusion constant for substitutional Cd (3) is far too low to be effective for the annealing times and temperatures that we have used. The sulfur-vacancy diffusion constant, while not known in detail, appears to have a value of about 10^{-5} at 800°C and a very low, but as yet undetermined, activation constant. A diffusion constant of this order would fit the relatively rapid change in resistance which we have observed on annealing.

The energy levels associated with Cd or S vacancies or with interstitial Cd are not known exactly, although there is general agreement in the literature that S vacancies result in electronic energy levels located roughly 0.2 ev below the conduction band, if doubly charged, and 0.5 ev below the conduction band, if singly charged (6).

In order to interpret the photovoltaic response data, we first discuss the photoconductivity and transmission data of Fig. 5 and 6. The photoconductive response curve in Fig. 5 is a plot of $\Delta\sigma/n_o$ *vs.* photon energy where $\Delta\sigma$ is the increase in photoconductivity and n_o is the photon flux. The expected large photoconductive response for photon energies near and above the band gap is evident. Also present in the photoconductivity data is a smaller peak in the neighborhood of 1.5 ev (830 mμ). Evidence for energy absorption at 1.5 ev was also obtained from transmission measurements.

The general character of the observed photovoltage *vs.* wavelength curves (Fig. 4) is seen to be approximated fairly closely by the spectral absorption curves of Fig. 6. Minor variations in the curve shapes with varying metallic electrodes can be partly understood in terms of differing reflectivities by the contacts themselves. In the short-wavelength region, the photovoltage *vs.* wavelength curves drop more rapidly than does the absorption coefficient curve. The short wavelength decrease in photovoltage occurs at different wavelengths depending on the metal forming the junction. The photon energies which correspond to the point at which the curves drop are proportional to the work function of the metal, as is evident in Fig. 8. Although too many factors are unknown for an exact quantitative analysis, the proportionality between work function and photovoltage decrease may be caused by the dependence of space-charge layer thickness on surface-barrier height. The short free-hole diffusion length in CdS would confine all photovoltaic effects to the space-charge layer, and hence any photoresponse would be a sensitive function of the depletion layer width, which, in turn, is dependent on the electrode metal's work function.[4]

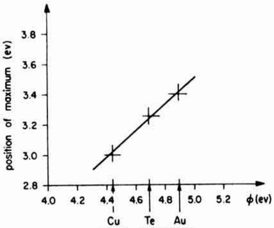

Fig. 8. Position of the first peak in the low wavelength region of the photovoltaic response as a function of the work function of the metal forming the junction.

No evidence is found in any of the samples of the presence of photoemission of electrons from the metal as found by Williams and Bube (7). There is in all the curves a background which could be interpreted according to Williams and Bube's theory, but no simple relation has been found between the responses obtained from samples with differing thicknesses of the metal layer and between the metal forming the junction and the shape of the curve. In the long wavelength region, where metallic photoemission should be observed under the Bube and Williams hypothesis, both the photoconductivity response and the transmission spectrum show evidence of transitions inside the CdS. The photoconductivity increases and the transmission shows many weak absorption and emission peaks. These points seem to suggest that the response in the region considered is probably due to the presence of distributed impurity and imperfection levels in the CdS. The peak at 850 mμ appears in all diodes studied and is therefore certainly due to a transition internal to the CdS.

Results quite similar to those obtained for the diodes fabricated in this laboratory were also measured on the diodes fabricated by the Hughes Semiconductor Division. Since the CdS layers in the Hughes diodes were almost ten times thicker than the CdS layers deposited in this laboratory, the response for energies higher than the band gap was nearly completely nulled by photon absorption in the CdS layer, when illuminating from the Al side of the Hughes diode. The response obtained with illumination from the Au side was quite similar to that obtained from the units fabricated in this laboratory. Also, for the Hughes diodes the response at higher wavelengths could be due both to photoemission and to distributed trapping levels in the CdS. Here we do not have any data on the CdS transmission and photoconductivity to be compared with the photovoltaic response. Again there is no evidence for photoemission from the metal, as no simple relation is found between the back and the front responses and between the responses of two units having differing thicknesses for the Au layer (Fig. 7). A rigorous comparison is not possible owing to the presence of superimposed oscillations in photovoltage *vs.* wavelength due to an interesting interference phenomenon in the CdS layer.

To prove the validity of an interference hypothesis in explaining these oscillations in measured photovoltage, we have compared the wavelength of the incident light corresponding to the maxima in the photovoltage oscil-

Table II. Measured and calculated wavelengths at photovoltage maxima

m	$2nd/m$, μm, calc	Maxima, μm, meas.
6	1310	1250
7	1125	1100
8	990	1000
9	878	875
10	790	775
11	716	725
12	660	670
13	607	600

---

[4] This mechanism was suggested by Professor A. C. English.

lations with the wavelength values obtained by assuming the effect to be caused by standing wave patterns formed from reflections at the Au and Al surfaces. If standing wave patterns are present one can predict the maxima to occur for $2nd = m\lambda$, where n is the refractive index of the CdS (2.5), $d = 1.58\mu$ is the thickness of the CdS layer, and m is an integer. In Table II the wavelengths of the maxima of sample a measured on Fig. 7 are compared with those calculated from the theory just proposed. A similar comparison holds for unit 6 of Fig. 7 which had a CdS layer 2.05μ thick.

It can be seen that the agreement between theory and measurements is quite reasonable. The presence of the interference phenomenon makes it difficult to detect clearly the position of any maxima in the long-wavelength region that may result from other physical mechanisms. The interference phenomenon is not present in the diodes fabricated in our laboratory because of the difference in structure and of the semitransparent metal layer.

Conclusion

CdS films obtained by evaporation with both the temperature of the substrate and the temperature of the source opportunely controlled show a microcrystalline structure, having a high degree of orientation. The pale-yellow color and the high resistivity of the films indicate that large amounts of excess Cd are not present. Metal junctions to these films show a photovoltaic effect when illuminated with light in the wavelength region between 350 and 500 mμ; the first limit depending on the metal involved. No evidence for photoemission in the long-wavelength region has been detected.

Manuscript received Jan. 28, 1965. This report was prepared by the University of California, Electronics Research Laboratory under USAF Contract No. AF-33(616)-7553 and AF-33(615)-1045.

Any discussion of this paper will appear in a Discussion Section to be published in the June 1966 JOURNAL.

REFERENCES

1. R. Zuleeg and E. J. Senkovits, Abstract 95, Paper presented at the Pittsburgh Meeting of the Society, April 15-18, 1963.
2. R. H. Bube, "Photoconductivity of Solids," p. 233, J. Wiley & Sons, Inc., New York (1960).
3. H. H. Woodbury, *Phys. Rev.*, **134**, A492 (1964).
4. H. Berger, E. Gutsche, W. Kahle, and G. Lebmann, *Phys. Stat. Sol.*, **3**, 265 (1963).
5. G. A. Somorjai and D. W. Jepsen, *J. Chem. Phys.*, September 1964.
6. R. H. Bube and L. A. Barton, *RCA Rev.*, **20**, 565 (1959).
7. R. Williams and R. H. Bube, *J. Appl. Phys.*, **31**, 968 (1960).

A Novel Crystal Growth Phenomenon: Single Crystal GaAs Overgrowth onto Silicon Dioxide

F. W. Tausch, Jr., and A. G. Lapierre, III

Engineering Department, Sylvania Semiconductor Division,
General Telephone and Electronics, Incorporated, Woburn, Massachusetts

ABSTRACT

Epitaxial growth of GaAs in windows on SiO_2-masked GaAs substrates has been studied and found to yield smooth-surfaced single crystal epitaxial layers. Single crystal overgrowth onto the SiO_2 films, initiating from the windows and growing out laterally over the SiO_2, has also been observed to occur in many instances. Studies of growth habits and patterns, inspection of cleaved sections, x-ray studies, and crystallographic considerations have led to a proposed growth mechanism which is not only consistent with the experimental window growth and overgrowth observations, but also indicates that the processes are highly controllable; it has been shown that overgrowth can be virtually inhibited, and it is concluded that with proper mask geometry single crystal overgrowth can occur over large areas almost without restraint.

In the course of investigating the SiO_2-masked epitaxial growth of GaAs in windows, which has never been reported in the literature, it was observed that not only window growth of excellent quality was obtained, but that the epitaxial layer frequently grew out laterally from the windows in the SiO_2 mask, resulting in an area of sandwich structure with the single crystal epitaxial GaAs layer separated from the GaAs substrate by the amorphous SiO_2 film (*e.g.*, see Fig. 6 and 7). This behavior is quite different from that reported for growth of silicon in windows [*e.g.*, ref. (4)], where lateral overgrowth has not been reported. Since this phenomenon of overgrowth appears to be not only novel but also potentially useful for device fabrication, it has been further investigated. This paper includes some preliminary results and conclusions derived from study of growth in windows and overgrowth.

Experimental

Substrates used in the work reported here were heavily doped (tellurium) n-type GaAs, cut and polished within 3° of the $(\overline{111})$ As faces. Essentially similar results were obtained on the (111) Ga faces. SiO_2 films of 100-10,000Å thickness were deposited conventionally

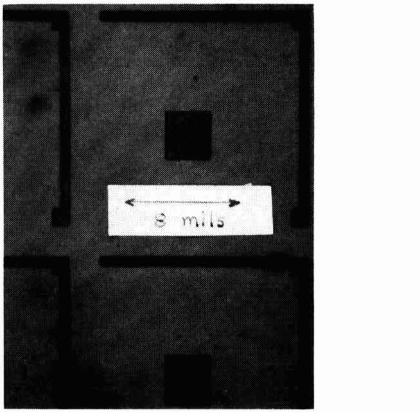

Fig. 1. Photomicrograph of L-shaped mask used in early work. Dark areas represent SiO_2 removal to GaAs substrate. Stripes are one-half mil wide and 13 mils long. Magnification approximately 95X.

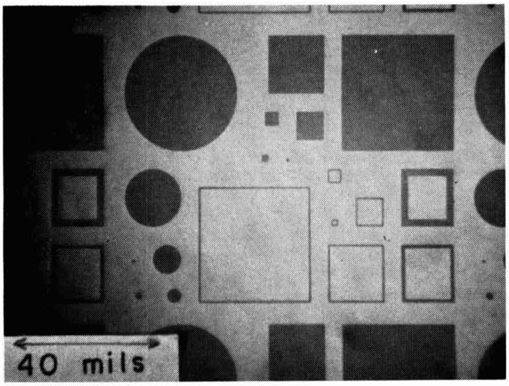

Fig. 2. Photomicrograph of specially designed mask for overgrowth study. Dark areas represent SiO_2 removal to GaAs substrate. Windows range from one-half to 32 mils over-all. Magnification approximately 25X.

by pyrolysis of tetraethyl orthosilane, and windows were opened in the SiO_2 by standard photolithographic techniques. Figure 1 shows the simple window pattern used in early work, consisting of an L-shape with legs 13 mils long and one-half mil wide, and with a 3 by 3 mil square in the center. Figure 2 shows a more elaborate pattern which was designed for study of overgrowth and which incorporates both round and square windows of various sizes (½-32 mils over-all) as well as frames of various sizes (2-32 mils over-all) and frame widths (½-2 mils). Masks were not intentionally aligned along specific crystallographic planes unless noted.

Epitaxial layers up to about 10μ thick were deposited on these slices in a conventional quartz vertical vapor transport reaction system, similar to that reported by Williams and Ruehrwein (1), utilizing an undoped GaAs source and either HCl or $AsCl_3$, in hydrogen, as the transport agent. Growth rates normal to the surface were generally 0.5-2.0 μ/min. The source temperature was 900°C, and the deposition temperature was from 710° to 730°C.

Results

Figures 3 and 4 show typical growths of about 10μ thickness obtained using the two masks previously described. It should be mentioned that most of the gross imperfections apparent in these growths are due to imperfect photolithographic work, incomplete removal of oxide, or imperfect cleaning of substrate surface. Laue back-reflection x-ray photographs confirm the single crystallinity of both growth in windows and overgrowths, except where obvious polycrystallinity exists.

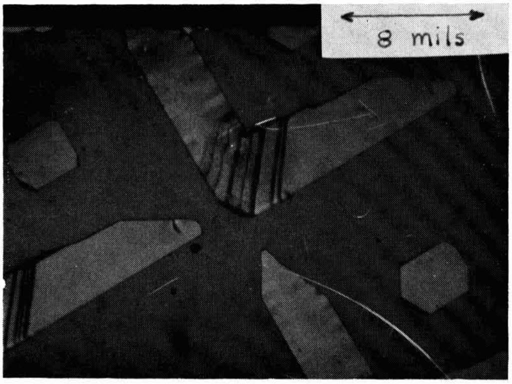

Fig. 3. Photomicrograph of growth in pattern shown in Fig. 1. Magnification approximately 125X.

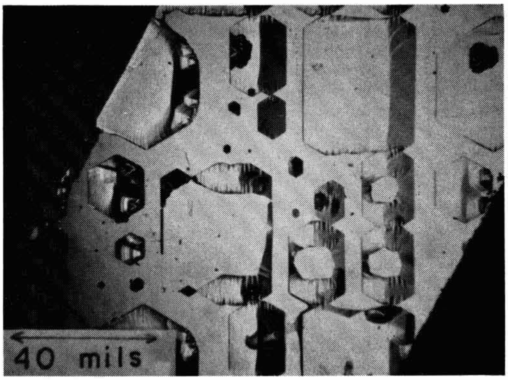

Fig. 4. Photomicrograph of growth in mask shown in Fig. 2. Magnification approximately 25X.

Comparison of Fig. 3 with Fig. 1 shows that lateral overgrowth of several mils has occurred from the one-half mil wide stripes, although growths of the central squares has tended to form hexagons and then virtually stop. Similarly, comparison of Fig. 4 with Fig. 2 shows that growth in all of the windows except the largest of the squares has formed hexagons, and that even the largest of the squares tend toward hexagons, and that the three smallest frames (2, 4, and 8 mils over-all) have been filled by overgrowth. Figures 5A, B, and C show an 8-mil frame before overgrowth, after almost complete overgrowth, and after complete overgrowth; these pictures not only demonstrate the development into the hexagonal shape, but also show that practically no growth occurred on two sides. It may be noted that the pattern is still faintly visible through the overgrowths of Fig. 5B and C. Finally, Fig. 5D and E show examples of better quality overgrowths of 2 and 4 mil frames, achieved by growing at a slower rate (*i.e.*, closer to 0.5 μ/min normal to the surface, rather than 1.0 or 2.0 μ/min).

A number of other features apparent in Fig. 3 and 4 may deserve comment here. For example, spurious nucleation occurred on a few places on the SiO_2 in some cases, especially at high growth rates, but was generally not a problem. Also, it can be seen that less perfect areas frequently occur wherever advancing growth fronts intersect; these may result in low-angle

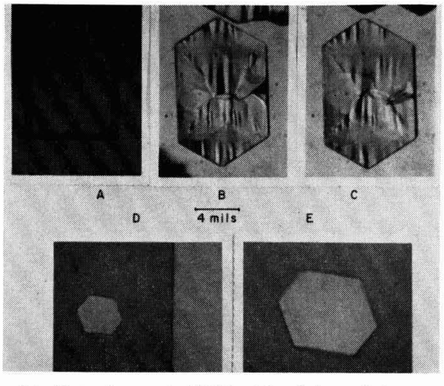

Fig. 5A. Photomicrograph (250X) of 8-mil frame before growth. Figure 5B and 5C. Same as Fig. 5-A except after almost complete overgrowth (5-B) and after complete overgrowth (5-C). Figure 5D. Photomicrograph (350X) of high quality overgrowth in 2-mil frame. Figure 5E. Photomicrograph (350X) of high quality overgrowth in 4-mil frame.

grain boundaries, which were observed in some x-ray photographs of these areas, although low-angle grain boundaries were also detected in some substrates. In any event, it will be shown later that the problem of intersecting growth fronts can be avoided by proper choice of mask geometry.

Identification of Faces

As previously mentioned, all growths reported here were carried out on the polished (111) surfaces of GaAs. The flat top surfaces of completed hexagons were in several instances measured to be oriented three degrees from the polished substrate surface by interferometry. Subsequent x-ray determination of the substrate orientation of these slices showed that the polished substrate surface was itself three degrees off the (111) plane in the corresponding direction. These observations not only indicate that the top surface tends to grow into a (111) facet, but also further support the single-crystallinity evidence of the growths. The tendency toward (111) facet formation may also explain some of the stepping which is apparent in Fig. 3 and 4, especially in large areas where not enough vertical growth has occurred to result in a single (111) facet across the entire top surface of the window.

In order to identify the slow-growing crystallographic planes bounding the growth figures, samples were cleaved along the {110} cleavage planes and inspected from the side; {110} cleavage was confirmed in several instances by x-ray orientation. It should be noted that there are three {110} cleavage planes, sixty degrees apart, perpendicular to any {111} face.

Referring again to Fig. 4, this is a top view of a sample twice cleaved along parallel {110} planes. It can be seen that these cleavage lines are perpendicular to one set of sides of any completed hexagon, and hence generally reveal the crystallography of the corresponding advancing growth front. A side view of such a cleavage through a completed hexagon invariable reveals a structure such as that sketched in Fig. 6A and 6B, and shown in photomicrograph 6C. The faces shown, at approximately 70° from the (111) plane, correspond to other {111} planes (see Table I). Consideration of the crystallography involved leads to the conclusion that the overhanging facet is chemically the same {111} plane (*i.e.*, either gallium or arsenic) as the top (111) face, while the upward sloping facet is chemically the same {111} face as the bottom $(\overline{111})$ face of the substrate wafer. In any of the top-view photographs the upward sloping facets appear dark due to the illumination, while the downward sloping facets are not visible. From the photomicrograph in Fig. 6C of the cross section of a completed hexagon can be seen the flat top (111) plane of the growth in the window, the 70° overhanging {111} side facet, and the small amount of overgrowth which has resulted from the formation of that facet. The SiO_2 masking can be seen in this photograph as the dark line separating the overgrown layer from the substrate. Cleavages across overgrown L-shaped patterns such as in Fig. 2, as well as across frames and windows where the hexagonal shape has not yet developed, frequently reveal leading edges at angles as shown in Fig. 7B. Referring again to Table I, the facet at about 35° to the (111) appears to correspond to a {110}, and that at about 55° appears to correspond to a {100}; usually the two facets have been of approximately equal magnitudes, as indicated by

Table I. Angles between (111) and x planes along $1\bar{1}0$ zone

It may be mentioned that the difference between the two columns, as referred to in the text, is that one always refers to upward sloping faces while the other always refers to downward sloping faces; hence in a cleavage which reveals two upward sloping faces, both planes will appear in the same column, while if the cleavage reveals both on upward and a downward sloping face, one will appear in each column.

X		X	
$\bar{1}\bar{1}2$	90° 0′	111	−0° 0′
$\bar{3}\bar{3}7$	85° 57′	332	−10° 2′
$\bar{1}\bar{1}3$	79° 58′	553	−12° 16′
$\bar{1}\bar{1}4$	74° 12′	331	−22° 0′
$\bar{1}\bar{1}5$	70° 32′	551	−27° 13′
$\bar{1}\bar{1}7$	66° 9′	771	−29° 30′
$\bar{1}\bar{1}9$	63° 40′	110	−35° 16′
001	54° 44′	$77\bar{1}$	−41° 2′
119	45° 48′	$55\bar{1}$	−43° 19′
117	43° 19′	$33\bar{1}$	−48° 32′
115	38° 56′	$55\bar{3}$	−58° 15′
114	35° 16′	$33\bar{2}$	−60° 30′
113	29° 30′	$11\bar{1}$	−70° 32′
337	23° 31′	$33\bar{5}$	−84° 57′
112	19° 28′	$11\bar{2}$	−90° 0′
335	14° 25′		
557	9° 27′		
111	0° 0′		

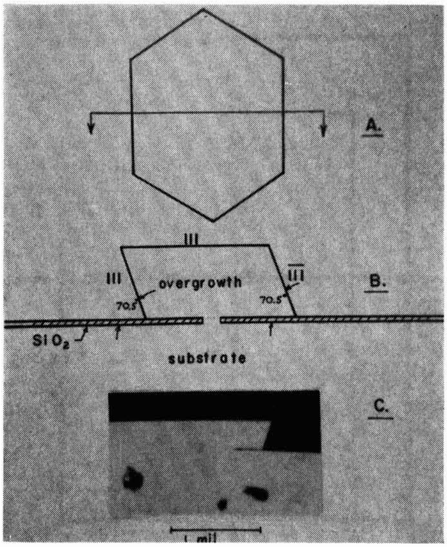

Fig. 6. Sketch of (110) cleavage of completed (grown) hexagon. Figure 6B. Side view of above cleavage through completed hexagon, showing opposing (111) facets. Figure 6C. Photomicrograph (1000X) of typical cleavage as above.

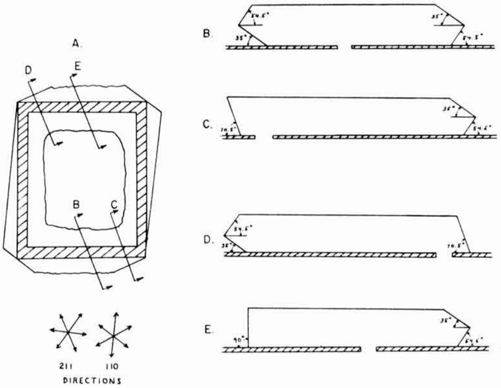

Fig. 7A. Partially overgrown frame with four cleavages indicated, for use with Fig. 7B through 7E. Figure 7B. Sketch of cleavage revealing both (100) over (110), and (110) over (100) double facets. Figure 7C. Cleavage revealing both a (111) facet and a (110) over (100) combination facet, also indicating relative lateral growth rates. Figure 7D. Cleavage revealing the other possible combination, with (111) and (100) over (110) facets. Figure 7E. Cleavage across a (110) perpendicular facet. (Note that vertical dimensions in side view sketches, Fig. 7B through 7E are exaggerated for clarity).

the sketches. Cross sections showing leading edges consisting of the {110} and {100} double facet on one edge and a {111} facet on the opposite edge have also been observed, as in Fig. 7C and 7D. The discovery of these combinations of facets is important in corroborating the identification of all the faces, since consideration of the crystallography involved (and reference to Table I) leads to the conclusion that the combinations pictured are the only ones consistent with the observed angles.

The above-mentioned existence of combination {110}-{100} faces deserves comment since it would be expected (2) that a (111) layer spreading over a substrate {111} surface in opposed [211] directions should result in a step along a {110} plane in one direction and a step along a {100} plane in the other direction. Similarly for the layer spreading over the chemically opposite (111) surface the {100} step should form in the first direction and the {110} step in the other. The distinctive feature of overgrowth, however, is that the (111) layer is effectively spreading over both (111) and ($\overline{111}$) faces simultaneously since the layer is growing over an SiO_2 substrate rather than a {111} oriented substrate; the combination growth front involving both {110} and {100} steps is thus not too surprising. It might be mentioned that epitaxial overgrowth is, in many respects, similar to dendritic growth.

Another facet frequently found on cleavage has been one at 90° to the (111) plane, as sketched in Fig. 7E. Although the {211} plane is in the {110} zone, and is 90° from the (111) plane (see Table I), it is not likely to form facets on GaAs (3). On checking the top view of these cleavages it was found that the cleavage {110} planes were not perpendicular to the growth front, as was true in Fig. 7A through 7D. Rather, the front was 60° from the cleavage plane, advancing in a direction 30° from any [211] direction. These directions are the [110] directions and, indeed, the 90° face is probably the {110} face. Note that in Fig. 4 the planes forming the interiors of the three 16-mil frames are 30° from the exterior {111} hexagonal facets and are probably these perpendicular {110} facets.

Facets at angles corresponding to other crystallographic planes have also been observed, but have not been identified with any degree of certainty.

Proposed Growth Mechanism

Considering now the factors which determine the growth pattern obtained, it is clear that the amount of overgrowth obtained with each possible facet as a leading edge will vary, and the {111} facets will advance most slowly (*i.e.,* at the same rate as the top (111) face).

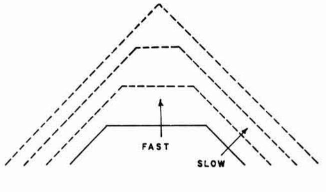

A. OUTWARD GROWTH

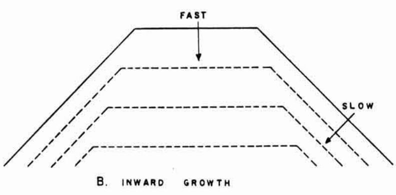

B. INWARD GROWTH

Fig. 8A. Sketch of effect of relative facial growth rates on habit of diverging growth front (outward growth). Figure 8B. Sketch of effect of relative facial growth rates on habit of converging growth front (*i.e.,* inward growth).

The factor determining which growth front forms is whether the growth front is diverging or converging. First consider the case where the growth front diverges, *i.e.* Fig. 8A. The length of the slow growing front increases at the expense of the fast growing front, and the final form is recognizable as the circumscribed {111} hexagonal facets to which all mask shapes tend to overgrow in the outward direction.

Considering next growth along a converging front, i.e., Fig. 8B, it is now the fast growing facets which tend to survive and predominate. For example, the interior overgrowths in the 16-mil frames of Fig. 4 appear to be forming facets which are aligned 30° from the {111} exterior facets, and hence are believed to be the relatively fast growing {110} perpendicular faces. The fact that fast growing faces are not self-annihilated in this case makes possible controlled rapid overgrowth of a converging growth front. The relatively extensive inward growth apparent in the L-shaped areas of Fig. 3 may be explained in terms of growth steps initiated at the inside corner.

It is interesting and informative to speculate briefly on some of the techniques by which overgrowths could be controlled, in the light of the previously developed mechanism. For example, by proper orientation of a hexagonal mask pattern, *i.e.,* with sides parallel to {111} faces, it should be possible to inhibit completely rapid overgrowth and thereby limit growth in all directions (including normal to the surface) to the slow {111} face growth rate; growth in circular windows approaches this condition. As another example, overgrowth over large areas should be possible by exploiting a geometry which avoids {111} facet formation, *i.e.,* straight lines or concave curvatures (see Fig. 8B). It may be noted that the problem of defects caused by intersecting growth fronts is avoided along straight or gently curving window openings.

Conclusions

It has been shown that single crystal epitaxial growth occurs in windows, and that the growth tends to rapidly overgrow the SiO_2 until a hexagonal figure bounded by {111} facets is formed. The overgrowth is itself single crystal, and rather extensive (several mils) overgrowths of good appearance have so far been achieved. A mechanism of overgrowth has been proposed which is not only consistent with the experimental observations, but also indicates that the overgrowth process is highly controllable; by proper geometrical relationship between the mask and the substrate crystallography overgrowth can be virtually inhibited, and it is concluded that overgrowth can also be made to occur over large areas almost without restraint. The integrity of the isolating SiO_2 film has been established since it is visible on sectioning and after the overgrown GaAs has been chipped away.

Acknowledgment

The authors would like to thank R. W. Berkstresser for x-ray analysis and for assistance in crystallographic determination.

Manuscript Feb. 1, 1965.

Any discussion of this paper will appear in a Discussion Section to be published in the June 1966 JOURNAL.

REFERENCES

1. F. V. Williams and R. A. Ruehrwein, *This Journal,* **108,** 177C (1961).
2. R. C. Sangster, in "Compound Semiconductors," Vol. 1, p. 249, Willardson and Goering, Editors, Reinhold Publishing Corp., New York.
3. *Ibid.*
4. A. F. McKelvey, Proceedings of the Third Annual Microelectronics Symposium, pp. II-B-1 to II-B-6, St. Louis, April 1964.

Kinetics of Epitaxial Silicon Deposition by a Low Pressure Iodide Process

John E. May

Semiconductor Products Department, General Electric Company, Auburn, New York

ABSTRACT

This report is primarily a study of the factors which control the vapor transport process of silicon in a modified closed tube low pressure cyclic iodide process. The kinetics of transport from the source to the substrate are examined and are found to agree with a diffusion controlled mechanism. The model is useful for estimating the deposition rate under a variety of conditions. The process is found capable of depositing silicon on silicon substrates at relatively high deposition rates. Impurity doping with this process is accomplished by incorporating the desired impurity into the source silicon.

Vapor phase transport-closed tube processes are of considerable interest for epitaxial deposition of semiconductor materials (1-4). Essentially, the process involves incorporating into a closed tube the substrate, the source of material to be deposited, and a carrier gas. By heating the source and substrate to different temperatures, the carrier gas reacts with the source material to form a volatile compound which then migrates to the substrate. Decomposition and deposition occurs at the substrate. The decomposition products may then travel back to the source to pick up more material. In the silicon-iodine system studied by Wajda and Glang (4), for instance, the substrate is maintained at about 950°C, the source at 1100°C, and iodine pressure at 20 atm. With a source to substrate distance of 10 to 15 cm they observe deposition rates of the order of 10 μ/hr. The dominant transport mechanism in this case is thermal convection.

Dash and Taft (5) on the other hand have used a low pressure silicon iodine cyclic process and have brought the source much closer to the substrate. The source and substrate can be heated inductively to different temperatures to achieve a steep temperature gradient. The close space geometry has been also used by Sirtl (6) and by Nicoll (7).

This paper shows that the combination of close spacing and low pressure lead to a substantially more rapid deposition rate, and that the process is diffusion controlled.

Preliminary Analysis

In this report we expand the initial work of Dash and Taft (5) on the cyclic iodide process, investigating further the effect of pertinent variables which control the transport and deposition processes. In addition, the kinetics and mechanism of transport are examined and estimates are made of the deposition rate as a function of the experimental variables.

An important feature of this process is the relatively small distance between the source and substrate. This distance is maintained by placing the substrate between two slabs of silicon which are separated by means of a quartz ring. Two arrangements are shown schematically in Fig. 1. One piece of silicon acts as the source of material and the other is the heater for the substrate. Transport from source to substrate is accomplished in an iodine atmosphere by heating the source to temperature T_1 and the substrate to temperature T_2 where $T_1 < T_2$. The iodine reacts with the source silicon to form a volatile iodide with an equilibrium partial pressure at the source greater than its equilibrium partial pressure at the substrate. This supersaturated iodide at the substrate drives the original reaction in the reverse direction leaving elemental silicon on the substrate. A concentration gradient of silicon iodide is therefore established between the source and substrate. At an average temperature of 1100°C and 1 mm of iodide pressure the mean free path is about 10^{-2} cm. We would expect then that a diffusion controlled process would operate down to spacer distances between source and substrate of the order of a millimeter.

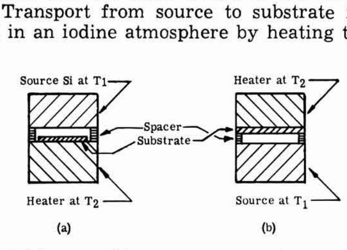

Fig. 1. Schematic of heater, substrate, and source assembly

For a diffusion controlled process the flux of material passing between the source and substrate is given by

$$J = -D\,\partial C/\partial X$$

where D is the gaseous interdiffusion coefficient of the iodide and $\partial C/\partial X$ is the equilibrium concentration gradient between the source and substrate. Since $C = n/v = p/RT$, the maximum growth rate (G) of the deposit is given by

$$G = D\,M\Delta p/\rho\,RT_a\,d \qquad [1]$$

where M is the atomic weight of Si, Δp is the difference in equilibrium iodide pressure between the source and substrate, ρ is the density of Si, R is a gas constant, T_a is the average temperature, and d is the distance between the source and substrate. Since Δp is a function of the iodine temperature and the temperature of the source and substrate, and D is a function of temperature and iodine pressure, we now have an expression containing the variables which influence the deposition rate. This approach is similar to that used by Schäfer *et al.* (8), in their study of metal-halide transport reactions.

This model assumes that there is no barrier to nucleation and growth of silicon on the substrate and that equilibrium iodide partial pressures are maintained at the source and substrate interfaces.

One important feature of silicon-iodine chemistry is that by varying the iodine pressure, silicon can be made to deposit in either the high or low temperature region (9). High pressures favor migration of silicon from the high temperature region to the low temperature region by means of the reaction

$$SiI_4 + Si \rightleftharpoons 2SiI_2 \qquad [2]$$

However (at low pressures) the additional reaction

$$SiI_4 \rightleftharpoons Si + 4I \qquad [3]$$

can occur, which in combination with reaction [2] will give the net reaction

$$SiI_2 \rightleftharpoons Si + 2I \qquad [4]$$

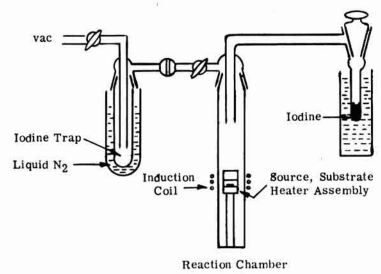

Fig. 2. Apparatus for epitaxial deposition by cyclic iodide process

Depending on whether reaction [3] or [4] is dominating, we would have

$$\Delta p \,\alpha\, p^4_{\mathrm{I}} \qquad [5]$$

or

$$\Delta p \,\alpha\, p^2_{\mathrm{I}} \qquad [6]$$

Another pressure sensitive term is the interdiffusion coefficient D. This varies as

$$D \,\alpha\, T^n/P \qquad [7]$$

where P is the pressure, T the temperature, and n a constant of about 1.5 to 2. Equations [5] or [6] in combination with Eq. [7] and [1] predict the rate of deposition to be proportional to the iodine pressure if SiI_2 is the dominant carrier species and proportional to p^3_{I} if SiI_4 is the dominant species. This dependence should be obeyed so long as the process is diffusion controlled, that is, when the source to substrate distance is about ten times the mean free path. At appreciably less than 1 mm iodine pressure, we would expect a departure from a diffusion controlled process with a source to substrate distance of 1 mm.

In the next sections we determine the effect of variables on the deposition rate and compare the results with those expected from the analysis.

Experimental

The apparatus used in this experiment is shown in Fig. 2. It is a demountable vacuum system consisting of a quartz reaction chamber with a tapered joint connected to an iodine source vessel and a liquid nitrogen trap to prevent the iodine from entering the vacuum pump. The source and substrate assembly which was used for most of this work is that shown in Fig. 1 (b) and consists of two Si rods (7/8 in. diameter x 1 in. long) of predetermined impurity content separated by a notched quartz ring. The source and substrate heater temperatures are established by positioning an induction coil at the appropriate elevation around the source and heater. The apparatus is enclosed by a box in which the interior can be heated above the iodine source temperature.

The operating procedure consists of pumping the system down to about 10^{-6} mm with the iodine source open to the liquid nitrogen trap. Once the desired temperatures of source and substrate are established the reaction chamber is closed off from the cold trap and vacuum pump, but the iodine source is kept open to the reaction chamber.

Temperatures were measured with an optical pyrometer by sighting on the periphery of the source and heater just above and below the quartz ring. The optical temperatures were corrected for emissivity (10) and true temperatures are reported here.

The iodine vapor pressure used here is that reported in the Handbook of Chemistry & Physics (11).

The substrates used here were 25 ohm-cm-N-type Si with (111) sufaces which were cleaned and then chemically polished with a solution of 100 cc HF, 180 cc acetic acid, 300 cc of HNO_3, and 0.35g of iodine. Immediately prior to loading in the reaction chamber they were immersed in HF and rinsed in deionized water.

The source silicon for this work was 0.01 ohm-cm P-type. Evaluation of deposit thickness was made by polishing a 6° bevel on the coated surface and staining the P region with HF-HNO_3 1000:1. The width of the P region was measured with a microscope and eye piece micrometer. This thickness was checked against the thickness determined from stacking fault measurements in order to determine whether a significant amount of diffusion of doping impurities into the substrate had occurred.

The deposition rates were obtained by dividing the deposit thickness by the total elapsed time starting after the desired temperatures were established and the cold trap was closed. Deposition rates determined in this manner could possibly be on the low side. Experiments have shown that it takes several minutes to achieve a linear growth rate. The total time of the run was therefore scheduled to be long compared with the time to achieve steady state conditions.

Results

Since Δp is a function of ΔT (the difference in temperature between the substrate and the silicon source), we shall present the deposition rate data *vs.* ΔT and then infer the proper iodide species from this and other data. The relationship between deposition rate and Δp will then be shown.

Dependence of epitaxial deposition rate on source and substrate temperatures.—In this experiment the substrate heater temperature was kept constant at 1290°C true temperature and the source temperature was varied. The iodine vapor pressure was maintained at 0.7 mm and the source to substrate distance was 1 mm. The data so obtained are shown in Fig. 3.

Dependence of deposition rate on iodine vapor pressure.—In this series of experiments the deposition rates were determined as a function of iodine pres-

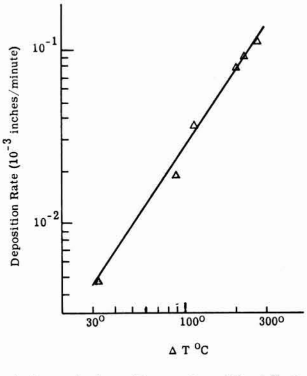

Fig. 3. Variation of deposition rate with ΔT. Iodine pressure, 0.7 mm Hg; separation, 1 mm; substrate temperature, 1290°C; source temperature, varied.

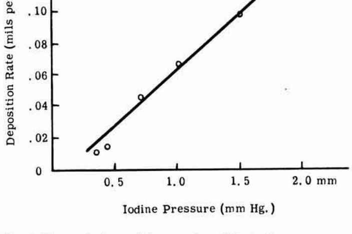

Fig. 4. Variation of deposition rate with iodine pressure. Substrate temperature, 1300°C; source temperature, 1150°C; separation, 1 mm.

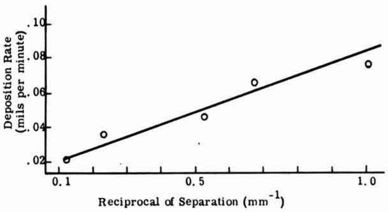

Fig. 5. Effect of source to substrate distance on deposition rate. Substrate temperature, 1300°C; source temperature, 1090°C; iodine pressure, 0.7 mm Hg.

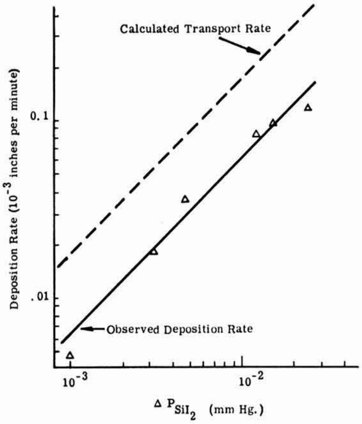

Fig. 6. Variation of deposition rate with ΔP_{SiI_2} and comparison with theory. Iodine pressure, 0.7 mm Hg; separation, 1 mm; substrate temperature, 1290°C; source temperature, varied.

sure over the range 0.3-2 mm. The source and heater were kept at 1150° and 1300°C, respectively, while the spacer distance was 1 mm. The results are shown in Fig. 4.

Effect of source to substrate distance on deposition rate.—The dependence of deposition rate on the distance between the source and substrate was studied with a source temperature of 1090°C, substrate heater temperature of 1300°C, and an iodine pressure of 0.7 mm. Quartz spacers of 1-9 mm were used. It was found that as the spacing increased, the uniformity of the deposit decreased. The data plotted in Fig. 5 indicates that the deposition rate is roughly proportional to the reciprocal of the distance.

Discussion and Results

The results of the study of the variation of deposition rate with iodine pressure indicates that the deposition rate is directly proportional to the iodine pressure at least within the limited range reported here. As discussed in the Preliminary Analysis, the result indicates that SiI_2 is the dominant species. This is in accordance with thermodynamic calculations. The slightly lower deposition rates at the lower iodine pressures are probably caused by the evaporation of silicon which becomes significant compared with the deposition rate.

With evidence that SiI_2 is the major transport species we can re-plot Fig. 4 ($G = f\Delta T$) as $G = f(\Delta p)_{SiI_2}$. For the net reaction

$$SiI_2 \rightleftharpoons Si + 2I \qquad [8]$$

we calculate from Schäfer and Morcher (9) the silicon diiodide pressure in equilibrium with iodine and silicon. This is given by

$$\log (P^2I/P\ SiI_2)_{mm} = 7.447 - 8256/T \qquad [9]$$

The experimental relationship $G\ (\exp) = f(\Delta p)$ is shown in Fig. 6 and is interpreted to indicate that the deposition rate is directly proportional to Δp_{SiI_2}, in qualitative agreement with Eq. [1].

Comparison of calculated and observed deposition rates.—It is of interest now to compare quantitatively the observed results with those predicted from Eq. [1]. It is important first to consider the geometry of our system. We have relatively hot silicon connected to a distance source of iodine maintained at millimeter pressures. The wall temperature of the apparatus is about 75°C, which is lower than the silicon temperature but higher than the iodine source temperature. We assume that the pressure of iodine in the space between the silicon source and substrate is about the same as the equilibrium iodine pressure maintained at the iodine source. At these pressures and silicon temperatures the iodine is practically completely dissociated.

The coefficient of interdiffusion of SiI_2 in iodine may be estimated from kinetic theory (12, 13). (See Appendix.) Combining Eq. [1] and [A-1] and evaluating the constants, we obtain the following expression for the maximum rate of deposition

$$G = 23.5\ (T_a)^{1/2}\ \Delta p\ SiI_2\ (atm)/d\ (cm)\ \Sigma P_{mm} \qquad [10]$$

G is in mils per minute, ΣP is the total gas pressure in mm, and Δp SiI_2 is computed from Eq. [9].

The results calculated from Eq. [10] are compared in Fig. 6 with the experimental results. We see that the calculated transport rates are about three times the observed deposition rates. However, with an apparatus modified to permit hydrogen cleaning of the substrate and source surfaces, we have observed deposition rates quite close to the calculated maximum rates. For instance, with the source at 1150°C, substrate at 1300°C, and iodine pressure at 3.5 mm, we have observed on occasion deposition rates of 0.35 and 0.47 mil/min which compare with a calculated rate of 0.5 mil/min. No doubt the rate at which gases enter the system during the deposition period is a variable. It increases ΣP which has not been taken into consideration in the calculation, and one which we have not determined. The formation of more stable gas-silicon compounds will also decrease the deposition rate. Considering the assumptions and estimates which have been made in the calculation then, the agreement between observed and calculated maximum deposition rates is good.

Acknowledgments

The author gratefully acknowledges the discussions of the cyclic iodide process with E. A. Taft, Jr. and Dr. W. C. Dash at an early stage in his investigation. Dr. F. H. Horn, R. E. Hysell, and F. E. Gentry reviewed the report and H. Sheldon, J. B. Crooks, and Mrs. M. Bestard assisted in various phases of the experimental work.

Manuscript received Nov. 23, 1964; revised manuscript received March 17, 1965.

Any discussion of this paper will appear in a Discussion Section to be published in the June 1966 JOURNAL.

REFERENCES

1. J. C. Marinac, *IBM Journal*, **4**, No. 3, 248 (1960).
2. E. S. Wajda, B. W. Kippenhan, and W. H. White, *ibid.*, **4**, 288 (1960).
3. R. Glang and B. W. Kippenhan, *ibid.*, **4**, No. 3, 299 (1960).
4. E. S. Wajda and R. Glang, "Metallurgy of Elemental & Compound Semiconductors," R. O. Grubel, Editor, p. 229, Interscience Publishers, New York (1961).
5. W. C. Dash and E. A. Taft, Private communication.
6. E. Sirtl, *J. Phys. Chem. Solids*, **24**, 1285 (1963).
7. F. H. Nicoll, *This Journal*, **110**, 1165 (1963).
8. H. Schäfer, H. Jacob, and K. Etzel, *Z. anorg. u. allgem. Chem.*, **286**, 27 (1956).
9. H. Schäfer and B. Morcher, *ibid.*, **290**, 279 (1957).
10. F. G. Allen, *J. Appl. Phys.*, **28**, 1510 (1957).

11. "Handbook of Chemistry and Physics," Thirty First Ed., Chemical Rubber Publishing Co., Cleveland (1948).
12. S. Dushman, "Scientific Foundations of Vacuum Technique," John Wiley and Sons, New York (1949).
13. E. H. Kennard, "Kinetic Theory of Gases With an Introduction to Statistical Mechanics," McGraw-Hill Book Co., New York (1938).

APPENDIX

The interdiffusion coefficient was calculated from the theory of Maxwell, Chapman, and Enskog [see Dushman (12) p. 75, or Kennard (13) p. 194], and is given by

$$D_{12} = \frac{(v^2{}_1 + v^2{}_2)^{1/2}}{3\pi\, n_{12}\, \sigma_{12}{}^2} \qquad \text{[A1]}$$

where v_1 and v_2 are the average velocities $\left(\frac{8}{\pi}\frac{RT}{M}\right)^{1/2}$ of species 1 and 2, $n_{12} = n_1 + n_2$ = number of molecules/cm^3 of species 1 and 2 and $\sigma_{12} = \frac{\sigma_1 + \sigma_2}{2}$ where σ is the molecular diameter of species 1 and 2. Using values of $\sigma_I = 2.8 \times 10^{-8}$ cm and $\sigma_{SiI_2} = 7.2 \times 10^{-8}$ cm we compute $D_{12} = 5.6 \times 10^2$ cm^2/sec at Ta = 1498°K and P = 0.7 mm.

The Anodic Synthesis of CdS Films

William McNeill, Leonard L. Gruss, and Dorsey G. Husted

Pitman-Dunn Institute for Research, Frankford Arsenal, Philadelphia, Pennsylvania

ABSTRACT

Cd is shown to behave as a typical "valve anode" in solutions of $Na_2S \cdot 9H_2O$ in ethanol and becomes covered with a film which acts as an electrical barrier, exhibits interference colors, increases in thickness as voltage is increased, and gives rise to sparking at voltages in excess of 150 V. Voltage-time curves, film thickness and electrical resistance, and x-ray diffraction analyses showing the films to be CdS are presented. The thickness-voltage ratio based on interference colors is 26 Å/v.

The synthesis and properties of anodic oxide barrier films on metals such as Al and Ta are well known and have been described in detail by Young (1). Among important properties of films of this type are: the approximate linear increase of thickness with formation voltage for nonporous films at constant current density (2); the appearance of interference colors during film growth (3); and the ability to sustain very large electric fields (4). The majority of papers on this subject deal with films which are composed mainly of oxides of the anode metal, although some work has been reported on non-oxide films such as AgCl (5, 6).

In this paper we describe the anodic behavior of Cd in electrolytes which contain sulfide ions.

Experimental

Electrolytes.—The anodic reaction of Cd was studied with a number of electrolytes, and "valve anode" properties were observed in solutions of Na_2S in dimethylformamide, liquid NH_3, CH_3OH, C_2H_5OH, and $Na_2S \cdot 9H_2O$ in C_2H_5OH. In all cases, anodic reaction products included CdS as shown by powder x-ray diffraction analyses. All further studies reported here were carried out in solutions of $Na_2S \cdot 9H_2O$ in C_2H_5OH. Reagent grade chemicals were used throughout.

The solutions of $Na_2S \cdot 9H_2O$ in C_2H_5OH were subject to slow air oxidation which resulted in formation of $S_8{}^o$ (rhombic), Na_2SO_3 and $Na_2SO_4 \cdot 10\, H_2O$ all of which were identified by powder x-ray diffraction. The stated concentrations of these solutions are therefore nominal and refer to conditions at the start of an experiment. Also, a yellow color, presumed due to polysulfide formation appeared in the solution during anodization.

Anodes.—Anodes were round Cd rods of 1.27 or 0.63 cm diameter. These were reagent grade Cd of 99.9% purity. Anodes used for study of voltage-time characteristics and determination of film structure and composition were machined to approximate hemispheric shape on one end, inserted in tight-fitting Teflon sleeves and chemically polished by alternate immersion in a 60:40 conc. HNO_3, glacial acetic acid solution, and water. This was followed by a 5 to 8 second immersion in a solution containing 32g CrO_3 and 6g Na_2SO_4 in 100 ml H_2O. The polishing solution was removed by washing in H_2O and the anode was given a final rinse in dry C_2H_5OH.

Anodes used for study of film thickness were embedded in polymethylmethacrylate blocks. These were subsequently cut and polished. In the polishing procedure a series of abrasive papers was employed through grit size No. 600. The specimens were then lapped on a gamal cloth wheel using first Al_2O_3 and finally a reagent grade MgO.

Anodic reaction.—Anodic reactions of Cd were studied at current densities of 0.0155, 0.0775, and 0.155 amp/cm^2 in 0.1*N* and in 0.05*N* $Na_2S \cdot 9H_2O$ in C_2H_5OH. Three replications were made for each set of conditions and the maximum cell voltages were reproducible within ±5%. Cell voltages are plotted as functions of time in Fig. 1. These curves exhibit the characteristic

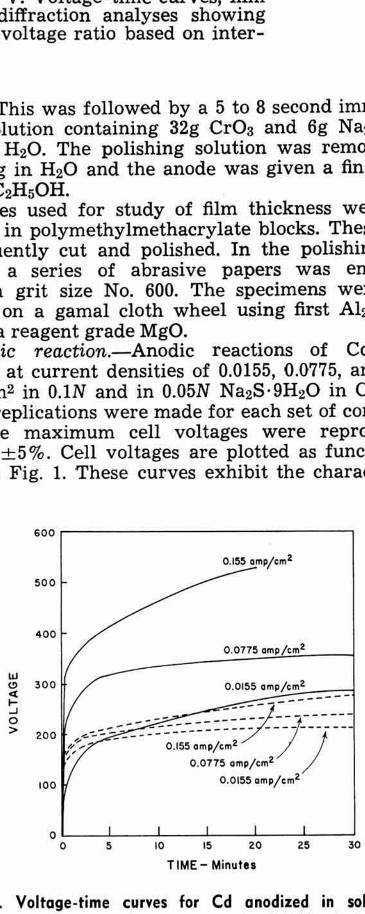

Fig. 1. Voltage-time curves for Cd anodized in solutions of $Na_2S \cdot 9H_2O$ in C_2H_5OH. Solid lines are for 0.05*N* solutions.

Table I. Electroluminescence and spark initiation voltages for anodic films on Cd in $Na_2S \cdot 9H_2O$ in C_2H_5OH

Conc. of $Na_2S \cdot 9H_2O$	Current density, amp/cm²	Electro-luminescence, v	Spark voltage, v
0.05*N*	0.155	40	230
0.05*N*	0.077	30	230
0.05*N*	0.015	35	200
0.10*N*	0.155	50	200
0.10*N*	0.075	30	170
0.10*N*	0.015	45	155

shape that is associated with the growth, breakdown, and sparking of anodic barrier films (7, 8). In the initial stage of the anode reaction, up to about 100v, the voltage rises very rapidly and is accompanied by the appearance of a film which exhibits a sequence of interference colors corresponding to increasing thickness. As the anodic film increases in thickness, its characteristic bright yellow color becomes more pronounced. In some cases, especially when films were grown at constant voltage, there was a tendency for films to be somewhat cloudy or opaque. The origin of this behavior is not clear as yet, but we assume it arises from contaminants in the electrolyte or in the anode, or from excessive current densities causing premature breakdown of the film. In the absence of such deleterious effects, it was usually possible to grow films to voltages in excess of 100v with no appreciable loss in transparency. In these cases gas evolution was observed starting at about 150v.

Electroluminescence and sparking were observed for the experimental conditions listed above, and the voltages at which these effects became visible are given in Table I. It is difficult to give precise voltages for the occurrence of these effects, but in replicate experiments the ranges for appearance of electroluminescence and sparking were approximately 5v and 10v respectively.

Films or coatings produced above the spark potential were all yellow or orange and opaque. The spark reaction products were normally adherent after completion of the anode reaction, but products of the same composition were ejected from the anode surface during the spark reaction.

Film and coating composition.—Qualitative chemical tests and powder x-ray diffraction analyses were used to determine film composition and structure.

Treatment of unsparked films with dilute HCl resulted in dissolution of the film, evolution of H_2S, and formation of a clear solution. No change in the appearance of smooth films, produced at 50v, was observed after immersion for two hours in CS_2. Some change such as pitting or erosion of the film would have been expected if elemental surfur had been present.

The results of powder x-ray diffraction analyses of anodic film samples obtained at different formation voltages is presented in Table II. The x-ray patterns were made on a Norelco x-ray unit using Ni filtered K_α radiation of Cu. Samples were exposed in a Debye-Scherrer camera for approximately 15 hr, with the beam at 18 ma and 40 kv.

The powder samples were prepared by scraping the film from the Cd anode after anodic formation and washing in C_2H_5OH. The Cd present in the 50 and 70v samples is introduced during the scraping and is not present in the samples of thicker coatings obtained at 90, 110, and 130v. Cd is present again in coatings formed at voltages in excess of 220v. All of the latter coatings were produced in the presence of sparking which may have been sufficiently energetic to dislodge metal from the anode. Attempts to obtain x-ray data from thin (50v) films *in situ* with the wide angle goniometer were unsuccessful and there was no evidence for either crystal structure or preferred orientation.

Electrical resistance.—The d-c electrical resistance was calculated from current and voltage values for films in contact with the electrolyte at various stages of formation. In this experiment the anodes were 1.27 cm diam Cd rods, 25 cm in length which were machined and chemically polished to produce smooth surfaces. These were masked with bands of a pressure-sensitive tape so that the anode surfaces prior to electrolytic treatment consisted of series of exposed areas 1.27 cm wide and separated by masked areas of equal width. The anodization procedure was to insert the anode to its full length in 0.05N $Na_2S \cdot 9H_2O$ in C_2H_5OH, anodize at predetermined constant voltage for periods of 10 and 45 min, and after each period of anodization to raise a section of the anode out of the electrolyte and increase the voltage to the next desired level. The data are plotted in Fig. 2. The resistance values are at least two orders of magnitude larger than the resistance of the solution in the anodic cell (which has a specific resistivity of approximately 1100 ohm cm), and thus the electrolyte contribution to the measured resistance is very small and may be neglected. The decrease in the resistance *vs.* formation voltage curves as shown in Fig. 2 at the higher voltages may be related to the development of crystal structure which the x-ray data in Table II show to occur to an increasing degree as formation voltage is increased.

Table II. X-ray diffraction analysis of films on Cd produced by anodic treatment in 0.05*N* $Na_2S \cdot 9H_2O$ in C_2H_5OH

Anodic formation voltage	Products determined by x-ray diffraction
50	Cd
70	Cd
90	CdS 3 diffuse lines
110	CdS 5 diffuse lines
130	CdS 10 diffuse lines
220 (sparking)	CdS 24 lines, Cd 20 lines
315 (sparking)	CdS 23 lines, Cd 11 lines
500 (sparking)	CdS 27 lines, Cd 8 lines
750 (sparking)	CdS 21 lines, Cd 15 lines

A series of resistance measurements was also made with a film formed on Cd for 16 hr at 100v in 0.05*N* $Na_2S \cdot 9H_2O$ in C_2H_5OH. After forming under the above conditions, the circuit was opened and a 10 K_Ω resistor was placed in series with the anode. The voltage drop across this resistor was measured with a vacuum tube voltmeter in order to calculate current flowing in the cell as voltage applied to the cell was raised in approximate 10v increments. At each voltage setting, current readings were taken over a period of time, sufficient for decay of transients, and the current density was plotted as a function of voltage on the film. These values are shown in Fig. 3. It is apparent from this plot that the current passing through the CdS film is nonlinearly dependent on the applied voltage.

Film thickness.—Film thicknesses were estimated from interference colors for samples prepared by anodizing in 0.05*N* $Na_2S \cdot 9H_2O$ in C_2H_5OH. The anodes were Cd rods mounted lengthwise in polymethylmethacrylate blocks and polished mechanically to expose a flat sur-

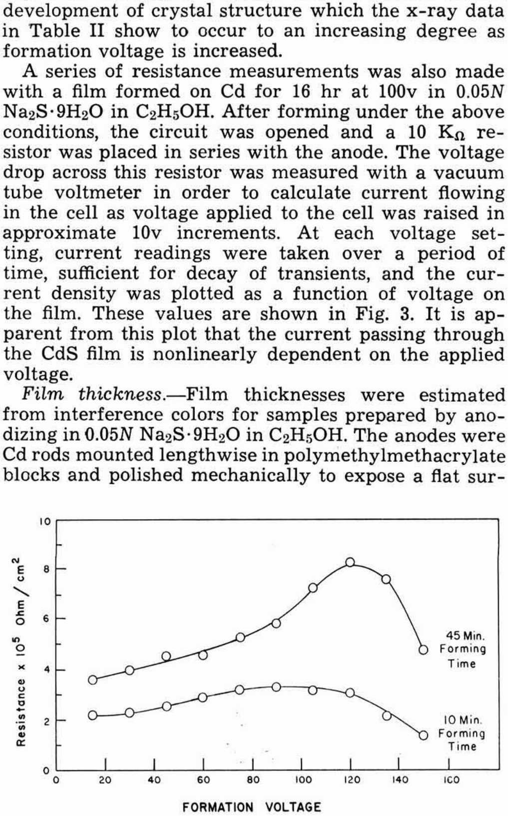

Fig. 2. Electrical resistance of anodic CdS films, formed and measured in 0.05*N* $Na_2S \cdot 9H_2O$ in C_2H_5OH at 25°C.

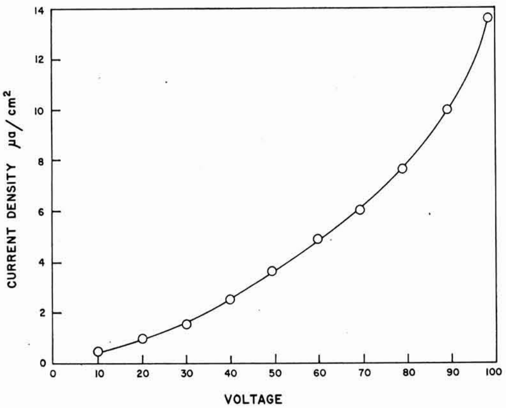

Fig. 3. Current density-voltage relation for CdS film: formed 16 hr; 100v; 0.05*N* $Na_2S \cdot 9H_2O$ in C_2H_5OH.

face measuring 0.7 x 2.4 cm. The film was prepared by anodizing at a current density which ranged between 0.3 to 2.5 ma/cm^2 as the applied voltage was increased from 0 to 200v at the rate of 2.4 v/min. The anode was simultaneously withdrawn from the electrolyte by means of a clock drive at a rate of 0.19 mm/min. Thus, a film increasing in thickness from 0 to that corresponding to 200v was displayed over a length of anode surface measuring 1.6 cm. There was some uncertainty as to the position of the first fringe but in the range 0 to 195v, fringes could be observed in sodium light (λ = 5893Å) and were found to be equally spaced, occurring at intervals of 45v. The last two fringes at about 150 and 195v were in a film that was slightly cloudy and it appears that in this voltage range, film growth and film breakdown occur simultaneously. Film thickness increase was calculated as a function of voltage with the aid of the expression cited by Booker and Benjamin (9)

$$d = r\frac{\lambda}{2n}$$

in which d is film thickness, r is the number of fringes, λ is the wavelength of incident light, and n is the refractive index. This latter value is assumed to be the same for the film as for bulk CdS in which n is 2.5 measured with light of the above wavelength (10). The film thickness difference between fringes is calculated at 1178Å and since this corresponds to a voltage interval of 45v, the thickness/voltage ratio is determined as 26Å/v.

Discussion

The experimental study, described in the preceding sections, of the anodic behavior of Cd in $Na_2S \cdot 9H_2O$ solutions in C_2H_5OH is of interest due to the barrier nature of the films which are produced, and the scientific and technical areas which appear as subjects for further investigation.

The barrier which forms on the Cd anodes consists of a thin film which sustains large electric fields as is shown by the appearance of interference colors, electroluminescence, and dielectric breakdown accompanied by sparking at elevated anodic voltages. Nearly all the voltage applied to the electrolysis cell is accounted for by the film since the solution resistance can account for only about 1% of the cell resistance. One can therefore estimate that fields in these films are of the order of 4 x 10^6 v/cm.

The question of composition of the films is not completely answered by the measurements made thus far, but it is clear that CdS is present in films obtained above 90v. The even spacing of interference fringes in films grown as wedges of uniformly increasing thickness, indicates that the refractive index of the film does not change appreciably over the voltage range 50 to 200v, and this would indicate that gross changes in film composition do not occur in this voltage range.

The ability to control anodic film composition and properties is of interest in connection with possible applications in electronic devices. We have prepared films similar to those described above on Cd anodes in which small quantities of Al, Cu and Mn were present as alloy constituents. Also, exploratory studies have shown that Cl can be incorporated in the CdS anodic films via anion deposition if NH_4Cl is added to the electrolyte.

The anodic formation of CdS films opens several areas of research which should yield useful results. Other Group II-IV and Group III-V compounds can probably be prepared in this form. It is also reasonable to expect that some of the compounds of Group V and VI elements with transition and inner transition metals will be accessible via anodic processes.

Acknowledgments

The authors are indebted to Dr. W. J. Kroeger of Frankford Arsenal, and to Dr. J. V. R. Kaufmann, of the U.S. Army Munitions Command, for encouragement and support of this work. Thanks are also due to Doctors F. Verderame, J. Varimbi, and H. Gisser for helpful discussions and review of the manuscript.

Manuscript received Dec. 17, 1964; revised manuscript received March 22, 1965. This work was supported by the Army Materiel Command, Project No. OMS 5010.11.838, "Basic Research in the Physical Sciences."

Any discussion of this paper will appear in a Discussion Section to be published in the June 1966 JOURNAL.

REFERENCES

1. L. Young, "Anodic Oxide Films," Academic Press, New York (1961).
2. G. Hass, *J. Opt. Soc. Amer.*, **39**, 532 (1949).
3. D. A. Vermilyea, *Acta Met.*, **1**, 282 (1953).
4. A. Guntherschulze and H. Betz, *Z. Physik*, **91**, 70 (1934).
5. W. Jaenicke, R. P. Tischer, and H. Gerischer, *Z. Elektrochem.*, **59**, 448 (1955).
6. A. Guntherschulze, *Ann. Physik*, **26**, 372 (1908).
7. L. L. Gruss and W. McNeill, *Electrochem. Tech.*, **1**, 283 (1963).
8. A. Guntherschulze and H. Betz, *Z. Physik*, **107**, 347 (1937).
9. G. R. Booker and C. E. Benjamin, *This Journal*, **109**, 1206 (1962).
10. J. E. Powderly, R. H. Fabrig, K. E. Beam, S. J. Rodrique, and W. E. Medcalf, "Research in Purification of CdS Crystals," Prog. Rpt. 7116, Contract No. AF33(6166203).

Conductivity Anomalies of Dimethyl Sulfone

Erik Kissa

Jackson Laboratory, Organic Chemicals Department,
E. I. du Pont de Nemours and Company, Wilmington, Delaware

ABSTRACT

The electrical conductivity of dimethyl sulfone has been measured while cooling it from 130° to 30°C at a rate of 0.5°C/min. Unlike diphenyl sulfone or chlorotriphenylmethane, dimethyl sulfone exhibited conduction anomalies attributable to proton conduction and interfacial polarization.

The chemical electret (1) was formed by solidifying a mixture of carnauba wax, resin, and beeswax in an electric field (2). Various substances have been shown to form electrets (3, 4). Unlike the classical electret, dimethyl sulfone exhibits long-lasting voltage reminiscence when a strong electric field is applied after freezing (5). Considering proton conduction and phase changes as possible causes, the conductivity-temperature relationship of dimethyl sulfone was studied.

Experimental

Purification.—Dimethyl sulfone was purified by neutralization of its acidic impurities and recrystallization from chloroform and from ethanol, dried *in vacuo* over metallic sodium, and sublimed twice. M.p. 108-109°C. Anal. Calc'd: C, 25.5; H, 6.4; S, 34.1. Found: C, 25.5; H, 6.4; S, 34.0.

Diphenyl sulfone was sublimed twice, M.p. 128°C. Anal. Calc'd: C, 66.0; H, 4.6; S, 14.7: Found: C, 66.1; H, 4.7; S, 14.7.

Chlorotriphenylmethane was recrystallized from a mixture of benzene and petroleum ether. M.p. 112-113°C. Anal. Calc'd: Cl, 12.7. Found: Cl, 12.6.

The purified compounds were stored and handled under anhydrous conditions.

Conductivity measurements.—The conductivity cells were 20 x 40 mm Pyrex vials equipped with a Teflon plug through which an inlet tube for dry argon, a thermocouple well, and two platinum wire electrodes, 10 mm apart, were introduced. The upper part of the electrodes was covered with a glass tubing, leaving a 10-mm long portion exposed.

The conductivity cells were charged with molten samples and cooled slowly to room temperature. After standing 16 hr they were heated to 130°C and cooled in an oil bath at a rate of 0.5°C/min. A General Radio impedance bridge was used at 1 kc frequency for measuring resistances up to 10^7 ohms. For higher resistances, a General Radio type 1862-B megohm-meter was used, by applying two 1-sec long d-c pulses of opposite polarity.

On heating from 28° to 130°C, dimethyl sulfone, diphenyl sulfone, and triphenylmethane did not exhibit conduction anomalies: the apparent conductivities increased gradually with the increasing temperature until melting occurred with a sharp conductivity increase.

Typical conductivity curves obtained by cooling the molten compounds from 130° to 30°C are shown in Fig. 1. The conductivity minimum slightly below the freezing point was present also with carbon electrodes or when switching from one pair of platinum electrodes to another pair arranged crosswise.

The conductivity of molten dimethyl sulfone changed only by 20% rel. when subjected to the (about 1-v a.c.) output of the impedance meter for 3 hr. However, an application of 50v d.c. increased the conductivity of molten dimethyl sulfone 2.7 times in 3 hr, and an acidic electrolysis product had formed.

Dielectric properties.—Dielectric measurements were carried out in the frequency range betwen 200 and 6000 cps with a General Radio Type 716-C capacitance bridge equipped with a Balsbaugh cell. The dielectric constant-temperature curve of cooling dimethyl sulfone exhibited a peak which was frequency-dependent and weakened with time. It was very strong at 200 cps and disappeared at 6000 cps (Fig. 2). The peak in the dissipation factor-temperature curve was also time- and frequency-dependent; at 200 cps (Fig. 2) it was too high to be measured.

Discussion

The conduction anomalies of dimethyl sulfone can be explained by accumulation of space charges associated with proton conduction and coexistence of two phases with different conductivities, already observed in long-chain alcohols (6). Frosch (7) explained the rise in dielectric constant of n-octadecanol by interfacial polarization, caused by the coexistence of liquid and solid phases. Hoffman and Smyth (8) believed this to be improbable and concluded that two solid phases formed on freezing. The highly conductive α phase, in which proton transfer was facilitated by molecular rotation, changed via a nonconductive β_1 form to the stable β_2 form.

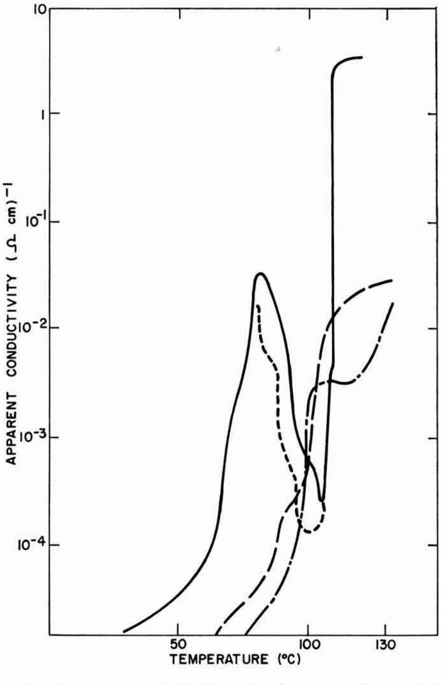

Fig. 1. Apparent conductivities of dimethyl sulfone, diphenyl sulfone, and chlorotriphenylmethane during cooling of their melts. ——, $CH_3SO_2CH_3$; — — —, $CH_3SO_2CH_3$ reversed direction; — - —, $C_6H_5SO_2C_6H_5$; ————, $(C_6H_5)_3$ CCl.

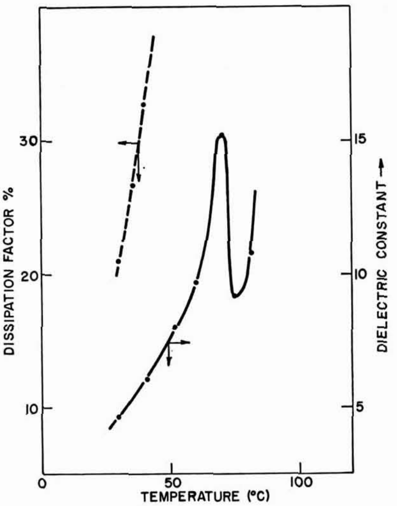

Fig. 2. Temperature dependence of the dielectric constant and the dissipation factor at 200 cps.

The conductivity minimum of freezing dimethyl sulfone appears with the formation of first crystals on the electrodes and is associated with interfacial polarization. With progressing solidification a conductive pseudo-solid is formed, in which molecular rotation may permit a proton transfer. On further cooling the metastable amorphous phase transforms into the stable crystalline form which does not permit molecular rotation, and the resistance increases again.

The release of protons in dimethyl sulfone under electric stress is indicated by its dielectric properties and by the formation of acidic electrolysis products. The somewhat acidic nature of hydrogen in dimethyl sulfone has been demonstrated by Hochberg and Bonhoeffer (9) who observed hydrogen-deuterium exchange in alkaline D_2O. Activation of hydrogen by the sulfonyl group is shown also by metalation with a Grignard reagent (10, 11).

Diphenyl sulfone and chlorotriphenylmethane cannot provide protons and do not show conductivity anomalies.

Measurements of electric conductivity change during phase transitions may provide a method for structure determination and identification of compounds which release a proton under electric stress.

Acknowledgment

The author is indebted to Dr. M. R. Kegelman for measurements of dielectric properties.

Manuscript received July 23, 1964; revised manuscript received Nov. 16, 1964.

Any discussion of this paper will appear in a Discussion Section to be published in the June 1966 JOURNAL.

REFERENCES

1. O. Heaviside, Electrical Papers #1.
2. M. Eguchi, *Phil. Mag.*, **49**, 178 (1925).
3. F. Gutmann, *Rev. Mod. Phys.*, **20**, 457 (1948).
4. C. P. Smyth, "Dielectric Behavior and Structure," McGraw Hill Co., New York (1955).
5. F. C. Chromey and E. Kissa, Unpublished work.
6. C. P. Smyth, "Dielectric Phenomena," in "Physics and Chemistry of the Organic Solid State," D. Fox, M. M. Labes and A. Weissberger, Editors, Vol. I, Interscience Publishers, New York (1963).
7. E. Frosch, *Ann. Physik*, **42**, 254 (1942).
8. J. D. Hoffman and C. P. Smyth, *J. Am. Chem. Soc.*, **71**, 431 (1949).
9. J. Hochberg and K. F. Bonhoeffer, *Z. Physik Chem.*, **A184**, 419 (1939).
10. W. E. Truce and K. R. Buser, *J. Am. Chem. Soc.*, **76**, 3577 (1951).
11. L. Field and J. M. McFarland, *ibid.*, **75**, 5583 (1953).

Hydrogen Overvoltage on Rhenium and Niobium Electrodes

M. J. Joncich[1] **and L. S. Stewart**[2]

Department of Chemistry, University of Tennessee, Knoxville, Tennessee

and F. A. Posey

Chemistry Division, Oak Ridge National Laboratory, Oak Ridge, Tennessee

ABSTRACT

Polarization curves of the hydrogen evolution reaction are presented for rhenium and niobium electrodes in dilute hydrochloric acid solutions as a function of temperature. The Tafel reaction is the rate-determining step in the hydrogen evolution reaction on rhenium. The behavior of niobium electrodes is much more complicated. The presence of the passive oxide layer on niobium produces an ohmic contribution to the total overvoltage. The corrected activation-overvoltage curves for niobium show a change of Tafel slope which is consistent with a Volmer-Tafel mechanism if certain assumptions are made about the distribution of potential at the interface. Activation energies of the hydrogen reaction are computed for both rhenium and niobium electrodes.

Comparatively few studies on the electrochemical behavior of rhenium and niobium electrodes have been reported. Pecherskaya and Stender (1) measured hydrogen overvoltage on rhenium. Hydrogen overvoltage on niobium was studied by Bockris (2), by Kononchuk and Barmashenko (3), and by Rotinyan and Kozhevnikova (4). The use of Nb as a *p*H-responsive electrode was investigated by Jensovsky (5) and by Galinker (6). An electrode potential-*p*H diagram for rhenium was constructed from available thermodynamic data by Pourbaix (7). Anodic oxidation of rhenium was studied by Lavrenko (8), while the anodic behavior of niobium has been the subject of a number of investigators (9-22).

Here we present data for hydrogen overvoltage on rhenium and niobium electrodes in dilute hydro-

---

[1] Present address: Department of Chemistry, Northern Illinois University, DeKalb, Illinois.

[2] Present address: Department of Chemistry, Rutgers University, New Brunswick, New Jersey.

chloric acid solutions. Current densities from 10^{-6} to 10^{-2} amp/cm^2 were used and measurements were made over the temperature range, 5°-45°C. Conclusions are drawn about the mechanism of the hydrogen evolution reaction on rhenium and niobium under these conditions and the apparent activation energies of the reactions are calculated.

Experimental

The experimental cell was similar to that described by Ammar and Awad (23) except for certain modifications which facilitated cleaning and equalization of hydrogen pressure in the three cell compartments. Teflon stopcocks were used throughout the apparatus. A platinum electrode of large area was employed as a polarizing electrode, and the current density at this electrode was kept low enough so that no significant oxygen evolution occurred (24).

The hydrogen reference electrode was constructed of 30-gauge platinum wire and checked frequently against a standard calomel electrode. Cathodes for pre-electrolysis were made of the same metal as the electrodes used in the experiments. Rhenium electrodes were constructed from wires fabricated from 99.99% pure rhenium powder by Sylvania Electric Products Inc. Spectroscopic analysis of this material showed Ca, 0.01-0.1%; Fe, 0.01%; and Si, 0.1%. Niobium metal was obtained from a sheet cold-pressed at 40 tons/in.^{2} and purified by a zone-refining method. Spectroscopic analysis of the niobium showed O, 0.01%; N, 0.018%; C, 0.010%; Zr, 0.04%; and Ta, 0.14% by weight. Rhenium and niobium electrodes were mounted in Teflon holders, cleaned by immersion in hydrochloric acid, and rinsed repeatedly with distilled water and with conductance water.

Electrolytic tank hydrogen was purified by passage through a train consisting of an alkaline solution of potassium permanganate, cocoanut charcoal, silica gel, Anhydrone, Hopcalite, Ascarite, DeOxy Catalytic Purifier, and silica gel. A gas washer located between the purification train and the cell was used to saturate the hydrogen gas with the test solution. Temperature control was accomplished by use of an insulated air bath; temperature was constant to within ± 0.1°C.

Hydrochloric acid solutions were prepared by dilution of a constant-boiling distillate of reagent grade hydrochloric acid and conductance water. Pre-electrolysis was conducted for a minimum of 50 hr with a current of 4-5 ma. Several hours were allowed for the establishment of temperature equilibrium. A L&N *p*H Indicator was used to measure both potentials and currents. Current was supplied from a bank of batteries and regulated by use of variable resistors. Electrode potentials were measured by the direct method within a few minutes after application or change of polarizing current as recommended by Schuldiner (25). Potentials measured in this manner were stable and polarization curves were reproducible. Stirring by hydrogen gas was continued during the measurements.

Results

Tafel plots of data for hydrogen overvoltage on rhenium electrodes in 0.037*N* and 0.145*N* HCl are shown in Fig. 1 and 2. Resistance overvoltage due to IR drop in the solution phase between the electrode surface and the tip of the reference electrode capillary contributes significantly to the measured overvoltage at the higher current densities. The resistive contribution was subtracted from the measured overvoltage values by a series of successive graphical approximations. Use of this correction, together with a correction due to the rate of the anodic reaction near the equilibrium potential, leads to the dashed Tafel lines in Fig. 1 and 2. The exact value of the resistance correction varied with each series of measurements because of unavoidable differences in the placement of the reference electrode capillary. Values of the resistance corrections for the data of Fig. 1 are 13.9, 13.7, 8.7, and 12.3 ohm-cm^2 at 5°, 15°, 25°, and 45°C, respectively. Corrections for resistance overvoltage for the data of Fig. 2 are similar, except that resistance values are only one-fourth as large as those necessary to correct the data of Fig. 1 because the solution concentration is approximately four times greater.

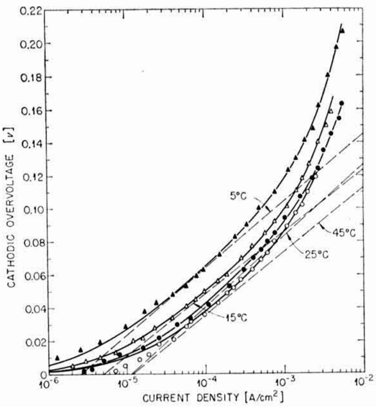

Fig. 1. Hydrogen overvoltage on rhenium in 0.037*N* HCl as a function of temperature; temperature in °C: ▲, 5; △, 15; ●, 25; ○, 45. Solid lines are calculated polarization curves; dashed lines are cathodic Tafel lines corrected for resistance overvoltage and the rate of the anodic reaction.

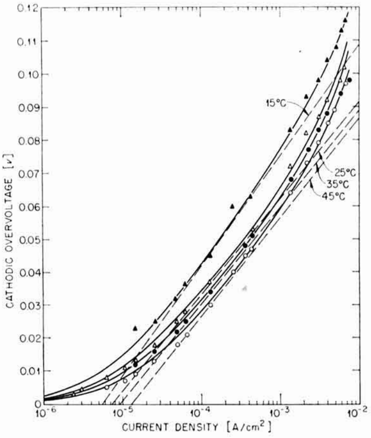

Fig. 2. Hydrogen overvoltage on rhenium in 0.145*N* HCl as a function of temperature; temperature in °C: ▲, 15; △, 25; ●, 35; ○, 45. Solid lines are calculated polarization curves; dashed lines are cathodic Tafel lines corrected for resistance overvoltage and the rate of the anodic reaction.

Tafel plots of the anodic reaction, calculated from the difference between the experimental data points and the dashed Tafel lines in Fig. 1 and 2 in the region near the equilibrium potential, show that the rate of this reaction is independent of the overvoltage. Use of this fact, taking into account the resistance overvoltage, leads to Eq. [1] for the total overvoltage. In Eq. [1], $|\eta|$ (V) is the absolute value of

$$|\eta| = |b| \log\left(1 + \frac{|j|}{j_o}\right) + |j|R_s \qquad [1]$$

the overvoltage, $|b|$ (V/decade of current) is the absolute value of the Tafel slope, $|j|$ (amp/cm^2) is the absolute value of the applied current density, j_o (amp/cm^2) is the exchange current density, and R_s (ohm-cm^2) is the resistance between the electrode surface

Table I. Parameters for hydrogen overvoltage on rhenium electrodes in dilute hydrochloric acid solutions

Solution	Temperature, °C	a, v	$b(\times 10^3)$, v	j_o, (amp/cm²)
0.037N HCl	5	−0.226	−40.5	2.65×10^{-6}
	15	−0.198	−37.5	5.1×10^{-6}
	25	−0.213	−43.0	1.14×10^{-5}
	45	−0.189	−38.4	1.18×10^{-5}
0.145N HCl	15	−0.176	−33.5	5.7×10^{-6}
	25	−0.150	−29.2	7.3×10^{-6}
	35	−0.147	−29.3	9.3×10^{-6}
	45	−0.147	−30.0	1.3×10^{-5}

and the reference electrode capillary tip.[3] Table I presents values of the Tafel a and b constants as well as values of the exchange current density calculated from the Tafel lines in Fig. 1 and 2. The a and b constants are defined conventionally by Eq. [2], which is Tafel's equation. Values of j_o, b, and R_s

$$\eta = a + b \log |j| \qquad [2]$$

were used with Eq. [1] to calculate the solid lines in Fig. 1 and 2; these theoretical lines fit the data very well.

Data for hydrogen overvoltage on niobium electrodes in 0.145N HCl are shown in Fig. 3. In this case, a large correction for resistance overvoltage is necessary; this correction was made in the same manner as that used for the data of Fig. 1 and 2. Resistive corrections in the case of the rhenium electrode in 0.145N HCl (cf. Fig. 2) average approximately 2.5 ohm-cm², which is consistent with the conductivity of the solution and the placement of the tubulus of the reference electrode, whereas those for the niobium electrode average approximately 216 ohm-cm². We suggest that, during the time necessary for the measurement of the overvoltage, no significant change occurs in the thickness of the oxide layer on the surface of the niobium electrodes. The poor electronic conductivity of the passive layer then accounts for the large resistive contribution to the measured overvoltage. Since the electronic conductivity of the passive oxide layer on niobium in solution is not known accurately, no reliable estimate can be given, in the absence of capacity measurements, of the film thickness on the electrodes used here. The resistive correction for the ohmic behavior of the film in this case may be defined by Eq. [3]

$$R_{ox} \equiv \Delta\phi_{ox}/j = l/\sigma_{ox} \qquad [3]$$

where R_{ox}(ohm-cm²) is the resistivity correction, $\Delta\phi_{ox}$ is taken to be the potential difference across the oxide layer, j is current density, l is the thickness of the layer, and σ_{ox} is the specific conductance of the layer. For R_{ox} = 200 ohm-cm², σ_{ox} would have a value between 10^{-9} and 10^{-7} ohm^{-1} cm^{-1} if the film thickness were between 20 and 2000Å. This order of magnitude of specific conductance for the Nb_2O_5 layer at the temperatures of this study is not unexpected in view of the results obtained elsewhere on the specific conductance of sintered and single crystal Nb_2O_5 specimens as a function of departure from stoichiometry and of temperature (27-29).

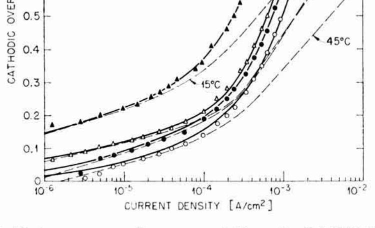

Fig. 3. Hydrogen overvoltage on niobium in 0.145N HCl as a function of temperature; temperature in °C: ▲, 15; △, 25; ●, 35; ○, 45. Solid lines are calculated polarization curves; dashed lines are cathodic Tafel lines corrected for resistance overvoltage and the rate of the anodic reaction.

Correction of the data of Fig. 3 for the ohmic contribution leads to the dashed Tafel lines shown in the graph. In this case, a change of Tafel slope occurs, corresponding to a change in the identity of the rate-determining step in the hydrogen evolution reaction. The corrected overvoltage data are described well by an expression of the form of Eq. [4]

$$j_c = \frac{j_{o,1}\, j_{o,2} \exp\left[-2.303\left(\frac{1}{b_1} + \frac{1}{b_2}\right)\eta\right]}{j_{o,1} \exp\left[-2.303\eta/b_1\right] + j_{o,2} \exp\left[-2.303\eta/b_2\right]} \qquad [4]$$

where j_c is the current density of the cathodic process, $j_{o,1}$ and $j_{o,2}$ are the exchange current densities obtained by extrapolation of the two Tafel regions to zero overvoltage, and b_1 and b_2 are the corresponding Tafel slopes (cf. Eq. [2]).[4] Values of parameters for the overvoltage in this case are given in Table II. The solid lines in Fig. 3 are theoretical polarization curves calculated by use of Eq. [4] and the data of Table II together with the correction for the ohmic behavior of the passive layer and for the rate of the anodic reaction near the equilibrium potential.

Estimated exchange current densities from the data of Fig. 1, 2, and 3 are plotted as a function of temperature in Fig. 4 and 5. In the case of the rhenium electrode, exchange current densities are essentially independent of the concentration of hydrogen ions, and the line shown in Fig. 4 is a least squares fit of all the data. The slope of the line is equivalent to an apparent enthalpy of activation of 5.96 kcal/mole. The apparent enthalpy of activation of the rate-determining process in the low current region on niobium is found from Fig. 5 to be 31.4 kcal/mole. The corresponding value for the process which determines the rate at larger overvoltages is 11.3 kcal/mole. Both values were determined by least squares fit of a simple Arrhenius-type equation to the available data.

Discussion

The data of Pecherskaya and Stender (1) for hydrogen overvoltage on rhenium were obtained in 2N

Table II. Parameters for hydrogen overvoltage on niobium electrodes in 0.145N HCl

Temperature, °C	a_1, v	$b_1(\times 10^3)$, v	$j_{o,1}$, (amp/cm²)	a_2, v	$b_2(\times 10^3)$, v	$j_{o,2}$, (amp/cm²)
15	−0.700	−71	9.4×10^{-9}	−1.429	−280	7.9×10^{-6}
25	−0.402	−57	8.8×10^{-8}	−1.472	−343	5.1×10^{-5}
35	−0.461	−75	7.0×10^{-7}	−1.569	−376	6.7×10^{-5}
45	−0.373	−64	1.5×10^{-6}	−1.153	−271	5.6×10^{-5}

---

[3] Equation [1] is essentially Hammett's relation (26) for the Tafel mechanism of the hydrogen evolution reaction. In this case the exchange current density (j_o) is equal to j_r, the limiting current density of the Tafel reaction, which is independent of electrode potential.

[4] Equation [4] is a generalized form for the cathodic polarization curve of the hydrogen evolution reaction in the case of a dual mechanism with small surface coverage of adsorbed hydrogen atoms. With $j_{o,1} = j_o{}^V/2$, $j_{o,2} = j_r$, $b_1 = 2.303\ RT/(1 - \alpha_V)F$, and $b_2 = 2.303\ RT/2F$, Eq. [4] is a form of the Hammett equation (30) for the Volmer-Tafel mechanism of the hydrogen evolution reaction. In this case, $j_o{}^V$ is the exchange current density of the Volmer reaction, j_r is the limiting current density of the Tafel or recombination reaction, and α_V is the transfer coefficient of the Volmer reaction. However, for $j_{o,1} = 2j_o{}^V$, $j_{o,2} = 2j_o{}^H$, $b_1 = 2.303\ RT/(1 - \alpha_V)F$, and $b_2 = 2.303\ RT/(2 - \alpha_H)F$, Eq. [4] is a form of Vetter's relation (31) for the Volmer-Horiuti reaction sequence. In this case, $j_o{}^V$ and $j_o{}^H$ are the exchange current densities of the Volmer and Horiuti reactions, respectively, and α_V and α_H are the corresponding transfer coefficients.

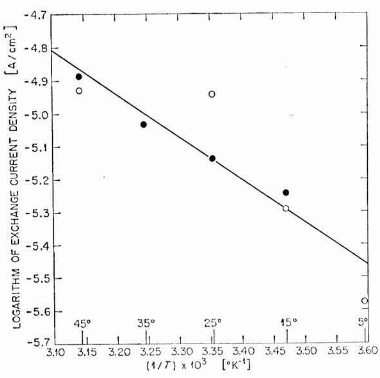

Fig. 4. Variation of the exchange current of the hydrogen reaction on rhenium with temperature. ○, 0.037*N* HCl; ●, 0.145*N* HCl.

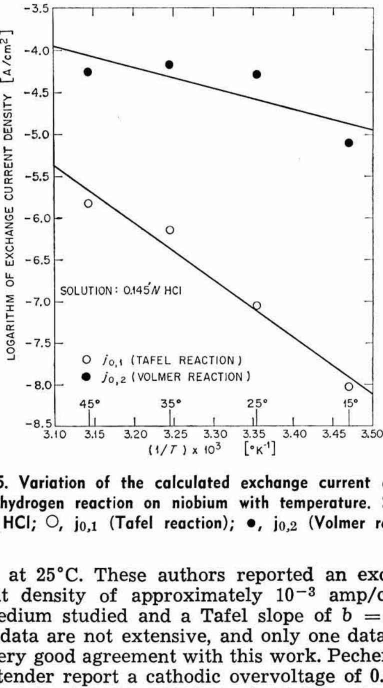

Fig. 5. Variation of the calculated exchange current densities of the hydrogen reaction on niobium with temperature. Solution, 0.145*N* HCl; ○, $j_{0,1}$ (Tafel reaction); ●, $j_{0,2}$ (Volmer reaction).

H_2SO_4 at 25°C. These authors reported an exchange current density of approximately 10^{-3} amp/cm² in the medium studied and a Tafel slope of $b = 0.14$v. Their data are not extensive, and only one data point is in very good agreement with this work. Pecherskaya and Stender report a cathodic overvoltage of 0.09v at a current density of 5 x 10^{-3} amp/cm²; this value compares favorably with the corrected Tafel lines of Fig. 1 and 2. Hydrogen overvoltage on rhenium is quite low; it is comparable to that found for iridium and rhodium (32).

We find that the Tafel slopes for the hydrogen evolution reaction on rhenium in dilute hydrochloric acid are close to 30 mv/decade (cf. Table I). The Tafel slopes obtained in 0.037*N* HCl are somewhat higher than this value, but double layer effects are probably important here, and the resistive correction is less certain in the more dilute solution. Calculations of the rate of the anodic reaction near the equilibrium potential show that the rate of this reaction is independent of potential, and the exchange current densities obtained by extrapolation of the Tafel lines are insensitive to the concentration of hydrogen ions in solution. These facts suggest that the Tafel reaction, $2H_{(ads.)} = H_{2(aq.)}$, determines the rate of the hydrogen evolution reaction on rhenium. This conclusion is supported by values of the stoichiometric numbers obtained from the polarization resistances and the estimated exchange current densities. All calculated stoichiometric numbers are near unity, ranging from 0.8 to 1.3.

Our value of the Tafel slope (30 mv/decade) may still be consistent with that of Pecherskaya and Stender (140 mv/decade) if a transition in the nature of the rate-determining step occurs near current densities of 10^{-2} amp/cm². In this case, an increase in cathodic polarization would increase the surface coverage of adsorbed atomic hydrogen to the point where the Tafel reaction would be essentially in equilibrium, and the rate of the over-all reaction would then be controlled by the Volmer reaction, $H^+_{(aq.)} + e^- = H_{(ads.)}$ (33). The apparent activation energy at the equilibrium potential of the hydrogen reaction on rhenium, obtained from Fig. 4 as 5.96 kcal/mole, refers in this case to the mean enthalpy of activation of the forward and reverse steps of the Tafel reaction.

The data on hydrogen overvoltage on niobium of Bockris (2) in 0.1*N* HCl and of Kononchuk and Barmashenko (3) in 1*N* H_2SO_4 are fragmentary, and the Tafel slopes do not agree with those observed here. The reason for this discrepancy is not known; it is possible that their measurements were influenced by the presence of impurities which could exert an important effect on the results in such a polarizable system. The measurements of Rotinyan and Kozhevnikova (4) are more extensive, and their observations resemble ours to a greater extent. These authors measured hydrogen overvoltage on niobium in 0.01-10.0*N* H_2SO_4 at temperatures from 25° to 55°C. They found nonlinear Tafel plots in the region 10^{-5}-10^{-4} amp/cm², whereas linear Tafel plots were obtained for current densities greater than 10^{-4} amp/cm². In addition, deviations from linearity were observed in dilute solutions for current densities greater than about 2 x 10^{-3} amp/cm² at 25°C.

The results of Rotinyan and Koshevnikova are understandable on the basis of the data in Fig. 3. The Tafel plot in the range, 10^{-5}-10^{-4} amp/cm², is nonlinear because of the effect of the anodic reaction and because the change in Tafel slope occurs in this range of current densities. Above approximately 10^{-4} amp/cm², linear Tafel plots could then be obtained in concentrated acidic solutions; under these conditions the thickness of the oxide layer on the surface of the niobium electrode and thus the ohmic contribution to the total overvoltage should be much less than in dilute acids. However, in dilute acids the ohmic properties of the passive oxide layer should contribute significantly to the total overvoltage, and in this case one should expect nonlinear Tafel plots, as found by Rotinyan and Kozhevnikova.

The Tafel slopes observed in the two linear regions of the polarization curves in Fig. 3 average $b_1 = 67$ mv and $b_2 = 318$ mv, respectively. Transitions in Tafel slope are expected for the hydrogen evolution reaction on electrodes with no superficial oxide layers for the Volmer-Tafel and the Volmer-Heyrovsky mechanisms (33). The Volmer-Tafel mechanism involves a transition in Tafel slope from 29 to 116 mv/decade at 25°C for normal values of the transfer coefficients, whereas Tafel slopes of the Volmer-Heyrovsky mechanism should show a transition from 39 to 116 mv/decade. Although the transition in Tafel slopes is observed on niobium, values of the slopes are roughly twice those expected at an interface with no passive oxide layer.

Unusual values of Tafel slopes for oxidation-reduction reactions on passive electrodes have been discussed by Posey, Cartledge, and Yaffe (34), Meyer (35), MacDonald and Conway (36), and Makrides (37). The dual-barrier model and its variations used by these authors account for high values of Tafel slopes which are frequently found on passive metals. In this model, the distribution of potential at the passive interface is recognized to be complex; only that part of the total potential difference between metal and solution which exists at the oxide-solution interface affects the rate of electrochemical charge-transfer steps of oxidation-reduction reactions. For cases where transfer of charge must occur across two energy barriers, both of which are affected by changes in the total interfacial potential difference, the Tafel slope of the over-all reaction is given by Eq. [5], where

$$b_{(\text{dual barrier})} = 2.303 \frac{(\beta_1 + \beta_2)RT}{\beta_1 \beta_2 F} \quad [5]$$

β_1 and β_2 are the transfer coefficients of the separate energy barriers (34). If $\beta_1 = \beta_2 = 1/2$, then the Tafel slope will be 2.303 ($4RT/F$) instead of 2.303 ($2RT/F$) for a simple reaction in a system involving a single barrier. The Tafel slopes of Fig. 3 can be understood on this basis. The dashed lines are corrected for the ohmic behavior of the passive layer, so that only the potential differences at the metal-oxide interface and at the oxide-solution interface need be considered. If both of these potential differences can vary with cathodic current, then the dual-barrier model and the formula of Eq. [5] should be applicable. The ratio of Tafel slopes for regions of high and low current density in the case of the Volmer-Tafel reaction is 4; that for the Volmer-Heyrovsky reaction is 3. The ratio of the average Tafel slopes of Fig. 3 is 4.7, although that for the results at 15° and at 45°C is 3.9 and 4.2, respectively. We conclude tentatively that the Volmer-Tafel mechanism of the hydrogen evolution reaction operates on niobium in dilute hydrochloric acid solutions and that the high Tafel slopes observed are a consequence of the existence of a passive layer which is described to a first approximation by a dual-barrier model.

Activation energies calculated from the plot of exchange current densities as a function of temperature in Fig. 5 are 31.4 kcal/mole for the Tafel reaction on the niobium surface and 11.3 kcal/mole for the Volmer reaction. These values represent the mean enthalpies of activation of the forward and reverse steps of the respective reactions. The value of 11.3 kcal/mole for the Volmer reaction is comparable to the value of 10.5 kcal/mole calculated by Rotinyan and Kozhevnikova from their data in the range from 10^{-4} to 10^{-2} amp/cm^2. Extrapolation of the lines in Fig. 5 to their point of intersection shows that the exchange current densities of the Volmer and Tafel reactions should be equal in the vicinity of 90°C. Therefore at temperatures higher than about 90°C, the Volmer reaction alone should govern the over-all rate of the hydrogen evolution reaction and no change of Tafel slope should be observed in the cathodic polarization curve of niobium.

Acknowledgment

Partial support of this project was provided by the Rhenium Fund of the University of Tennessee.

Manuscript received June 22, 1964; revised manuscript received Nov. 16, 1964. This paper was presented at the Los Angeles Meeting, May 6-10, 1962. A portion of this work was taken from a thesis submitted by one of the authors (L.S.S.) to the University of Tennessee in partial fulfillment of the requirements for the MSc degree; another portion was sponsored by the United States Atomic Energy Commission under contract with the Union Carbide Corporation.

Any discussion of this paper will appear in a Discussion Section to be published in the June 1966 JOURNAL.

REFERENCES

1. A. G. Pecherskaya and V. V. Stender, *Zhur. Fiz. Khim.*, **24**, 856 (1950).
2. J. O'M. Bockris, *Trans. Faraday Soc.*, **43**, 417 (1947).
3. T. I. Kononchuk and I. B. Barmashenko, *Ukrain. Khim. Zhur.*, **26**, 25 (1960).
4. A. L. Rotinyan and N. M. Kozhevnikova, *Zhur. Fiz. Khim.*, **37**, 1818 (1963).
5. L. Jensovsky, *Coll. Czech. Chem. Comm.*, **16**, 127 (1951).
6. V. S. Galinker, *Izvest. Vysshikh Ucheb. Zavedenii, Khim. i Khim. Tekhnol.*, **4**, 189 (1961).
7. M. Pourbaix, *Z. Elektrochem.*, **62**, 670 (1958).
8. V. O. Lavrenko, *Zhur. Fiz. Khim.*, **35**, 198 (1961).
9. L. Young, *Trans. Faraday Soc.*, **52**, 502, 515 (1956).
10. L. Young, *Acta Met.*, **4**, 101 (1956).
11. D. A. Vermilyea, *This Journal*, **104**, 427 (1957).
12. Yu. M. Valokobinskii, *Dokl. Akad. Nauk S.S.S.R.*, **113**, 1023 (1957).
13. G. B. Adams and T. Kao, *AECU-3769* (1957), U.S.A.E.C. Tech. Inf. Div., Oak Ridge, Tennessee.
14. L. Young, *Can. J. Chem.*, **38**, 1141 (1960).
15. W. M. Graven, R. E. Salomon, and G. B. Adams, *TID-6514* (1960), U.S.A.E.C. Tech. Inf. Div., Oak Ridge, Tennessee.
16. G. B. Adams and T. Kao, *This Journal*, **107**, 640 (1960).
17. L. Young, "Anodic Oxide Films," p. 186, Academic Press, London (1961).
18. A. Yu. Shatalov and T. P. Bondareva, *Dokl. Akad. Nauk S.S.S.R.*, **147**, 1137 (1962).
19. A. Yu. Shatalov, T. P. Bondareva, and L. E. Tsygankova, *Zhur. Priklad. Khim.*, **36**, 588 (1963).
20. A. Yu. Shatalov and T. P. Bondareva, *Zhur. Fiz. Khim.*, **37**, 868 (1963).
21. R. E. Salomon, G. B Adams, and W. M. Graven, *This Journal*, **110**, 1163 (1963).
22. P. H. G. Draper, *Electrochim. Acta*, **8**, 847 (1963).
23. I. A. Ammar and S. A. Awad, *J. Phys. Chem.*, **60**, 837 (1956).
24. S. Schuldiner, *This Journal*, **101**, 426 (1954).
25. S. Schuldiner, *ibid.*, **99**, 488 (1952).
26. L. P. Hammett, *J. Am. Chem. Soc.*, **46**, 7 (1924).
27. E. H. Greener, D. H. Whitmore, and M. E. Fine, *J. Chem. Phys.*, **34**, 1017 (1961).
28. E. H. Greener and W. M. Hirthe, *This Journal*, **109**, 600 (1962).
29. R. F. Janninck and D. H. Whitmore, *J. Chem. Phys.*, **37**, 2750 (1962).
30. L. P. Hammett, *Trans. Faraday Soc.*, **29**, 770 (1933).
31. K. J. Vetter, *Z. Elektrochem.*, **59**, 435 (1955).
32. J. P. Hoare and S. Schuldiner, *J. Chem. Phys.*, **25**, 786 (1956).
33. K. J. Vetter, "Elektrochemische Kinetik," pp. 410 ff, Springer-Verlag, Berlin (1961).
34. F. A. Posey, G. H. Cartledge, and R. P. Yaffe, *This Journal*, **106**, 582 (1959).
35. R. E. Meyer, *ibid.*, **107**, 847 (1960).
36. J. J. MacDonald and B. E Conway, *Proc. Roy. Soc. (London)*, **269A**, 419 (1962).
37. A. C. Makrides, *This Journal*, **111**, 392, 400 (1964)

Conduction Properties of Valve Metal-Oxide Systems

I. A New Theory

M. J. Dignam

Department of Chemistry, University of Toronto, Toronto, Ontario, Canada

ABSTRACT

A theory of cooperative ion transport in anodic oxide films on valve metals has been developed on the basis of a dielectric mosaic model. The oxide, which is "amorphous," is considered to be composed of very small crystallites or polymeric units. Ion transfer from one such unit to another is strongly influenced by the distribution of ions within these units since the field assisting the transfer will be a function of the polarization of the dielectric oxide medium. Transient ionic conduction phenomena and anomalous charging currents arise as a result of the slow adjustment of the polarization of the medium to new conditions. Two mechanisms for the rate of change of the polarization are employed, one involving thermally activated ion migration, the other being associated with the large energies dissipated during an ion transfer event. The equations arising from this model have been solved for a number of particular experimental conditions.

Recent data (1-8) concerning the anodic oxidation of the valve metals have revealed serious limitations in all previous quantitative theories dealing with the growth mechanism for these oxides. The purpose of this paper is to present a new theory which is in accord with the facts now available. In the following paper this theory is compared with previous theories, the principal one being the high field Frenkel defect theory (9), in relation to most pertinent data.

It seems likely that the main fault of previous theories lies in their failure to allow for cooperative phenomena associated with ion migration through the film. Although the possibility of such phenomena has been mentioned by Young (9) no attempt has been made previously to allow quantitatively for them. According to the high field Frenkel defect theory, transient conduction phenomena arise as a result of a slow readjustment of the concentration of ionic current carriers following a change in the field strength or current density. In the present theory the transients are ascribed to cooperative transport phenomena, the concentration of current carriers being essentially independent of field strength and current density. The detailed model, which rests on time dependent dielectric polarization phenomena, can be regarded at the very least as an "incorrect model" which nevertheless leads to the correct form for the cooperative phenomena, and at most a satisfactory approximation to the "true model."

The paper is divided into five sections with this section followed by Outline of Theory and Summary and Discussion providing the descriptive development of the theory. The detailed mathematical development has been confined to the remaining two sections. The major support for the theory is presented in the following paper (10) in which excellent agreement between the present theory and data is demonstrated.

Outline of Theory

In the present theory the oxide is treated as a nonuniform dielectric, being composed of very small crystallites or polymeric "molecular" units. Since the bonding possesses a considerable covalent character (11), the intra-"molecular" bonding will be stronger than the inter-"molecular" bonding. This will lead to regions of low density, or quasi gaps, between adjacent molecular units. The low density found for these oxides compared with their bulk densities is consistent with the above model.

Two simultaneous rate-controlling processes for ion transport through such an oxide must be considered. The one is associated with the transfer of ions from one molecular unit to the next, and the other with ionic migration within the molecular units. We shall focus attention initially on the former.

Because of the discontinuous nature of the dielectric medium, the electric field, E_e, assisting this ion transfer process will depend on the polarization of the oxide, P, so that we may write

$$E_e = E + \delta P/\mathcal{E}_o \qquad [1]$$

where E is the applied field, $\mathcal{E}_o$ the permittivity of free space, and δ a geometric factor of the order of unity introduced since the detailed geometry of these quasi gaps is unknown.

In order to take account of ion migration within the molecular units, the polarization term is separated into two terms, $P = P_1 + P_2$, where P_1 is considered to arise from conventional inertial and electronic polarization processes and P_2 from ion transport within the individual molecular units. The ordinary polarization, P_1, will have a small relaxation time and may be considered to follow the applied field in the normal manner

$$P_1 = \mathcal{E}_o \chi_1 E \qquad [2]$$

where χ_1, the electric susceptibility of the oxide measured at sufficiently high frequencies, say 1 kc, is to a good approximation independent of field and time. The ion transport polarization, P_2, however, since it involves mass transport, will have a large relaxation time so that it will vary linearly with the applied field only under steady-state conditions of constant field and current density.

In attempting to predict the variation of the transport polarization, P_2, with the field strength, time, and current density, there are several factors which should be borne in mind. If the effective field strength, E_e, is sufficiently high to cause a significant number of ion transfer events per unit time per unit volume, then the energy imparted to the molecular units as a result of these events will be very important and must be taken into account. From the available kinetic data (12) one can estimate that the energy imparted to a molecular unit receiving a charged species will be, for example, about 5 ev or more for a tantala film, which in relation to the estimated diameter of a molecular unit, 9Å (10), represents a very considerable energy density. Indeed such a unit will possess about 10^3 degrees of freedom, giving an impact energy per degree of freedom of about 0.2 kt at room temperature, or about ½ the mean thermal energy. The impact energy will be highly localized initially, making its effect greater than the above estimate would suggest. Under conditions where the collision process will be important, that is for ion current densities which are not too small, it is to be expected that the rate of change of the transport polarization, P_2, is controlled almost solely by the collision density per unit time, the rate associated with conventional thermally activated processes being negligible by comparison. For sufficiently low ion current densities, however, thermally activated polarization processes must predominate.

A possible mechanism for the collisionally activated polarization process follows: Immediately following an ion transfer event, the donor and acceptor molecular units will be depolarized or perhaps even acquire a dipole moment in the opposite direction. To re-establish their previous dipole moments or acquire their equilibrium dipole moments, ion migration in each is required. The high impact energy involved in the ion transfer event should be more than enough to produce both defects and sufficient vibrational excitation to establish in a short time the local equilibrium dipole moment for both the donor and acceptor molecular units.

To complete the outline of the theory, some statement as to how the ion current density varies with E_e and time is required. At any given moment it is apparent that certain of the molecular units will have a net electrostatic charge by virtue of their possessing an excess or deficit of the mobile species involved in the ion transfer process. Provided that the number density of these charged molecular units is independent of E_e at fixed temperature, the ion current density can be represented as a function of E_e and temperature only, the functional form being very similar to the exponential relationship conventionally used to interpret steady-state anodic oxidation data. Accepting this provision for the moment, we see that, for the present model, transient ionic conduction phenomena arise entirely from the time dependent polarization phenomena within the oxide film. The most critical tests of this model will therefore involve the measurement of transients, although certain unique predictions concerning steady-state anodic oxidation can also be subject to verification.

Mathematical Development of Model

In this section the model outlined will be used to obtain first a specific equation relating the ion current density to the effective field strength, then a differential equation for the variation with time of the dielectric polarization, and finally solutions of these equations for certain special cases.

Dependence of ion current on the effective field strength.—We shall assume, in accord with normal practice, that only one species bearing a charge rZe is involved in the ion transfer process and further that the majority of the molecular units are electrostatically neutral (where Z is the absolute value of the oxidation state of the species, e the charge on the proton, and $r = 1$ or -1 according to the sign of the charge on the species). The small contribution to kinetic processes made by units possessing a charge which differs from zero or $\pm Ze$ will be neglected.

From the above it is sufficient to consider the following four types of ion transfer processes:

1. Transfer from a neutral species to an adjacent neutral species, with a transfer probability, p_o
2. Transfer from a species with a charge rZe to an adjacent neutral species, with a transfer probability, $p_{+r} >> p_o$.
3. Transfer from a neutral species to an adjacent species with a charge $-rZe$, with a transfer probability, $p_{-r} >> p_o$.
4. Transfer from a species with a charge rZe to an adjacent species with a charge $-rZe$, with a transfer probability $>> p_{+r}$ or p_{-r}.

In a previous publication (12) it was shown that the net activation energy, $W'(E_e)$, for the transfer of a charged species across a potential energy barrier in the presence of a high electrostatic field, E_e, is given by

$$W'(E_e) = \phi' - E_e\mu^{*\prime}(1 - E_e\mu^{*}/C'\phi')$$

where ϕ' is the zero field activation energy, $\mu^{*\prime}$ the zero field "activation dipole" (*i.e.*, effective charge times activation distance for the ion transfer process), and C' a dimensionless parameter the value for which depends on the shape of the potential energy barrier.[1] The transfer probability per unit time from a given molecular unit will therefore be given by

$$p_o = N'\nu \exp\{-[\phi' - E_e\mu^{*\prime}(1 - E_e\mu^{*\prime}/C'\phi')]/kT\} \quad [3]$$

Associating Eq. [3] with process 1 and assuming that a charge rZe on a molecular unit will change the transfer probability to or from this unit simply by contributing a constant additional field term, $\mathcal{E}_r$, to the effective field which would exist in the absence of such a charge, we may write

$$p_{+r} = N'\nu \exp\{-[\phi' - [E_e + \mathcal{E}_{+r}] \mu^{*\prime}(1 - [E_e + \mathcal{E}_{+r}]\mu^{*\prime}/C'\phi')]/kT\} \quad [4]$$

or

$$p_{+r} = \kappa_{+r}p_o \quad [5]$$

where

$$\kappa_{+r} = \exp\{\mathcal{E}_{+r}\mu^{*\prime}[1 - (2E_e + \mathcal{E}_r)\mu^{*\prime}/C'\phi']/kT\} \quad [6]$$

A corresponding set of equations is obtained for p_{-r} from the above by replacing $+r$ with $-r$. The terms $\mathcal{E}_{+r}$ and $\mathcal{E}_{-r}$ will be positive and represent the constant field contributed by the net charge on one of the molecular species. From geometric considerations, it follows that $\mathcal{E}_{+r} > \mathcal{E}_{-r}$ and hence that $\kappa_{+r} > \kappa_{-r}$. If the quadratic term in the field in the net activation energy did not exist (*i.e.*, $1/C' = 0$), then κ_{+r} and κ_{-r} would be strictly independent of E_e. The presence of the quadratic term introduces a variation in κ_{+r} and κ_{-r} with E_e which is negligible compared with the variation of p_o with E_e provided that $\mathcal{E}_{+r}\mu^{*\prime}/C'\phi' << 1$, a statement in accord with the values obtained experimentally for aluminum (10). Associating the ion current (*i.e.*, the current leading to film growth) i, with the ion transfer processes 1 to 4, we may write

$$i = Zed[n_op_o + n_{+r}\kappa_{+r}p_o + n_{-r}\kappa_{-r}p_o + (\kappa_{+r} + \kappa_{-r})p_od(f\sigma')n_{+r}n_{-r}] \quad [7]$$

where d is the mean dimension of a molecular unit along the field direction and n_o, n_{+r}, and n_{-r} the volume concentrations of molecular units which bear changes of zero, $+rZe$ and $-rZe$, respectively. The final term within the square brackets of Eq. [7] requires some explanation. It represents the rate of annihilation of charged molecular units by transfer process 4, which has been treated as a "collision" annihilation with a "capture" cross-sectional area $(f\sigma')$, which should be about equal to or somewhat greater than the mean cross-sectional area, σ' ($=1/Nd$, where N is the volume concentration of molecular units), of the molecular units in a plane normal to the applied field. In an analogous manner, the net rate of formation of charged molecular units is given by

$$\frac{dn_{+r}}{dt} = \frac{dn_{-r}}{dt} = n_op_o - (\kappa_{+r} + \kappa_{-r})p_od(f\sigma')n_{+r}n_{-r} \quad [8]$$

If at some time steady-state concentrations prevail (*i.e.*, $dn_{+r}/dt = 0 = dn_{-r}/dt$) it follows from Eq. [8] that any subsequent changes in the field, E_e, under isothermal conditions, will have a negligible effect on n_{+r}, n_{-r}, and n_o (since the variation of κ_{+r} and κ_{-r} with E_e is negligible). The equation

$$dn_{+r}/dt = dn_{-r}/dt \simeq 0$$

will therefore be satisfied even under conditions of rapidly changing field. Thus Eq. [8] reduces to

$$n_{+r}n_{-r} = n_o/(\kappa_{+r} + \kappa_{-r})d(f\sigma')$$

---

[1] It is probably more correct to regard ϕ' and $\mu^{*\prime}$ as extrapolated values, the extrapolation to $E_e = 0$ being based on the behavior at high fields only (12).

$$\simeq n_o^2/(\kappa_{+r} + \kappa_{-r})f$$

since for

$$n_o >> n_{+r} \text{ and } n_{-r}, d\sigma' \simeq 1/n_o$$

In the bulk of the film, remote from the interfaces, the mean space charge will be essentially zero, so that we may set $n_{+r} = n_{-r}$. Under these conditions Eq. [7] and [9] yield

$$i = \frac{Ze}{\sigma'}\left[2 + \left(\frac{\kappa_{+r} + \kappa_{-r}}{f}\right)^{1/2}\right] p_o \qquad [10]$$

Equation [10] will only be valid remote from the interfaces. To allow for space charge phenomena, Eq. [7] and [9] must be solved in conjunction with Poisson's equation. For the present, however, we shall assume that the films involved are thick enough that Eq. [10] may be used without serious error.

It is now convenient to write Eq. [10] in the following form

$$i = (Ze/\sigma)\kappa^{1/2} p_o \qquad [11]$$

where

$$\sigma = \sigma'\left[2 + \left(\frac{\kappa_{+r} + \kappa_{-r}}{f}\right)^{1/2}\right] \Big/ \kappa^{1/2}$$

and κ is identically κ_{+r} or κ_{-r}, whichever is the greater. (From previous discussion, $\kappa_{+r} > \kappa_{-r}$.) κ is therefore given by

$$\kappa = \exp\{\mathcal{E}\mu^{*\prime}[1 - (2E_e + \mathcal{E})\mu^{*\prime}/C'\phi']/kT\} \qquad [12]$$

where the subscript, r, has been omitted for brevity. It follows from our earlier assumption, $n_o >> n_{\pm r}$, that $\kappa^{1/2} >> 1$. Since f probably lies between about 1 and 2, we may set the following limits on σ, $\sqrt{2} \gtreqless \sigma/\sigma' \gtreqless 1/\sqrt{2}$. Furthermore, from the equations for κ_{+r} and κ_{-r} it is easily shown that σ/σ' will vary not more than 0.15% for a 1% change in absolute temperature. Its variation with the effective field, E_e, will be totally negligible. It follows, therefore, that $\sigma \simeq \sigma'$ and is for all practical purposes independent of both temperature and field strength (provided of course σ' is independent of these).

Combining Eq. [3], [11], and [12], the desired relationship is obtained

$$i = i_o \exp\{-[\phi - E_e\mu^* (1 - E_e\mu^*/C\phi)]/kT\} \qquad [13]$$

where

$$i_o = ZeN'\nu/\sigma \qquad [14]$$

$$\phi = \phi'\left[1 - \frac{\mathcal{E}\mu^{*\prime}}{2\phi'} + \frac{1}{2C'}\left(\frac{\mathcal{E}\mu^{*\prime}}{\phi'}\right)^2\right] \qquad [15]$$

$$\mu^* = \mu^{*\prime}\left[1 - \mathcal{E}\frac{\mu^{*\prime}}{C'\phi'}\right] \qquad [16]$$

$$C = C'\left[1 - \frac{\mathcal{E}\mu^{*\prime}}{C'\phi'}\right]^2 \Big/ \left[1 - \frac{\mathcal{E}\mu^{*\prime}}{2\phi'} + \frac{1}{2C'}\left(\frac{\mathcal{E}\mu^{*\prime}}{\phi'}\right)^2\right] \qquad [17]$$

From the space charge data for the anodic oxidation of aluminum, one can estimate that $\mathcal{E}\mu^{*\prime}/C'\phi' \simeq 0.07$ (10). Using this value and setting $C' \simeq 3.6$ (12) we have for this system

$$(\phi' - \phi)/\phi' \simeq 0.12$$

$$(\mu^{*\prime} - \mu^*)/\mu^{*\prime} \simeq 0.07$$

$$(C' - C)/C' \simeq 0.02$$

Experimentally determined values for ϕ', μ^*, and C will provide, therefore, reasonably good estimates of the more fundamental primed parameters.

Rate of change of the dielectric polarization.—In determining the rate of change of the dielectric polarization, and hence of E_e, as a function of the appropriate variables, it is convenient to work with the dipole moments of the individual molecular units. For conditions of uniform polarization of the oxide, the dipole moment per unit volume will be the same throughout the oxide, so that the dipole moment associated with a given molecular unit will be proportional to its volume. Since the volume of a molecular unit might vary from one unit to the next, the dipole moment per molecular unit appears at first to be a poor parameter with which to work. However, since the ultimate form of the equations involves a simple linear summation over all the molecular units, mean values for the dipole moments and polarizabilities may be used at the outset without it introducing an approximation in the final equations.

Accordingly, we shall define the following parameters:

E_e	field effective in assisting the ion transfer process
E_p	field effective in polarizing a given molecular unit
N	number of molecular units per unit volume
μ	dipole moment per molecular unit
μ_1	dipole moment per molecular unit associated with the fast polarization process.
μ_2	dipole moment per molecular unit associated with the slow, ion transport, polarization process
α_s	static polarizability associated with μ (*i.e.*, $\alpha_s = \mu/E_p$ for static conditions)
α_1	differential polarizability associated with μ_1 (*i.e.*, $\alpha_1 = (\partial\mu_1/\partial E_p)_{\mu_2}$)
α_2	static polarizability associated with μ_2 (*i.e.*, $\alpha_2 = \mu_2/E_p$ for static conditions)
i	ion current density associated with the growth of film (as opposed to charging current)
Ze	absolute magnitude of the charge transferred during an ion transfer process
d	mean dimension of a molecular unit along the applied field direction
σ'	mean cross-sectional area of a molecular unit in a plane normal to the applied field direction, $= 1/Nd$

Using these parameters, Eq. [1] becomes

$$E_e = E + \delta N\mu/\mathcal{E}_o \qquad [18]$$

where δ is a factor of the order of unity which allows for the uncertainty as to the precise contribution of the polarization of the medium to the effective field strength, E_e. Similarly, we have

$$E_p = E + \delta' N\mu/\mathcal{E}_o \qquad [19]$$

where δ' is a factor analogous to δ, introduced for the same reason. By definition, we also have

$$\mu = \mu_1 + \mu_2 \qquad [20]$$

For μ_2 constant, $(\partial\mu_1/\partial E_p)_{\mu_2} = \alpha_1$. However, the presence of μ_2 introduces a depolarization field proportional to μ_2 ($\gamma\mu_2/\alpha_2$ say), acting in the opposite direction to E_p. We may therefore write

$$\mu_1 = \alpha_1[E_p - \gamma\mu_2/\alpha_2] \qquad [21]$$

where $1 \geqq \gamma \geqq 0$, since for steady-state conditions, $\mu_2/\alpha_2 = E_p$.

From Eq. [20] and [21] it follows that

$$\alpha_s = \alpha_1(1 - \gamma) + \alpha_2 \qquad [22]$$

The principal equation now lacking is that for the rate of change of μ_2 with time, in accordance with the collisionally induced and thermally activated polarization processes discussed previously. We shall treat the collisionally induced process first.

The ion transfer frequency per unit volume of oxide is clearly given by i/Zed. In accordance with our previous assumption, ion transfer processes type 2 and 3 will predominate so that the effect of processes 1 and 4 on the rate of change of polarization will be neglected. This approximation amounts to neglecting $\kappa^{-1/2}$ compared with unity. Immediately before an ion transfer event, the uncharged molecular unit taking part in the event will have, on the average, a dipole moment nearly equal to the average of the dipole moments for all units. Following the ion transfer process, the dipole moment will be the equilibrium value, $\alpha_2 E_p$, so that the contribution to the change in $N\mu_2$ per collision made by the initially uncharged molecular unit is on the average $(\alpha_2 E_p - \mu_2)$.

The contribution made by the charged molecular unit must be calculated differently. Being few in number, a charged molecular unit will have been involved in a collision process much more recently on the average than the uncharged unit and hence will have, in general, a dipole moment differing appreciably from the average value. The contribution to the change in $N\mu_2$ made by the initially charged molecular unit can be represented approximately by $\alpha_2 (dE_p/dt)\, \Delta t$ where $(dE_p/dt)\Delta t$ approximates the change in E_p between consecutive ion transfer processes involving the unit in question, Δt being an appropriately weighted average lifetime for a charged unit. For a molecular unit of charge rZe, the average lifetime is $1/p_{+r}$, while for a charge $-rZe$ it is $1/p_{-r}$. The combined average lifetime, weighted according to transfer frequency, is therefore given by

$$\begin{aligned}\Delta t = {} & [p_{+r}/(p_{+r} + p_{-r})](1/p_{+r}) + \\ & [p_{-r}/(p_{+r} + p_{-r})](1/p_{-r}) \\ & = 2/(p_{+r} + p_{-r}) = 2/p_0(\kappa_{+r} + \kappa_{-r}) \\ & \simeq ZeNd/i\kappa^{1/2}\end{aligned}$$

where the last step involves Eq. [10].

Multiplying the ion transfer frequency per unit volume by the total change in $N\mu_2$ per transfer process, we now obtain the following equation

$$\left(\frac{d(N\mu_2)}{dt}\right)_c = \frac{i}{Zed}[\alpha_2 E_p - \mu_2] + \frac{N}{\kappa^{1/2}}\alpha_2 \frac{dE_p}{dt}$$

or

$$\left(\frac{d\mu_2}{dt}\right)_c = \frac{i\sigma'}{Ze}[\alpha_2 E_p - \mu_2] + \frac{\alpha_2}{\kappa^{1/2}}\frac{dE_p}{dt} \qquad [23]$$

where the subscript, c, denotes that it is the collisionally induced component of $(d\mu_2/dt)$. Ultimately, it will be shown that the term in dE_p/dt can be neglected, so that the approximations involved in obtaining it are of little consequence. This is fortunate since this term is too large for sufficiently small i. (For $i = 0$ this term should be zero.)

The thermally activated component of $d\mu_2/dt$ will be equal to the ion current per molecular unit within the molecular units arising most probably as a result of surface ion transport. Assuming a single ionic species to predominate in this transport process, we may write

$$\begin{aligned}\frac{d\mu_2}{dt} = {} & \frac{i\sigma'}{Ze}[\alpha_2 E_p - \mu_2] + \frac{\alpha_2}{\kappa^{1/2}}\frac{dE_p}{dt} \\ & + 2Z'eb\nu'n'\left[\exp\left(-\frac{Q}{kT}\right)\right]\sinh\left[\frac{w^{*\prime}\theta}{kT}\left(E_p - \frac{\mu}{\alpha_s}\right)\right]\end{aligned} \qquad [24]$$

where the new symbols are defined as follows:

$Z'e$	absolute magnitude of the charge associated with the ionic species
b	mean jump distance for the ionic species (*i.e.*, mean distance travelled per activation)
ν'	vibrational frequency along the reaction coordinate associated with the ionic species
n'	number of ionic species per molecular unit in preferred sites for migration
Q	zero field activation energy for migration of ionic species from preferred sites
$w^{*\prime}$	activation dipole associated with Q (*i.e.*, activation distance times effective charge)

The first two terms of Eq. [24] come directly from Eq. [23], the final term being that for conventional ion transport allowing for the possibility of high field strengths (13). The internal field effective in assisting the ion transport will be proportional to $E_p - \mu/\alpha_s$. (This clearly has the correct form for $\mu = 0$ and also for $\mu = \alpha_s E_p$, *i.e.*, $d\mu_2/dt = 0$ for $\mu = \alpha_s E_p$.) The proportionality constant, θ, would appear to be somewhat greater than unity.[2] The quadratic term in the field strength, such as introduced in Eq. [3] (*i.e.*, the term containing C'), should be entirely negligible in the present case since $E_p - \mu/\alpha_s$ is at least a factor of 10 less than E_e for a given applied field, E. This statement can be verified readily from the equations presented in the remainder of this section and from empirical values for the constants presented in the following paper (10). However, the nature of the model would suggest a range of values for the parameters Q and $w^{*\prime}$, so that the hyperbolic sine function term in Eq. [25] can only be regarded as a rather rough approximation.

Elimination of E_p, μ_1, μ_2, and α_2 from Eq. [19], [20], [21], [22], and [24], and replacing $w^{*\prime}\theta$ with $w_e^{*\prime}$ yields

$$\begin{aligned}\frac{d\mu}{dt} & + \left(\frac{1 - \delta' N\alpha_s/\mathcal{E}_0}{1 - \delta' N\alpha_1'/\mathcal{E}_0}\right)\frac{i\sigma'\mu}{Ze} = \left(\frac{\alpha_1'}{1 + \delta' N\alpha_1'/\mathcal{E}_0}\right)\frac{dE}{dt} \\ & + \left(\frac{\alpha_s}{1 - \delta' N\alpha_1'/\mathcal{E}_0}\right)\frac{i\sigma'}{Ze}E + \left[\frac{\alpha_s - \alpha_1}{\alpha_s - \alpha_1(1-\gamma)}\right] \\ & \left[\frac{2Z'eb\nu'n'}{1 - \delta' N\alpha_1'/\mathcal{E}_0}\right]\left[\exp\left(-\frac{Q}{kT}\right)\right] \\ & \sinh\left[\frac{we^{*\prime}}{kT}\left(E - \frac{\mu}{\alpha_s}\left\{1 - \frac{\delta' N\alpha_s}{\mathcal{E}_0}\right\}\right)\right]\end{aligned} \qquad [25]$$

where $\alpha_1' = \alpha_1 + \dfrac{\alpha_s - \alpha_1}{\kappa^{1/2}}$. Assuming, as before, that $\kappa^{1/2} >> 1$, one may neglect $(\alpha_s - \alpha_1)/\kappa^{1/2}$ compared with α_1, thus eliminating this term as previously mentioned.

Equation [25] may be simplified considerably by introducing the dynamic and static electric susceptibilities, χ_1 and χ_s, respectively, defined as follows

$$\chi_1 = \frac{N}{\mathcal{E}_0}\lim_{\dot{E}\to\infty}\frac{d\mu}{dE} \qquad [26]$$

$$\chi_s = \frac{N}{\mathcal{E}_0}\lim_{\dot{E}\to 0}\frac{d\mu}{dE} \qquad [27]$$

From Eq. [25]

$$\chi_1 = N\alpha_1'/\mathcal{E}_0(1 - \delta' N\alpha_1'/\mathcal{E}_0) \qquad [28]$$

$$\chi_s = N\alpha_s/\mathcal{E}_0(1 - \delta' N\alpha_s/\mathcal{E}_0) \qquad [29]$$

Eliminating α_1' and α_s from Eq. [25], [28], and [29] and substituting $\mu = P/N$ where P is the polarization of the oxide, we obtain the desired equation

$$\begin{aligned}\frac{dP}{dt} = {} & \mathcal{E}_0\chi_1\frac{dE}{dt} + Bi[\mathcal{E}_0\chi_s E - P] + \\ & i_{co}[\exp(-Q/kT)]\sinh[w_e^{*\prime}(E - P/\mathcal{E}_0\chi_s)/kT]\end{aligned} \qquad [30]$$

where

$$B = \left(\frac{1 + \delta'\chi_1}{1 + \delta'\chi_s}\right)\frac{\sigma'}{Ze},$$

$$i_{co} = \frac{(\chi_s - \chi_1)(1 + \delta'\chi_1)2Z'eb\nu'\eta' N}{\chi_s - \chi_1[1 - \gamma(1 + \delta'\chi_s)]}$$

Alternatively, eliminating $P = N\mu$ from Eq. [18] and [30], an equation for the effective field strength, E_e, is obtained

---

[2] For the simple electrostatic model in which the crystallites are treated as dielectric spheres in a uniform field, E_p, the internal field assumed to be the Lorentz field, and γ assumed to be unity, it can be shown that $\theta = (1 - \alpha_1/\alpha_s)^{-1}$. A more general treatment of the problem suggests a somewhat smaller value for θ.

$$\frac{dE_e}{dt} + BiE_e = (1+\delta\chi_1)\frac{dE}{dt} + Bi(1+\delta\chi_s)E + (\delta i_{co}/\mathcal{E}_o)[\exp(-Q/kT)] \sinh\left\{\frac{w_e^{*\prime}}{kT}\left[\frac{(1+\delta\chi_s)E - E_e}{\delta\chi_s}\right]\right\} \qquad [31]$$

To complete the development of the basic equations for the model, we note that the current flowing in the external circuit, I, will be given by

$$I = i + i_c + i_e \qquad [32]$$

where i is the ion current leading to film growth, given by Eq. [13]; i_c is the total charging current, $d[P + \mathcal{E}_o E]/dt$, and i_e the current arising from electronic conduction through the film, which we shall assume to be zero. From Eq. [18] and [30], the charging current is given by

$$i_c = \mathcal{E}_o K_1 \frac{dE}{dt} + \frac{Bi\mathcal{E}_o}{\delta}[(1+\delta\chi_s)E - E_e] + i_{co}[\exp(-Q/kT)]\sinh\left\{\frac{w_e^{*\prime}}{kT}\left[\frac{(1+\delta\chi_s)E - E_e}{\delta\chi_s}\right]\right\} \qquad [33]$$

where $K_1 = 1 + \chi_1$ is the dynamic dielectric constant for the oxide.

Elimination of E_e, i_c, and i from Eq. [13], [31], [32], and [33] leads to a differential equation which may in principal be solved to obtain I as a function of time, given E as a function of time and a suitable boundary condition. In the following sections we shall use these equations to obtain I as a function of E or t for a number of special cases, thus providing equations which are readily amenable to experimental verification. In general, however, digital computer methods are required.

Particular Solutions of Basic Equations

For simplicity, no case will be considered for which the rate of change of the polarization brought about by collision is of the same magnitude as that brought about by thermally activated ionic conduction. The discussion of transient phenomena will therefore be classified according to i large (*i.e.*, collision process dominant) and i small (*i.e.*, thermally activated process dominant). We shall begin, however, by obtaining the steady-state solution.

Steady-state solution.—For steady-state conditions ($dE/dt = di/dt = 0$) it follows from Eq. [13] and [31] that $E_e = (1 + \delta\chi_s E)$ and hence from Eq. [32] and [33] that $I = i$. Substituting these results into Eq. [13], we obtain the desired solution

$$I = i_o \exp\left\{-\left[\phi - E\mu_s^*\left(1 - \frac{E\mu_s^*}{C\phi}\right)\right] \Big/ kT\right\} \qquad [34]$$

where $\mu_s^* = (1 + \delta\chi_s)\mu^*$. We note that, apart from space charge effects, four parameters, i_o, ϕ, μ_s^*, and C are sufficient to define the steady-state behavior according to this model.

It is convenient to define the steady-state reciprocal Tafel slope, β_s, as follows

$$\beta_s = \underset{\dot{E}\to 0}{\text{Limit}} \frac{d\ln I}{dE} \qquad [35]$$

from which we have

$$\beta_s = \frac{\mu_s^*}{kT}\left[1 - \frac{2\mu_s^* E}{C\phi}\right] \qquad [36]$$

General transient behavior for i large.—For i sufficiently large, the collisionally activated polarizing process will dominate so that the final term in Eq. [31] and [33] may be neglected. Equation [31] can then be written

$$\frac{d(\mu^* E_e)}{dt} + Bi(\mu^* E_e) = \mu_1^* \frac{dE}{dt} + Bi\mu_s^* E \qquad [37]$$

where $\mu_1^* = (1 + \delta\chi_1)\mu^*$. From Eq. [32] and [33], and setting $[K_1 + (1-\delta)/\delta] \simeq K_1$, we obtain

$$I - \mathcal{E}_o K_1 \frac{dE}{dt} = i\left[1 + B\mathcal{E}_o K_1\left(\frac{\mu_s^* E - \mu^* E_e}{\mu_1^*}\right)\right] \qquad [38]$$

For both alumina and tantala the term in B does not exceed about 0.05 for any realizable experiment (10) so the above approximation should normally be a satisfactory one, particularly since one would expect δ to be close to unity and K_1 is large compared to unity.

Eliminating $\mu^* E_e$ and i from Eq. [13], [37], and [38], it is seen that apart from K_1, which is readily determined independently, only two parameters, μ_1^* and B, are required in addition to the steady-state parameters to define transient behavior for i large. Unfortunately, the solution of even this equation generally requires the use of a digital computer, although two important exceptions are for the cases $\dot{E}$ very large and $\dot{E} = 0$.

Transient behavior for i and Ė large.—In considering this case, it is convenient to define the transient reciprocal Tafel slope, β_1, as follows

$$\beta_1 = \underset{\dot{E}\to\infty}{\text{Limit}} \frac{d\ln I'}{dE} \qquad [39]$$

where $I' = I - \mathcal{E}_o K_1\, dE/dt$ can be obtained readily from the experimental measurements. Using the boundary condition that at $t = 0$, $E = E_o$, and $\mu^* E_e = \mu_s^* E_o$ (*i.e.*, steady-state conditions prevailed immediately before commencing the rapid change in field) Eq. [13], [37], [38], and [39] yield

$$\beta_1 = \frac{\mu_1^*}{kT}\left[1 - \frac{2\mu_s^* E_o}{C\phi} - \frac{2\mu_1^* \Delta E}{C\phi}\right] + B\mathcal{E}_o K_1\left[\frac{\mu_s^* - \mu_1^*}{\mu_1^*}\right] \qquad [40]$$

where $\Delta E = E - E_o$ and the approximation

$$1 >> B\mathcal{E}_o K_1\left(\frac{\mu_s^* - \mu_1^*}{\mu_1^*}\right)\Delta E$$

has been made. The final term in Eq. [40] contributes less than 3% to β_1 for both alumina and tantala (10) so may usually be neglected. The integrated form of Eq. [39] and [40] can be written

$$\frac{1}{\Delta E}\ln\frac{I'}{I_o} = \frac{\mu_1^*}{kT}\left[1 - \frac{2\mu_s^* E_o}{C\phi} - \frac{\mu_1^* \Delta E}{C\phi}\right] + B\mathcal{E}_o K_1\left[\frac{\mu_s^* - \mu_1^*}{\mu_1^*}\right] \qquad [41]$$

$$\simeq \beta_1 \text{ for } \Delta E \text{ small}$$

where I_o is the steady-state current density before effecting the rapid change in E. It is noteworthy that the variation of β_1 with E_o is closely related to the variation of β_s with E (Eq. [36]), a prediction which can readily be checked (10).

Constant field transients for i large.—From Eq. [37], on setting $\dot{E} = 0$, we obtain

$$\frac{d(\mu^* E_e)}{dt} = Bi(\mu_s^* E - \mu^* E_e) \qquad [42]$$

Also, from Eq. [13] and [34], respectively, we have

$$kT\ln(i/A) = \mu^* E_e - (\mu^* E_e)^2/C\phi \qquad [43]$$

$$kT\ln(I_s/A) = \mu_s^* E - (\mu_s^* E)^2/C\phi \qquad [44]$$

where $A = i_o \exp(-\phi/kT)$ and I_s is the steady-state current density for the field, E, in question.

From Eq. [42], [43], and [44], the following equation may be readily verified

$$\frac{d \ln i}{dt} = Bi \ln (I_s/i) + \frac{(\mu_s{}^*E - \mu^*E_e)^2}{kT\, C\phi} \qquad [45]$$

Solving for μ^*E_e and $\mu_s{}^*E$ from Eq. [43] and [44], respectively, we obtain

$$\mu_s{}^*E - \mu^*E_e = \frac{C\phi}{2}\left[\left(1 - \frac{4kT}{C\phi}\ln\frac{i}{A}\right)^{1/2} - \left(1 - \frac{4kT}{C\phi}\ln\frac{I_s}{A}\right)^{1/2}\right] \qquad [46]$$

It is readily proven that for $a_1 < 1$ and $a_2 < 1$, $(1 - a_1)^{1/2} - (1 - a_2)^{1/2} = \frac{1}{2}(a_2 - a_1)/(1 - \xi)^{1/2}$ for some ξ in the interval (a_1, a_2), the first approximation value for ξ being $(a_1 + a_2)/2$.[3] Equation [46] can therefore be written

$$\mu_s{}^*E - \mu^*E_e = (kT/z^{1/2}) \ln (I_s/i) \qquad [47]$$

where

$$z = 1 - (4kT/C\phi) \ln (i_*/A) \qquad [48]$$

and i_* is some current in the interval (I_s, i), a first approximation for which is given by: $i_* \simeq (I_s i)^{1/2}$. An alternative expression for z can be obtained by replacing I_s in Eq. [44] by i_s (to avoid confusion of symbols), solving for $\mu_s{}^*E$ and evaluating $dE/d \ln i_s$

$$\frac{dE}{d \ln i_s} = \frac{1}{\beta_s(i_s)} = (kT/\mu_s{}^*)[1 - 4(kT/C\phi) \ln (i_s/A)]$$

where $\beta_s(i_s)$ is the steady-state reciprocal Tafel slope for a current density i_s. We may therefore write

$$z^{1/2} = kT\, \beta_s(i_*)/\mu_s{}^* \qquad [49]$$

From Eq. [45] and [47] we now have

$$\frac{d \ln i}{dt} = Bi \ln (I_s/i)\left[1 + \frac{kT}{zC\phi} \ln (I_s/i)\right] \qquad [50]$$

Eliminating $\mu_s{}^*E - \mu^*E_e$ from Eq. [38] and [47] we obtain

$$I = i\left[1 + B\mathcal{E}_oK_1 \frac{kT}{\mu_1{}^*z^{1/2}} \ln (I_s/i)\right] \qquad [51]$$

Recalling that the term in B is small compared with unity, we may write

$$\ln (I_s/i) = \ln (I_s/I)\left[1 + B\mathcal{E}_oK_1 \frac{kT}{\mu_1{}^*z^{1/2}}\right] \qquad [52]$$

Since $1 + B\mathcal{E}_oK_1\, kT/\mu_1{}^*z^{1/2}$ varies only slowly with z, and z in turn varies only slowly with I, we may set

$$\frac{d}{dt}(1 + B\mathcal{E}_oK_1\, kT/\mu_1{}^*z^{1/2} \simeq 0$$

and obtain from Eq. [52]

$$\frac{d \ln i}{dt} \simeq \frac{d \ln I}{dt}\left[1 + B\mathcal{E}_oK_1 \frac{kT}{\mu_1{}^*z^{1/2}}\right] \qquad [53]$$

Eliminating $d \ln i/dt$, i and $\ln (I_s/i)$ from Eq. [50] using Eq. [53], [51], and [52], respectively, we obtain

$$\frac{d \ln I}{dt} = BI \ln (I_s/I)[1 + a \ln (I_s/I)] \qquad [54]$$

where

$$a = \frac{kT}{zC\phi}\left[1 - \frac{B\mathcal{E}_oK_1C\phi z^{1/2}}{\mu_1{}^*}\right]\left[1 + B\mathcal{E}_oK_1 \frac{kT}{\mu_1{}^*z^{1/2}}\right]$$

Fortunately, for both aluminum and tantalum (10), $a \simeq 10^{-2}$ for typical conditions. It appears, therefore, that the term in a may usually be neglected. Accordingly, integration of Eq. [54] gives

$$\frac{1}{I} \simeq \frac{1}{I_o} - B\int_o^t \ln \frac{I_s}{I}\, dt \qquad [55]$$

where I_o is the value of I at $t = 0$. An alternative integrated form of Eq. [54] may be written (neglecting the term in a)

$$\ln (I_s/I) = [\ln (I_s/I_o)] \exp (-Bq) \qquad [56]$$

where

$$q = \textstyle\int_o^t I\, dt$$

is the charge passed per unit area. We note that for a fixed value of I_s/I_o, $\ln (I_s/I)$ is a function of q only, being independent of both the steady-state current density and the temperature. The duration of these transients will of course depend on the current density.

The approximations made in deriving Eq. [55] and [56] should be valid within experimental error for $|\log I_s/I| \leq 2$. If approximate values for the various constants are known, a may be calculated as a function of I and the correction term included. In general, however, other sources of error will be more important.

It is perhaps worthwhile pointing out that the term in a in Eq. [54] arises as a result of two effects, the quadratic term in the field in the net activation energy (Eq. [3]), and the ionic contribution to the charging current. The two effects tend to cancel one another.

General transient behavior for i small.—For i sufficiently small so that the collisionally activated contribution to the polarization process may be neglected, Eq. [30] becomes

$$\frac{dP}{dt} = \mathcal{E}_o\chi_1 \frac{dE}{dt} + i_{co}\left[\exp\left(-\frac{Q}{kT}\right)\right] \sinh\left[\frac{w_e{}^{*\prime}}{kT}\left(E - \frac{P}{\mathcal{E}_o\chi_s}\right)\right] \qquad [57]$$

For both alumina and tantala near 25°C Eq. [57] is a reasonable approximation only when i is vanishingly small, that is when $I = i_c$ (10). For other metal-oxide systems, however, or for alumina and tantala at sufficiently high temperatures, it is possible that $i_{co} \exp (-Q/kT)$ will be sufficiently large that Eq. [57] would apply even for reasonably large values of i. Before limiting the discussion to the case $i \approx 0$, therefore, the case where $i \gtrsim i_c$, yet is sufficiently small for the present approximation to be valid, will be considered.

Constant field transients for i small.—Making the substitutions

$$y = \frac{w_e{}^{*\prime}}{kT}\left(\frac{P}{\mathcal{E}_o\chi_s} - E\right)$$

and

$$g = w_e{}^{*\prime}i_{co}[\exp (-Q/kT)]/\mathcal{E}_o\chi_s\, kT$$

Eq. [57] becomes, for $\dot{E} = 0$,

$$dy/\text{sinh} y = -gdt$$

which on integration gives

$$\ln [\tanh (y_o/2)] - \ln [\tanh (y/2)] = gt \qquad [58]$$

or

$$-y = 2\tanh^{-1}[De^{-gt}]$$

where

$$D = \tanh (-y_o/2)$$

and

$$y = y_o \text{ at } t = 0$$

We may replace y by $(w_e{}^*/\mu_s{}^*)(\mu^*E_e - \mu_s{}^*E)/kT$ where $w_e{}^* = (1 + 1/\delta\chi_s)w_e{}^{*\prime} \simeq w_e{}^{*\prime}$ and obtain

$$\left(\frac{\mu_s{}^*E - \mu^*E_e}{kT}\right) = \frac{2\mu_s{}^*}{w_e{}^*}\tanh^{-1}[De^{-gt}] \qquad [59]$$

and

$$g \simeq w_e{}^*i_{co}[\exp (-Q/kT)]\, \mu_1{}^*/\mu_s{}^*\, \mathcal{E}_oK_1\, kT$$

---

[3] Defining $F(\xi) = (1 - \xi)^{1/2}[(1 - a_1)^{1/2} - (1 - a_2)^{1/2}] - \frac{1}{2}(a_2 - \alpha_1)$, by substitution we have $F(\alpha_1) = -F(\alpha_2)$, so that $F(\xi)$, which is continuous in the interval (a_1, a_2), changes sign in the interval and hence is zero for some ξ in (a_1, a_2). Also, since $F(a_1) = -F(a_2)$, linear interpolation gives $\xi \cong (a_1 + a_2)/2$.

Eliminating $\mu^* E_e$ from Eq. [47] and [59] the following result is obtained

$$\ln (I_s/i) = 2z^{1/2} (\mu_s^*/w_e^*) \tanh^{-1} [De^{-gt}] \qquad [60]$$

Since z varies only slowly with i, we may to a first approximation set it equal to the mean of the extreme values of z, given approximately by (see Eq. [48] and [49])

$$\overline{z} \simeq 1 - (4kT/C\phi) \ln \left(\frac{i_o I_s^3}{A^4} \right)^{1/4} = (kT\,\overline{\beta_s}/\mu_s^*)^2$$

where $i = i_o$ at $t = 0$ and $\overline{\beta_s}$ is the steady-state reciprocal Tafel slope for a current density equal to $(i_o I_s^3)^{1/4}$. Equation [60] therefore becomes

$$\ln (I_s/i) \simeq (2kT\,\overline{\beta_s}/w_e^*) \tanh^{-1} [De^{-gt}] \qquad [61]$$

where $D \simeq \tanh [(w_e^*/2kT\overline{\beta_s}) \ln (I_s/i_o)$. Because of the complex form of the equation (derived in the next section) for the charging current, interpretation of data in terms of Eq. [61] will only be feasible for $I \simeq i$ (*i.e.*, $i >> i_c$).

We note that Eq. [61] predicts $\ln (I_s/i)$ to be a function only of time for i_o/I_s and temperature fixed. The duration of these transients is therefore independent of the steady-state current density, but is highly dependent on the temperature, since g contains a Boltzmann factor. This behavior is in marked contrast to that for constant field transients at high ion currents (cf. Eq. [56]). The two cases can therefore be readily distinguished experimentally.

Charging current for i small.—For i sufficiently small, we may combine Eq. [57] with the relation

$$i_c = d[P + \epsilon_o E]/dt$$

and obtain

$$i_c' = A_c \sinh \left[\frac{w_e^*}{kT} \left(\frac{\mu_s^* - \mu_1^*}{\mu_s^*} \right) \left(E - E_* - \frac{q_c'}{\mathcal{E}_o(\chi_s - \chi_1)} \right) \right]$$

or setting

$$1 + \chi_s \simeq (1 + \chi_1)\,(1 + \delta\chi_s)/(1 + \delta\chi_1) = K_1 \mu_s^*/\mu_1^*$$

$$i_c' \simeq A_c \sinh \left\{ \frac{w_e^*}{kT} \left[\left(\frac{\mu_s^* - \mu_1^*}{\mu_s^*} \right) (E - E_*) - \frac{\mu_1^*}{\mu_s^*} \frac{q_c'}{\mathcal{E}_o K_1} \right] \right\} \qquad [62]$$

where $i_c' = i_c - \mathcal{E}_o K_1\, dE/dt$ is the ionic contribution to the charging current; $A_c = i_{co} \exp\ (-Q/kT)$, $q_c' = \int_o^t i_c' dt$, $E_* = (P_o/\mathcal{E}_o - \chi_1 E_o)/\ (\chi_s - \chi_1)$ and P_o and E_o are the values of P and E at $t = 0$. For a fully annealed film, the ionic contribution to the polarization will be zero at $t = 0$ (*i.e.*, $P_o = \mathcal{E}_o \chi_1 E_o$) so that $E_* = 0$ for this case. If equilibrium polarization conditions prevail at $t = 0$ (*i.e.*, $P_o = \mathcal{E}_o \chi_s E_o$) then $E_* = E_o$.

The analysis of data in terms of Eq. [62] requires numerical integration to obtain q_c'. If we consider the special case of constant field, the charging current may be obtained as an explicit function of time. Accordingly, differentiation of Eq. [58] with respect to time yields

$$i_c = 2DA_c\, e^{-gt}/(1 - D^2\, e^{-2gt}) \qquad [63]$$

where

$$D = \tanh \left[\frac{w_e^*}{2kT} \left(\frac{\mu_s^* - \mu_1^*}{\mu_s^*} \right) (E_o - E_*) \right]$$

and E = a constant = E_o. An equation somewhat more convenient for fitting to empirical data is obtained by solving for e^{gt} and taking logarithms. The resulting equation is

$$\ln \left[\frac{|i_c/A_c|}{(1 + i_c^2/A_c^2)^{1/2} - 1} \right] = gt - \ln |D| \qquad [64]$$

Summary and Discussion

A theory of cooperative ion migration in valve metal oxide films has been developed on the basis of a dielectric mosaic model of the film. The cooperative phenomena arise then as a result of time dependent polarization properties of the oxide film. Thus the ion current leading to film growth depends not only on the applied field strength and temperature but also on the polarization of the medium. The transient conduction properties of these systems are therefore determined by the kinetics of the polarization processes.

In addition to conventional "fast" polarization processes, for this model a "slow" polarization process, associated with ionic migration within a single mosaic component (crystallite or polymeric unit) must exist. Two independent mechanisms for the kinetics of the slow polarization process have been proposed; the "high ion current mechanism" in which the change in the slow component of the polarization is induced by the transfer of ions from one polymeric unit to the next and the "low ion current mechanism" in which the ionic migration within the polymeric units takes place by a conventional high field ionic conduction process. The terms "high" and "low" are of course only relative, implying correctly that at sufficiently high ion current densities, for a given temperature, one mechanism will predominate, while the other will predominate at sufficiently low ion current densities. For a given range of ion current densities, the low ion current mechanism should predominate at sufficiently high temperatures, and vice-versa.

In discussing the model it is convenient to consider steady-state and high ion current conditions separately from low ion current conditions.

For steady-state conditions, the following kinetic parameters are required to define the behavior of the system: a pre-exponential factor, i_o, an activation energy, ϕ, an effective charge-activation distance product, μ_s^*, and a parameter, C, to allow for the nonlinear dependence of the net activation energy on the field strength. A precisely analogous set of parameters is required for the high field Frenkel defect theory (14). For high ion current transient experiments, the present model required an additional two parameters; another effective charge-activation distance product, μ_1^*, and a constant, B, related to the cross-sectional area of a polymeric unit. For similar experiments, the high field Frenkel defect theory requires three additional parameters; parameters analogous to μ_1^* and B, plus an additional parameter similar to C of the present model (5).

As the high field Frenkel defect model does not predict anything analogous to the low ion current phenomena predicted by the present model, comparison in this area is not really possible. However, in order to predict conduction phenomena associated with annealing experiments (4, 5), the Frenkel defect theory requires a knowledge of an additional activation energy and another exponential factor. The present model is extended to cover these phenomena and also phenomena relating to low ion currents by the addition of three new parameters; a pre-exponential factor, i_{co}, an activation energy, Q, and an effective charge-activation distance product, w_e^*. The present model therefore involves, in total, the same number of disposable constants as does the Frenkel defect theory, so that agreement with data is not achieved simply by introducing more disposable constants. As most of the data presently available in fact are concerned with high ion current conditions (10), the present theory generally involves one less disposable constant.

Apart from the obvious tests which can be applied to most theories (*i.e.*, that they lead to functional forms in agreement with data and to reasonable values for the parameters) the present model offers two additional checks for internal consistency. The parameter, C, can be determined from both steady-state (Eq. [36]) and transient (Eq. [41] Tafel slope measurements. The parameters μ_s^* *and* μ_1^* can be evaluated from high ion current measurements (Eq. [36] and [41], respectively), with the ratio μ_s^*/μ_1^* also being obtainable from charging current measurements, since

$\mu_s^*/\mu_1^* \simeq K_s/K_1$, the ratio of the static to dynamic dielectric constant.

The parameters i_o, ϕ, μ_s^*, and C are most readily obtained from steady-state measurements (Eq. [34]); the parameter μ_1^* from high ion current measurements for conditions of rapidly changing field (Eq. [41]); and the parameter B from constant field transients for high ion current conditions (Eq. [55] or [56]). The remaining three parameters, i_{co}, Q, and w_e^* can be obtained from charging current measurements for fields sufficiently low so that the ion current is essentially zero (Eq. [62] and [64]).

In the following paper (10) the model is discussed in relation to existing theories and presently available data.

Acknowledgments

The author wishes to express his appreciation to Dr. J. P. Valleau for reading the manuscript and for many useful discussions.

Manuscript received Nov. 24, 1964. This paper was presented in part at the Pittsburgh Meeting, April 15-18, 1963.

Any discussion of this paper will appear in a Discussion Section to be published in the June 1966 JOURNAL.

REFERENCES

1. B. Verkerk, P. Winkel, and D. G. de Groot, *Philips Research Repts.*, **13**, 506 (1958).
2. G. Amsel and D. Samuel, *J. Phys. Chem. Solids*, **23**, 1707 (1962).
3. J. A. Davies and B. Domeij, *This Journal*, **110**, 849 (1963).
4. D. A. Vermilyea, *ibid.*, **104**, 427 (1957).
5. L. Young, *Proc. Roy. Soc.*, **A263**, 395 (1961).
6. M. J. Dignam, *This Journal*, **109**, 184 (1962).
7. P. J. Ryan and M. J. Dignam, *Can. J. Chem.*, **40**, 1875 (1962).
8. M. J. Dignam and P. J. Ryan, *ibid.*, **41**, 3108 (1963).
9. L. Young, "Anodic Oxide Films," Chap. 3, Academic Press, London (1961).
10. M. J. Dignam, *This Journal*, **112**, 729 (1965).
11. A. F. Wells, "Structural Inorganic Chemistry," p. 37, 2nd ed., Oxford University Press (1952).
12. M. J. Dignam, *Can. J. Chem.*, **42**, 1155 (1964).
13. F. S. Stone, "Chemistry of the Solid State," Chap. 2, Edited by W. E. Garner, Butterworth's Scientific Publications (1955).
14. L. Young, *Proc. Roy. Soc.*, **A258**, 496 (1960).

Conduction Properties of Valve Metal-Oxide Systems

II. Comparison of Data with New Theory

M. J. Dignam

Department of Chemistry, University of Toronto, Toronto, Ontario, Canada

ABSTRACT

Data from the literature for the anodic oxidation of a number of the valve metals have been analyzed in terms of the dielectric polarization theory of ionic transport, developed in Part I, and previous theories. The unique predictions of this theory were found to be in excellent accord with the data.

In the preceding paper (1) a theory of cooperative ion transport has been developed and equations appropriate to various experimental conditions derived. The purpose of the present paper is to test this theory against available data and compare its predictions with those of other theories. In respect to the latter, special attention will be paid to the high field Frenkel defect theory, proposed originally by Bean, Fisher, and Vermilyea (2) as this is the only other theory capable of describing, even qualitatively, most of the observed phenomena. Very briefly, in this theory the transient ionic conduction phenomena are attributed to a slow adjustment of the field dependent population of Frenkel defects to a change in the field. A detailed description of this model and others can be found elsewhere (3).

The theory and available data will be discussed under the headings: Steady-State Data, Tafel Slope Data, Constant Field Transients, and Space Charge Effects.

Examination of Available Data

Steady-state data.—The conventional empirical equation used to fit steady-state ionic conduction data can be written

$$I = \alpha \exp \beta E \qquad [1]$$

where α contains the Boltzmann factor for the zero field activation energy. In most previous theoretical treatments, β is predicted to have the form aq/kT where a is an activation distance or mean activation distance for the field assisted displacement of an ion of charge q.

In relation to Eq. [1], three kinds of anomalous behavior have been observed:

1. For zirconium, the parameters α and β have been found by Young (4) to depend on the thickness of the anodic film. The data for tantalum (5), aluminum (6), niobium (7), bismuth (8), and titanium (9) show no such anomaly for films thicker than about 100Å.

2. The Tafel slope, $(d \ln I/dE)_T$, has been found to vary more slowly with the absolute temperature than predicted by setting $\beta = aq/kT$, for both tantalum (5, 10) and niobium (7). For titanium, β appears to decrease more rapidly than $1/T$ with increasing temperature. Sufficiently accurate data are not available for other valve metals to check the temperature dependence of β.

3. For both tantalum (5) and aluminum (6) a variation of the Tafel slope with field strength at a given temperature has been observed. The data for other valve metals are not sufficiently precise to allow this observation to be made.

With regard to the first anomaly, zirconium appears to be unique among the valve metals in displaying film thickness dependent kinetic behavior for films thicker than about 100Å. This suggests either that additional complicating factors are present (for example film inhomogeneity) or that a different mechanism is involved. Young has suggested (4), and indeed it appears not unreasonable, that zirconium oxidizes anodically in accord with Dewald's two barrier model (11). The difficulty with this model, however, is that it requires no less than six disposable constants to define steady-state behavior, while Young's generalization of the model involves at least seven disposable constants (12). With such flexibility, agreement between data of limited scope, such as steady-state data, is almost guaranteed regardless of the validity of the model. Nevertheless, this model must be regarded as a possibility in connection with the anodic oxidation of zirconium.

Dewald's model has also been applied to the steady-state anodic oxidation of tantalum (10, 13) and niobium (14) with the purpose of explaining the Tafel slope anomalies mentioned above. With the exception that the dependence on thickness predicted by this model has never been detected, the Tafel slope anomalies were accounted for quantitatively. Once again, however, it must be emphasized that this improvement over Eq. [1] is gained by introducing three new parameters, for a total of six. By contrast, Eq. [13] of the previous paper (1), reproduced below for convenience, is also able to account for the Tafel slope anomalies for the above metals and for aluminum (15) with the addition of only one positive parameter, *C*.

$$I = i_o \exp\left\{ - \left[\phi - E\mu_s^* \left(1 - \frac{E\mu_s^*}{C\phi}\right)\right] / kT \right\} \quad [2]$$

An equation of the form of [2] was first suggested by Young (5) on empirical grounds. He later justified the presence of a quadratic term in the field on the basis of a postulated variation of activation energy with the condenser pressure (16). In a recent paper by the author (15) it is pointed out that the condenser pressure effect is probably too small to explain the observed phenomena. Further, it is shown that the quadratic term arises quite naturally from a more detailed consideration of ion transfer processes at high electrostatic fields. Specifically, it was shown that not only the form of Eq. [2], but also the empirical values for *C* for Ta, Nb, and Al are predicted correctly by assuming that the interaction potential between the mobile ion and its immediate surroundings can be represented by a Morse function for small displacements. If one accepts the Morse function postulate, *C* is not an independent constant, so that the Tafel slope anomalies for Ta, Nb, and Al may be explained quantitatively without increasing the number of disposable constants above three. It would appear, therefore, that Eq. [2] represents a far more satisfactory explanation for the Tafel slope anomalies than does Dewald's model, at least in the cases of Ta, Nb, and Al, particularly since Dewald's model does not lend itself readily to explaining even qualitatively the transient conduction phenomena observed for the anodic oxidation of these metals.

It should be emphasized at this point that Eq. [2] cannot be regarded as specific to the theory developed in the preceding paper. An essentially identical equation can be expected for the Mott-Cabrera theory (17), the high field Frenkel defect theory, or Verwey's theory (18). The only way in which the present theory can be regarded as in any way unique in relation to Eq. [2] is that a Morse function interaction potential is more in accord with the new theory than it is with the other theories mentioned. Indeed, the ion transfer process from one molecular unit to the next would appear to be not unlike the dissociation of a diatomic molecule.

The Tafel slope anomaly for titanium cannot be interpreted in the same way as that for Ta, Nb, and Al, since the effect, being in the opposite direction, requires a negative value for *C*. A negative value for *C* can be explained in terms of a range or distribution of values for the activation energy and activation distance, as outlined by Young (5). However, an equally probable explanation of the titanium results would be that the current efficiency for formation of the film decreases with increasing temperature and decreasing current density. A further explanation is that the theory of the previous paper is applicable, but that μ_s^* decreases with increasing temperature as a result of a variation of χ_s, the static electric susceptibility, with temperature. A re-examination of titanium using the optical techniques developed by Young should resolve this uncertainty.

The situation is, therefore, that Ta, Nb, and Al give data in agreement with Eq. [2] where the values of *C* are in accord with that predicted on the basis of a Morse interaction potential; the data for Bi (8) are also consistent with this equation although of insufficient precision to verify the term in *C*; the data for Ti are uncertain since the current efficiency for film formation is unknown; and finally, the data for Zr are definitely not in accord with this equation. Accordingly, in this paper we shall be concerned primarily with the behavior of Ta and Al, for which the major amount of data are available, and to a lesser extent Nb and Bi. The data for other metals or semimetals which exhibit valve metal film forming properties are not sufficiently complete or precise to distinguish between alternative mechanisms.

A brief comment on the magnitude of the parameters found experimentally is relevant at this point. For Ta, Young (5) obtained a value for μ_s^* (*qa* in his notation) of 35 eÅ which on choosing the maximum possible effective charge on the mobile ion, + 5e gives an effective activation distance of 7Å, an extremely large value. If we assume a value for *C* for the anodic oxidation of Bi of the same order as that found for Ta, Nb, and Al (*i.e.*, about 3.3) then a value of 129 eÅ for μ_s^* may be calculated from Young's data (8). In this case, the value for the effective activation distance is no less than 43Å. Even without making any allowance for the covalent bonding in these oxides (which would be expected to lead to effective changes appreciably less than +5e and + 3e, respectively) it is seen that these values for μ_s^* are very much too large to be equated to the product of a charge and activation distance. The other valve metals also give high values for the steady-state effective activation dipole, μ_s^*. These high values are immediately explained in terms of the new theory, since $\mu_s^* = (1 + \delta\chi_s)\mu^*$ where μ^* is the "true" activation dipole, χ_s the static electric susceptibility of the oxide, and δ a geometric factor of the order of unity. A more quantitative consideration of this matter will be reserved for the following section. At this point, however, it is worth noting that the suggestion that the field effective in causing ion migration is greater than the applied field is by no means a new one. Indeed in 1941, Maurer (19) explained the temperature dependence of the ionic conduction of glasses on the assumption that the effective field was given by the static dielectric constant times the applied field. The point was first raised in connection with anodic oxide films by Young (20) in 1954. Until now, however, this concept has received very little attention.

Perhaps the most serious limitation of all previous theories lies in their failure to account for the recent data (21-25) regarding anionic and cationic transport in certain valve metal oxides. I wish to draw particular attention to the excellent work of Davies and colleagues (21-23) in which using β-spectroscopy in conjunction with Xe^{125} and Rn^{222} marker experiments, they were able to evaluate the transport numbers appropriate to the anodic oxidation of Al, W, Ta, and Zr. The anionic transport numbers were found to be (23) for Al_2O_3 0.45 ± 0.5; for WO_2 and Ta_2O_5 0.65 ± 0.04; and for ZrO_2 0.99 ± 0.01. In addition the transport numbers for Al_2O_3 were found to be independent of current density over the range 10^{-4} to 10^{-2} amp/cm^2, with a similar result found for WO_2 and ZrO_2. The effect of current density on transport numbers for Ta_2O_5 had not been investigated at the time this paper was prepared.

For previous theories to be compatible with these data, one must first assume that the activation dipole for anionic and cationic defects present in the film are nearly identical, since the transport numbers are independent of field strength. Next, since pre-exponential factors will be comparable for all defects, one must assume that the zero field activation energies for migration of the anionic and cationic defects are nearly the same. Such postulates if proposed to explain the results for only a single metal-oxide system should be regarded with great scepticism and must be considered entirely out of the question when required to explain the data for more than one metal oxide system. Indeed, if any of the previous theories are to be accepted even tentatively, one is forced to reject the validity of the transport number data.

Let us now examine the data of Davies and collaborators in terms of the newly proposed theory. The transport numbers will be determined largely by the fraction of the charge carried through the individual molecular units by anions and cations, respectively, since the gap between molecular units is presumably quite small compared with the dimensions of such units. Immediately following an ion transfer event, the donor and acceptor molecular units will be depolarized. To re-establish their equilibrium dipole moments, ion migration in each is required. In general one would expect both anionic and cationic defects to be produced in a somewhat random manner in the two molecular units by the highly exoenergetic ion transfer process. As the impact energy for ion transfer will be very nearly independent of current density, no significant dependence on current density would be expected. From this model we deduce, therefore, transport behavior, in accord with the above data. The theory is also in accord with the transport data presented in a recent paper by Amsel and Samuel (25) and an earlier paper by Verkerk, Winkel, and Groot (24).

Tafel slope data.—Two kinds of Tafel slope determinations have been made on a number of the valve metal-oxide systems: steady-state Tafel slopes, evaluated from the steady-state relation between current and field strength, and transient Tafel slopes, obtained from the relation between current and field strength when the field (or current) is changed very rapidly. The steady-state and transient reciprocal Tafel slopes, β_s and β_1, respectively, are given by Eq. [36] and [40] (or [41]) of the previous paper

$$\beta_s = \underset{\dot{E} \to 0}{\text{Limit}} \frac{d \ln I}{dE} = \frac{\mu_s{}^*}{kT}\left[1 - \frac{2\mu_s{}^* E}{C\phi}\right] \qquad [3]$$

$$\beta_1 = \underset{\dot{E} \to \infty}{\text{Limit}}$$

$$\frac{d \ln I'}{dE} \simeq \left(\frac{\Delta \ln I'}{\Delta E}\right)_{\Delta t \to 0} \simeq \frac{\mu_1{}^*}{kT}\left[1 - \frac{2\mu_s{}^* E_o}{C\phi}\right] \qquad [4]$$

where the approximations amount to neglecting $\mu_1{}^*\Delta E/C\phi$ compared with unity and a further small term, cf (1) Eq. [40] and following.

From the excellent data of Young (5, 26), the field dependence of the Tafel slopes for the tantalum system are represented by the following equations

$$\beta_s\, kT = 34.98\ (1 - 9.58E)\ e\text{Å} \qquad [5]$$

$$\beta_1\, kT = 11.15\ (1 - 9.50\, E_o)\ e\text{Å} \qquad [6]$$

The manner in which β_1 was determined was such that $\Delta E << E$ so that the approximations contained in Eq. [4] are justified in this instance. We now note that the empirical coefficients of E and E_o in the above expressions are the same well within experimental error, as predicted by Eq. [3] and [4]. The same agreement within experimental error has been found for aluminum from recent data obtained in this laboratory (6, 27). Unfortunately, however, we have as yet been unable to obtain the coefficient of E_o in the expression for the transient Tafel slope any more accurately than ± 30%. Data of sufficient precision to test this prediction for other value metals are lacking at present.

On the basis of previous theories, and in particular the high field Frenkel defect theory, the agreement between the coefficients of E and E_o (Eq. [5] and [6]) must be regarded as entirely fortuitous, whereas it is a specific prediction of the present theory.

It is of interest at this point to show how χ_s may be estimated from Tafel slope data. If complete data are available, $\mu_s{}^*$ and $\mu_1{}^*$ can be determined from β_s and β_1 *vs.* E and E_o, respectively, from which one obtains

$$(\delta\chi_s + 1)/(\delta\chi_1 + 1) = \mu_s{}^*/\mu_1{}^*$$

or assuming $\chi_s >> (1/\delta - 1)$ and $\chi_1 >> (1/\delta - 1)$,

$$\mu_s{}^*/\mu_1{}^* \simeq K_s/K_1 \qquad [7]$$

where K_s and K_1 are the static and dynamic dielectric constants. Using standard a-c capacitance data at sufficiently high frequencies (1000 cps would appear to be sufficiently high) the dynamic dielectric constant can be calculated and thence an estimate of the static electric susceptibility, χ_s, or static dielectric constant, K_s, obtained from $\mu_s{}^*/\mu_1{}^*$. If data for the variation of the Tafel slopes with field strength are not available, then for measurements such that $E \simeq E_o$ and ΔE small, it follows that

$$\beta_s/\beta_1 \simeq \mu_s{}^*/\mu_1{}^* \simeq K_s/K_1$$

To date, no independent determinations of K_s are available to test the validity of Eq. [7].

One of the more fundamental predictions of the present theory is that the transient Tafel slope and conventional dynamic dielectric constant are related, since

$$\mu^* = \mu_1{}^*/(1 + \delta\chi_1) \text{ or } \delta\mu^* = \mu_1{}^*/(1/\delta + \chi_1) \simeq \mu_1{}^*/K_1$$

$$[\text{for } K_1 >> (1/\delta - 1)]$$

If oxygen ions are the ones involved in the ion transfer process for all the valve metal systems, then $\delta\mu^*$ should not differ greatly from one system to the next, so that $\mu_1{}^*/K_1$ will be approximately a constant. The variation in ionic character, bond strength, and structure will of course introduce some variation in $\mu_1{}^*/K_1$. The real justification for assuming oxygen ion transport between crystallites is, of course, that this postulate is in accord with the results. However, a reasonable case can be made for this postulate simply on the basis of the proposed model. Since the oxides are partially ionically bonded, the radius of the oxygen species will be appreciably larger than that of the metal species. The oxygen "ions" will therefore stand out from the surface of the crystallites, in relation to the metal "ions," so that the effective field at the oxygen ions should be somewhat higher. The higher polarizability of the anionic species should also favor oxygen ion transport between crystallites rather than cation transport.

Table I lists values of μ_1/K_1 for the systems tantalum, aluminum, niobium, and bismuth and their respective oxides. Young's values for $\mu_1{}^*$ (26) and K_1 (28) for Ta_2O_5 are reported, along with the corresponding values for Al_2O_3 obtained recently in the author's laboratory (27). In a previous publication (15) Young's data (7) for Nb_2O_5 were used to calculate $\mu_s{}^*$. Combining this result with Young's value for K_1 (29) and Vermilyea's (30) determination of $\mu_s{}^*/\mu_1{}^* = 2.1$ ($q\lambda$ effective/$q\lambda$ initial, in his terminology) gives the required values of $\mu_1{}^*$ and K_1 for Nb_2O_5. Young's data for Bi_2O_3 (8) provides values for β_s, β_1, ψ, and K_1. Since the quadratic parameter, C, is nearly the same for Ta_2O_5, Nb_2O_5, and Al_2O_5 (15), $\mu_1{}^*$ for Bi_2O_3 was calculated from Eq. [4] and [5] assuming $C \simeq 3.3$.

As predicted, the values of $\mu_1{}^*/K_1$ in Table I show much less variation than do the values of either $\mu_1{}^*$ or K_1 individually. Furthermore, the variation in $\mu_1{}^*/K_1 \simeq \delta\mu^*$ can be explained qualitatively on the assumption that it is due primarily to a variation in the effective charge on the oxygen "ion" from oxide to oxide. Thus the oxides in which the metal is in an

Table I. Relation between transient activation dipole and dynamic dielectric constant

Oxide	$\mu_1{}^*$ eÅ	K_1	$\mu_1{}^*/K_1 \simeq \delta\mu^*$ eÅ
Ta_2O_5	11.1_5	27.6	0.40
Nb_2O_5	16	41.4	0.39
Al_2O_3	7.8	8.8_5	0.88
Bi_2O_3	40	62	0.65

oxidation state of +3 should involve a higher proportion of ionic *vs.* covalent bonding than those involving a metal oxidation state of + 5, so that μ^* for Al_2O_3 and Bi_2O_3 should be appreciably greater than μ^* for Ta_2O_5 and Nb_2O_5. Between Ta_2O_5 and Nb_2O_5, according to the usual variation with ionic size, Ta_2O_5 should be slightly more ionic (31). The argument favoring more ionic bonding for Al_2O_3 than for Bi_2O_3 rests on the fact that the first ionization potential for Al is 1.3 ev lower than that for Bi (32).

Finally, as a check on the reasonableness of the magnitudes of the kinetic parameters μ_1^* and μ_s^*, we shall attempt to estimate the magnitude of the effective activation distance. From the crystal lattice parameters, Wells (33) estimates that the bonding in α Al_2O_3 is about 50% ionic. Assuming about the same proportion of ionic bonding is involved in the anodically formed oxide, we may estimate the effective charge on the oxygen species in Al_2O_3 to be about 1e. This leads to an effective activation distance at zero field strength of about $0.9/\delta$ Å, which for $\delta \simeq 1$ is an eminently reasonable value. It is tempting to suggest that this calculation justifies choosing a value for δ of about unity, however, the assumptions involved in this estimate are sufficiently bold to make such a proposition somewhat hazardous. Nevertheless, the calculation does indicate that the values of μ_1^* are of the correct magnitude.

In summary, the Tafel slope data for Ta, Nb, Al, and Bi are in complete accord with the theory presented in the previous paper. It would be very difficult to rationalize the data of Table I on the basis of any previous theory.

Constant field transients.—Measurements of transient conduction phenomena under conditions of very nearly constant field strength have been made by Young (26) on tantalum and in the author's laboratory on aluminum (27). Typical examples of these data are reproduced in Fig. 1 and 2. Young's data were obtained by heating a previously anodized sample to 100°C for a few minutes then returning it to the cell, applying suddenly an appropriate constant voltage and recording the current for the first few seconds. Our measurements were made following thermal treatment both for 1 hr at 60°C and for a few minutes at room temperature. The voltage was not applied suddenly but increased to its final value at a rapid linear rate, as shown in Fig. 2.

There are several points of interest in these curves which we shall discuss primarily with reference to Fig. 2. The initial upswing in the current during the voltage build-up stage and the fall in current immediately after the voltage becomes constant cannot be explained by any previous theory, except by postulating fissures in the anodic film as Young has done (26). On the present theory, such charging currents are to be expected and represent strong evidence in support of an anomalous polarizing process which we have referred to as the transport polarization process.

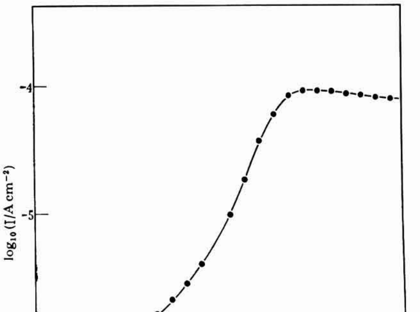

Fig. 1. Young's data for tantalum (26). Logarithm of the current density, *I*, as a function of time on reapplication of a fixed anodic potential.

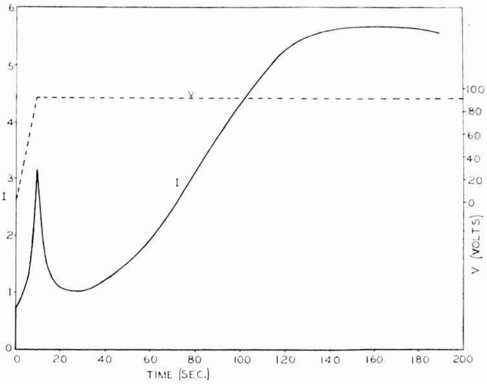

Fig. 2. Current density, *I* ($\mu a\ cm^{-2}$) as a function of time for aluminum on reapplication of anodic potential, *v*, as illustrated.

A second point of interest is the fact that, apart from the present theory, there exists no quantitative theory even for the shape of the curves beyond the point where the anomalous charging currents will make a significant contribution. The high field Frenkel defect theory predicts a curve shape (log *I vs. t* or *I vs. t*) which is at all times concave downward, as pointed out by Young (26), whereas experimentally (Fig. 1 and 2) the curves are at first distinctly concave upward. It has previously been suggested to the author that effects such as these are likely brought about as a result of structural changes during thermal treatment, but all these same features have been observed in the author's laboratory for aluminum samples which have been merely held at room temperature and zero applied voltage for a minute before re-applying the voltage. Such an explanation, therefore, seems improbable.

Before attempting a quantitative fit of these transient measurements to the present theory, it is worthwhile to give a qualitative description, in terms of the present theory, of the processes occurring over the various regions of Fig. 2.

On applying the linearly increasing voltage, the conventional charging current rapidly achieves its constant value of $\mathcal{E}_0 K_1(dE/dt)$, giving rise to the initial current jump. This is then followed by the more sluggish build-up of the "anomalous" charging current, dP_2/dt, under conditions where the growth current, i, is negligible, so that the collision process is not contributing to dP_2/dt. This initial build-up of the charging current should be given by Eq. [62] of the previous paper, from which we see that the current should rise approximately according to a hyperbolic sine function of the voltage, in qualitative agreement with the observed shape. When the voltage rise is stopped, the polarization of the medium is still well below the equilibrium value for the applied field, so that E_e is still too small to produce a significant number of ion transfer events. The total current observed is therefore still only the charging current, which should drop abruptly by an amount $\mathcal{E}_0 K_1(dE/dt)$, equal to the initial abrupt rise, then decay approximately as a negative exponential of the time, according to Eq. [63] of the previous paper. Unfortunately, the slow response of the recorder used did not permit the resolution of the initial fast drop from the subsequent decay.

Up to about 200 sec, therefore, the polarization of the medium, and hence the effective field, E_e, has been increasing almost exclusively by the thermally activated polarization process, the effective field being too small to cause a significant number of ion transfer events to take place. Somewhat after 20 sec, however, the growth current starts to become of significance, so that by 30 sec the rate of increase of the growth current effected by the increasing polarization of the medium has more than overcome the rate of fall of the thermally activated component of the charging current. From about 30 sec onward, the thermally activated polarization process becomes negligible compared with the collision induced process and the charging current small compared with the growth current, i. As the growth current increases, it increases the rate of change of the polarization of the medium, and hence of E_e, thus increasing the rate of increase of i and producing the concave upward portion of the curve from 30 to 80 sec. Ultimately, this "autocatalytic" process is overcome as the polarization of the medium approaches its steady-state value, leading to the rounding off from 80 to 140 sec. The decrease in current beyond 160 sec is caused by the slow fall in the applied field resulting from the slow film growth.

The data relating to the charging current are not sufficiently accurate to warrant quantitative treatment. Measurements are now being undertaken in this laboratory to test this aspect of the theory. We shall at present analyze quantitatively only that part of the data for which the thermally activated component of the charging current can be neglected. The correct equation for these conditions, Eq. [55] of (1), is recorded below

$$1/I = 1/I_o - B\int_0^t \ln(I_s/I)\,dt \qquad [8]$$

where I_o is the current density at $t = 0$, and I_s is the steady-state current density.

In Figure 3, the data for aluminum are plotted according to Eq. [8] for the experimental points lying between about 30 and 150 sec. In order to illustrate more clearly the quality of the agreement between the data and Eq. [8], the data for tantalum have been plotted in Fig. 4 according to a rearranged form of Eq. [8], *viz.*

$$F = [1/I - B\textstyle\int_0^t \ln(I/I_o)\,dt] = 1/I_o - [B\ln(I_s/I_o)]t \quad [8']$$

Both these sets of data are in excellent accord with Eq. [8] and hence with the present theory. The values of B calculated from the slopes are 8.0 x 10^3 cm^2/coulomb for tantalum and 11.4 x 10^3 cm^2/coulomb for aluminum. A number of values for aluminum have been obtained which are in agreement to about ± 5%. From the theory we have

$$B = (\sigma'/Ze)(1 + \delta'\chi_1)/(1 + \delta'\chi_s) \simeq (\sigma'/Ze)(\mu_1{}^*/\mu_s{}^*)$$

since

$$(1 + \delta'\chi_1)/(1 + \delta'\chi_s) \simeq (1 + \delta\chi_1)/(1 + \delta\chi_s) = \mu_1{}^*/\mu_s{}^*$$

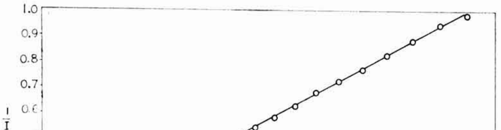

Fig. 3. Data of Fig. 2, plotted according to Eq. [8] (I in μa cm^{-2}, t in sec).

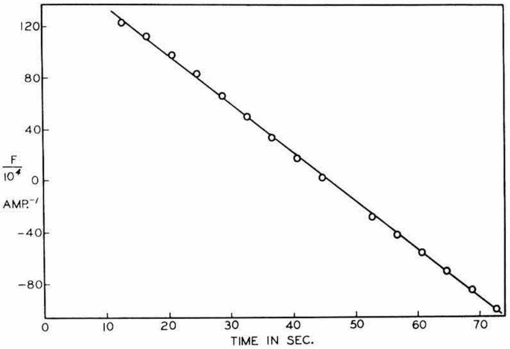

Fig. 4. Data of Fig. 1 plotted according to Eq. [8′]

for $\chi_1 >> 1/\delta'$ and $1/\delta$, or $\delta' \simeq \delta$. Setting $Z = 2$ we then obtain $\sigma'^{1/2} = 8.9$Å for tantala and 11Å for alumina. On the reasonable assumption that the crystallites should contain at least one unit cell and be sufficiently small to give rise to the observed diffuse diffraction patterns, $\sigma'^{1/2}$ should lie between about 4 and 20Å, in excellent accord with the above values.

From the experimental value for the pre-exponential factor for the tantalum system, $i_o = 1.7_4$ x 10^8 amp/cm^2 (5), and the theoretical form for i_o, cf. Eq. [14] in (1), it follows that

$$1.7_4 \times 10^8\ (\mathrm{amp/cm^2}) = ZeN'\nu/\sigma \simeq N'\nu\mu_1{}^*/\mu_s{}^*B$$

On substituting the empirical values for $\mu_1{}^*/\mu_s{}^*$ and B we obtain $N'\nu \simeq 4 \times 10^{12}$ sec^{-1}, an eminently reasonable result since N', the number of charged species per molecular unit located at suitable sites for transfer to the next molecular unit, would be expected to be close to unity.

Since B contains a molecular unit dimension parameter, it is entirely possible that it will vary somewhat with film formation conditions. A thorough investigation to look for such an effect has not as yet been carried out but the present results (27) indicate that a variation in B of 20% or more can be effected by the choice of formation current density.

As stated previously, the data relating to the "anomalous" charging current are not sufficiently accurate to warrant quantitative treatment. A computer calculation to generate the entire experimental curve shown in Fig. 2, starting from Eq. [1], [13], [30], and [32] of the previous paper, has, however, been carried out. The result of this calculation was good qualitative, but not quantitative agreement with the experimental data. The failure to achieve a quantitative fit was traced to the form chosen for the "anomalous" charging current, dP_2/dt, *i.e.*, final term Eq. [30] of (1) or final term Eq. [24] of (1). It appears that the variation of dP_2/dt with E is in accord with Eq. [30] of (1) since the initial build-up of the charging current could be fitted well and for reasonable values of the parameters ($w_e{}^* \simeq 1.6$ eÅ and $Q \sim 0.8$ ev). The decrease of dP_2/dt from the peak under conditions of constant E, however, are not in accord with Eq. [30] of (1). The present equations appear to predict the wrong functional dependence of the anomalous charging current on P_2 or P. In view of the approximations made in deriving the equation for the thermally activated polarization process, this is not too surprising. It is felt, however, that this aspect of the theory can be substantially improved without altering the basic model. Efforts in this direction are now under way.

Influence of space charge on steady-state anodic oxidation.—As mentioned in the previous paper, Eq. [10] and hence Eq. [19] of the previous paper are only valid in a region of the film where the space charge is negligible. We shall now investigate the influence of

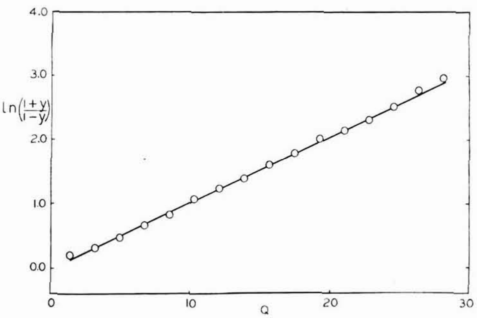

Fig. 5. Space charge data for aluminum (34) plotted according to Eq. [15]. (Q is charge passed in mcoul/cm^2).

space charge for steady-state anodic oxidation conditions.

From Eq. [7] and [9] of the previous paper and Poisson's equation, and assuming $\kappa_{+r} >> \kappa_{-r}$ we may write

$$i = ZedN + r\kappa p_o \qquad [9]$$

$$n_{+r}n_{-r} = n_o^2/f\kappa = n_\infty^2 \qquad [10]$$

$$dE/dx = (n_{+r} - n_{-r})Ze/\mathcal{E} \qquad [11]$$

where $\kappa \simeq \kappa_{+r}$, $\mathcal{E}$ is the permittivity of the oxide ($K_s\epsilon_o$ for steady-state conditions), n_∞ the value of n_{+r} and n_{-r} beyond the space charge zone and x the distance into the oxide measured from the interface away from which the species of charge rZe move. The assumption $\kappa_{+r} >> \kappa_{-r}$ (or the converse) is required to obtain agreement with the data and would appear to be justified providing the molecular units are sufficiently small. Since $\sigma' \simeq 100Å^2$, we may assume a radius for a molecular unit of about 5Å and a nuclear separation between surface oxygen species on adjacent molecular units of about 2Å. The ratio of the two field terms (1), $\mathcal{E}_{+r}$ and $\mathcal{E}_{-r}$, should then be given approximately by $(\mathcal{E}_{+r}/\mathcal{E}_{-r}) \sim (5 + 2)^2/5^2 \simeq 2$. Therefore for $\kappa_{+r} \simeq 10^6$ (the value consistent with the experimental data reported below), $\kappa_{-r} \sim (10^6)^{1/2} = 10^3$ so that $\kappa_{+r}/\kappa_{-r} \sim 10^3$.

Returning to Eq. [9] to [11], we can write

$$dE/dx = (y - 1/y)Zen_\infty/\epsilon \qquad [12]$$

where $y = p_{o\infty}/p_o$ and $p_{o\infty}$ is the value of p_o beyond the space charge zone. Since we shall consider only steady-state conditions y is given by

$$y = \frac{\exp\left[E_\infty\mu_s^*(1 - E_\infty\mu_s^*/C\phi)/kT\right]}{\exp\left[E\mu_s^*(1 - E\mu_s^*/C\phi)/kT\right]}$$

or

$$y = \exp\left[\overline{\beta_s}(E_\infty - E)\right] \qquad [13]$$

where

$$\overline{\beta_s} = \frac{\mu_s^*}{kT}\left[1 - \frac{(E_\infty + E)\mu_s^*}{C\phi}\right]$$

and E_∞ is the field beyond the space charge zone, $\overline{\beta_s}$ is the steady-state reciprocal Tafel slope for thick films (*i.e.*, thicker than the space charge zone) measured at a field strength $(E_\infty + E)/2$ (see Eq. [3]). Since the small variation in the Tafel slope with field strength is only just detectable, taking $\overline{\beta_s}$ independent of field will be a satisfactory approximation for E close to E_∞.

Using the above expression for y and making the approximation that $\overline{\beta_s}$ is constant, Eq. [12] can be written

$$dy/dS \simeq (1 - y^2)/2 \qquad [14]$$

where

$$S = (2\overline{\beta_s}Zen_\infty/\mathcal{E})x$$

Integrating this equation we obtain

$$\ln[(1 + y)/(1 - y)] = S + S_o \qquad [15]$$

where S_o is the integration constant, so that a plot of $\ln[(1 + y)/(1 - y)]$ *vs.* distance from the appropriate interface should yield a straight line of slope $(2\overline{\beta_s}Zen_\infty/\mathcal{E})$. The space charge data previously published for aluminum (34) is plotted in Fig. 5 according to Eq. [15]. Differential field strengths as a function of charge passed were calculated from measurements of the time derivative of the anodic overpotentials as a function of charge passed. Details of the experimental procedure and assumptions involved in interpreting these data can be found in the original paper. However, it is worth pointing out that the assumptions are consistent with the present model.

As can be seen, the data fall on an excellent straight line. In the original paper it was shown that the slope of such plots was independent of current density, a result in conflict with the basic postulate of the high field Frenkel defect model and probably in conflict with any model which predicts a significant dependence of the bulk defect concentration on current density. Such a result, however, is in accord with the predictions based on the present model.

The slope of the graph was found to be $1.0_4 \times 10^2$ coulomb^{-1}, which for an oxide density of 3.2 g/cm^3 (35) corresponds to $1.8_6 \times 10^6$ cm^{-1}. Comparing this with the theoretical slope and setting $\overline{\beta_s} = 4.8 \times 10^{-6}$ cm/v (35), $\mathcal{E} = K_s\mathcal{E}_o \simeq (\beta_s/\beta_1)K_1\mathcal{E}_o \simeq 25.8\ \mathcal{E}_o$ (27), and $Z = 2$, we obtain $n_\infty = 1.4 \times 10^{18}$ cm^{-3}. Estimating n_o as follows: $n_o \simeq (\sigma')^{-3/2} \simeq 1.3 \times 10^{21}$ cm^{-3}, we have $n_\infty/n_o \simeq 10^{-3}$, a reasonable result.

We can obtain an estimate of $\mathcal{E}_r = \mathcal{E}$ in the following manner. From Eq. [10], $\kappa = (n_o/n_\infty)^2/f \simeq 10^6$. From Eq. [12], [15], [16], and [17] of the previous paper, it can be shown that

$$\ln\kappa \simeq \frac{\mathcal{E}\mu^*}{kT}\left[1 - \frac{2E_e\mu^*}{C\phi}\left(1 - \frac{4\mathcal{E}\mu^*}{C\phi}\right)\right] \qquad [16]$$

where terms of the order of $(\mathcal{E}\mu^*/C\phi)^2$ have been neglected in comparison with unity. Assuming steady-state conditions and setting $(1 + \delta\chi_1) \simeq \delta K_1$ Eq. [16] can be written

$$\ln\kappa \simeq \frac{\mathcal{E}\beta_1}{\delta K_1} + \frac{8E\mu_s^*}{K_1^2kT}\left(\frac{\mathcal{E}\mu_1^*}{\delta C\phi}\right)^2 \qquad [17]$$

where the term in $\mathcal{E}^2$ is fairly small compared to that in $\mathcal{E}$. Using previously reported values (*i.e.*, $\mu_s^* \simeq 23.5$ eÅ (15), $C\phi \simeq 7.8$ ev (15), $\mu_1^* \simeq 7.8$ eÅ, $K_1 \simeq 8.8_5$, and setting $E \simeq 8.5 \times 10^6$ v/cm. and $\kappa \simeq 10^6$, we calculate $\mathcal{E}/\delta \simeq 5 \times 10^7$ v/cm. (From this value, $\mathcal{E}\mu^*/C\phi \simeq \mathcal{E}\mu_1^*/\delta K_1C\phi = 0.07$, a result consistent with the approximation made, *i.e.*, $(\mathcal{E}\mu^*/C\phi)^2 << 1$.) The value of $\mathcal{E}$ estimated in this way appears to be of the correct order, although a reliable independent estimate based on electrostatic considerations is difficult to make.

Summary

In the previous sections, selected data from the literature have been examined in the light of the newly proposed theory. The theory has by no means been applied, however, to the majority of the vast amount of data available in this field, an undertaking which lies outside the scope of the present paper. The principal features of the steady-state and transient behavior of electrodes formed by anodic oxidation of Ta, Al, Nb, and Bi have been examined and found to be in excellent accord with the theory. Specifically, the present theory is the only one to provide a reasonable explanation for: (*a*) the transport number data (Ta, Al); (*b*) the correlation between the field dependence of the transient and steady-state Tafel slopes (Ta, Al); (*c*) the correlation between the transient charge-activation distance product and the dielectric constant (Ta, Nb, Al, Bi); and (*d*) the form of constant field transients (Al, Ta). In addition, the theory provides a quantitative interpretation of space charge phenomena for thin films (Al). Again, all of the parameters deduced on the basis of this model are of precisely the expected magnitude. Even the apparently discrepant behavior of Zr, mentioned earlier, can be reconciled with the present model. In this regard, the most obvious assumption to make is that the metal-oxide interface plays a major role in the conduction process.

Much additional data are required to properly test this theory. At present, however, it is the only quantitative theory which accounts for most of the observed conduction properties for these systems.

Manuscript received Nov. 29, 1964. This paper was presented in part at the Pittsburgh Meeting, April 15-18, 1963.

Any discussion of this paper will appear in a Discussion Section to be published in the June 1966 JOURNAL.

REFERENCES

1. M. J. Dignam, *This Journal*, **112**, 722 (1965).
2. C. P. Bean, J. C. Fisher, and D. A. Vermilyea, *Phys. Rev.*, **101**, 551 (1956).
3. L. Young, "Anodic Oxide Films," Chap. 3, Academic Press, London (1961).
4. L. Young, *Trans. Faraday Soc.*, **55**, 632 (1959).
5. L. Young, *Proc. Roy. Soc. Series A*, **258**, 496 (1960).
6. M. J. Dignam, D. G. W. Goad, and M. Sole, *Can. J. Chem.*, **43**, 800 (1965).
7. L. Young, *Trans. Faraday Soc.*, **52**, 502 (1956).
8. L. Masing and L. Young, *Can. J. Chem.*, **40**, 903 (1962).
9. W. Mizushima, *This Journal*, **108**, 825 (1961).
10. H. G. Draper and P. W. M. Jacobs, *Trans. Faraday Soc.*, **59**, 2888 (1963).
11. J. F. Dewald, *This Journal*, **102**, 1 (1955).
12. L. Young, *Can. J. Chem.*, **37**, 276 (1959).
13. A. R. Bray, P. W. M. Jacobs, and L. Young, *Proc. Phys. Soc.*, **71**, 405 (1958).
14. L. Young, *Trans. Faraday Soc.*, **52**, 515 (1956).
15. M. J. Dignam, *Can. J. Chem.*, **42**, 1155 (1964).
16. L. Young, *This Journal*, **110**, 589 (1963).
17. N. Cabrera and N. F. Mott, *Rept. Progr. Phys.*, **12**, 163 (1949).
18. E. J. W. Verwey, *Physica*, **2**, 1059 (1935).
19. R. J. Maurer, *J. Chem. Phys.*, **9**, 579 (1941).
20. L. Young, *Trans. Faraday Soc.*, **50**, 159 (1954).
21. J. A. Davies, J. P. S. Pringle, R. L. Graham, and F. Brown, *This Journal*, **109**, 999 (1962).
22. J. A. Davies and B. Domeij, *ibid.*, **110**, 849 (1963).
23. J. A. Davies, Private communication.
24. P. Verkerk, P. Winkel, and D. G. Groot, *Philips Research Repts.*, **13**, 506 (1958).
25. G. Amsel and D. Samuel, *J. Phys. Chem. Solids*, **23**, 1707 (1962).
26. L. Young, *Proc. Roy. Soc. Series A*, **263**, 395 (1961).
27. M. J. Dignam and P. J. Ryan, In preparation.
28. L. Young, *Proc. Roy Soc.*, **A244**, 41 (1958).
29. L. Young, *Can. J. Chem.*, **38**, 1141 (1960).
30. D. A. Vermilyea, *This Journal*, **104**, 427 (1957).
31. L. Young, "Anodic Oxide Films," p. 186, Academic Press, London (1961).
32. W. M. Latimer, "The Oxidation States of the Elements and their Potentials in Aqueous Solutions," Prentice-Hall, Inc., New York (1952).
33. A. F. Wells, "Structural Inorganic Chemistry," 2nd ed., p. 37, Oxford University Press (1952).
34. M. J. Dignam and P. J. Ryan, *Can. J. Chem.*, **41**, 3108 (1963).
35. W. J. Bernard and J. W. Cook, *This Journal*, **106**, 643 (1959).
36. L. Young, "Anodic Oxide Films," Chap. 11, Academic Press, London (1961).

A Method for the Dynamic Measurement of Capacity at Electrode Interfaces

C. C. Krischer and R. A. Osteryoung

North American Aviation Science Center, Thousand Oaks, California

ABSTRACT

A potentiostatic method to permit determination of double layer capacity of electrodes under dynamic conditions has been developed. Small potential pulses are superimposed on a d-c sweep and the capacity is determined from the magnitude of current changes observed at the initiation and cessation of the pulse. Further, a method utilizing a transistor is described which permits rapid switching of a potentiostat from galvanostatic to potentiostatic operation.

Although several methods for the dynamic measurement of double-layer capacity have been reported, they appear to suffer from certain disadvantages. Breiter (1) utilized an a-c impedance technique to obtain qualitative curves at solid electrodes.

Boddy and Sundburg (2) developed a simple method of measuring the capacity continuously and rapidly. The authors used a current sweep which had superimposed short duration current pulses. The analysis of the resulting potential-time transients, properly displayed on a cathode ray tube, gave the value of the capacity over the whole length of the sweep. The disadvantage of this method is that the potential change, dE/dt, is not constant with time for a linear current sweep. dE/dt varies depending on the current-potential characteristic of the electrode. To keep dE/dt approximately constant these authors used a nonlinear sweep.

A potentiostatic method would be more convenient and is reported here. A linear d-c sweep voltage is applied directly to the electrode via a potentiostat. Superimposed on this potentiostatic sweep are low amplitude potential pulses. The pulse is short compared to the RC time constant of the electrode network.

In the first part of this paper it is shown how the electrode capacity can be calculated from the current transient that is caused by a potential pulse.

The advantage of using a linear potential sweep rather than a linear current sweep is quite evident if one recalls that the differential capacity curve that one is interested in lies in a potential region where dE/di of the indicator electrode has a maximum. Employing a galvanostatic method, the potential region of interest is passed rapidly if a linear current sweep is used.

In carrying out our work on germanium electrodes (3) we desired and devised a method to permit rapid switching of the cell from a potentiostatic mode to a galvanostatic mode of operation which is reported in the second part of this paper.

Dynamic Potentiostatic Measurement of Electrode Capacity

The electrical equivalent of the impedance of an indicator electrode in the potentiostatic circuit is shown in Fig. 1. It consists of a resistor, R, representing all series resistances in the circuit such as uncompensated resistance in the electrolyte, in the indicator electrode, etc., a resistor, R_p, representing the

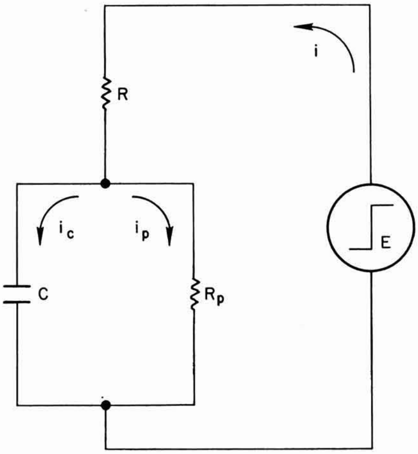

Fig. 1. Electrical equivalent circuit for the application of a potential step (potentiostatic operation) at a metal (or semiconductor) electrolyte interface.

impedance of the faradaic reaction and a capacitor, C, the capacitance of the double layer. [In the case of a germanium electrode, C represents the capacitance due to a space charge layer within the germanium (4).] The potentiostat is a potential source of effectively zero internal impedance. If it delivers a positive potential step of the magnitude, E, a current, i, will flow through the circuit. At $t=0$ the capacitor acts as a short circuit of R_p and an initial current

$$i_o = E/R \qquad [1]$$

will flow. The charging current i_c decays exponentially

$$i_c = \frac{E}{R} \exp\left(-\frac{t}{R'C}\right) \qquad [2]$$

where $R' = \dfrac{RR_p}{R + R_p}$. Simultaneously a current i_p starts to build up exponentially

$$i_p = \frac{E}{R + R_p}\left[1 - \exp\left(-\frac{t}{R'C}\right)\right] \qquad [3]$$

The total current i is the sum of the two

$$i = i_c + i_p = \frac{E}{R}\exp\left(-\frac{t}{R'C}\right) + \frac{E}{R + R_p}\left[1 - \exp\left(-\frac{t}{R'C}\right)\right] \qquad [4]$$

The initial slope of this curve is given by

$$\left(\frac{di}{dt}\right)_{t\to 0} = -\frac{E}{R^2C} \qquad [5]$$

At $t = \Delta t$ a negative step of the same amplitude, $-E$, is delivered (the sequence of the two steps is a rectangular pulse, Δt is the pulse width). At the beginning of the negative step the current changes by $-E/R$, followed by an exponential current-time behavior analogous to the one expressed in Eq. [4]. If the pulse width

$$\Delta t << R'C \qquad [6]$$

Eq. [5] can be approximated by

$$\Delta i = -\frac{\Delta t E}{CR^2} \qquad [7]$$

where Δi is the change in current during the time interval of the pulse. In this equation C and R are unknown; but according to Eq. [1], $R = E/i_o$ so the unknown capacity C becomes

$$C = \frac{\Delta t}{E}\,\frac{{i_o}^2}{\Delta i} \qquad [8]$$

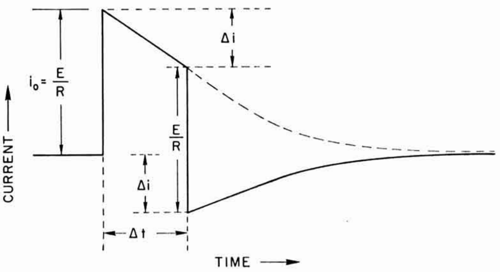

Fig. 2. Schematic of the current time behavior that results by application of a potential pulse in the circuit of Fig. 1 for $R_p >> R$. The line from which i_o rises represents the d-c level.

From this relationship it is seen that one can calculate C if at a known pulse width Δt and amplitude E the quantities i_o and Δi are measured. Figure 2 represents a schematic of the current transient that is caused by a potential pulse. The dashed line indicates the current decay that would occur if the negative step were missing. Note that the quantities i_o and Δi which are needed for the calculation of the capacity are the maximum positive and negative amplitudes of the transient.

In order to measure the capacity potential curve in a dynamic manner a single (or repetitive) linear potential sweep with superimposed short duration pulses is applied to the electrode. The duration of the pulses has to be sufficiently short so that the sweep d-c level may be considered constant over the interval of the pulse. The current transient which results as a consequence of this polarization is characteristic for the electrode impedance-potential curve. Figure 3 gives an example. The line with maximum intensity represents the d-c current through R_p of Fig. 1. This trace corresponds to the base line from which i_o rises, see Fig. 2. As the potential sweep is linear with time, this curve represents a conventional current potential plot. The envelope curves of low intensity above and below the most intense line are caused by the current excursions due to the superimposed pulses. Since there are 250 pulses of 3 μsec duration per horizontal division in Fig. 3, the current transients, one of which is

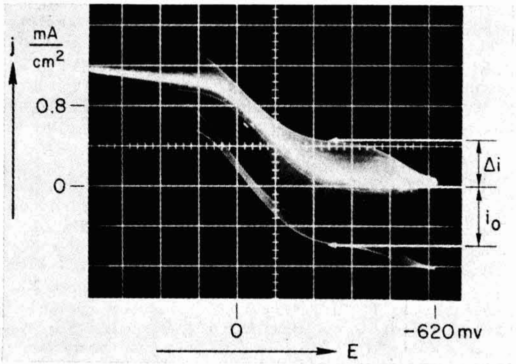

Fig. 3. Example of a current potential curve obtained potentiostatically with a single d-c sweep of 0.24 v/sec which had superimposed negative pulses of 100 mv amplitude and 3 μsec width. Repetition rate of the square wave pulse generator: 500 sec^{-1}. Electrode: 10 ohm cm n-Ge. Electrolyte 0.5M $NaClO_4$ 0.1M buffer pH 7, unstirred. The intense line (d-c voltage curve) within the trace became wider during the course of reproduction; it should be as narrow as in the left side of the figure. The arrows indicate typical current-transient amplitudes, see Fig. 2 and text.

shown in Fig. 2, merge together to yield an area of low intensity compared to the intensity of the main current-potential curve resulting from the voltage sweep. If the intensity of the oscilloscope beam is sufficient to permit observation of the current transients resulting from the voltage pulses, the main current potential trace from the voltage sweep is brighter and diffuse because of its longer duration relative to the transients. This problem, which affects the accuracy of the measurement, may be partially solved by intensifying the beam during appropriate portions of the trace. The deviations on either side of the d-c current trace directly represent the current amplitudes i_o and Δi, compare Fig. 2 and 3. With Eq. [8] one can then calculate C at any desired potential. From Fig. 3 it is seen that the condition $\Delta i << i_o$ is in most potential regions not fulfilled. Therefore, the exponential is at $t = \Delta t$ no longer near linear, condition [6] is not strictly fulfilled. Equation [8] then yields capacity values which are larger than in the case of validity of condition [6]. This error is however partly compensated by another effect. The rise time of the potentiostat tends to round off edges of the current transient: i_o will be measured smaller than it should be. These two errors tend to cancel each other. We found the accuracy to be within ±20%. The systematic error for one particular system will, however, be constant so that relative changes are easily detectable. In ref. (3) capacity potential curves are reported which are in good agreement with the calculated curves.

Intermittent Galvanostatic Switching of a Potentiostat

For the purpose of studying the surface of electrodes it may be desirable to polarize the electrode by a known amount of charge prior to the measurement of the characteristic. Most conveniently the charging is carried out under constant current conditions for a given time interval, *i.e.*, in a galvanostatic mode of operation. In order to minimize changes of the resulting state of the electrode before the capacity measurement is initiated, rapid switching to the potential where the capacity measuring sweep starts is required. A versatile, yet simple circuit is described which meets this requirement.

A transistor is placed in series with the cell. A voltage, E, is applied from the potentiostat to cause a potential drop, E_{trans}, across the transistor sufficient to drive it well into its limiting current region (reverse bias), (see Fig. 4). This results in the current through the cell being controlled by the limiting current characteristics of the transistor. The limiting current can be selected by appropriate transistor base current input (see Fig. 5). Changes in the voltage across the cell have little effect on the current through the system provided that such changes occur within the limiting current region of the transistor. When the voltage, E, is such as to result in a potential drop across the transistor which brings it into the forward biased region, there is little potential drop across the transistor. The current through the transistor can change appreciably with little change in potential drop across the transistor.[1]

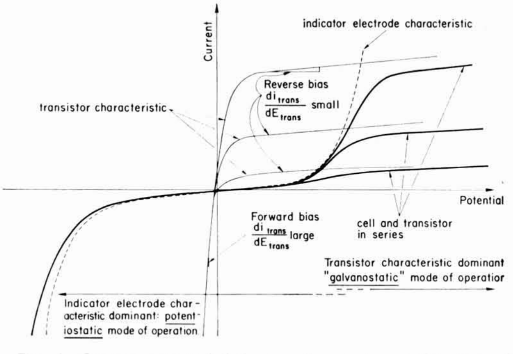

Fig. 4. Current potential behavior of a series combination of cell and transistor. The voltage drops as a function current are: dashed, of the indicator electrode; thin, of the transistor with three different base currents; and bold, of the cell and the transistor with three different base currents in series.

It was found (3) that in steep portions of the transistor characteristic (forward bias) the transistor capacity was much larger than the capacity of a germanium electrode in the flat part of its current potential curve. In this potential region, in which the potentiostatic mode prevails, the transistor capacity does not introduce a significant error in the measurement of the electrode capacity. Figure 4 represents a schematic construction of the current potential curves that result if a transistor with three different base currents is placed in series with an electrode which has an activation controlled current-potential characteristic. It is seen that the introduction of the transistor yields current clamping in one direction. It is in the potential region of small currents where the differential capacity curve is measured potentiostatically.

To summarize, placing the transistor in series with the indicator electrode serves the purpose of controlling the current through the cell. This is accomplished by applying a voltage that brings the transistor into reverse bias. The transistor characteristic then dominates. Under forward bias of the transistor, the indicator electrode characteristic prevails, and the transistor introduces only a slight perturbation on the indicator electrode characteristic. The base current, which has to be supplied by a current source other than the potentiostat, has two functions: (i) it determines the limiting current during the galvanostatic period, and (ii) it diminishes the interference of the transistor during the potentiostatic period. The perturbation of the indicator electrode characteristic during this period may be kept small by injecting a large base current, top curve in Fig. 4.

The design of the electrical circuit has to fulfill two requirements: short rise time of the potentiostat and versatility in the input system. The latter is needed in order to provide well-defined galvanostatic prepolarization followed by potentiostatic capacity measurement. We therefore employed the Wenking potentiostat in the adder configuration (6) rather than in the conventional differential mode. An oscilloscope with a delayed sweep capability is a convenient source of prepolarizing pulse and measuring sweep. The time base of such oscilloscopes may deliver two sawtooth and square wave voltages. One couple of sawtooth and square wave voltages corresponds to the normal or delaying sweep, the other to the delayed sweep. The voltages are of fixed amplitude and polarity. Attenuation and in some cases inversion is needed. The durations of the wave forms are calibrated and variable within a wide range. The beginning of the delayed sweep with respect to the normal sweep (and normal gate) is determined by the setting of the calibrated delay time potentiometer.

The details of the experimental arrangement are shown in Fig. 5. The response of the circuit is demonstrated in Fig. 6. It represents a photograph of a typical current transient that is caused by a rectangular potential pulse. The rise time is a little less than one μsec.

---

[1] Since the transistor is in series with the cell,

$$i_{\text{trans}} = i_{\text{cell}} = i(E_{\text{trans}})$$

and

$$E_{\text{trans}} = E - E_{\text{cell}}$$

$$\frac{di}{dE_{\text{cell}}} = \frac{di_{\text{trans}}}{dE_{\text{trans}}} \cdot \frac{dE_{\text{trans}}}{dE_{\text{cell}}} = -\frac{di_{\text{trans}}}{dE_{\text{trans}}}$$

$$di = -\frac{di_{\text{trans}}}{dE_{\text{trans}}} \cdot dE_{\text{cell}}$$

In the region of reverse bias, $di_{\text{trans}}/dE_{\text{trans}}$ is very small (*ca.* 10^{-6} ohm^{-1}) so that a change in the cell voltage does not change i. In the forward bias region $di_{\text{trans}}/dE_{\text{trans}}$ is very large, there is very little potential drop across the transistor, and dE_{cell} is unaffected by changes in i.

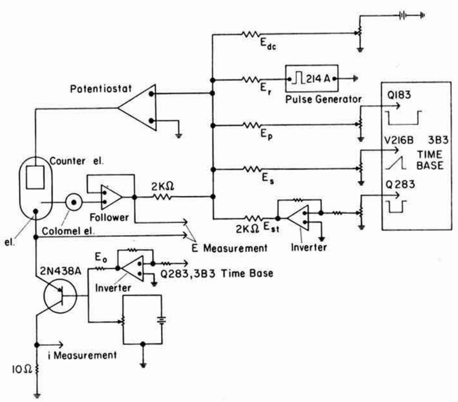

Fig. 5. Schematic representation of the electrical circuit for galvanostatic prepolarization followed by rapid potentiostatic measurement of the current and capacity-potential curve. The amplifiers are Philbrick, type P65A. The 3B3 time base is a Tektronix module, the numbers refer to the switching diagram of the time base manual. The pulse generator is a Hewlett-Packard product, type 214A. The potentiostat is a Wenking model.

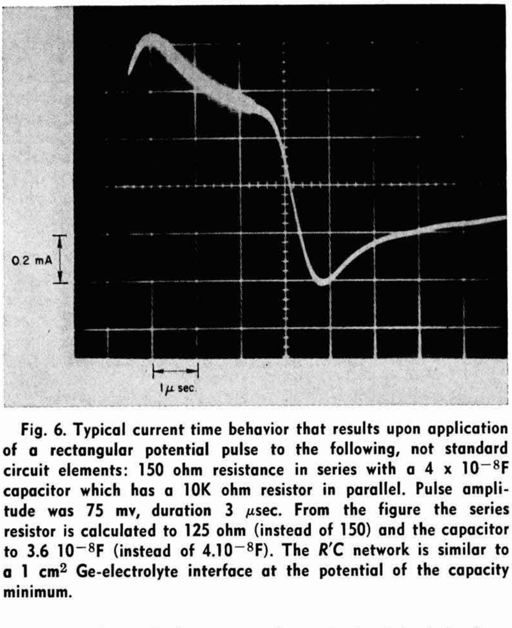

Fig. 6. Typical current time behavior that results upon application of a rectangular potential pulse to the following, not standard circuit elements: 150 ohm resistance in series with a 4 x 10^{-8}F capacitor which has a 10K ohm resistor in parallel. Pulse amplitude was 75 mv, duration 3 μsec. From the figure the series resistor is calculated to 125 ohm (instead of 150) and the capacitor to 3.6 10^{-8}F (instead of 4.10^{-8}F). The R′C network is similar to a 1 cm² Ge-electrolyte interface at the potential of the capacity minimum.

For studies of the germanium-electrolyte interface we were interested in pretreating the electrode with known amounts of cathodic charge prior to the impedance measurement. Therefore, in the circuit of Fig. 5 a n-p-n transistor was used to limit the cathodic current. For anodic pretreatment a p-n-p transistor would be chosen. Both current directions can also be limited if two transistors, n-p-n and p-n-p, with appropriate base currents, are placed in series.

Three waveforms of the timebase combined with two other voltage sources are used. The task of the individual potential sources is as follows:

1. Prior to the polarizing cycle the potential has to be set at a d-c level, $E_{d\text{-}c}$, which yields a reproducible steady state of the surface.

2. For the capacity measurements free running short duration rectangular pulses are needed. We used a Hewlett Packard 214A pulse generator.

3. To drive the transistor into its limiting current region in order to prepolarize, a high amplitude prepolarizing pulse, E_p, is applied. We chose the square wave of the normal or delaying sweep of the time base.

4. Furthermore, the measuring linear sweep, E_s, is needed. The sawtooth of the delayed sweep is used. The delay time of this delayed sweep with respect to the beginning of the normal sweep thereby determines the duration of the prepolarizing pulse.

5. In order to initiate the sweep at any desired potential, an additional pulse, E_{st} is required. Without this pulse the linear sweep would start in the limiting current region. The changeover from galvanostatic to potentiostatic mode would be gradual instead of abrupt. The gate of the delayed sweep which occurs simultaneously with the sawtooth can be used for E_{st} advantageously.

As indicated in Fig. 5, this latter pulse source, *i.e.*, the timebase, is also utilized to increase the transistor base current. Thereby a transistor characteristic is selected which causes the least interference of the indicator electrode characteristic at small current densities, compare Fig. 4. For further experimental details see Fig. 5 and its legend.

Figure 7 is a schematic representation of the waveform that appears at the output of the potentiostat by application of voltages 1-5 as listed above.

Listed below are some polarization cycles that can easily be obtained with the circuit of Fig. 5.

Prepolarization, anodic sweep (PA).—The cycle of Fig. 7 is described above in detail in which the voltage is increasing with time. This sweep will be called an anodic sweep. Decreasing voltage with time is called a cathodic sweep.

Prepolarization, cathodic sweep (PC).—If the same potential region as in Fig. 7 should be measured with a cathodic sweep, the amplitude of E_{st} is increased by the amount of E_s and E_s itself is inverted.

Anodic sweep (A).—If anodic sweep without galvanostatic prepolarization is desired one can (i) make the transistor limiting current very small by omitting the base current and making the delay time ~ 0 or (ii) E_p is omitted and an inverted gate, $-E_{st}$, brings the sweep to a potential, $E_{d\text{-}c} - E_{st}$, which is desired as the sweep starting potential.

Cathodic sweep (C).—If cathodic sweep and no prepolarization is desired, the cathodic sweep is simply initiated at $E_{d\text{-}c}$. E_p and E_{st} are omitted.

Although our original interest in devising this procedure was focused on the studies of the germanium-electrolyte interface the technique is applicable to other electrodes such as metal electrodes and the dropping mercury electrode. For example, we have examined the differential capacity at a dropping mercury electrode in various electrolytes by this method and obtained agreement with literature results. Because a dropping mercury electrode has a longer time constant R′C than a germanium interface, the pulse dura-

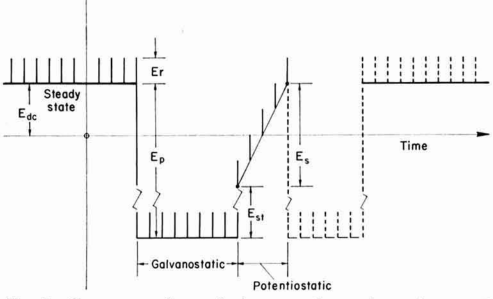

Fig. 7. Output waveform of the potentiostat for galvanostatic pulsing followed by a potentiostatic sweep. The voltages are with reference to Fig. 5. The dashed part following the sweep represents the termination of the galvanostatic pulse.

tion was chosen longer than in the case of germanium. Adjusting the pulse width to the particular *RC* network of the electrochemical system is necessary to obtain reasonable accuracy.

For low values of the time constant *R'C* of the indicator electrode the method may be used up to high sweep rates $v = dE/dt$. At germanium electrodes sweep rates up to 300 v/sec were employed (3). For convenience we chose a combination of square wave and sawtooth voltages for the prepolarization and potential variation. The circuit described above allows, however, the use of other wave forms as well, such as a triangular or a sine wave. An application of this method to the study of germanium electrodes will be reported (3).

Summary

A dynamic capacity measuring method is devised. It is based on the analysis of current transients that are caused by short duration potential pulses. The dynamic variation of the potential is achieved with a linear potential sweep on which the pulses are superimposed. An oscilloscope serves as a sweep generator. The charge flow during the measurement of the capacity potential curve may be kept very small (in the order of a few μa sec/cm^2) if appropriate values of the sweep starting potential and the sweep rate $v = dE/dt$ are chosen.

This method may be employed advantageously in connection with a novel technique of switching the cell from the normal potentiostatic into a galvanostatic mode, as is also described in this paper. A transistor, placed in series with the indicator electrode, represents the fast switching element. The galvanostatic mode serves to charge the electrode surface to a known extent. The same oscilloscope (with delayed sweep capability) that delivers the sweep controls also the prepolarization time. With the method described above one is able to measure the electrochemical characteristic of a prepolarized electrode, since its state remains practically undisturbed in the course of the measurement. The galvanostatic prepolarization may be chosen in the cathodic, anodic or both current directions.

Manuscript received Jan. 25, 1965.

Any discussion of this paper will appear in a Discussion Section to be published in the June 1966 JOURNAL.

REFERENCES

1. M. W. Breiter, *J. Electroanal. Chem.*, **7**, 38 (1964).
2. P. J. Boddy and W. J. Sundburg, *This Journal*, **110**, 1170 (1963).
3. C. C. Krischer and R. A. Osteryoung, *ibid.*, To be published.
4. K. Bohnenkamp and H. J. Engell, *Z. Electrochem.*, **61**, 1184 (1957).
5. W. Guggenbuhl, M. J. O. Strutt, and W. Wunderlin, "Halbleiter Bauelemente," I, Birkhauser Verlag, Basel, Stuttgart (1962).
6. George Lauer, Helmar Schlein, and R. A. Osteryoung, *Anal. Chem.*, **35**, 1789 (1963).

The Effect of Dislocations and Orientation on the Electrical Double Layer Capacity of Silver Surfaces

R. G. Rein, C. M. Sliepcevich, and R. D. Daniels

University of Oklahoma, Norman, Oklahoma

ABSTRACT

This study was undertaken in an attempt to obtain a better understanding of the effects of dislocations, crystal orientation, and surface imperfections on the catalytic activity of metals. Relative surface areas of pure silver crystals were determined from measurements of double layer capacities for {110}, {111}, and {211} planes with dislocation densities ranging from 10^6 to 10^8 cm^{-2}. Care was taken to insure that clean, oxide-free surfaces were used during measurements. Although it was found that the relative areas of {110} and {211} planes were proportional to the log of dislocation density, the relative area of {111} planes was found to be independent of dislocation density. The behavior of the double layer capacity as influenced by abrasion, cracks, notches, grain boundaries, and dislocations is discussed in terms of changes in physical area and changes in effective area resulting from additional dislocations. Models of metal surfaces and knowledge about the structure of the double layer are inadequate, at present, to allow positive conclusions to be drawn about the effect of dislocations on double layer capacity. The double layer capacity of mercury in 0.2*N* H_2SO_4 was experimentally determined to be 19.4 ± 2.2 μf/cm^2 which agrees favorably with values reported recently.

Crystal imperfections and surface orientation, particle geometry and surface irregularities are factors which can influence the activity of catalysts (1-3). The effectiveness of a metallic catalyst has been found to be dependent on the crystal face exposed to the reactants (4-8). In addition, Liedheiser and Gwathmey have found that {100} planes of copper become roughened while catalyzing the reaction of oxygen and hydrogen; whereas {111} planes remained smooth (6). Introducing imperfections into a crystal has also been reported to influence catalytic activity (9-12). Barnes and Mazey (13) show a change in surface area with irradiation, a common method for disturbing a metal lattice.

Although the BET area has been used frequently in correlating kinetic data for catalytic reactions, in most cases the superficial area, or some equivalent, is used without giving any consideration to surface conditions. Since it is possible that significant information can be masked if differences in surface area between crystal planes and differences in area due to crystal imperfections are not considered, this investigation was undertaken to determine changes in area as influenced by dislocation density and crystal orientation.

The many methods for determining surface areas have been summarized by Adamson (14), Brunauer (15), and Gregg (16). Of the methods mentioned, only the various adsorption methods, such as the well-known BET technique and the double layer capacity method are generally applicable. Gas adsorption techniques are not satisfactory in the case of metals because of their small area to volume ratio. The relative decrease in pressure or volume of the adsorbed gas is too small, for a reasonable size sample, to allow accurate analysis. For this reason the double layer capacity method first proposed by Bowden and Rideal (17) was used to determine the effective surface areas of the silver crystals employed in this study.

Throughout this paper three different area terms will be used: (*a*) superficial area, which is determined by the gross dimensions of the sample; (*b*) physical area, which takes into account all mechanical surface irregularities such as roughness, notches, cracks, misorientation at grain boundaries, regardless of the scale of dimensions; and (*c*) effective area, which is determined by the double layer capacity measurement and which may be influenced both by the physical area as defined above and by energy factors associated with crystal surface orientation and crystal defects.

The double layer capacity method as originally conceived was based on the assumption that the double layer capacities of metal electrodes with equal physical areas are the same and independent of the metal being investigated. However, it is conceivable that the double layer capacity measurement considers not only the physical area but also area affects arising from crystal orientation and defects. Consequently, an attempt was made to isolate these latter factors by taking special precautions to maintain a constant physical area while varying only the dislocation density and crystal orientation.

The measured double layer capacity is given by

$$\left.\frac{\partial\Gamma}{\partial E}\right)_{T,\,P,\,\text{etc.}} = C\ (\text{at time} = 0) \qquad [1]$$

where Γ is the charge in coulombs on the double layer per unit superficial area, E is the potential in volts across the double layer, and C is the differential capacity applicable for short durations of time (time < 0.10 sec) in farads per unit superficial area. The units of superficial area are hereafter denoted by an asterisk (cm^2)*. Thus, $\partial\Gamma/\partial E$ represents the instantaneous measured value of the capacity at time equal zero.

If the superficial area of a metal and the effective area for capacity determination are identical, $\partial\Gamma/\partial E = C'$ will have the units of (farads/effective area in cm^2). The assumption is made for a mercury electrode that the effective area for capacity determinations is identical to its superficial area. Therefore the capacity of any metal electrode, C, divided by the capacity of a mercury electrode, C', gives the effective area of the metal electrode relative to its superficial area.

$$CAR = \frac{C}{C'}\,\frac{(\text{cm}^2)}{(\text{cm}^2)^*} \qquad [2]$$

The abbreviation, *CAR*, refers to the capacity area ratio and will be used throughout the paper. It is an indication of the effective area.

In these measurements care must be taken to eliminate concentration and ohmic polarization, which would distort the value of the potential applicable to the double layer. For reproducibility and accuracy of measurement, care must also be exercised to eliminate impurities on the electrode surface and in the electrolytic solution as impurities also tend to affect the capacity of the double layer (14, 17, 18).

Procedure

Apparatus and General Considerations

The effective areas of silver specimens were measured by the double layer capacity first proposed by Bowden and Rideal (17). The electrical circuit is shown in Fig. 1.

The oscilloscope (O) was used in conjunction with an oscilloscope camera to record the potential E (t) of the silver electrode. The integrated current through the cell Γ (t) was obtained from readings on the recorder (R) of the voltage across the capacitor. The output of the signal generator (SG) was a square wave of frequency 0.05 cps and supplied the polarizing current for the cell. The steady-state current density through the cell was 10^{-4}-10^{-3} amp/(cm^2)*.

Since the signal generator output was from plus volts to minus volts and the desired output was from zero to plus volts, the circuit SGB was used to bias out the undesired negative output.

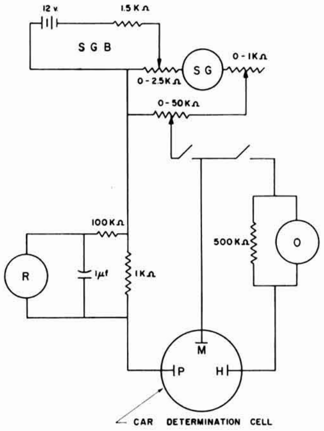

Fig. 1. Electrical circuit

(H) is a standard hydrogen electrode, (P) a platinum electrode, and (M) the metal electrode whose effective area is being determined.

The effects of ohmic polarization were minimized by putting the electrodes near each other (at the corners of an equilateral triangle of side 4 cm). Hydrogen bubbling from the hydrogen electrode agitated the solution to eliminate concentration polarization.

The electrolyte was 0.2*N* H_2SO_4 which had been freed from dissolved oxygen by heating under a slight vacuum for 1-2 hr and cooled to room temperature in a hydrogen atmosphere.

Although Bowden and Rideal (17) state that the determinations may be made either during polarization or depolarization of the double layer, the larger part of the data were obtained during polarization; however some data, which agreed with that obtained by polarization, were obtained during depolarization. All data were obtained at temperatures between 75° and 80°F.

Crystal Preparation

The silver single crystals used for effective area determinations were grown in the laboratory (19). The crystals were oriented by the Laue back-reflection x-ray technique and cut with a standard, water-cooled cut-off machine, so as to expose either {211}, {111}, or {110} planes. The desired surfaces were then mechanically polished with successively finer grit polishing disks, the final treatment being with a 600C disk. The crystals were then deformed to introduce a controlled number of dislocations. Two methods of deformation were used: (a) The crystals were bent to a U shape by either a 1.00 or a 4.00 cm radius plunger-die combination (see Fig. 2a); the deforming force was applied normal to the surface whose area was to be measured.

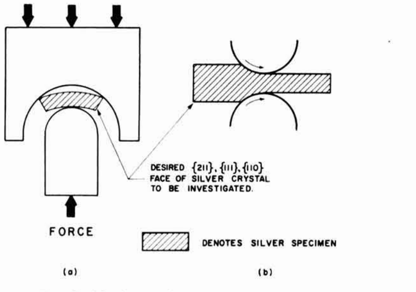

Fig. 2. Methods of crystal deformation

(b) The crystals were cold-rolled to a given reduction; the applied force again was normal to the surface whose area was to be measured (see Fig. 2b).

The crystals, after deformation were electropolished in a 5 w/o (weight per cent) KCN solution. This treatment lasted for 3-6 min at 1-2 amp/cm^2. The electropolished surfaces appeared bright, shiny, and free from microscratches as determined by microscopic examinations at 300X. The surfaces were also strain-free as evidenced by the distinct poles rather than smears obtained on a Laue back-reflection pattern of a sample prepared in this manner.

A thermal-etching technique applicable to silver (19, 20) was used to determine the dislocation density. The samples were annealed at 600°-615°C for 45-90 min in an argon atmosphere, etched 10-15 min in a 10% oxygen-90% argon mixture, and cooled to room temperature in an argon atmosphere. Etch pits were counted at magnifications of 1500-2500X on a metallograph. Figure 3 is representative of the etch pit observations. The macroscopic dimensions of the specimens were then measured with a micrometer and used to calculate the superficial area.

After thermal etching, an electrical lead was connected to the sample by an alligator clip and the sample was mounted in Koldmount. The face which was to be subjected to *CAR* determinations was protected by a strip of fiberglass tape during mounting. After mounting, the tape was removed, and the surface cleaned with methanol to remove traces of adhesive and fingerprints.

To insure the absence of any oxide layer either of two final surface preparations was used: (a) The samples were again electropolished for 15-20 sec, washed with distilled water, and then placed in the *CAR* determination apparatus, a technique found acceptable by Wisdon and Hackerman for iron (21). (b) The samples were subjected to 2-4 hr of electrolytic reduction to reduce any oxide layer (22, 23). For this treatment the sample served as the cathode, oxygen-free 0.2N H_2SO_4 as the electrolyte and platinum as the anode. A steady-state current density was passed through the cell; the range of densities used was between 5-15 μa/cm^2*. After this pretreatment the samples were immediately placed in the *CAR* apparatus.

The double layer capacity, and hence the *CAR*, was found to be independent of the two techniques used for final surface preparation.

To isolate the dependence of *CAR* on undesirable effects, the following exceptions were made to the general procedure mentioned: (*a*) Sample *E*, an undeformed sample: the final polish was with a 240C polishing disk, instead of electropolishing, to determine the effect of scratches on the *CAR*. (*b*) Sample F, deformed 62% by rolling: it completely recrystallized during the annealing treatment. (*c*) Samples I and J: the *CAR* was measured after use of these samples as catalysts for the decomposition of formic acid. The surface of sample J was not cleaned prior to the *CAR* tests, while sample I was subjected to 4 hr of electrolytic reduction. (*d*) Sample K: the thermal etching treatment and determinations of dislocation density were made after the *CAR* tests to minimize possible recrystallization effects.

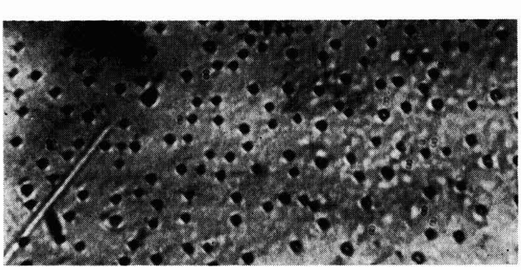

Fig. 3. Etch pits on a {211} plane of silver (2000X and 1.2 x 10^7 dislocations/cm^2).

Table I. Capacity area ratio (*CAR*) Data

Sample	Crystal face exposed	Dislocation density	Double layer capacity f/(cm^2)*	*CAR*	Number of determinations
A	211	3.2×10^6	52.6 ± 1.6	2.71	11
B	211	1.0×10^7	68.5 ± 2.6	3.53	16
C	211	1.7×10^7	67.2 ± 2.3	3.46	19
I[a]	211	3.2×10^6	50.3 ± 1.6	2.59	9
J[b]	211	3.2×10^6	59.6 ± 3.2	3.07	7
S	211	7.3×10^7	73.3 ± 6.2	3.78	14
U	211	1.1×10^7	66.0 ± 2.6	3.40	15
K	110	7.1×10^7	76.9 ± 3.8	3.97	13
L	110	3.2×10^6	56.3 ± 6.4	2.90	13
W	110	1.3×10^7	68.3 ± 3.5	3.52	17
M	111	7.3×10^5	71.2 ± 4.0	3.67	29
N	111	1.3×10^6	69.6 ± 5.9	3.59	24
O	111	3.0×10^6	64.9 ± 3.4	3.34	14
T	111	3.4×10^6	69.0 ± 5.8	3.56	15
V	111	6.0×10^7	71.1 ± 4.5	3.66	9
F[c]	110	1.0×10^8	83.8 ± 2.6	4.22	12
E[d]	211	Scratched	128.1 ± 4.9	6.60	10
Hg	—	—	19.4 ± 2.2	1.00	18

[a] *CAR* determined after sample was used to catalyze the decomposition of formic acid. Surface cleaned prior to determination.
[b] *CAR* determined after sample was used to catalyze the decomposition of formic acid. Surface not cleaned prior to determination.
[c] Sample recrystallized.
[d] Final surface preparation was with 240C polishing disk.

It is possible that the cold work used to introduce dislocations into the specimens could cause recrystallization of the samples during the annealing and thermal etching treatment. The grain boundaries thus formed could also affect the area measurements. To determine the extent of recrystallization, if any, several specimens were etched in an ammonium persulfate-sodium cyanide solution. Sample F (noted above) was the only one which exhibited recrystallization.

To determine the double layer capacity of the mercury, a fresh pool of mercury was placed in a plastic tube; electric contact was made via a copper disk connected to a lead in the bottom of the tube. The tube was immediately placed in the cell and the necessary data were obtained. Sufficient holes and slots were cut in the tube to eliminate the possibility of concentration polarization.

Results

The results of this investigation are shown graphically in Fig. 4-7, and are given in tabular form in

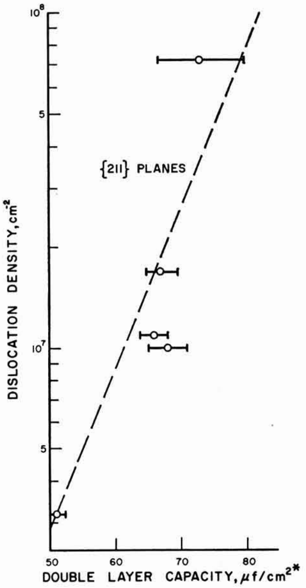

Fig. 4. Dislocation density vs. double layer capacity {211} planes

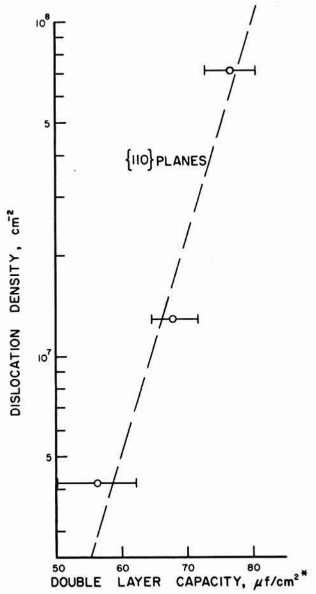

Fig. 5. Dislocation density *vs.* double layer capacity {110} planes

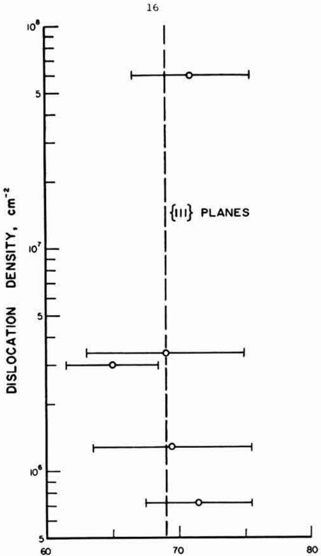

Fig. 6. Dislocation density *vs.* double layer capacity {111} planes

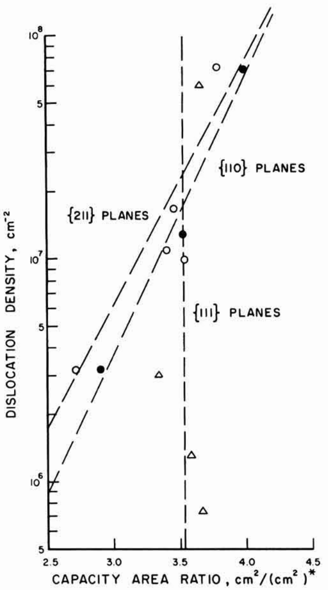

Fig. 7. Dislocation density *vs.* capacity area ratio for various planes: △, values for {111} planes; ○, values for {211} planes; ●, values for {110} planes.

Table I. Since there is no theoretical correlation available, the data are represented by straight lines rather than resorting to curve fitting. Figures 4-6 are plots of log dislocation density in units of surface intersections per square centimeter for various crystal planes *vs.* double layer capacity (within 95% confidence limits). Double layer capacity, as noted earlier, has been assumed to be a measure of the effective area which takes into account both physical area and energy factors. However, since precautions were taken to keep the physical area constant, the changes in double layer capacity are attributed to energy effects arising from changes in crystal surface orientation and dislocation density. In Fig. 7 the previous results are condensed on a single graph to illustrate the influence of planar orientation on the effective area. In this figure double layer capacity is converted to *CAR*.

As indicated by Fig. 4-6, the *CAR* of {211} and {110} planes, which are the double layer capacities of these planes divided by that of mercury, appear to be sensitive to changes in dislocation density, while the *CAR* of {111} planes is insensitive to these changes. From Fig. 7, the effective area of {111} planes is about 3½ times the superficial area, while for {211} and {110} planes it changes from approximately 2½ times the superficial area at low dislocation densities to 4 times at higher densities.

In Table I notice that the effective area of sample E is 2½ times as great as that for undeformed, smooth {211} surfaces (samples A and I). This result is to be expected since the final surface preparation of sample E involved polishing with a 240C disk instead of electropolishing.

Comparison of data for samples A and I, with clean surfaces, and sample J, with a contaminated surface, indicates the necessity of clean surfaces.

As mentioned earlier, the *CAR* is merely the double layer capacity of the silver surface divided by that of a mercury surface. The capacity of mercury surfaces was found, within 95% confidence limits, to be 19.4 ± 2.2 μf/cm^2 (Table I).

Discussion

The value of 19.4 ± 2.2 μf/cm^2 for the double layer capacity of mercury in $0.2N$ H_2SO_4 obtained in this investigation agrees favorably with other recently determined values (24-27) and serves to confirm the reliability of the results obtained in this study.

Referring again to Table I, sample E was not electropolished after mechanical polishing with a 240C disk. In this case the double layer capacity of the single silver crystal was 128 ± 4.9 μf/(cm^2)* or 6½ times that of mercury. It is assumed that this increase in effective area is indicative of an increase in physical area due to surface roughening. A comparable value was given by Bowden and Rideal (17) for a silver specimen which was polished with "flour" sandpaper. The value is 100 ± 10 μf/(cm^2)*. The agreement is acceptable considering that the degree of mechanical polishing of the specimen used by Bowden and Rideal is not accurately known. Furthermore, it is not known whether their specimen was polycrystalline or a single crystal.

In Table I, the double layer capacity for sample F which was electropolished, but was polycrystalline, was found to be 83.8 μf/(cm^2)*. This value is in the range of the double layer capacity for other polycrystalline metal surfaces in H_2SO_4; 70 μf/(cm^2)* having been observed for copper (28) and 85.5 μf(cm^2)* for a 10μ zinc coating on aluminum (29). These values are somewhat higher than those for the electropolished, single crystals and can possibly be attributed to increased area due to grain boundaries in the metals. In addition, surface irregularities in the substrate for the zinc coating could cause an increase in the area.

Figures 4-6 indicate that the precision involved in these measurements is not great, as evidenced by the spread of 95% confidence limits. Data of Bowden and Rideal (17) exhibit a similar lack of precision, which they attribute to the very small quantities being measured. Regardless of the precision involved, it appears that the *CAR* of {211} and {110} faces (Fig. 4 and 5) tends to increase with increasing dislocation density, while that of {111} faces (Fig. 6) does not. In addition, successive determinations of *CAR* on the same sample (constant dislocation density) gave a random spread of results, indicating that the silver surface did not become roughened during the measurements.

In considering the effect of dislocations on double layer capacity, and thus on the *CAR*, it is believed that the tendency of the double layer capacity to increase with increasing dislocation density (as in the cases of {110} and {211} planes) is not due to an increasing physical area since the intersection of dislocations with a surface which has been electropolished leads to no change in the physical area of that surface. In addition, since the specimens were not recrystallized the apparent change in double layer capacity or effective area is not produced by the introduction of grain boundaries. It appears that the *CAR* or effective area is influenced by something other than changes in physical area. This additional contribution to the effective area is assumed to be caused by the energy of dislocations intersecting the surface. However, present theoretical models of metal surfaces are inadequate quantitatively to analyze this effect; a more atomistic model is needed to characterize the surface in regions of defects and distortion.

In summary:

1. The double layer capacity for abraded metal electrode surfaces is significantly greater than that for electropolished surfaces; the difference is attributed to the increased physical area due to abrasion.

2. The double layer capacities of electropolished polycrystalline metal electrode surfaces are greater than those of electropolished single crystal surfaces, but far less so than those of abraded surfaces. Part of this difference in effective area is probably due to an increased physical area caused by grain boundaries. However, a portion of the change in effective area is thought to be caused by dislocations.

3. The double layer capacity of electropolished single crystal silver electrodes increases with increasing dislocation density on the {211} and {110} planes but not on the {111} planes.

Acknowledgment

This work was supported in part by the Office of Naval Research. The valuable suggestions of T. D. Perkins and W. R. Upthegrove in the experimental phases of this work are acknowledged.

Manuscript received Aug. 24, 1964; revised manuscript received March 15, 1965.

Any discussion of this paper will appear in a Discussion Section to be published in the June 1966 JOURNAL.

REFERENCES

1. G. C. Bond, "Catalysis by Metals," p. 468, Academic Press, New York (1962).
2. R. H. Griffith and I. D. F. Marsh, "Contact Catalysis," 3rd Edition, p. 129, Oxford University Press, London (1957).
3. S. M. Walas, "Reaction Kinetics for Chemical Engineers," p. 153, McGraw-Hill Book Co., New York (1959).
4. A. J. Crocker and A. J. B. Robertson, *Trans. Faraday Soc.*, **54**, 931 (1958).
5. R. E. Cunningham and A. T. Gwathmey, *Adv. in Catalysis*, **10**, 89 (1957).
6. H. Liedheiser, Jr. and A. T. Gwathmey, *J. Am. Chem. Soc.*, **70**, 1200 (1948).
7. H. Liedheiser, Jr. and A. T. Gwathmey, *ibid.*, **70**, 1206 (1948).
8. H. M. C. Sosnovsky, *J. Chem. Phys.*, **23**, 1486 (1955).
9. J. Eckell, *Z. Electrochem.*, **39**, 433 (1933) as discussed by L. E. Cratty and A. V. Granto in *J. Chem. Phys.*, **26**, 96 (1957).
10. H. E. Farnsworth and R. F. Woodcock, *Adv. in Catalysis*, **9**, 123 (1956).
11. J. W. Hall and H. F. Rose, *Industrial and Engineering Chemistry Fundamentals*, **3**, 158 (1964).
12. H. M. C. Sosnovsky, *J. Phys. Chem. of Solids*, **10**, 308 (1959).
13. R. S. Barnes and P. J. Mazey, *Proc. Roy. Soc. (London)*, **A275**, 47 (1963).
14. A. W. Adamson, "Physical Chemistry of Surfaces," Chap. 10, Interscience Publishers, Inc., New York (1960).
15. S. Brunauer, "The Adsorption of Gases and Vapors," Chap. 9, Oxford University Press, London (1945).
16. S. J. Gregg, "The Surface Chemistry of Solids," 2nd Edition, Reinhold Publishing Corp., New York (1961).
17. F. P. Bowden and E. K. Rideal, *Proc. Roy. Soc. (London)*, **A120**, 59 (1928).
18. J. A. V. Butler, "Electrical Phenomena at Interfaces," p. 47, Methuen and Co., Ltd., London (1951).
19. T. D. Perkins, Ph.D. Thesis, University of Oklahoma (1963). Also Final Report, Office of Naval Research Contract Nonr 982-(08), Task No. NR 051-418, March 1, 1963.
20. A. A. Hendrickson and E. S. Machlin, *Acta Met.*, **3** (1955).
21. N. E. Wisdon and N. Hackerman, *This Journal*, **110**, 319 (1963).
22. J. A. Allen, *Trans. Faraday Soc.*, **48**, 273 (1952).
23. F. W. Salt and J. G. N. Thomas, *Nature*, **178**, 434 (1956).
24. I. M. Barclay and J. A. V. Butler, *Trans. Faraday Soc.*, **36**, 128 (1940).
25. F. P. Bowden and K. E. W. Grew, *Faraday Soc. Disc.*, **1**, 93 (1947).
26. V. E. Past and Z. A. Iofa, *Zhur. Fiz. Khim.*, **33**, 13 (1959).
27. M. Proskurin and A. Frumkin, *Trans. Faraday Soc.*, **31**, 110 (1935).
28. J. O'M. Bockris and B. E. Conway, *J. Chem. Phys.*, **28**, 707 (1958).
29. A. M. Yampol'shii, *Zhur. Priklad. Khim.*, **33**, 1967 (1960).

Molybdenum Oxidation Kinetics at High Temperatures

R. W. Bartlett[1]

Aeronutronic Applied Research Laboratories, Philco Corporation, Newport Beach, California

Oxidation of molybdenum results in condensed oxides at moderate temperatures and evaporation of gaseous oxide species at temperatures above approximately 700°C. Seven oxidation rate studies have been made at temperatures in excess of 1000°C (1-7). The recent investigation by Gulbransen *et al.* (6), was carried to the highest temperature, 1700°C. These studies have been conducted in air and oxygen but over narrow pressure ranges. The present study was conducted between 1380° and 2470°C (molybdenum mp 2625°C) and over a wider oxygen pressure range, 1 x 10^{-6} atm to 1 atm.

The experimental technique employed a 24-in. diameter cold wall furnace chamber. This permitted free convection around the sample without apparatus constraints on gas mixing or oxygen diffusion within the boundary layer formed by molybdenum oxide vapors diffusing outward from the sample. Polycrystalline molybdenum rods, 0.125-in. initial diameter, were used as samples and heated electrically. The furnace chamber was maintained at the appropriate oxygen pressure by controlling the flow of dry oxygen through the system. Oxidation rates were determined by measuring the sample diameter at suitable intervals using an optical technique. Temperatures were measured with either a color-ratio optical pyrometer or a disappearing filament pyrometer corrected for the emissivity of molybdenum. The apparatus and procedures are described more completely in a previous paper concerning oxidation of tungsten (8). Commercially pure molybdenum was used. The major impurities determined by spectrographic analysis were silicon 0.12%, iron 0.22%, and nickel 0.089%.

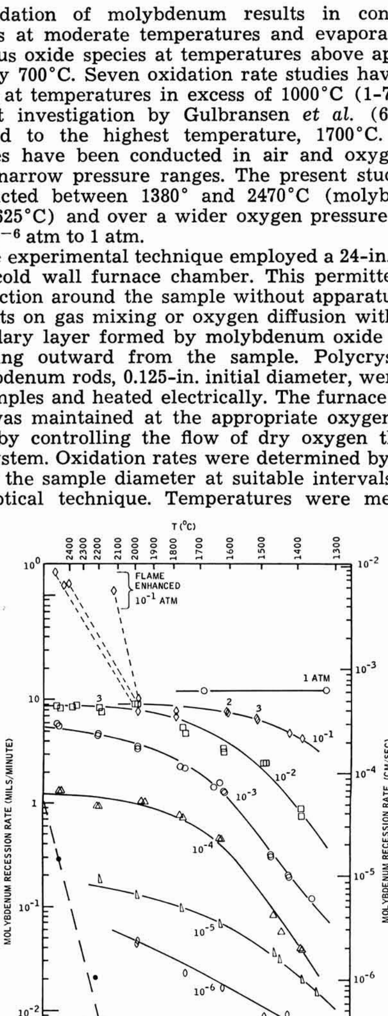

Fig. 1. Arrhenius plot of recession rate of molybdenum; isobars at indicated system oxygen pressure.

The surface recession data conformed with a linear rate law. This condition is consistent with either a surface reaction or transport within the gas boundary film acting as the rate controlling step. An Arrhenius plot of the rate data is shown in Fig. 1. Evaporation rates measured at a total pressure below 1 x 10^{-7} atm are plotted in the lower left-hand corner of Fig. 1. These data show that evaporation of molybdenum was not affecting the oxidation rates in Fig. 1.

Oxidation products were transported away from the sample and deposited on the chamber walls. X-ray diffraction analysis of several samples of this powder residue indicated MoO_3 to be the principal constituent. Variable amounts of Mo_9O_{26}, always below 30%, were also present in these samples.

The oxidation behavior of molybdenum at high temperatures is similar to the oxidation behavior of tungsten (8). The rate has an exponential temperature dependence at lower temperatures that is typical of chemical systems. Since the activation energy is too high for gaseous diffusion, an activation energy barrier at the surface is indicated. Above 1700°C the oxidation rates become less sensitive to temperature. Near the melting point the rate is independent of temperature provided the oxygen pressure is above 10^{-5} atm. The bends in the oxidation rate isobars plotted in Fig. 1 occur in the same temperature range as for tungsten. However, because of the lower melting point of molybdenum, an extended temperature region in which the rate was independent of temperature was not observed. The molybdenum oxidation rates are slightly lower at high pressures and considerably higher at low pressures than the corresponding tungsten oxidation rates. The change in temperature dependence of the rate suggests a transition in rate-controlling step from a chemically activated process to a gas kinetic process at high temperatures. For both processes, the boundary layer present at higher pressures probably affects the results by lowering the oxygen partial pressure at the surface compared with the oxygen pressure beyond the boundary layer. Although a boundary layer analysis was not attempted, the rate results are valid for any free convection application of molybdenum.

Comparisons with other investigators are difficult because of the variable effects caused by different experimental systems on the boundary layer. Gulbransen *et al.* (6) measured molybdenum oxidation rates in 0.1 atm of oxygen. Their samples were oxidized in a closed end tube which probably restricted oxygen input and oxide vapor purging. This system complicates the boundary layer analytical problem, but it makes the rate more sensitive to gas flow at moderate

---

[1] Present address: Stanford Research Institute, Menlo Park, California.

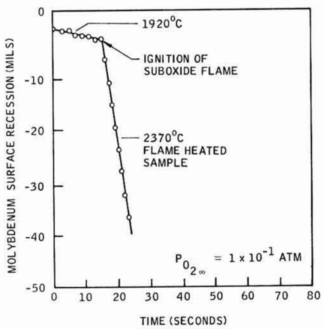

Fig. 2. Transition in the oxidation rate of molybdenum caused by ignition of the suboxide diffusion flame at 15 sec.

velocities than an open system. Their fastest rate data are consistent with the rate data at equivalent temperatures and pressures (10^{-1} atm) from this study. Rosner and Allendorf (7) measured the oxidation rate in an oxygen partial pressure of 3 x 10^{-2} Torr (4 x 10^{-5} atm) and reported molybdenum/oxygen molecule reaction probabilities. Their data were converted to equivalent slab recession rates, assuming a gas temperature of 300°K. An extrapolation of these rates to 1400°C joins the 1 x 10^{-4} atm Arrhenius isobar of Fig. 1, which is fair agreement. The molybdenum oxidation rates observed by Modisette and Schryer (4) in slow moving air above 1400°C vary between 1.3 and 2.8 mils/min. This rate is about 1/5 the oxidation rate in pure oxygen of the same partial pressure, 0.21 atm, observed in the present study. A lowered rate in air is expected because nitrogen impedes diffusion of oxygen in the boundary layer.

The most interesting aspect of oxidizing molybdenum at high temperatures and pressures is a large discontinuous increase in rate observed at oxygen pressures near 1 atm. This change in rate was accompanied by a sudden rise in temperature even when external heating was removed. Furthermore, the samples were surrounded by a typical gas flame, indicating the combustion of fuel in the gas phase rather than on the surface of the metal rod. Although oxidation of tungsten at 10^{-1} atm and 1 atm was self-supporting at high temperatures once initiated, the flame phenomena and discontinuous increases in rate were not observed with tungsten (8). The transition in behavior associated with flame ignition was easily distinguished. Rods burning normally without an accompanying flame appeared as bright incandescent objects. The surrounding cloud caused by condensation of molybdenum oxide particles could only be detected by reflected light. After flame ignition the reverse in light intensity occurred. The incandescent rod could not be visually distinguished from the flame surrounding it unless filters were used. Prior to ignition, temperature could not be detected by optical pyrometry within the vapor cloud. After ignition, the color temperature of the flame, measured by a color ratio optical pyrometer, varied from 2200° to 2500°C in 0.1 atm of oxygen and between 2700° and 2800°C in 1 atm of oxygen. These temperatures were recorded using fields of view which excluded the sample. The high flame temperature associated with an oxygen pressure of 1 atm caused the sample to melt within a few seconds after ignition of the flame.

Table I. Effect of the diffusion flame on molybdenum recession rates at high temperatures (temperature independent region) and high oxygen pressures

	$P_{O_2} = 0.1$ atm	$P_{O_2} = 1$ atm
Avg. rate without flame	9 mils/min	12 mils/min
Avg. rate with flame	133 ± 25 mils/min	470 mils/min*

* Burn out prevented accurate rate data acquisition on four other samples.

Sample diameters were measured photographically using filters. A typical rate curve resulting from gas flame enhanced oxidation is shown in Fig. 2. Oxidation of the sample continued to obey a linear rate law after ignition but proceeded at a much faster rate. The flame enhanced oxidation rates at 0.1 atm were included in the Arrhenius plot, Fig. 1; average values are listed in Table I.

In experiments conducted at both 0.1 atm and 1 atm oxygen pressures, ignition of the flame did not occur unless a temperature above approximately 1900°C was used. This temperature corresponds with the temperature at which the suboxide, $MoO_2(g)$, becomes appreciably more prevalent than $MoO_3(g)$ as the oxidation product determined by Berkowitz-Mattuck *et al.* (10), using mass spectrometric methods. This relation indicates that the flame results from the outward diffusion of the $MoO_2(g)$ and the subsequent reaction of $MoO_2(g)$ with oxygen to produce $MoO_3(g)$. Polymerization reactions are also strongly exothermic in this system. The heat released by these chemical reactions can account for the gaseous diffusion flames observed. The reactions are summarized as follows: neglecting the small amount of $MoO_3(g)$ produced at the metal surface, the primary surface oxidation reaction is formation of the molybdenum dioxide monomer

$$Mo + O_2 \rightarrow MoO_2(g)$$

The net secondary reaction in the gas phase, including oxidation and polymerization to the dominant equilibrium species $(MoO_3)_3(g)$, is

$$\frac{3}{2} O_2 + 3MoO_2(g) \rightarrow (MoO_3)_3(g)$$

$$\Delta H^\circ = -598 \text{ kcal/mole of product}$$

This reaction is 50% more exothermic than the equivalent reaction in the tungsten system (11, 12)

$$\frac{3}{2} O_2 + WO_2(g) \rightarrow (WO_3)_3(g)$$

$$\Delta H^\circ = -405 \text{ kcal/mole}$$

This difference in released heat provides a possible explanation for the presence of the diffusion flame with molybdenum under conditions where it was not observed with tungsten.

The casual relation between the adjacent diffusion flame and the increased metal surface oxidation rate is uncertain. The increased turbulence and temperature in the boundary layer caused by the flame may explain the rate increase. Analysis of mass transfer in turbulent boundary layers and flames is complex and was not attempted.

Acknowledgment

This research was sponsored by the Air Force Materials Laboratory, Research and Technology Division, Air Force Systems Command, U. S. Air Force. The author is indebted to Dr. W. M. Fassell, Jr., and Mr. J. P. Pope for assistance in conducting this investigation.

Manuscript received Nov. 16, 1964; revised manuscript received Feb. 16, 1965.

Any discussion of this paper will appear in a Discussion Section to be published in the June 1966 JOURNAL.

REFERENCES

1. C. R. Wilks, "Effects of Temperature, Pressure and Mass Flow on Oxidation of Molybdenum," SAMPE Eastern Division Meeting, MIT, Cambridge, Mass., May 1960.
2. E. S. Bartlett and D. N. Williams, *Trans. AIME*, **212**, 280 (1958).
3. North American Aviation, Inc., "High Temperature Oxidation of Molybdenum Under High Altitude

Conditions," Air Force Contract AF 33(600)-28469, ASTIA No. 147839, NAA Rept. No. AL-2617, Sept. 1957.
4. J. L. Modisette and D. R. Schryer, "An Investigation of the Role of Gaseous Diffusion in the Oxidation of a Metal Forming a Volatile Oxide," NASA Tech. Note D-222, March 1960.
5. J. W. Semmel, Jr., "High Temperature Materials," pp. 510-19, J. Wiley & Sons, Inc., New York (1959).
6. E. A. Gulbransen, K. F. Andrew, and F. A. Brassart, *This Journal*, **110**, 952 (1963).
7. D. E. Rosner and H. D. Allendorf, *J. Chem. Phys.*, **40**, 3441 (1964).
8. R. W. Bartlett, *Trans. AIME*, (in press).
9. R. B. Bird, W. E. Stewart, and E. L. Lightfoot, "Transport Phenomena," Chap. 16, J. Wiley & Sons, Inc., New York (1960).
10. J. B. Berkowitz-Mattuck, A. Büchler, J. L. Engelke, and S. N. Goldstein, *J. Chem. Phys.*, **39**, 2722 (1963).
11. P. E. Blackburn, M. Hoch, and H. L. Johnston, *J. Phys. Chem.*, **62**, 769 (1958).
12. J. Berkowitz, W. A. Chupka, and M. G. Inghram, *J. Chem. Phys.*, **27**, 85 (1957).

Effect of Concentration on the Fluorescence of Samarium in Cerium Dioxide

Michael Kestigian, Ronald H. Curry, and Fredric D. Leipziger

Sperry Rand Research Center, Sudbury, Massachusetts

This note is concerned with the effect of concentration on the fluorescence of samarium in cerium dioxide. A study of the spectral properties of rare earth phosphors was recently carried out by Ropp (1). This investigation was concerned with rare earth sesquioxide systems. The existence of a samarium-activated cerium-dioxide phosphor was first reported by Tomaschek (2).

Experimental Procedure

Cerium-dioxide samples in which the molar concentration was 0.01% or less were prepared by the addition of appropriate amounts of a solution of samarium ion to cerium dioxide. These preparations were completely dried, ground in an agate mortar, and calcined in platinum vessels at 1350°C in oxygen for 12 hr. On removal from the furnace, the specimens were cooled, reground, and the calcination procedure repeated. An oxygen atmosphere was used in the calcination process to ensure the formation of stoichiometric cerium dioxide. Cerium-dioxide samples in which the molar concentration of samarium was greater than 0.1% were prepared from the oxides. These preparations were ground under ethanol, dried, and calcined as outlined above. The cerium dioxide used was prepared from the oxalate by decomposition in an oxygen atmosphere (3). The chemicals were all reported to be 99.9+% pure.

The fluorescence was measured using a Jarrell-Ash 82-00 monochromator equipped with a 15,000 lpi grating, a fixed-slit width of 100μ, and a slit height of 5 mm. An EMI-9558A photomultiplier tube (S-20) was used as a detector. Standard amplification and recording techniques were applied. The excitation radiation used to record the samarium fluorescence was 3600Å. The intensity of the fluorescence observed with 2537Å excitation was insufficient for quantitative recording of the spectrum.

The samarium content of the cerium-dioxide samples was analyzed by a mass spectrograph using an AEI-MS7 spark-source instrument. The powdered specimens were mixed with equal weights of pure graphite powder and pressed into 1/8 x 3/4 in. electrodes. The electrodes were sparked for a sufficient length of time to produce sensitivities of 1 in 10^{-8}. Analysis for samarium was performed by measuring the lines produced by the Sm^{147} and Sm^{149} isotopes. These lines were free of interference from other rare earth metals and rare earth oxides. Ilford Q-II plates were used to record the spectra and were developed and measured using standard techniques.

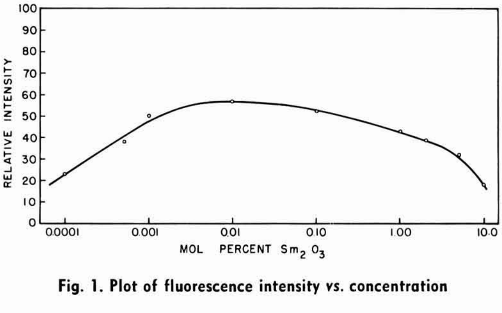

Fig. 1. Plot of fluorescence intensity vs. concentration

Experimental Results

Spectrographic studies indicated that four peaks were present in the fluorescence spectra of samarium-activated cerium dioxide. These were located at 573, 607, 615, and 621 mμ. Only the 573 and 615 mμ peaks were strong enough to be studied quantitatively. The decision to study the concentration dependence of samarium in cerium dioxide by investigation of the 573 mμ line was made because of the better signal-to-noise ratio of the photoelectric instrument described above. This fluorescence (573 mμ) was observed at concentrations as low as 10^{-4} mole % Sm_2O_3. A plot of fluorescence intensity versus concentration is shown in Fig. 1. Referring to the figure, it can be seen that the fluorescence intensity shows a slow increase with increased samarium-oxide concentration to a broad maximum at about 0.01 mole % followed by a decrease to a concentration of about 10 mole % Sm_2O_3. The fluorescence was not detectable at concentrations above 10 mole % Sm_2O_3. It was surprising that the maximum in the fluorescence-intensity curve occurred at so low a concentration. In most examples of concentration quenching, the effect does not become significant until concentrations of the order of 1% are reached. To what extent these anomalies are due to the use of finely divided powders or truly represent intrinsic material properties is not clear at this point.

In the course of this investigation, it was observed that numerous high-purity cerium compounds exhibited the same fluorescence described above. The fluorescence was observed in some cerium-dioxide samples in the "as-is" condition, while in other cerium-dioxide and cerium containing raw materials the fluorescence became visible only after calcination at high temperature. These samples were all found to be contaminated with other rare earths in concentrations ranging from 0.05 to 100 ppm. Samarium was present as an impurity in all cerium-dioxide samples which exhibited the fluorescence. The level of samarium ranged from 5 to 50 ppm ±50%.

Summary

The fluorescence of samarium as a function of concentration in a cerium-dioxide matrix has been investigated. Fluorescence is observed when only a few ppm Sm are present in CeO_2. The fluorescence intensity increases with concentration until 0.01 mole % Sm_2O_3 has been added, after which concentration quenching sets in and the fluorescence intensity decreases with increased Sm concentration.

Acknowledgment

The authors gratefully acknowledge Dr. Roger Newman for helpful discussions and comments.

Manuscript received Nov. 12, 1964.

Any discussion of this paper will appear in a Discussion Section to be published in the June 1966 JOURNAL.

REFERENCES

1. R. C. Ropp, *This Journal*, **111**, 311 (1964).
2. R. Tomaschek, *Z. Elektrochem.*, **36**, 737 (1930).
3. A. Glasner and M. Steinberg, *Bull. Research Council, Israel*, **8A**, 174 (1959).

Epitaxial Growth of GaAs Through Cracks in SiO_2 Masks

M. Michelitsch

International Business Machines Corporation Laboratories, Boeblingen, Germany

SiO_2 layers several thousand Ångströms thick on GaAs wafers have shown excellent masking characteristics against epitaxial growth and diffusion (1, 2). Such films are commonly produced by pyrolytic decomposition of gaseous $Si(C_2H_5O)_4$ on GaAs wafers at several hundred degrees centigrade. About 5000Å can easily be obtained within 30 min.

Figure 1 shows the epitaxial growth apparatus. It consists of three quartz tubes, 20 mm in diameter. Two of these contain the separate source materials As and Ga (and if desired a dopant such as Se), the third one the GaAs wafer (seed). The source tubes are connected with the seed tube by capillaries 1 mm in diameter. To prevent deposition on the outer wall of the seed tube it is lined with a separate removable tube, which is surrounded by a H_2 counter flow. By changing the direction of the H_2 counter flow "growth" or "no growth" can be obtained. For no growth, the reaction gases pass through only the source tubes (HCl/H_2 in the Ga tube, H_2 in the As tube), and the reaction at the source materials can reach a steady state. The gases leave the system through valves A and B. Because of a hydrogen counter flow through the seed tube and the capillaries to the source tubes, no growth can occur. For growth, valves A and B are closed and valve C is opened. The reacted gases from the source tubes enter a mixing chamber through both capillaries near the quartz observation window. From there the gas mixture passes over the seed and leaves the system through the liner tube and valve C.

Each tube is heated by a separate furnace with three heating zones each. The observation window (mixing chamber) is heated by a separate small furnace to prevent GaAs deposition there. By means of a long focus microscope it is possible to observe the growth process while it occurs.

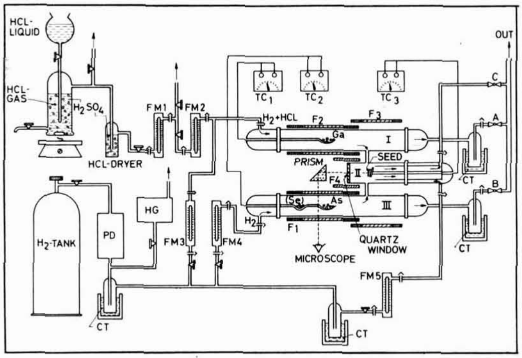

Fig. 1. Ga-As-HCl-H_2 synthesis system: FM, flow meters; TC, thermocouples and millivoltmeters; CT, cold traps (liquid nitrogen); PD, puridrier; HG, hygrometer; F_i, furnaces; I, Ga-tube; II, seed tube; III, As tube; A, B, C, valves.

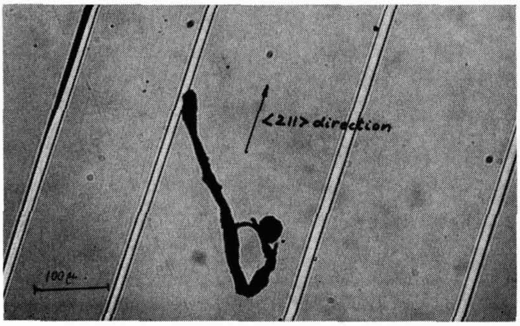

Fig. 2. SiO_2 covered GaAs (111) surface with epitaxial depositions through <211> oriented cracks.

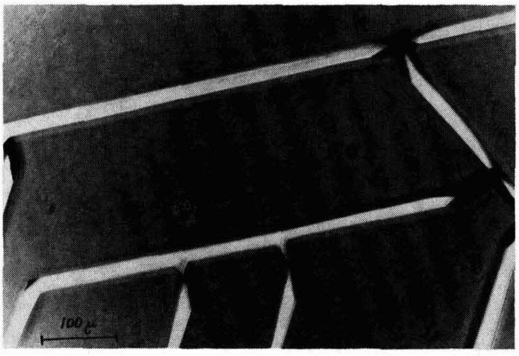

Fig. 3. *Epitaxial deposition through <211> oriented cracks intersecting at 60°.*

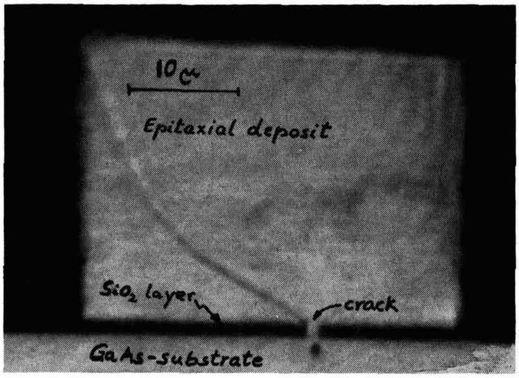

Fig. 4. Cross section (cleaved) of a crack with epitaxial overgrowth.

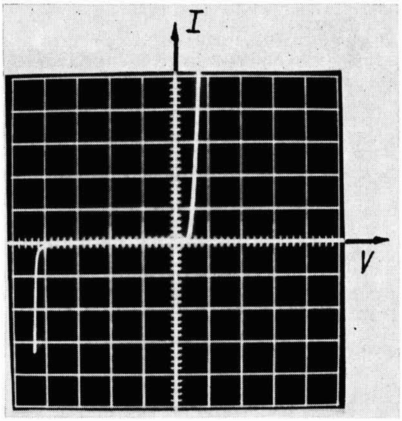

Fig. 5. I-V characteristic of a "crack diode" (substrate approx. 10^{18} cm^{-3} Zn-doped, epitaxy 5 x 10^{17} cm^{-3} Se-doped). Vertical, 0.1 ma/div; horizontal: 2v/div.

Typically the temperature at the Ga boat was 500°C, at the As boat 450°C, at the mixing chamber 900°C, and at the seed 780°C. The flow rates were 10 and 70 cm^3/min HCl and H_2, respectively, in the Ga tube, and 70 cm^3/min in the As tube.

During investigations of the epitaxial growth of GaAs on partially SiO_2 masked GaAs (111)-substrates, cracks in the SiO_2 layers were frequently observed during heat-up, which were due to differential thermal expansion of the SiO_2 and GaAs. Cracking occurs if the SiO_2 layer is thicker than about 5000Å. The cracks described in the following were about 0.5-1μ wide, several millimeters long, and parallel to <211> directions in the (111) oriented substrate. The bottoms of the cracks serve as nucleation sites for epitaxial growth. Once the cracks are filled up with epitaxial material, the growth spills over the SiO_2 layer (Fig. 2, 3, 4). Overgrowth 25μ high was produced in 2 min. Although the growth rate is rather high, it is consistent with rates obtained on uncoated substrates under similar conditions, and the material grown through the cracks which was examined by electron diffraction was shown to be monocrystalline having the same orientation as the substrate.

As the cleavage planes in GaAs are {110}, the line of intersection of the cleavage planes with a (111) surface lies in the <211> direction. It is therefore possible to produce long and narrow GaAs bars by cleaving. If the epitaxial layer has the opposite conductivity type to the substrate, GaAs diodes with long but extremely narrow junctions can be obtained. The electrical characteristics (Fig. 5) of such narrow vapor growth junctions are usually better than those of junctions grown on chemically cleaned GaAs substrates. This is due to the extreme cleanliness of GaAs surface in the cracks, which are not formed until the heat-up, just prior to deposition.

With proper doping this method should be useful for producing laser diodes. Other structures, such as, for example, narrow heterojunctions are possible.

Acknowledgments

The author wishes to thank Dr. G. Hellbardt for suggesting the design of the vapor growth furnace, Mr. K. Brack for performing the electron diffraction measurements, Miss H. Leistikow for performing the SiO_2 masking of the GaAs wafers, and Mr. C. E. Kelly for preparing Fig. 3.

Manuscript received Nov. 22, 1964.

Any discussion of this paper will appear in a Discussion Section to be published in the June 1966 JOURNAL.

REFERENCES

1. S. W. Ing, Jr., and W. Davern, *This Journal,* **111,** 120 (1964).
2. S. R. Shortes, J. A. Kanz, and E. C. Wurst, Jr., *Trans. Met. Soc. AIME,* **230,** 300 (1964).

Transpiration Studies of the Gallium-Hydrogen Iodide-Hydrogen System

V. J. Silvestri

International Business Machines Corporation, Watson Research Center, Yorktown Heights, New York

The transport of gallium by means of hydrogen iodide is of interest because of its importance in gallium arsenide synthesis and epitaxial growth systems (1). In addition, hydrogen iodide has been useful for transporting gallium as a dopant during the epitaxial growth of germanium (2).

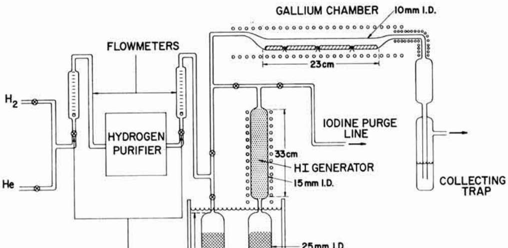

Fig. 1. Schematic representation of the flow system employed for transpiration studies.

In a recent thermodynamic evaluation of the Ga-HI-H_2 system, the conditions of temperature and pressure under which the efficient transport of gallium occurs were discussed (3). The application of these data to an experimental flow system requires that equilibrium be assured at the gallium bed. It was therefore the purpose of this investigation to determine gas flow conditions under which a hydrogen iodide-hydrogen mixture comes into equilibrium with a gallium source. The measurements also served to check the validity of the thermodynamic data employed in the evaluation of the system.

Apparatus and Experimental Procedure

Figure 1 depicts schematically the flow system used. It consists of an iodine chamber followed by a hydrogen iodide generator, a gallium bed, and a collecting trap. The gases used were purified with molecular sieves,[1] to remove oxygen, primarily to avoid oxidation of the gallium. The latter presented a surface area of approximately 23 cm^2 to the flowing gas stream.

---

[1] J. Mickel Associates.

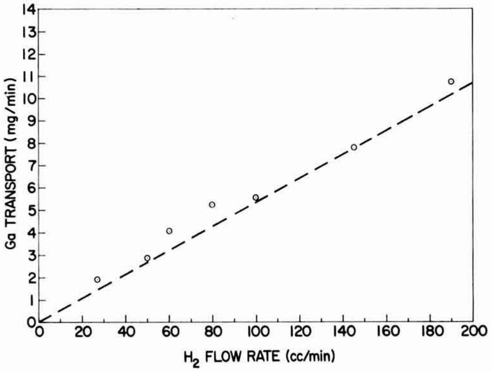

Fig. 2. Gallium transport as a function of hydrogen flow rate. Pressure of HI, 21.4 Torr; gallium temperature 433.4°C. Broken line represents the thermodynamically predicted gallium transport; ⊙, experimental values.

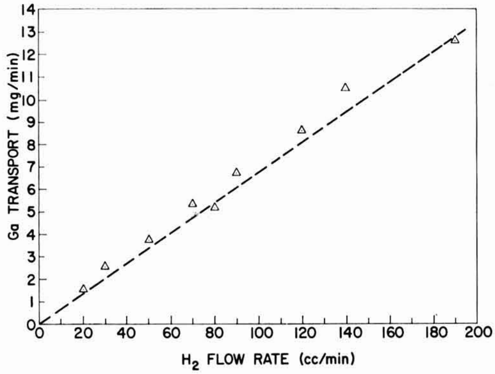

Fig. 3. Gallium transport as a function of hydrogen flow rate. Pressure of HI, 34.4 Torr; gallium temperature 408.8°C. Broken line represents the thermodynamically predicted gallium transport; △, experimental values.

For the experiments, monitored flows of hydrogen were passed through calibrated flow meters into the iodine source. The iodine bed was designed on the basis of previous iodine evaporation studies (4) such that vapor saturation would be achieved in this chamber. The temperature at the iodine source was controlled to ±0.5°C in a thermostated water bath. The catalysis of the reaction between hydrogen and iodine was effected by the platinum wool at 300°C, and the effluent from this column was then carried into the gallium bed. Here the following reactions to form gallium iodides occurred:

$$\mathrm{Ga(l)} + 3\mathrm{HI(g)} \rightleftarrows \mathrm{GaI_3(g)} + 3/2\mathrm{H_2(g)}$$
$$2\mathrm{Ga(l)} + \mathrm{GaI_3(g)} \rightleftarrows 3\mathrm{GaI(g)} \quad (5)$$

The resulting iodides were collected in the two sectioned trap shown at the end of the system in Fig. 1. Condensation of the iodides occurred for the most part in the upper portion of the cold trap. The lower section contained a 6*N* KOH solution where any products escaping the freezeout zone were dissolved. The contents of both regions were then analyzed, using wet chemical techniques, for gallium and iodine.

Two different hydrogen iodide input pressures (21.4 and 34.4 Torr) were used at two different gallium bed temperatures (433.4° and 408.8°C), respectively, and for each set of conditions the amounts of gallium and iodine collected were determined for various flow rates. Experimental pressures and temperatures were chosen on the basis of thermodynamic calculations made specifically for a gallium arsenide flow system (1).

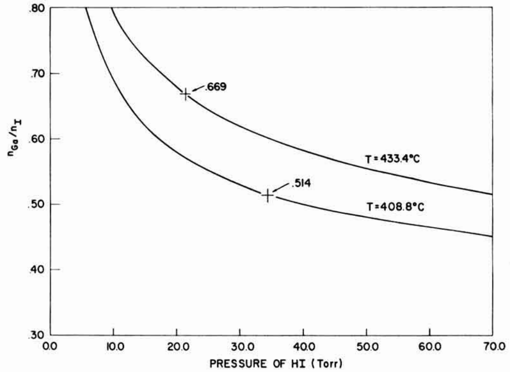

Fig. 4. Equilibrium data extracted from ref. (3) showing the predicted molar gallium to iodine ratio as a function of an initial pressure of HI entering a gallium bed at the indicated temperatures.

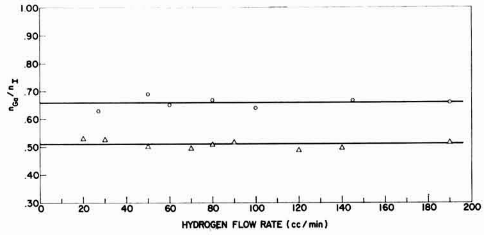

Fig. 5. Experimentally determined gallium to iodine molar ratios plotted as a function hydrogen flow rate: ⊙, pressure of HI, 21.4 Torr, gallium temperature 433.4°C; △, pressure of HI, 34.4 Torr, gallium temperature 408.8°C.

Results and Discussion

In order to determine whether equilibrium is achieved the data may be plotted in several ways. A comparison of either the gallium transport rate or the gallium to iodine ratio with those predicted thermodynamically may be made. Data as given below provide both comparisons.

In Fig. 2 and 3 the gallium transport rate has been plotted as a function of hydrogen flow rate for the two experimental conditions previously described. The agreement of the experimentally obtained values with the theoretical rates shows equilibrium was achieved for all flow rates.

In Fig. 4 the predicted (3) gallium to iodine molar ratios have been plotted for the two temperatures under consideration as a function of the initial pressure of hydrogen iodide entering a gallium source. For the experimental hydrogen iodide pressures employed, the indicated predicted ratios in Fig. 4 are obtained. Figure 5 presents the experimentally determined molar gallium to iodine ratios as a function of hydrogen flow rate. As would be expected from Fig. 2 and 3 the ratio is constant and the values are in close agreement with the predicted values in Fig. 4.

Acknowledgment

The author wishes to thank B. L. Olsen of IBM's analytical group for his part in the work and to acknowledge the helpful discussions with H. Leonhardt, A. Reisman, and S. A. Alyanakyan.

Manuscript received Jan. 15, 1965. This paper was presented at the Washington Meeting, Oct. 11-15, 1964. The work was supported in part by AFCRL Contract No. AF19(628)-2468.

Any discussion of this paper will appear in a Discussion Section to be published in the June 1966 JOURNAL.

REFERENCES

1. H. R. Leonhardt, *This Journal*, **112**, 237 (1965).
2. A. Reisman, Private communication.
3. A. Reisman and S. A. Alyanakyan, *This Journal*, **111**, 1154 (1964).
4. A. Reisman, M. Berkenblit, and S. A. Alyanakyan, *ibid.*, **112**, 241 (1965).
5. V. J. Silvestri and V. J. Lyons, *ibid.*, **109**, 963 (1962).

Theoretical Electromotive Forces for Cells Containing a Single Solid or Molten Fluoride, Bromide, or Iodide

Walter J. Hamer, Marjorie S. Malmberg,[1] and Bernard Rubin[2]

National Bureau of Standards, Washington, D. C.

In a previous paper (1) an electromotive force series for solid and molten chlorides was presented for temperatures ranging from 25° to 1500°C. This series was based on the Gibbs energy (free energy) of formation of the respective solid and molten chlorides and corresponded to the reversible emfs of cells of the type

metal | metallic chloride | chlorine gas [1]

It was also shown that it was unnecessary for practical purposes to divide the emfs into separate anodic and cathodic potentials, although one could assume that the potential of the chlorine electrode is zero (2) for each solid or molten chloride; the potential of each metal would then be, by convention, equal to the emf of the whole cell [1].

In this paper similar series are given for solid and molten fluorides, bromides, and iodides. These are given, respectively, in series arrangement, in Tables I, II, and III. A heavy vertical line in the tables indicates that the values to the left of the line are for solid halides while those to the right are for molten halides. When a sublimation, vaporization, or decomposition temperature is given in parenthesis, the emf directly above it is for that temperature rather than for the one heading the column. These potentials are given a positive sign here to be consistent with the procedure followed in the previous paper (1) on the chlorides. The emfs, therefore, correspond to the Gibbs energy of formation of the respective halides. If the Stockholm convention (3) were followed the opposite sign would be used and the emfs would correspond to the Gibbs energy of decomposition of the halides. As was done previously the Gibbs energies used were those published by Brewer (4) or the National Bureau of Standards (5) and the heat capacities used were those published by Kelley (6). In some cases the necessary heat capacity data were not available. In those cases the values were estimated using either the Kelley rule (7), namely, 7.0 thermochemical calories per degree C and mean gram-atom for solid compounds, 8.0 for liquid compounds, 7.3 for solid metals, and 7.5 for liquid metals, or the Shomate method (8) using the enthalpy and heat capacity data given by the National Bureau of Standards (5). Other compilations of thermochemical data are available, for example, the "Janaf Thermochemical Tables," Dow Chemical Company, Midland, Michigan, Loose Data Sheets, 1960—. Although these new compilations are undoubtedly in a better state of revision than NBS Circular 500 the latter source was adhered to here so that the fluoride, bromide, and iodide series, here presented, would be internally consistent with the chloride series previously published (1). The necessary equations and the sequence of the calculations for obtaining the emfs at different temperatures were given in the previous paper and need not be repeated here.

The uncertainties in emf listed in the tables for the solid cell at 25°C correspond to the uncertainties in the enthalpy of formation of the halides at 25°C quoted by Brewer; these uncertainties were assumed to apply also to the data in the National Bureau of Standards Circular (5) since these values agree closely with those of Brewer and the sources of the two sets of data are nearly the same. The uncertainties in entropy values are generally small compared to those in enthalpy values and accordingly the uncertainties in emf here listed are based on uncertainties in enthalpy rather than Gibbs energies of formation. In addition, the authors are more concerned with the order of the respective halides in any one series than with the actual values and these orders will probably remain the same whether the uncertainties are based on enthalpies or Gibbs energies.

It is emphasized here, as in the previous paper on the chlorides, that these emfs are for theoretical cells, *i.e.*, for ones in which there is no interaction between the metals or the halogen with the halides, no solubilities of the metals in the halides, or vice versa, or any other factors that would lead to deviations of the metals, the halides, or the halogens from their standard states. These emfs nevertheless have value in serving to indicate if deviations from the ideal state are present in actual cells.

In each table the values for the aqueous cell at 25°C are given for comparison (9). Since for these solid and molten systems at high temperatures, bromine and iodine exist as gases, the data for the aqueous system in these cases are for the gaseous state even though the stable state at this temperature is the liquid and solid, respectively. The emfs for liquid bromine and solid iodine for aqueous systems at 25°C would be 0.016v and 0.100v lower, respectively, than those given in the tables. In each case it may be noted that the order of the elements does not parallel that of the aqueous system. Furthermore, the orders for the solid and molten fluorides, chlorides (1), bromides, and iodides are not the same, *i.e.*, there is not a constant difference between any two halide series. Relative reducing power of an element, magnesium for example, must be confined to a single halide series. For example, if lithium were placed in fused barium fluoride it would displace the barium (1) with the formation of lithium fluoride, thus

$$2Li + BaF_2 \rightarrow 2LiF + Ba$$

However, in fused bromides or iodides the reverse would occur, namely

$$Ba + 2LiBr \text{ (or LiI)} \rightarrow BaBr_2 \text{ (or } BaI_2) + 2Li$$

Manuscript received Nov. 4, 1964.

Any discussion of this paper will appear in a Discussion Section to be published in the June 1966 JOURNAL.

REFERENCES

1. W. J. Hamer, M. S. Malmberg, and B. Rubin, *This Journal*, **103**, 8 (1956).
2. R. W. Laity, "Reference Electrodes," D. J. G. Ives

---

[1] Present address: Department of Chemistry, University of Maryland, College Park, Maryland.

[2] Present address: AF Cambridge Research Laboratories, Office of Aerospace Research, L. G. Hanscom Field, Bedford, Massachusetts.

and G. J. Janz, Editors, Chap. 12, Academic Press, New York (1961).
3. J. A. Christiansen and M. Pourbaix, *Compt. rend. conf. union intern. chim. pure et appl., 17th Conf., Stockholm*, p. 83 (1953).
4. L. Brewer, "The Chemistry and Metallurgy of Miscellaneous Materials, Thermodynamics," L. L. Quill, Editor, McGraw-Hill Book Co., Inc., New York (1950).
5. "Selected Values of Chemical Thermodynamic Properties," *Nat. Bur. Standards, Circ.* 500 (1952); also Series III (1948-1953).
6. K. K. Kelley, *U. S. Bur. Mines, Bull.* 383(1935), 393(1936), 476(1949), 584(1960).
7. Ref. 6, *Bull.* 476, p. 206.
8. C. H. Shomate, *J. Am. Chem. Soc.*, **66**, 928 (1944).
9. W. M. Latimer, "The Oxidation States of the Elements and Their Potentials in Aqueous Solutions," 2nd ed., Prentice-Hall, Inc., New York (1952).

Table I. Standard electromotive forces for single, solid, or molten metallic fluorides*

		E°														
Order 25°C	Metal ion	25°C (aqueous) v	25°C (solid) v	Uncertainty (25°C) v	100°C v	200°C v	300°C v	350°C v	400°C v	450°C v	500°C v	550°C v	600°C v	800°C v	1000°C v	1500°C v
1	Eu^{+2}	6.266	6.234	±0.15	6.167	6.080	5.996	5.955	5.914	5.874	5.834	5.795	5.756	5.602	5.453	| 5.101
2	Li^{+1}	5.911	6.054	±0.09	5.981	5.881	5.775	5.722	5.669	5.617	5.564	5.512	5.461	5.256	| 5.071	4.495
3	Ca^{+2}	5.736	6.021	±0.01	5.953	5.864	5.776	5.732	5.689	5.646	5.603	5.560	5.517	5.350	5.182	| 4.785
4	Sm^{+2}	<6.03	6.017	±0.15	5.950	5.863	5.779	5.738	5.698	5.657	5.617	5.578	5.539	5.385	5.236	4.884
5	Sr^{+2}	5.756	6.012	±0.002	5.943	5.854	5.768	5.726	5.684	5.643	5.602	5.562	5.522	5.364	5.203	| 4.768
6	Ba^{+2}	5.766	5.952	±0.02	5.885	5.797	5.712	5.670	5.629	5.588	5.547	5.507	5.468	5.310	5.154	| 4.803
7	Ra^{+2}	5.786	5.941	±0.07	5.871	5.781	5.694	5.651	5.608	5.566	5.524	5.483	5.442	5.277	5.111	4.566
8	La^{+3}	5.386	5.811	±0.10	5.743	5.656	5.571	5.530	5.489	5.448	5.408	5.368	5.329	5.174	5.020	4.648
9	Ce^{+3}	5.346	5.739	±0.10	5.671	5.584	5.499	5.457	5.416	5.376	5.335	5.295	5.255	5.097	4.938	4.555
10	Pr^{+3}	5.336	5.710	±0.10	5.645	5.563	5.483	5.444	5.405	5.367	5.329	5.291	5.254	5.109	4.965	4.621
11	Nd^{+3}	5.306	5.652	±0.10	5.584	5.496	5.411	5.369	5.327	5.286	5.245	5.204	5.164	5.004	4.843	4.458
12	Pm^{+3}	5.286	5.637	±0.10	5.573	5.490	5.410	5.370	5.332	5.294	5.256	5.218	5.181	5.035	4.894	4.560
13	Na^{+1}	5.580	5.607	±0.01	5.534	5.429	5.325	5.273	5.221	5.170	5.119	5.068	5.017	4.818	4.529	3.781
14	Sm^{+3}	5.276	5.594	±0.10	5.530	5.447	5.367	5.328	5.289	5.250	5.213	5.175	5.138	4.992	4.850	4.517
15	Gd^{+3}	5.266	5.580	±0.10	5.515	5.433	5.352	5.313	5.274	5.236	5.198	5.161	5.123	4.977	4.836	4.504
16	K^{+1}	5.791	5.525	±0.02	5.446	5.338	5.230	5.176	5.123	5.070	5.017	4.965	4.913	4.674	4.355	3.630
17	Tb^{+3}	5.256	5.522	±0.10	5.457	5.375	5.295	5.255	5.217	5.178	5.140	5.103	5.065	4.920	4.778	4.447
18	Dy^{+3}	5.216	5.493	±0.10	5.429	5.346	5.266	5.226	5.188	5.149	5.111	5.074	5.036	4.891	4.749	4.419
19	Y^{+3}	5.236	5.478	±0.10	5.414	5.331	5.251	5.212	5.173	5.135	5.097	5.059	5.022	4.876	4.735	4.407
20	Ho^{+3}	5.186	5.449	±0.10	5.385	5.302	5.222	5.183	5.144	5.106	5.068	5.030	4.993	4.847	4.706	4.376
21	Mg^{+2}	5.236	5.438	±0.02	5.369	5.278	5.188	5.144	5.100	5.056	5.013	4.969	4.926	4.746	4.567	3.994
22	Rb^{+1}	5.791	5.421	±0.04	5.348	5.250	5.153	5.105	5.057	5.009	4.961	4.913	4.865	4.583	4.274	| 3.670
23	Lu^{+3}	5.116	5.407	±0.10	5.342	5.259	5.179	5.140	5.100	5.062	5.025	4.987	4.950	4.804	4.662	4.336
24	Er^{+3}	5.166	5.406	±0.10	5.342	5.259	5.179	5.140	5.101	5.063	5.025	4.987	4.950	4.804	4.662	4.333
25	Eu^{+3}	5.276	5.392	±0.10	5.327	5.245	5.164	5.125	5.086	5.048	5.010	4.973	4.935	4.790	4.648	4.316
26	Tm^{+3}	5.146	5.392	±0.10	5.327	5.245	5.164	5.125	5.086	5.048	5.010	4.973	4.935	4.789	4.648	4.320
27	Cs^{+1}	5.789	5.217	±0.01	5.140	5.037	4.935	4.884	4.833	4.783	4.733	4.682	4.632	4.367	4.055	| 3.677
28	Yb^{+3}	5.136	5.175	±0.10	5.111	5.028	4.948	4.908	4.870	4.831	4.793	4.756	4.719	4.573	4.431	4.104
29	Sc^{+3}	5.946	5.059	±0.10	4.999	4.921	4.845	4.809	4.772	4.736	4.701	4.666	4.631	4.495	4.363	4.076
30	Th^{+4}	4.766	4.925	±0.11	4.864	4.786	4.710	4.673	4.637	4.600	4.565	4.529	4.494	4.355	4.220	3.962
31	Zr^{+3}	—	4.813	±0.36	4.753	4.676	4.601	4.565	4.529	4.493	4.458	4.424	4.389	4.255	4.123	3.825
32	Be^{+2}	4.716	4.705	±0.11	4.652	4.586	4.524	4.494	4.464	4.435	4.407	4.379	4.352	4.247	4.073	| 4.058
33	Zr^{+4}	4.396	4.586	±0.33	4.527	4.452	4.380	4.345	4.310	4.276	4.242	4.208	4.175	4.045	3.964 (903S)	
34	U^{+4}	4.366	4.564	—	4.505	4.430	4.357	4.322	4.287	4.252	4.217	4.183	4.149	4.015	3.881	| 3.626
35	Hf^{+4}	4.566	4.477	±0.43	4.419	4.344	4.271	4.236	4.202	4.168	4.134	4.100	4.067	3.939	3.860 (927S)	
36	Ti^{+3}	ca 4.076	4.329	±0.22	4.274	4.204	4.137	4.104	4.072	4.040	4.009	3.978	3.947	3.828	3.712	3.499
37	$(Al^{+3})_2$	4.526	4.250	±0.07	4.188	4.107	4.026	3.986	3.946	3.906	3.867	3.828	3.789	3.629	3.471	3.275
38	V^{+3}	4.086	3.896	±0.43	3.841	3.771	3.704	3.671	3.639	3.608	3.577	3.546	3.516	3.398	3.284	3.087
39	Mn^{+2}	4.046	3.881	±0.11	3.828	3.760	3.695	3.663	3.632	3.601	3.570	3.540	3.510	3.391	3.289	3.044
40	Ti^{+4}	—	3.794	±0.22	3.741	3.673	3.619 (284V)									
41	Cr^{+2}	3.771	3.708	±0.07	3.655	3.587	3.523	3.492	3.461	3.430	3.400	3.371	3.341	3.227	3.115	2.883
42	V^{+2}	ca 4.046	3.664	±0.43	3.606	3.531	3.460	3.425	3.391	3.358	3.325	3.292	3.260	3.133	3.011	2.754
43	Cr^{+3}	3.606	3.601	±0.07	3.543	3.471	3.401	3.366	3.333	3.300	3.267	3.234	3.202	3.076	2.954	| 2.742
44	Zn^{+2}	3.629	3.591	±0.07	3.535	3.465	3.397	3.365	3.332	3.299	3.265	3.231	3.198	3.068	2.912	2.439
45	Ga^{+3}	3.496	3.440	±0.14	3.376	3.292	3.211	3.171	3.132	3.093	3.055	3.017	2.980	2.923 (952S)		
46	Fe^{+2}	3.306	3.417	±0.04	3.362	3.291	3.223	3.191	3.158	3.126	3.094	3.062	3.030	2.905	2.780	2.529
47	Cd^{+2}	3.269	3.356	±0.02	3.303	3.234	3.169	3.135	3.101	3.068	3.035	3.002	2.969	2.826	2.605	2.109
48	In^{+3}	3.208	3.353	±0.04	3.289	3.206	3.123	3.083	3.043	3.003	2.964	2.925	2.887	2.736	2.589	| 2.447
49	V^{+4}	—	3.307	±0.43	3.253	3.186	3.121	3.104 (327D)								
50	Co^{+2}	3.143	3.231	±0.02	3.177	3.110	3.045	3.014	2.983	2.952	2.922	2.892	2.862	2.746	2.631	2.391
51	Ni^{+2}	3.116	3.226	±0.02	3.169	3.096	3.026	2.992	2.958	2.924	2.890	2.857	2.825	2.697	2.573	2.338
52	Pb^{+2}	2.992	3.221	±0.04	3.155	3.082	3.011	2.975	2.938	2.901	2.865	2.829	2.793	2.654	2.525	| 2.350
53	Mn^{+3}	2.583	3.209	±0.07	3.152	3.079	3.009	2.975	2.941	2.908	2.875	2.842	2.810	2.682	2.557	| 2.383
54	Fe^{+3}	2.902	3.166	±0.19	3.109	3.036	2.966	2.932	2.899	2.865	2.832	2.800	2.767	2.640	2.513	| 2.354
55	Sb^{+3}	—	2.946	—	2.898	2.839	| 2.782	2.758	2.746 (376S)							
56	Bi^{+3}	—	2.891	—	2.834	2.761	2.690	2.652	2.615	2.578	2.542	2.506	2.470	| 2.381 (1027V)		
57	V^{+5}	—	2.706	±0.17	2.657	| 2.652 (111V)										
58	Tl^{+1}	3.202	2.602	±0.22	2.549	2.481	2.416	| 2.385	2.359	2.333	2.308	2.284	2.260	2.234 (655V)		
59	Cu^{+2}	2.529	2.526	±0.09	2.471	2.400	2.333	2.301	2.269	2.237	2.206	2.176	2.145	2.028	| 1.922	1.693
60	Co^{+3}	3.288	2.472	±0.14	2.415	2.342	2.273	2.239	2.205	2.172	2.139	2.107	2.075	1.949	| 1.826	1.670 (1327V)
61	Tl^{+3}	2.145	2.306	±0.14	2.250	2.180	2.113	2.078	2.044	2.011	1.978	| 1.945	1.918	1.815	1.718 (927V)	
62	Pd^{+2}	1.879	2.212	±0.22	2.158	2.091	2.026	1.995	1.964	1.934	1.904	1.874	1.845	1.741	| 1.660	1.574
63	Rh^{+3}	2.066	2.081	±0.29	2.025	1.952	1.882	1.849	1.815	1.782	1.750	1.717	1.684	1.554	1.424	| 1.099 (1427S)
64	Ag^{+1}	2.067	1.917	±0.04	1.871	1.815	1.762	1.736	1.711	| 1.690	1.674	1.660	1.646	1.597	1.551	1.509 (1147V)
65	Hg^{+2}	2.012	1.800	±0.22	1.735	1.653	1.574	1.535	1.476	1.414	1.353	1.293	1.233	| 1.180 (647D)		
66	Pd^{+3}	—	1.518	±0.29	1.457	1.380	1.360 (227D)									
67	Au^{+3}	1.366	1.243	±0.43	1.194	1.131	1.071	1.042	1.014	0.986	0.958	0.931	0.904	| 0.809	0.734	0.555 (1197V)
68	Au^{+2}	<1.381	1.019	±0.43	0.966	0.899	0.834	0.803	0.772	0.742	0.712	0.683	0.654	| 0.538	0.421	0.144 (1252V)
69	Au^{+1}	1.186	0.607	±0.17	0.565	0.513	0.464	0.440	0.415	0.391	0.367	0.342	| 0.318	0.220	0.123	−0.121 (1202V)

S, sublimation; V, vaporization; D, decomposition.

* Values listed at the sublimation, vaporization, or decomposition temperatures obviously apply to cells with the solid or molten electrolyte, that is, slightly below the sublimation, vaporization, or decomposition temperature.

Table II. Standard electromotive forces for single, solid, or molten metallic bromide*

Order 25°C	Metal ion	E°														
		25°C (aqueous) v	25°C (solid) v	Uncertainty (25°C) v	100°C v	200°C v	300°C v	350°C v	400°C v	450°C v	500°C v	550°C v	600°C v	800°C v	1000°C v	1500°C v
1	Cs^{+1}	4.004	3.988	±0.01	3.918	3.824	3.730	3.683	3.637	3.590	3.544	3.498	3.452 |	3.204	2.903	2.468 (1300V)
2	Ra^{+2}	4.001	3.957	±0.07	3.890	3.803	3.718	3.676	3.635	3.594	3.553	3.513	3.473	3.310 |	3.154	2.667
3	K^{+1}	4.006	3.946	±0.01	3.874	3.775	3.677	3.628	3.580	3.532	3.485	3.438	3.391 |	3.187	2.904	2.385 (1383V)
4	Rb^{+1}	4.006	3.936	±0.04	3.866	3.773	3.681	3.635	3.589	3.543	3.497	3.452	3.407 |	3.151	2.852	2.348 (1352V)
5	Ba^{+2}	3.981	3.814	±0.01	3.750	3.669	3.590	3.552	3.514	3.476	3.438	3.401	3.364	3.216 |	3.084	2.791
6	Sm^{+2}	<4.24	3.708	±0.15	3.649	3.572	3.498	3.462	3.426	3.391	3.355	3.321	3.286 |	3.165	3.062	2.822
7	Sr^{+2}	3.971	3.621	±0.01	3.559	3.479	3.402	3.363	3.326	3.288	3.251	3.214	3.178 |	3.053	2.930	2.595
8	Na^{+1}	3.795	3.613	±0.02	3.544	3.445	3.348	3.299	3.251	3.203	3.156	3.108	3.061 |	2.889	2.667	2.107 (1392V)
9	Li^{+1}	4.126	3.569	±0.09	3.514	3.441	3.363	3.324	3.287	3.249	3.212	3.176 |	3.147	3.040	2.940	2.798 (1310V)
10	Ca^{+2}	3.951	3.416	±0.02	3.357	3.280	3.206	3.170	3.134	3.099	3.064	3.028	2.994 |	2.861	2.740	2.447
11	La^{+3}	3.601	3.122	±0.04	3.061	2.983	2.907	2.870	2.833	2.797	2.761	2.725	2.690 |	2.553	2.438	2.167
12	Ce^{+3}	3.561	3.050	±0.04	2.989	2.911	2.835	2.798	2.761	2.724	2.688	2.652	2.616 |	2.482	2.363	2.085
13	Pr^{+3}	3.551	3.011	±0.04	2.951	2.874	2.799	2.763	2.727	2.691	2.655	2.620	2.585 |	2.462	2.354	2.092
14	Nd^{+3}	3.521	2.986	±0.04	2.928	2.852	2.778	2.742	2.706	2.670	2.634	2.599	2.564 |	2.441	2.327	2.060
15	Pm^{+3}	3.501	2.934	±0.04	2.877	2.803	2.732	2.697	2.662	2.628	2.594	2.561	2.527 |	2.413	2.314	2.086
16	Sm^{+3}	3.491	2.891	±0.10	2.833	2.760	2.689	2.653	2.619	2.585	2.551	2.517	2.484 |	2.372	2.328 (887D)	
17	Gd^{+3}	3.481	2.862	±0.04	2.805	2.731	2.660	2.625	2.590	2.556	2.522	2.488	2.455 |	2.329	2.227	1.998 (1487V)
18	Tb^{+3}	3.471	2.819	±0.04	2.761	2.688	2.616	2.581	2.547	2.512	2.478	2.445	2.412	2.282 |	2.177	1.950 (1487V)
19	Dy^{+3}	3.431	2.775	±0.04	2.714	2.636	2.560	2.522	2.485	2.448	2.412	2.376	2.341	2.201 |	2.079	1.829 (1477V)
20	Y^{+3}	3.451	2.761	±0.04	2.700	2.621	2.545	2.508	2.471	2.434	2.398	2.362	2.326	2.187 |	2.062	1.815 (1467V)
21	Ho^{+3}	3.401	2.746	±0.04	2.686	2.607	2.531	2.493	2.456	2.420	2.383	2.347	2.312	2.172 |	2.047	1.805 (1467V)
22	Er^{+3}	3.381	2.717	±0.04	2.657	2.578	2.502	2.464	2.427	2.391	2.354	2.318	2.283	2.143 |	2.013	1.774 (1457V)
23	Eu^{+3}	3.491	2.689	±0.10	2.631	2.558	2.486	2.451	2.417	2.382	2.348	2.315	2.282 |	2.164	2.120 (887D)	
24	Tm^{+3}	3.361	2.689	±0.04	2.628	2.549	2.473	2.435	2.398	2.362	2.325	2.289	2.254	2.114 |	1.984	1.755 (1437V)
25	Lu^{+3}	3.331	2.645	±0.04	2.584	2.506	2.429	2.392	2.355	2.318	2.282	2.246	2.211	2.071 |	1.940	1.726 (1407V)
26	Mg^{+2}	3.451	2.606	±0.01	2.548	2.474	2.403	2.368	2.333	2.299	2.265	2.232	2.199 |	2.078	1.980	1.824 (1227V)
27	Zr^{+2}	—	2.528	±0.43	2.471	2.397	2.326	2.292	2.257	2.224	2.190	2.157	2.124 |	1.992	1.860	1.710 (1227V)
28	Sc^{+3}	3.161	2.506	±0.01	2.446	2.367	2.291	2.253	2.216	2.180	2.143	2.107	2.072	1.932 |	1.846 (929S)	
29	Zr^{+3}	—	2.433	±0.29	2.373	2.296	2.222	2.186	2.150	2.115	2.080	2.044	2.010	1.875 |	1.857 (827 dp)	
30	Yb^{+3}	3.351	2.428	±0.10	2.368	2.289	2.213	2.175	2.138	2.102	2.065	2.029	1.994	1.854 |	1.726 (ca 1000D)	
31	U^{+3}	2.881	2.397	—	2.342	2.272	2.205	2.171	2.138	2.106	2.073	2.041	2.009 |	1.889	1.793	1.569
32	Th^{+4}	2.981	2.378	±0.11	2.318	2.241	2.164	2.127	2.090	2.053	2.017	1.981	1.945 |	1.820	1.788 (857V)	
33	Hf^{+4}	2.781	2.201	±0.32	2.142	2.066	1.993	1.977 (322S)								
34	U^{+4}	2.581	2.060	—	2.003	1.929	1.858	1.823	1.789	1.755	1.721 |	1.691	1.663	1.573 (ca 766V)		
35	V^{+2}	ca 2.261	2.016	±0.43	1.958	1.883	1.810	1.775	1.740	1.706	1.672	1.639	1.605	1.476 |	1.374	1.269 (1227V)
36	Zr^{+4}	2.611	2.006	±0.22	1.948	1.873	1.801	1.766	1.761 (357S)							
37	Ti^{+2}	2.711	1.995	±0.22	1.940	1.869	1.801	1.768	1.735	1.703	1.671	1.639	1.608 |	1.511	1.424	1.331 (1227V)
38	Mn^{+2}	2.261	1.908	±0.04	1.854	1.786	1.719	1.687	1.654	1.623	1.591	1.560	1.529 |	1.422	1.334	1.322 (1027V)
39	Be^{+2}	2.931	1.869	±0.11	1.818	1.755	1.695	1.666	1.638	1.610 |	1.584	1.581 (527V)				
40	Ti^{+3}	ca 2.281	1.843	±0.14	1.788	1.717	1.649	1.615	1.582	1.550	1.518	1.486	1.454	1.331 (927 dp)		
41	$(Al^{+3})_2$	2.741	1.761	±0.03 |	1.707	1.649	1.617 (257V)									
42	Tl^{+1}	1.417	1.738	±0.02	1.686	1.619	1.553	1.517	1.480	1.444 |	1.416	1.391	1.367	1.275	1.267 (819V)	
43	Ti^{+4}	—	1.731	±0.11 |	1.710	1.687	1.680 (230V)									
44	In^{+1}	ca 1.331	1.717	±0.22	1.659	1.582 |	1.156	1.487	1.458	1.429	1.401	1.374	1.347	1.318 (662V)		
45	Zn^{+2}	1.844	1.624	±0.02	1.567	1.494	1.424	1.390 |	1.357	1.329	1.301	1.272	1.245	1.192 (702V)		
46	Cr^{+2}	1.985	1.539	±0.11	1.486	1.418	1.353	1.321	1.289	1.258	1.227	1.197	1.167	1.049 |	0.954	0.900 (1127V)
47	Cd^{+2}	1.484	1.537	±0.02	1.475	1.395	1.318	1.278	1.238	1.198	1.159	1.120 |	1.085	0.944	0.876 (863V)	
48	Ge^{+4}	—	1.409	±0.16 |	1.364	1.316 (189V)										
49	Pb^{+2}	1.207	1.366	±0.02	1.309	1.234	1.160	1.122	1.089	1.059 |	1.031	1.003	0.976	0.876	0.823 (914V)	

Table II (Continued)

		E°														
Order 25°C	Metal ion	25°C (aqueous) v	25°C (solid) v	Uncertainty (25°C) v	100°C v	200°C v	300°C v	350°C v	400°C v	450°C v	500°C v	550°C v	600°C v	800°C v	1000°C v	1500°C v
50	$(Si^{+3})_2$	—	1.344	±0.14	| 1.298	1.245	1.213 (240V)									
51	Sn^{+2}	1.217	1.331	±0.02	1.280	1.215	| 1.153	1.122	1.093	1.063	1.036	1.008	0.981	0.960 (639V)		
52	In^{+3}	1.423	1.321	±0.04	1.264	1.189	1.114	1.078	1.062 (371S)							
53	Ga^{+3}	1.611	1.297	±0.01	1.244	| 1.183 (314V)										
54	Fe^{+2}	1.521	1.247	±0.01	1.194	1.127	1.062	1.030	0.999	0.968	0.937	0.907	0.876	| 0.780	0.730 (927V)	
55	V^{+4}	—	1.225	±0.43	| 1.183	1.131	1.108 (247V)									
56	Co^{+2}	1.358	1.149	±0.02	1.097	1.030	0.965	0.934	0.902	0.872	0.841	0.811	0.781	| 0.684	0.635 (927V)	
57	Ni^{+2}	1.331	1.106	±0.04	1.049	0.977	0.907	0.872	0.838	0.804	0.771	0.738	0.705	0.576	| 0.527 (877V)	
58	Cu^{+1}	0.560	1.049	±0.03	1.000	0.939	0.881	0.853	0.826	0.799	| 0.774	0.754	0.736	0.667	0.605	0.494 (1318V)
59	Ag^{+1}	0.282	1.011	±0.01	0.966	0.911	0.860	0.836	0.814	| 0.795	0.781	0.767	0.754	0.706	0.659	0.520
60	Si^{+4}	—	0.999	±0.01	| 0.953	0.922 (153V)										
61	Sn^{+4}	1.074	0.987	±0.01	| 0.939	0.880	0.877 (207V)									
62	$(Hg^{+1})_2$	0.292	0.942	±0.01	0.871	0.779	0.690	0.646	0.582	0.573 (407D)						
63	Fe^{+3}	1.117	0.888	±0.06	0.836	0.769	| 0.716	0.692	0.669	0.647	0.625	0.604	0.583	0.571 (627V)		
64	Sb^{+3}	—	0.831	—	| 0.776	0.719	0.672 (288V)									
65	Bi^{+3}	—	0.824	—	0.774	0.710	| 0.657	0.630	0.604	0.578	0.573 (461V)					
66	B^{+3}	—	0.773	±0.06	| 0.742 (91V)											
67	Hg^{+2}	0.227	0.737	±0.01	0.663	0.566	| 0.483	0.469 (319V)								
68	Cu^{+2}	0.744	0.662	±0.02	0.609	0.541	0.476	0.459 (327D)								
69	As^{+3}	—	0.636	—	| 0.597	0.551	0.542 (221V)									
70	Mo^{+2}	—	0.585	±0.15	0.538	0.477	0.419	0.391	0.363	0.336	0.309	0.283	0.257	0.198 (727D)		
71	Rh^{+1}	0.481	0.564	±0.12	0.521	0.468	0.418	0.394	0.370	0.347	0.324	0.301	0.279	0.224 (727D)		
72	Mo^{+3}	1.281	0.520	±0.07	0.467	0.399	0.333	0.301	0.270	0.253 (427D)						
73	Rh^{+3}	0.281	0.506	±0.04	0.452	0.384	0.318	0.286	0.254	0.223	0.192	0.176 (527D)				
74	Pd^{+2}	0.094	0.492	±0.06	0.441	0.376	0.314	0.284	0.254	0.225	0.196	0.167	0.139	| 0.061	0.028 (927V)	
75	Ir^{+1}	—	0.477	±0.12	0.435	0.382	0.332	0.308	0.285	0.262	0.240	0.217	0.196	0.184 (627D)		
76	Mo^{+4}	—	0.434	±0.04	0.381	0.314	0.249	| 0.221 (347V)								
77	Pt^{+4}	—	0.390	±0.04	0.337	0.268	0.203	0.185 (327D)								
78	Ir^{+2}	−0.019	0.369	±0.07	0.315	0.247	0.182	0.150	0.119	0.088	0.071 (477D)					
79	W^{+2}	—	0.369	±0.15	0.321	0.260	0.202	0.174	0.146	0.126 (437D)						
80	In^{+3}	−0.069	0.361	±0.07	0.308	0.240	0.174	0.142	0.110	0.094 (427D)						
81	W^{+4}	—	0.325	±0.05	0.272	0.203	0.138	0.120 (327S)								
82	Os^{+2}	0.231	0.325	±0.11	0.277	0.217	0.159	0.131	0.103	0.076	0.049	0.023	−0.003	| −0.094	−0.162	−0.202 (1127V)
83	W^{+5}	—	0.321	±0.13	0.271	0.207	| 0.149	0.134 (333V)								
84	Ru^{+3}	—	0.289	±0.04	0.236	0.168	0.102	0.085 (327D)								
85	Pt^{+3}	—	0.289	±0.10	0.236	0.167	0.101	0.069	0.037	0.035 (405D)						
86	Pt^{+2}	ca −0.119	0.282	±0.07	0.228	0.160	0.094	0.063	0.031	0.025 (410D)						
87	W^{+6}	—	0.275	—	0.267 (37D)											
88	Pt^{+1}	—	0.260	±0.13	(dp)											
89	Au^{+1}	−0.599	0.169	±0.04	0.125	0.069	0.063 (212D)									
90	Au^{+3}	−0.419	0.153	±0.07	0.106	0.053 (187D)										

S, sublimation; V, vaporization; D, decomposition; dp, disproportionates.

* Values listed at the sublimation, vaporization, or decomposition temperatures obviously apply to cells with the solid or molten electrolyte, that is, slightly below the sublimation, vaporization, or decomposition temperature.

Table III. Standard electromotive forces for single, solid, or molten iodides*

		E°														
Order 25°C	Metal ion	25°C (aqueous) v	25°C (solid) v	Uncertainty (25°C) v	100°C v	200°C v	300°C v	350°C v	400°C v	450°C v	500°C v	550°C v	600°C v	800°C v	1000°C v	1500°C v
1	Cs^{+1}	3.559	3.557	±0.01	3.491	3.397	3.303	3.257	3.211	3.164	3.119	3.073	3.028 |	2.791	2.500	2.080 (1280V)
2	Rb^{+1}	3.561	3.474	±0.04	3.406	3.315	3.224	3.179	3.134	3.089	3.045	3.000	2.956 |	2.705	2.406	1.967 (1304V)
3	K^{+1}	3.561	3.441	±0.01	3.369	3.269	3.171	3.122	3.074	3.026	2.979	2.931	2.884 |	2.686	2.387	1.923 (1324V)
4	Ra^{+2}	3.556	3.350	±0.07	3.283	3.195	3.110	3.068	3.027	2.986	2.945	2.905	2.865 |	2.713	2.578	2.111
5	Eu^{+2}	4.036	3.231	±0.15	3.172	3.095	3.021	2.985	2.948	2.913	2.878 |	2.846	2.819	2.712	2.613	2.384
6	Ba^{+2}	3.536	3.187	±0.01	3.124	3.042	2.963	2.924	2.886	2.848	2.811	2.773	2.737 |	2.598	2.479	2.205
7	Sm^{+2}	<3.80	3.122	±0.15	3.063	2.987	2.913	2.876	2.840	2.805	2.769 |	2.738	2.710	2.604	2.504	2.269
8	Na^{+1}	3.350	3.035	±0.01	2.967	2.871	2.776	2.729	2.682	2.636	2.589	2.544	2.498 |	2.353	2.135	1.703 (1304V)
9	Sr^{+2}	3.526	3.014	±0.01	2.953	2.874	2.797	2.759	2.722	2.685	2.648 |	2.617	2.589	2.480	2.370	2.063
10	Li^{+1}	3.681	2.914	±0.09	2.860	2.788	2.712	2.675	2.639 |	2.603	2.572	2.541	2.511	2.398	2.292	2.208 (1171V)
11	Ca^{+2}	3.506	2.845	±0.01	2.784	2.705	2.628	2.591	2.554	2.517	2.480	2.444	2.407 |	2.272	2.150	2.015 (1227V)
12	La^{+3}	3.156	2.486	±0.01	2.423	2.341	2.261	2.222	2.184	2.146	2.108	2.070	2.033 |	1.891	1.770	1.535 (1402V)
13	Ce^{+3}	3.116	2.457	±0.01	2.398	2.321	2.246	2.209	2.173	2.137	2.101	2.066	2.031 |	1.897	1.779	1.560 (1397V)
14	Pr^{+3}	3.106	2.414	±0.01	2.352	2.272	2.194	2.156	2.118	2.081	2.044	2.007	1.971 |	1.836	1.720	1.507 (1377V)
15	Nd^{+3}	3.076	2.371	±0.01	2.309	2.229	2.151	2.113	2.075	2.037	2.000	1.962	1.925 |	1.782	1.657	1.440 (1367V)
16	Pm^{+3}	3.056	2.327	±0.02	2.266	2.188	2.111	2.074	2.037	2.000	1.964	1.928	1.892 |	1.752	1.639	1.443 (1367V)
17	Sm^{+3}	3.046	2.284	±0.10	2.220	2.138	2.058	2.019	1.980	1.942	1.904	1.866	1.829	1.682 (820D)		
18	Gd^{+3}	3.036	2.201	±0.01	2.138	2.056	1.977	1.938	1.900	1.861	1.824	1.787	1.749	1.603 |	1.470	1.282 (1337V)
19	Tb^{+3}	3.026	2.183	±0.03	2.118	2.035	1.953	1.913	1.874	1.835	1.796	1.758	1.719	1.570 |	1.430	1.240 (1327V)
20	Dy^{+3}	2.986	2.154	±0.01	2.090	2.007	1.927	1.887	1.848	1.810	1.771	1.733	1.696	1.548 |	1.409	1.228 (1317V)
21	Y^{+3}	3.006	2.139	±0.03	2.077	1.995	1.916	1.878	1.839	1.801	1.764	1.727	1.690	1.545	1.404 |	1.237 (1307V)
22	Ho^{+3}	2.956	2.110	±0.01	2.046	1.962	1.881	1.841	1.801	1.762	1.723	1.685	1.647	1.497	1.351 |	1.174 (1297V)
23	Er^{+3}	2.936	2.096	±0.01	2.034	1.954	1.876	1.837	1.800	1.762	1.725	1.688	1.652	1.509	1.370 |	1.212 (1277V)
24	Tm^{+3}	2.916	2.067	±0.01	2.006	1.926	1.849	1.812	1.774	1.737	1.701	1.664	1.628	1.487	1.350 |	1.207 (1257V)
25	Eu^{+3}	3.046	2.038	±0.10	1.974	1.890	1.809	1.769	1.729	1.691	1.651	1.613	1.575	1.425	1.369 (877D)	
26	Zr^{+2}	—	2.038	±0.43	1.980	1.905	1.833	1.798	1.763 |	1.733	1.709	1.685	1.661	1.571	1.484	1.473 (1027V)
27	Lu^{+3}	2.886	1.995	±0.01	1.932	1.851	1.772	1.733	1.695	1.657	1.619	1.582	1.545	1.400	1.259 |	1.137 (1207V)
28	Mg^{+2}	3.006	1.951	±0.01	1.893	1.819	1.747	1.712	1.676	1.643	1.609	1.575	1.542 |	1.423	1.353 (927V)	
29	Zr^{+3}	—	1.922	±0.29	1.861	1.781	1.704 |	1.683 (327 dp)								
30	Sc^{+3}	2.716	1.908	±0.01	1.847	1.768	1.692	1.655	1.617	1.581	1.544	1.508	1.473	1.333	1.257 (909S)	
31	Yb^{+3}	2.906	1.807	±0.10	1.742	1.659	1.577	1.538	1.498	1.459	1.420	1.382	1.344	1.194	1.048	1.029 (1027D)
32	U^{+3}	2.436	1.767	—	1.714	1.647	1.581	1.549	1.517	1.486	1.455	1.424	1.393	1.270	1.146	0.837
33	Hf^{+4}	2.336	1.648	±0.32	1.586	1.507	1.430	1.392	1.355	1.335 (427S)						
34	Th^{+4}	2.536	1.496	±0.11	1.435	1.356	1.279	1.241	1.203	1.166	1.129	1.093 |	1.060	0.939	0.918 (837V)	
35	Zr^{+4}	2.166	1.496	±0.22	1.438	1.363	1.290	1.255	1.220 |	1.199 (431S)						
36	U^{+4}	2.136	1.467	—	1.410	1.336	1.265	1.230	1.195	1.160	1.126	1.092	1.058	0.923	0.788	0.383
37	V^{+2}	ca 1.816	1.453	±0.43	1.399	1.331	1.266	1.235	1.203	1.172	1.142	1.112	1.083 |	0.970	0.915 (927V)	
38	Ti^{+2}	2.266	1.409	±0.22	1.351	1.277	1.205	1.169	1.135	1.100	1.066	1.033	0.999 |	0.894	0.799	0.787 (1027V)
39	Mn^{+2}	1.816	1.388	±0.04	1.333	1.263	1.196	1.163	1.130	1.098	1.066	1.034	1.002 |	0.903	0.890 (827V)	
40	Tl^{+1}	0.972	1.388	±0.02	1.334	1.264	1.196	1.159	1.122 |	1.087	1.059	1.032	1.005	0.902	0.890 (823V)	
41	Cr^{+2}	1.541	1.279	±0.15	1.226	1.157	1.091	1.059	1.027	0.995	0.964	0.933	0.903 |	0.784	0.771 (827V)	
42	Ti^{+3}	ca 1.846	1.250	±0.14	1.194	1.122	1.052	1.020 (347 dp)								
43	Ti^{+4}	—	1.212	±0.11	1.159 |	1.094	1.037	1.010	0.995 (377V)							

Table III (Continued)

		E°														
Order 25°C	Metal ion	25°C (aqueous) v	25°C (solid) v	Uncertainty (25°C) v	100°C v	200°C v	300°C v	350°C v	400°C v	450°C v	500°C v	550°C v	600°C v	800°C v	1000°C v	1500°C v
44	Be^{+2}	2.486	1.203	±0.11	1.150	1.084	1.020	0.990	0.960	0.930 ❙	0.910 (487V					
45	Zn^{+2}	1.399	1.185	±0.01	1.130	1.060	0.993	0.960	0.928 ❙	0.895	0.868	0.841	0.815	0.750 (727V)		
46	$(Al^{+3})_2$	2.296	1.184	±0.01	1.129 ❙	1.057	0.999	0.971	0.952 (386V)							
47	In^{+1}	ca 0.886	1.171	±0.22	1.107	1.020	0.931	0.887 ❙	0.853	0.819	0.785	0.752	0.720	0.650 (715V)		
48	Cd^{+2}	1.039	1.141	±0.02	1.086	1.016	0.949	0.914 ❙	0.882	0.860	0.839	0.819	0.799	0.711 (796V)		
49	Ge^{+2}	0.636	1.084	±0.33	1.031	0.962 ❙	0.905	0.879	0.854	0.829	0.805	0.781	0.758	0.724 (677V)		
50	Ge^{+4}	—	1.019	±0.16	0.963 ❙	0.896	0.838	0.810	0.795 (377V)							
51	Pb^{+2}	0.762	1.008	±0.01	0.944	0.870	0.799	0.763	0.726 ❙	0.696	0.670	0.644	0.620	0.532	0.504 (872V)	
52	In^{+3}	0.978	0.911	±0.04	0.860	0.793 ❙	0.738	0.713	0.687	0.663	0.639 (500V)					
53	Ga^{+3}	1.166	0.853	±0.01	0.797	0.725 ❙	0.665	0.638 (349V)								
54	Sn^{+2}	0.772	0.849	±0.07	0.794	0.725	0.652 ❙	0.612	0.589	0.550	0.520	0.491	0.462	0.396 (714V)		
55	Cu^{+1}	0.115	0.821	±0.04	0.771	0.707	0.645	0.615	0.586	0.557	0.528	0.500 ❙	0.474	0.396	0.324	0.244 (1207V)
56	Ag^{+1}	−0.163	0.788	±0.01	0.743	0.696	0.659	0.641	0.624	0.607	0.590	0.574 ❙	0.563	0.528	0.496	0.401
57	Fe^{+2}	1.076	0.759	±0.04	0.706	0.639	0.574	0.542	0.511	0.480	0.449	0.418 ❙	0.390	0.306	0.295 (827V)	
58	$(Hg^{+1})_2$	−0.153	0.677	±0.02	0.609	0.521	0.444 (290D)									
59	Co^{+2}	0.913	0.646	±0.02	0.596	0.531	0.469	0.439	0.409	0.379	0.350 ❙	0.326	0.306	0.229	0.219 (827V)	
60	Hg^{+2}	−0.218	0.607	±0.01	0.542	0.459 ❙	0.387	0.358	0.355 (354V)							
61	B^{+3}	—	0.549	±0.07 ❙	0.510	0.464	0.460 (210V)									
62	Ni^{+2}	0.886	0.542	±0.02	0.487	0.415	0.346	0.312	0.278	0.245	0.212	0.179	0.147	0.053 (747S)		
63	Si^{+4}	—	0.452	±0.01	0.399 ❙	0.335	0.282 (288V)									
64	Sb^{+3}	—	0.452	—	0.403 ❙	0.341	0.288	0.263	0.238	0.225 (427V)						
65	Bi^{+3}	—	0.441	—	0.386	0.315	0.244	0.207	0.170	0.164 (408D)						
66	Mo^{+2}	—	0.369	±0.15	0.315	0.247	0.182	0.150	0.119	0.088	0.058	0.027	−0.004	−0.127	−0.249	−0.555
67	Rh^{+3}	−0.164	0.361	±0.14	0.308	0.239	0.174	0.156 (327D)								
68	Pd^{+2}	−0.351	0.325	±0.17	0.272	0.203	0.138	0.106	0.074 ❙	0.046	0.021	−0.002	−0.026	−0.082 (827V)		
69	Rh^{+1}	0.036	0.325	±0.13	0.277	0.217	0.159	0.132	0.104 ❙	0.090 (427D)						
70	As^{+3}	—	0.318	—	0.268 ❙	0.209	0.157	0.132	0.108	0.101 (414V)						
71	Ir^{+1}	—	0.304	±0.12	0.261	0.208	0.159	0.135	0.111	0.088	0.065	0.054 (527D)				
72	Mo^{+4}	—	0.304	±0.04	0.253	0.187	0.120	0.086	0.053 ❙	0.038 (422V)						
73	Ir^{+2}	−0.464	0.217	±0.07	dp											
74	Pt^{+3}	—	0.217	±0.10	0.160	0.086	0.032 (277D)									
75	Pt^{+4}	—	0.206	±0.04	0.150	0.078	0.024 (277D)									
76	Pt^{+2}	ca −0.564	0.195	±0.07	0.142	0.073	0.008	−0.010 (327D)								
77	Au^{+1}	−1.044	0.194	±0.04	0.165	0.138 (177D)										
78	Ir^{+3}	−0.514	0.152	±0.07	0.060	−0.059	−0.176	−0.233	−0.290	−0.321 (427D)						
79	W^{+2}	—	0.130	±0.15	0.077	0.009	−0.009 (227V)									
80	Rh^{+2}	0.036	0.108	±0.11	dp											
81	Pt^{+1}	—	0.108	±0.13	0.061	0.000	−0.058 (300 dp)									
82	W^{+4}	—	0.108	±0.11	0.055	0.029 (137D)										

S, sublimation; V, vaporization; D, decomposition; dp, disproportionates.

* Values listed at the sublimation, vaporization, or decomposition temperatures obviously apply to cells with the solid or molten electrolyte, that is, slightly below the sublimation, vaporization, or decomposition temperature.

Hydrogen Peroxide Reactions on Gold Electrodes

A. K. M. S. Huq[1] and A. C. Makrides

Tyco Laboratories, Incorporated, Waltham, Massachusetts

Studies of the kinetics of oxygen reduction on metal electrodes are generally complicated by the formation of surface oxides which are stable in the potential range of interest (1). Frequently, both the two-electron and four-electron reductions occur, with the result that the kinetics are further complicated by reactions involving hydrogen peroxide (2). The difficulties introduced by surface oxide films are absent with gold electrodes; in this case, the oxide film is reduced at potentials above 1.0v (3,4) so that oxygen reduction and the peroxide reactions can be studied on an oxide-free metal electrode over a relatively wide potential range.

The hydrogen peroxide reactions on platinum and gold electrodes have been examined by a number of authors (5-8). The suggested mechanisms assume either a surface saturated with adsorbed hydroxyl radicals (6), or postulate reactions with either adsorbed hydrogen or oxygen atoms on the electrode (7). Some results, presented below, on the H_2O_2 reactions on Au show that the mechanisms suggested so far are not correct. A more detailed discussion of the reaction mechanisms is given elsewhere.

The standard experimental procedure and precautions for electrochemical measurements were followed. The electrolytic cell was a three-compartment, Pyrex vessel and was cleaned in chromic-sulfuric solution. The test electrodes, gold cylinders of spectroscopic purity,[2] were electropolished in a cyanide bath and were mounted so that only Teflon and the electrode were exposed to solution (9). The test electrodes were cleaned either in chromic-sulfuric or in hot, concentrated nitric acid and rinsed with distilled water and test solution before use. Both cleaning procedures gave the same results. The counterelectrode was platinized platinum or gold and the reference electrode was saturated calomel. The cell was thermostated at 30.0° ± 0.1°C.

Triply distilled water, one distillation being from $KMnO_4$, was used to make up solutions of H_2SO_4 (C. P. reagent). *p*H measurements were carried out both before and after a run with a Beckman *p*H meter. The solution was de-aerated either with a stream of nitrogen or of argon.

The steady-state, current-potential curves were established potentiostatically with a Wenking potentiostat. After a rest potential was established, the electrode was subjected to the following cycle: the potential was decreased stepwise (50 or 100 mv per step) to 0.0v *vs.* a reversible H^+/H_2 in the same solution; then it was increased stepwise through the rest potential to about 1.2v *vs.* a reversible H^+/H_2 in the same solution, and then back to the rest potential. Any number of cycles could be traced in this fashion with reproducible results.

Current densities are expressed in amp/cm² of geometric area. The electrode area (~ 1 cm²) was determined for each run. Reported current densities can be converted to current densities per true cm² by dividing by a roughness factor of about 1.1. All potentials are expressed *vs.* the standard hydrogen electrode (S.H.E.).

The rest potential.—The rest potential of Au in H_2O_2 solutions is essentially independent of the concentration of H_2O_2 (0.05- 2.1 M/l) at constant *p*H (0.4). The *p*H dependence of the rest potential is shown in Fig. 1; it follows the relation

$$\text{Rest potential} = 0.816 - 0.052\ p\text{H at } 30°\text{C}$$

This is in fair agreement with the results of Bockris and Oldfield (6) who found

$$\text{Rest potential} = 0.842 - 0.059\ p\text{H at } 25°\text{C}$$

Electrochemical reduction and oxidation.—The overall reactions for the electrochemical reduction and oxidation of H_2O_2 are

$$H_2O_2 + 2e^- + 2H^+ \rightarrow 2H_2O$$

and

$$H_2O_2 \rightarrow O_2 + 2H^+ + 2e^-$$

Typical Tafel curves for reduction and oxidation are given in Fig. 2. The main point which we wish to emphasize in this communication is that the reaction rate at a fixed potential increases directly with peroxide concentration both for oxidation and for reduction (Fig. 2). Thus, the electrochemical orders of both reactions are unity with respect to H_2O_2.

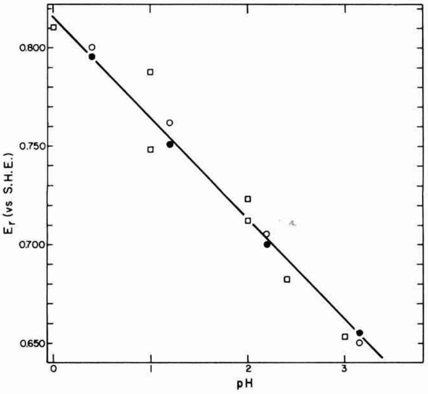

Fig. 1. Rest potential of gold in H_2O_2 solutions as a function of *p*H. Squares show values given by Bockris and Oldfield (6); open circles and solid circles are from this work.

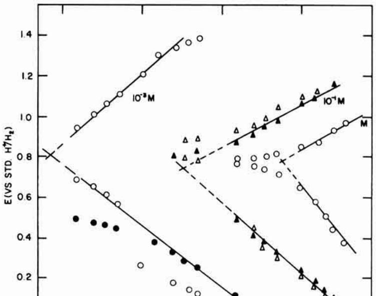

Fig. 2. Polarization curves for gold in H_2O_2 solutions. The solution was 0.1*N* H_2SO_4 in this instance. Open points are for increasing and full points for decreasing current densities.

---

[1] Present address: Atomic Energy Center, Dacca, Pakistan.
[2] Supplied by Johnson, Matthey & Company, Ltd., London.

These experimental results are not consistent with the mechanism advanced by Bockris and Oldfield (6) to account for the pH dependence of the rest potential. These authors suggested that the rest potential is determined by the activity of adsorbed OH radicals and that at even small H_2O_2 concentrations, the surface is saturated with OH radicals. This mechanism implies a zero order of reaction with respect to H_2O_2 which is contrary to observation.

Bianchi and collaborators (7) proposed that peroxide decomposes by a chemical, rather than electrochemical, process. According to these authors, peroxide decomposition takes place on cathodic polarization by reaction with atomic hydrogen adsorbed on the electrode surface, *i.e.*,

$$H_2O_2 + 2H_{ads} \rightarrow 2H_2O$$

A substantial cathodic current ($>10^{-5}$ amp/cm^2) was observed on gold at 0.5v *vs.* H^+/H_2. At this potential, no adsorbed hydrogen is detectable on gold. Therefore, this mechanism is not tenable. Furthermore, this mechanism does not account for the Tafel slope.

According to Bianchi *et al.* (7), H_2O_2 decomposes anodically by reacting with a surface metal oxide according to

$$M(0) + H_2O_2 \rightarrow M + H_2O + O_2$$

This mechanism does not account for the Tafel slope observed here on anodic polarization. It is of interest to note that in experiments with $C_{H_2O_2} = 10^{-1}$M, the anodic overpotential increased sharply at 1.4v *vs.* H^+/H_2, *i.e.*, at the potential where appreciable oxide formation takes place (4). Thus, contrary to the suggestion of Bianchi *et al.* (7), oxide formation may actually inhibit the electrochemical oxidation of H_2O_2 on gold electrodes.

It is apparent that the electrochemical reactions of H_2O_2 on gold are complicated. They are similar in some respects to those on platinum. For example, Gerischer and Gerischer (8) found Tafel behavior on Pt and a first order dependence on $C_{H_2O_2}$, but a highly complicated pH dependence: The coefficient $(\partial \log i/\partial pH)_E$ was a function of pH and changed from —0.3 at pH = 1 to —0.6 at pH = 5, while for anodic polarization this coefficient varied from 0.6 to 0.2 in the same pH range. No mechanism was advanced by these authors which explained these observations (8).

Finally, the suggestion that platinum or gold electrodes are reversible with respect to hydrogen ion in solutions containing H_2O_2 (2, 6), and that their operation does not depend on the activity of H_2O_2, provided some small amount is present (2, 6), are also not borne out by these studies. The relatively simple dependence of the rest potential on pH and its independence on the H_2O_2 activity are essentially accidental: they arise from summing up partial reactions which are not reversible and which have fairly complicated mechanisms.

Acknowledgment

The authors are grateful to Mrs. M. J. Turner for her skillful experimental assistance. This work was supported by the Harry Diamond Laboratories of the U. S. Army under Contract No. DA-49-186-AMC-136(D).

Manuscript received June 4, 1964.

Any discussion of this paper will appear in a Discussion Section to be published in the June 1966 JOURNAL.

REFERENCES

1. M. Breiter in "Advances in Electrochemistry and Electrochemical Engineering," Vol. I, p. 123, P. Delahay, Editor, Interscience, New York (1961).
2. "Reference Electrodes," Chap. 7, D. J. G. Ives and G. J. Janz, Editors, Academic Press, New York (1961).
3. H. A. Laitinen and M. S. Chao, *This Journal,* **108,** 726 (1961).
4. S. B. Brummer and A. C. Makrides, *ibid.,* **111,** 1122 (1964).
5. J. Weiss, *Trans. Faraday Soc.,* **31,** 668, 1547 (1935).
6. J. O'M. Bockris and L. Oldfield, *ibid.,* **51,** 249 (1955).
7. G. Bianchi, F. Mazza, and T. Mussini, *Electrochim. Acta,* **7,** 457 (1962); G. Bianchi, G. Caprioglio, S. Malaguzzi, F. Mazza, and T. Mussini, AFOSR TN 60-299, May 1960.
8. R. Gerischer and H. Gerischer, *Z. physik. Chem.* (*N.F.*), **6,** 178 (1956).
9. M. Stern and A. C. Makrides, *This Journal,* **107,** 782 (1960).

Brief Communication

Etching Characteristics and Light Figures of the {111} Surfaces of GaAs

Isamu Akasaki and Hiroyuki Kobayasi

Matsushita Research Institute Tokyo, Inc., Ikuta, Kawasaki, Japan

Because of various interesting properties and practical importance, the physical, chemical, and electrical properties of GaAs have been extensively investigated (1-3). GaAs has a zinc-blende structure and exhibits crystallographic polarity along the <111> directions (4), that is, the outermost atom layer in each {111} face consists of either Ga or As atoms which are triply bonded to the lattice. Conventionally (4) the former is designated as A(111) and the latter B($\bar{1}\bar{1}\bar{1}$). These two {111} faces are physically and chemically different.

In this paper, the differences in orientations of etch pits and light figures of both the {111} faces are described. An explanation for this will also be given in terms of the relative reactivities of some principal planes and the structural properties of GaAs. On the basis of these differences both types of {111} faces are easily distinguished.

Orientations of Etch Pits and Light Figures

To determine the crystallographic indices of facets developed on a crystal surface by grinding or chemical etching, the light figure method was used. The sample was cut from a GaAs single crystal in the form shown in Fig. 1. The base and both sides were ground within a few degrees parallel to the planes ($2\bar{1}\bar{1}$), Ga(111), and As($\bar{1}\bar{1}\bar{1}$), respectively. Figure 2 illus-

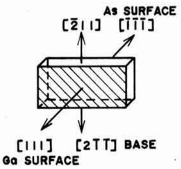

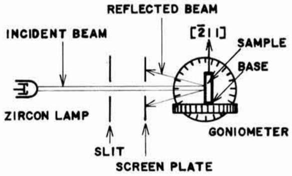

Fig. 1 (left). Form and orientations of sample. Fig. 2 (right). Light figure apparatus and arrangement of sample.

trates the light figure apparatus in which the sample was arranged with the [$\bar{2}$11] direction up, and with a narrow beam of light (about 1 mm in diameter) normal to the {111} faces and the screen plate. The compositions of etchants and etching times used are similar to those summarized by Faust (2) (see Table I).

Ga *surface*.—Figure 3 shows a photomicrograph and a light figure of Ga(111) face ground with No. 500 emery powder. The light figure consists of threefold symmetrical arrows pointing in the [$\bar{2}$11], [1$\bar{2}$1], and [11$\bar{2}$] directions. As seen in Fig. 4 and 5, upon the A-1 etching, the mechanically damaged layer was gradually removed, the <$\bar{2}$11> arrows of the light figure becoming faint and giving way to three <2$\bar{1}\bar{1}$> arrows in opposite positions. This change of light figure is schematically depicted in Fig. 6. Similar light figures pointing in <2$\bar{1}\bar{1}$> directions were also obtained by the A-2 etching.

As *Surface*.—Optically the ground As($\bar{1}\bar{1}\bar{1}$) face resembled that of the Ga(111)) face, Fig. 3(a). The light figure from a ground As surface was also similar to that from a ground Ga surface, Fig. 3(b), and correspondingly pointed in [2$\bar{1}\bar{1}$] directions. Since surface grinding introduces a center of symmetry, the resulting Laue symmetry m3m is that of the diamond structure. A light figure from the Ga(111) face of threefold symmetry with the arrows pointing in the [$\bar{2}$11], [1$\bar{2}$1], and [11$\bar{2}$] directions, respectively, corresponds to a related light figure from the As($\bar{1}\bar{1}\bar{1}$) face with the arrows of the threefold symmetry pointing in the three opposite directions [2$\bar{1}\bar{1}$], [$\bar{1}$2$\bar{1}$], and [$\bar{1}\bar{1}$2], respectively.

Figure 7 shows a photomicrograph and a light figure of an etched As($\bar{1}\bar{1}\bar{1}$) face with the B-1 etchant. The vertices of the triangular etch patterns and the arrows of the light figure point in the [2$\bar{1}\bar{1}$], [$\bar{1}$2$\bar{1}$], and [$\bar{1}\bar{1}$2] directions. B-2 etchant produces the more complex light figure seen in Fig. 8. The form of the light figure has not yet been analyzed, but the arrows also point in <2$\bar{1}\bar{1}$> directions. Contrary to the case of Ga surface, these light figures from ground and etched As surfaces are always oriented in the same directions.

Etching Rate Measurement

Since the incident beam is normal to the {111} faces, the arrow parts of the light figures show reflectograms of many oblique facets developed on the surfaces. Accordingly the directions of arrows give the crystallographic indices of the facets; for example in the case of Ga surface, the <$\bar{2}$11> arrows indicate that the oblique micro-facets may be {$\bar{1}$11} or {110} planes assuming that only low index planes are developed. In surface grinding, {110} planes seem important, since these planes are predominantly developed in the microcleavage of GaAs (1, 2).

The directions of the light figure shown in Fig. 5 are the same as those of the Ga surface etched with Schell etchant, and the latter orientations were the [2$\bar{1}\bar{1}$], [$\bar{1}$2$\bar{1}$], and [$\bar{1}\bar{1}$2] directions as reported by Abrahams *et al.* (5). Therefore the side facets of the etch pits appearing on Ga surface with HNO_3-H_2O etchants may be {100} planes. An explanation for this is given by the relative reactivities of some principal planes with the etchant, because pits developed by etching are generally bounded by planes of minimum reactivity. Samples (about 5 x 10 x 1 mm in size) were cut from undoped n-type single crystal GaAs with carrier concentration of about 10^{17} cm^{-3} and were polished by Br_2-CH_3OH solution (6) previously to remove the mechanically damaged layers. One large surface of each sample within a few degrees parallel to Ga(111), (110), (100), or As($\bar{1}\bar{1}\bar{1}$) was prepared, and the remaining surfaces were completely coated with Apiezon

Table I. Compositions of etchants and etching times for production of light figures

Etchant				
Notation	Composition	Volume ratio	Etching time	Surface
A-1	$HNO_3 : H_2O$	1 : 1	7 min	Ga
A-2	$HNO_3 : H_2O$	2 : 1	10 sec	Ga
B-1	$HF : H_2O_2 : H_2O$	2 : 1 : 8	50 min	As
B-2	$HF : HNO_3 : H_2O$*	3 : 1 : 2	7 min	As

Concentration (wt %) : HNO_3, ~60; HF, 46; H_2O_2, 30.
H_2O : deionized water.
* Several drops of 1% $AgNO_3$ are added in mother solution of about 30 ml.

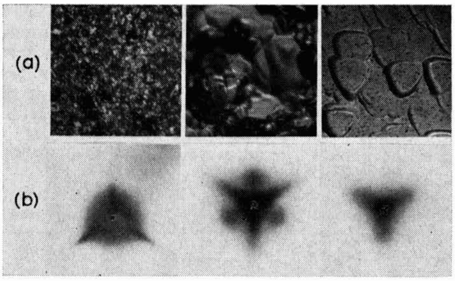

Fig. 3-5, 7, 8. In each figure, (a) shows photomicrograph (magnification 490X) of surface and (b) light figure. Fig. 3 (left) Ga surface ground with No. 500 emery powder; Fig. 4 (center) and 5 (right). Ga surface which had been ground and then etched with A-1 etchant for about 3 min (Fig. 4) and for about 7 min (Fig. 5).

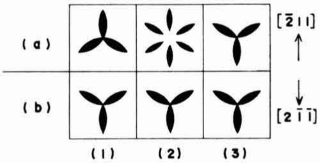

Fig. 6. Schematic illustration of orientations of various light figures from Ga surface (a) and As surface (b). 1, ground surface; 2, ground and slightly etched surface; 3, etched surface.

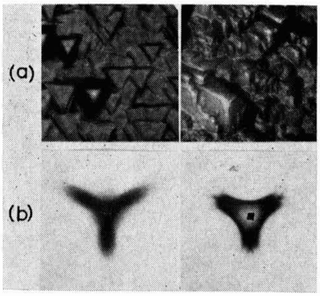

Fig. 7 (left) and 8 (right). As surface etched with B-1 etchant for about 50 min (Fig. 7) and with B-2 for about 7 min (Fig. 8).

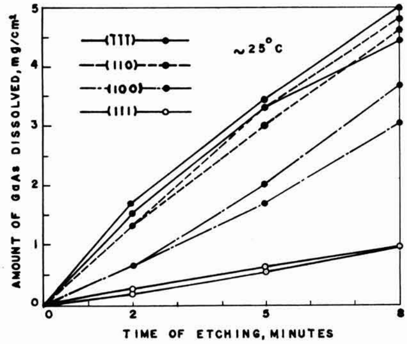

Fig. 9. Amount of GaAs dissolved with A-1 etchant as a function of orientation.

wax to protect them from the etchant. The etching rates of the respective planes were determined from weight losses of the samples which were simultaneously immersed in the A-1 etchant. The temperature of the etchant was kept at about 25°C. The results of Fig. 9 show that the etching rate decreases in the following order: As$\{\bar{1}11\}>\{110\}>\{100\}>Ga\{111\}$, which differs from the order in InSb for the etchants reported in (7). Since the $\{\bar{1}11\}$ planes developed on Ga(111) face consist of As atoms only (4), it is not necessary to take account of the reactivity of Ga$\{1\bar{1}\bar{1}\}$ planes. It appears that the pits obtained on the Ga(111) face by the A-1 etching are bounded by {100} planes which are more stable than the others.

On the other hand, the results of Fig. 6 suggest that the side facets of pits appearing on the As$(\bar{1}\bar{1}\bar{1})$ face by chemical etching may be represented by either planes $\{\bar{1}\bar{1}0\}$ or $\{1\bar{1}\bar{1}\}$. The etching rate of the four crystallographic planes with the B-1 etchant is in this order: As$\{\bar{1}11\}\simeq\{110\}\simeq\{100\}>Ga\{111\}$, which is in agreement with the results obtained by the A-1 etching. In this case, the reactivity of the Ga$\{1\bar{1}\bar{1}\}$ planes must be compared with that of the $\{\bar{1}\bar{1}0\}$ planes. Thus these side facets are thought to be the most stable Ga$\{1\bar{1}\bar{1}\}$ family planes.

It is of interest that the side facets of etch pits appearing on the Ga surface may be {100} planes, whereas on the As surface {111} planes are predominantly revealed by these etchants. The former type of etch pit corresponds to the positive trigon pit and the latter to the negative trigon pit,[1] as observed in Ge (8). This relation differs from the case that etch pits on A surfaces of two kinds of III-V compounds. namely, GaP and InAs, are positive and negative trigon pits, respectively (2). As shown in Fig. 6, the light figures from the ground and etched Ga surfaces are oppositely oriented, while those of the As surface are in the same directions. These relations easily lead to the differentiation of both the {111} faces. From the orientations of light figures,[2] any crystallographic orientation of a sample can be readily determined with considerable accuracy.

Acknowledgment

The authors would like to express their thanks to Dr. Y. Koike and to Dr. K. Miyaji for their interests in this work. This experiment was greatly assisted by Messrs. T. Hara and M. Hashimoto.

Manuscript received Jan. 4, 1965; revised manuscript received April 12, 1965.

Any discussion of this paper will appear in a Discussion Section to be published in the June 1966 JOURNAL.

REFERENCES

1. C. Hilsum and A. C. Rose-Innes, "Semiconducting III-V Compounds" in "International Series of Monographs on Semiconductors," H. K. Henisch, Editor, Vol. 1, Pergamon Press, New York (1961).
2. "Preparation of III-V Compounds" in "Compound Semiconductors," R. K. Willardson and H. L. Goering, Editors, Vol. 1, Reinhold Publishing Corp., New York (1962).
3. O. Madelung, "Physics of III-V Compounds," Translated by D. Meyerhofer, John Wiley & Sons, Inc., New York (1964).
4. H. C. Gatos and M. C. Lavine, *This Journal,* **107,** 427 (1960).
5. M. S. Abrahams and L. Ekstrom, "Properties of Elemental and Compound Semiconductors," H. C. Gatos, Editor, Metallurgical Society Conferences, Vol. 5, p. 225, Interscience Publishers, New York (1960).
6. C. S. Fuller and H. W. Allison, *This Journal,* **109,** 880 (1962).
7. M. C. Lavine, A. J. Rosenberg, and H. C. Gatos, *J. Appl. Phys.,* **29,** 1131 (1958).
8. T. Arizumi and I. Akasaki, *Japan. J. Appl. Phys.,* **2,** 143 (1963).
9. Unpublished results.

---

[1] The pits developed on both the Ga(111) and As$(\bar{1}\bar{1}\bar{1})$ faces of GaAs by iodine vapor at higher temperatures were found to be oriented in $<\bar{2}11>$ and $<2\bar{1}\bar{1}>$ directions, respectively, indicating that they were negative trigon pits (9).

[2] All photographs of light figures lack the detail and sharpness of the direct view on the screen plate.

Monographs of The Electrochemical Society

ECS Series

The following are books developed and sponsored by The Electrochemical Society and published by John Wiley & Sons, Inc., 605 Third Ave., New York 17, N. Y. Members of The Electrochemical Society can receive a 33 1/3% discount by ordering volumes from Society Headquarters, 30 East 42 St., New York, N. Y., 10017. Book and invoice will be mailed by John Wiley & Sons. Nonmembers (including subscribers) should order direct from Wiley.

Corrosion Handbook. Edited by Herbert H. Uhlig. Published 1948, 1188 pages, **$16.00**

Modern Electroplating, Second Edition. Edited by Frederick A. Lowenheim. Published 1963, 769 pages, **$16.00.**

Abstracts of the Literature on Semiconducting and Luminescent Materials and Their Applications. Compiled by Battelle Memorial Institute.

Vol. I, 1953 Issue—published 1955, 169 pages, **$5.00** (soft cover); **Vol. II, 1954 Issue**—published 1955, 200 pages, **$5.00** (soft cover); **Vol. III, 1955 Issue**—Edited by E. Paskell; published 1957, 322 pages, **$10.00** (hard cover); **Vol. IV, 1956 Issue**—Edited by E. Paskell, published 1959, 456 pages, **$12.00** (hard cover); **Vol. V, 1957 Issue**—Edited by C. S. Peet; published 1960, 449 pages, **$12.00** (hard cover); **Vol. VI, 1958 Issue**—Edited by J. J. Bulloff and C. S. Peet; published 1961, 528 pages, **$14.00** (hard cover); **Vol. VII, 1959 Issue**—Edited by J. J. Bulloff and C. S. Peet; published 1962, 728 pages, **$20.00 (hard cover).**

Electrochemistry in Biology and Medicine. Edited by Theodore Shedlovsky. Published 1955, 369 pages, **$11.50**

Vapor Plating (The Formation of Metallic and Refractory Coatings by Vapor Deposition), by C. F. Powell, I. E. Campbell, and B. W. Gonser. Published 1955, 158 pages, **$6.00**

High-Temperature Technology (Materials, Methods, and Measurements). Edited by I. E. Campbell. Published 1956, 526 pages, **$15.00** (Out of print; new edition in course of preparation)

Stress Corrosion Cracking and Embrittlement. Edited by W. D. Robertson. Published 1956, 202 pages, **$7.50**

Arcs in Inert Atmospheres and Vacuum. Edited by W. E. Kuhn. Published 1956, 188 pages, **$7.50**
(Papers Presented at the Symposium on Arcs in Inert Atmospheres and Vacuum of the Electrothermics and Metallurgy Division of The Electrochemical Society, April 30 and May 1, 1956, San Francisco, Calif.)

Technology of Columbium (Niobium). Edited by B. W. Gonser and E. M. Sherwood. Published 1958, 120 pages, **$7.00**
(Papers Presented at the Symposium on Columbium—Niobium of the Electrothermics and Metallurgy Division of The Electrochemical Society, May 15 and 16, 1957, Washington, D. C.)

The Structure of Electrolytic Solutions. Edited by Walter J. Hamer. Published 1959, 441 pages, **$18.50**
(Based on a Symposium held in Washington, D. C., in May 1957, sponsored by The Electrochemical Society, New York, and The National Science Foundation, Washington, D. C.)

Mechanical Properties of Intermetallic Compounds. Edited by J. H. Westbrook. Published 1959, 435 pages, **$9.50**
(A Symposium, Sponsored by the Electrothermics and Metallurgy Division of The Electrochemical Society, May 4, 5, and 6, 1959, Philadelphia, Pa.)

The Surface Chemistry of Metals and Semiconductors. Edited by Harry C. Gatos, with the assistance of J. W. Faust, Jr., and W. J. La Fleur. Published 1960, 526 pages, **$12.50**
[Proceedings of an International Symposium Sponsored Jointly by the Office of Naval Research and The Electrochemical Society, Inc. (Corrosion and Electronics Divisions), October 19, 20, and 21, 1959, Columbus, Ohio]

Transactions of the Symposium on Electrode Processes. Edited by Ernest Yeager. Published 1961, 374 pages, **$20.00** (The papers and discussions of the Symposium on Electrode Processes, sponsored jointly by the U. S. Air Force, Office of Scientific Research, and The Electrochemical Society, Inc., Philadelphia, Pa., May 1959).

Iodide Metals and Metal Iodides, by Robert F. Rolsten. Published 1961, 441 pages, **$17.50**

Ultrafine Particles, Editor-in-Chief—William E. Kuhn. Published 1963, 561 pages, **$15.00.**

First International Conference on Electron and Ion Beam Science and Technology, Edited by R. Bakish. Published 1965, 945 pages, $24.50. (Sponsored by the Electrothermics and Metallurgy Division of The Electrochemical Society and the Metallurgy Society of AIME.)

Other ECS Publications

Vacuum Metallurgy, third printing, 1958. Edited by J. M. Blocher, Jr.; 216 pages; **$5.00,** less a 20% discount to ECS members only. Available from Electrochemical Society Headquarters, 30 East 42 St., New York 17, N. Y. (Papers Presented at the Vacuum Metallurgy Symposium of the Electrothermics and Metallurgy Division of The Electrochemical Society held in Boston, Mass., October 6 and 7, 1954)

Rhenium, Edited by B. W. Gonser. Published by Elsevier Publishing Co., 1962. 225 pages; **$11.00.** (Papers Presented at the Symposium on Rhenium of the Electrothermics and Metallurgy Division of The Electrochemical Society, May 3 and 4, 1960, Chicago, Ill.) ECS Members can obtain a 30% discount by sending their orders direct to Society Headquarters, 30 East 42 St., New York 17, N. Y. Remittance, made payable to American Elsevier Publishing Co., 52 Vanderbilt Ave., New York 17, N. Y. should accompany the order. Nonmembers must order direct from the publisher.

Iron Ore Reduction, Edited by R. R. Rogers. Published by Pergamon Press Ltd., New York and London, 1962. 359 pages; **$12.50.** (Proceedings of a Symposium of the Electrothermics and Metallurgy Division of The Electrochemical Society, held in Chicago, Ill., May 3-5, 1960) Send all orders to The Macmillan Co., 60 Fifth Ave., New York, N. Y.

Feature Section

Our Society

Presidential Address[1]

Lyle I. Gilbertson[2]

One of the rewards of the Presidency is the opportunity to address this friendly, captive audience as a gesture of farewell and thanks. On such an occasion it is only natural to select a subject about which one knows a great deal and which is also close to one's heart. The only impersonal topic on which I can qualify on these criteria is The Electrochemical Society.

The Society is my senior in age by one year. When I joined, we were about thirty-five. For twenty years I have been active in the Society, during which time the Society has grown and has changed in many ways. I would like to review some of the most significant changes; discuss them briefly in the light of the present; and make a few guesses as to our future. I shall try to be brief.

The founding of our Society followed a period of significant activity in the development of sources of electric power and coincided with the first large-scale availability of hydroelectric power in this country. The first dynamo was built in 1867 and the foundations of electrochemical industry were laid in the twenty years that followed. In this time: Siemens and Heroult had produced a number of furnaces; Hall had invented a process for metallic aluminum; Willson had made calcium carbide in an attempt to make calcium metal; Fowler had extruded electrodes from coke and tar; Acheson had patented processes for making silicon carbide and graphite; and Moissan had published his classical experiments with the electric furnace. By 1900 a number of industries were established which were electrochemical in nature. Interest in this new form of power was high—and the desirability of an association of individuals having a common interest in electrochemistry was recognized.

I am not entirely certain on this point, but I believe that it was Professor Joseph W. Richards of Lehigh University whom on October 19, 1901 addressed a letter to thirty persons who he believed might be interested in forming an electrochemical society. At the time, Professor Richards was Vice-President of the American Chemical Society.

This inquiry led to a preliminary meeting in Philadelphia when ten of the thirty invited persons agreed that if seventy-five persons could be interested in joining, a society would be formed. A few weeks later letters were addressed to members of such organizations as the American Chemical Society and the American Institute of Electrical Engineers and to any individuals who might be interested. As the result, a meeting was held on April 3, 1902 in Philadelphia which was attended by fifty-two persons who organized the society, known then as the American Electrochemical Society. At the time 337 applications for membership were on hand from thirty-six of the United States and from eight other countries. From this time forward the Society grew rapidly and by the time of the fourth meeting there were 600 members. However this rapid growth did not continue, and forty years later our membership was only about 1200 to 1500.

I believe that it is worthwhile noting that from the start, as at the present, our membership did not suffer limitations as to discipline or vocation. Joined by a common interest in a new area of science and its engineering, as well as commercial applications were: scientists, engineers, industrialists, inventors, and teachers. It is even more interesting, I think, to note that until about twenty years ago all papers were presented to a single session at our regular meetings. This provided a cross-fertilization which is much needed today; and the Society was modern then—even a Society of the Future—in this respect. As to attendance at meetings—260 attended the meeting in New York City just one year after the Society was founded. Thirty-five years later the meetings were not quite double this number.

This is perhaps enough to give a picture of our Society in its early days. With this background I would like to comment on a few subjects, particularly with respect to the changes that have taken place in the last twenty years or so.

Management of the Society

From the start, and until about 1947, the management of the Society was in the hands of the Officers and a group of elected managers. The interests of different technical groups were coordinated by a technical committee for each interest. Later, when the Divisions of the Society were formed, these Committees were dissolved. For example, when the Electrothermics Division (which is now Electrothermics and Metallurgy) was formed in 1922, eight Technical Committees were joined. The Local Sections have been organized at various times but the most recent activity has been in the period 1954-1959 in which seven Local Sections were authorized by the Board of Directors. Their local operations have been autonomous and different from each other.

When the Society was incorporated in 1930, the name was changed to The Electrochemical Society, in recognition of the international nature of our membership. Provision was also made putting the management control of the Society in the Board of Directors. This Board now consists of the Officers of the Society, the Chairman of each Division, two representatives from the Council of Local Sections and the two most recent Past Presidents. This is a representative group but it has the disadvantage of being quite large and furthermore it is constantly changing. Although the latter is certainly not a disadvantage from the standpoint of representation, it has led, in the past, to extended Board meetings—largely informative in nature. In order to simplify the transaction of business at meetings of the Board, all matters first are considered by one of four principal committees and these committees then recommend action for the consideration of the Board of Directors. These Committees are: Finance; Publication; Ways and Means (concerned with legislation); and Technical (concerned with programs, symposia and other matters relating to the technical interests of the Society). Although much of the work of these Committees is done by correspondence, they hold regular meetings just prior to the meetings of the Directors. Nearly all day last Sunday was devoted to these committee meetings—the Board met last evening. Although most Board business is transacted at the time of our two regular meetings, an interim meeting is also held early in January at the Headquarters Office in New York.

For many years the Secretary of the Society carried the load of the day-to-day operations as a part time labor of love. However, by the late 1940's it had become evident that the business of the Society had become too much for such an arrangement.

---

[1] Delivered at the San Francisco Meeting, May 11, 1965.

[2] Head, Department of Chemistry, South Dakota School of Mines and Technology, Rapid City, South Dakota.

It was just about ten years ago that the late Robert Shannon was employed as our first Executive Secretary. He came to us from many years of experience in a somewhat similar organization and capably took over the responsibility for the National Office. For the first time we had the facility for the establishment of a business-like operation. Until then our financial operations were based on a clumsy voucher procedure which required the signature of the President and the Secretary as well as the Treasurer's signature on the check to pay the smallest and most routine bills. We could not present a financial report in the form of a balance sheet for want of the necessary information. These and other ancient procedures were changed and our business was modernized. It was fortunate that we made the step when we did, as this marked the beginning of a period of growth in activities and in membership—all of which greatly increased the work of the National Office. It would take a long time for me to enumerate the many contributions which Mr. Shannon made to streamline and make more effective our headquarters operations, but in any narration of the history of our Society his name should be recognized as one of the substantial contributors. With his untimely death about eighteen months ago we were found wanting in not having anticipated the early need for a successor—fortunately for us we were able to secure the services of our present Executive Secretary, Mr. Ernest G. Enck, who has contributed substantially from his many years of industrial management experience. The result is that we are now in the best position we have ever been, so far as the efficiency and effectiveness of the National Office is concerned.

In the course of the increased activities of the last ten years we have evolved a sort of a training program for potential Presidents. As you know, Vice-Presidents are elected for three-year terms. Under our charter the Vice-President does not automatically succeed to the Presidency. In some similar societies a President-elect has a one year opportunity to prepare himself for his anticipated responsibilities. Perhaps this would be a good plan for us. But as we now operate, our Vice-Presidents in turn serve on each of three of our principal committees, Finance, Technical, and Ways and Means. In most cases our future Presidents also have had experience in the affairs of publication but not always formally. Perhaps it should be made so. Quite recently, in the term of office of President La Que, a plan was put into effect to provide for an annual visit to each of the Sections of the Society by a Vice-President, or by the President. It has taken three years to get this plan into operation and I hope that it will be continued. Our Local Sections are a substantial part of the framework of the Society and until recently have been regarded somewhat casually from the standpoint of the National Office. I believe that this has been due in part to the fact that each Section is unlike any other, and in part to the seeming lack of Sectional interests on the part of the Council of Local Sections. I believe that the annual visits of the Officers of the Society will help to restore the Local Sections to their original strength and activity.

This has been a sketchy preparation for some comments that I would like to make on specific subjects to which I think that we should be attentive in the future; but because so many of you are all too familiar with our history I have tried to include only enough to inform our more recent members. If any of you are interested further, I suggest that you read in Volume **99** of our JOURNAL which was published in our 50th year and which contains many excellent historical descriptions of our technical interests as well as of the founding and early days of the Society. And now for the Comments.

Membership

For many years our membership was open to anyone who was of good character and who was interested in electrochemistry. This was good in that it set a precedent for multidisciplinary membership, bringing together inventors, industrialists, scientists, engineers, chemists, physicists, mathematicians, and metallurgists. But it was not good in at least two ways. As the Society became larger its meetings began to savor, at least to an extent, of commercialism. Some of our members qualified only as salesmen. Also, for lack of stated standards the material which was presented at our meetings and which was, on occasion, published, sometimes did not meet the quality standards of a learned society. In an effort to correct this situation our present membership requirements were established and an Admissions Committee was appointed to review applications to insure that the requirements are met. Whether a result of this action or not, our present membership meets high standards of academic training and experience. A recent survey showed that about one third of our members are listed in American Men of Science (which of course does not include our many distinguished foreign members).

It should be pointed out in this connection that almost as many nonmembers attend our meetings, and that a very large proportion of these also meet our membership standards. Despite an almost punitive registration fee differential and an offsetting credit which is offered to nonmembers who apply for membership at our meetings we still are not getting enough of these potential memberships. We know that a very large number of these persons are repeat visitors and our membership committee has tried hard to make as many contacts at meetings as possible. I hope that those of us who have made no personal effort to bring in new members will do so—a membership committee representative is always as close as the registration desk.

Our membership classes provide for individuals who have not yet qualified as to years of experience and also for students. We cannot expect to have a large number of Associate Members since this classification is temporary, pending the accumulation of the necessary years of experience. But we should have many more Student Members. We have not, as a Society, flourished as we should in the universities. This may in part be the result of our name "Electrochemical." Possibly another designation would seem to tie us in more closely with the disciplines concerned with physics, electronics, metallurgy, crystallography, and engineering. Yet our membership includes all of these and more. It may be that we should sponsor undergraduate interests in interdisciplinary activities and patterned more closely to our general meetings. I can see no reason why our university activities should have to be sponsored by the chemistry department. Where this department is disinterested, we should go to another which is interested.

Just a word about the number of members. I know that there are those who recall fondly the period of about thirty-five years ago when our membership was almost constant. We shall never return to those times but we might well consider what it was about them that was so good. I think that everyone, who can recall the days when each paper was presented to the Society assembled, remembers the interesting discussions which were stimulating and informative. They were made even more so by the distribution in advance of the entire paper, as a preprint. This afforded the opportunity to study the presentation in advance. The increased potency of questions and comments naturally resulted in increased stimulation of the participants, sometimes just a little short of fisticuffs. The many diverse basic interests of the members made these meetings an excellent source of cross-fertilization and new ideas. The rapidly growing popularity of our extended abstracts seems to indicate a desire to return to something closer to our early meetings, although we may never again have fewer than the eight simultaneous sessions of this meeting. Our Society will surely continue its present rate of growth which has quite quickly brought us near the 4000 mark. I hope that we will not too closely follow the example of those societies which seem to exist only for the presentation of endless numbers of ten- and fifteen-minute papers followed by two minutes for discussion. While this system provides for the largest number of papers, the worthwhile part of the meetings takes place in the hotel lobby. Some consideration of ways of relieving our two general meetings from the pressure of increasing size would be in order now, as it takes a number of years to change the preparations for a meeting such as this.

Publications

In the early days of the Society the preprints and the discussions were published in a volume of TRANSACTIONS following each meeting. This was an excellent plan but it is costly to hold type for months pending the editing of the comments, and it does not lend itself well to the publication of a monthly journal.

In 1950 the JOURNAL OF THE ELECTROCHEMICAL SOCIETY was published monthly. Volume **97** continued the number series following TRANSACTIONS Volume **96**. With this change no more preprints were published as such.

By 1963 it had become evident that a second publication devoted to the practical aspects of the interests of the Society would be a worthwhile venture and ELECTROCHEMICAL TECHNOLOGY began publication on the basis of six issues a year. The acceptance of the new publication has been good by members and by nonmembers. When the time comes that we can publish twelve issues a year, I hope that the Board of Directors will permit members to elect either of our monthly publications with membership dues. Those who wish that this could be done soon should be patient. It would not be difficult to obtain technological papers to permit twelve issues right now, except that in order to do so we would have to lower the very high standard that has been set by our Editors. I am sure that we do not wish our publications to grow in size at the cost of quality. A few misinformed individuals have been reluctant to publish except in the JOURNAL. If any are here present—please be informed that the two publications differ in the nature of the subject matter, but not in the standard excellence required for acceptance. We must insist that this not be changed.

Not only do we publish two periodicals. As I mentioned before, Extended Abstracts are growing rapidly in popularity. And in addition, since about 1950 we have published twenty-three Monographs and will publish three more (a total of four) this year. Two of these are in second editions and one is in the third. A recent check shows that in various stages of preparation there are twenty-five more, and there is every indication that in about two years our number of published Monographs will be doubled.

In order that we might have better coordination of all of these efforts, Mr. Robert Kolbe, Assistant Executive Secretary, was this year also made Manager of Publications. His excellent performance in this position has proved the desirability of centralized control of publication. As the load increases we might well consider removing at least certain editorial functions from the "labor of love" category.

Financial

Many changes have taken place. When I became Treasurer in 1955 we were still trying to operate with a system of vouchers of ancient vintage. Many signatures were required and much correspondence was necessary to pay a relatively small, often recurring, expense. We were unable to produce a balance sheet type of financial report for want of a system of accounting that would permit it. Mr. Shannon laid the foundation for our present system of accounting and Mr. Enck has revised it extensively in the direction of efficiency. Some of you recall that your last billing was on a punch card.

About ten years ago we became concerned as to what might happen in the event that a sharp change in our national economy would leave us with a decreasing membership and with the responsibility of publishing but with a decreased budget. It was decided by the Board to set aside certain revenues, in part, as a reserve. One of these sources of revenue is part of the nonmember registration differential at our meetings. In order that the Treasurer might not have the total responsibility for the investment of these funds, a panel of senior members having suitable experience was appointed as an Investment Advisory Panel. This sage group has provided us with a well-balanced portfolio which has increased well and which has also shown good earnings. Our original objective of a reserve equal in amount to our budget for one year has not yet been accomplished but this has been due in part to the rate at which publication costs have risen. However, the sum is, in my opinion, such as to assure reasonable protection and it has been accumulated in a manner as not to have taken away any part of members' dues.

I do not know the date of the first Sustaining Membership or the company which provided it. But for many years many companies have assisted us by annual contributions in this way. At present we have 127 Sustaining Memberships. I think that we should have many more. I doubt that there are many companies who are willing to pay the expense for a representative at one of our meetings—who would not be pleased to have their company name listed on our programs and in our publications with the distinguished group we now have. If your company is not so listed, tell someone who really counts that the cost is only $135 yer year including the JOURNAL and one membership. Our members as individuals can do much to insure our continuing financial stability in this way. The relatively low proportion of Sustaining Members in the aerospace and electronic industries does not speak well for the activity of these members—who rank high in the presentation of papers and in publishing. If this shoe fits—put it on.

Seven Companies are distinguished as Patron Members. These companies each make a substantial annual contribution. If you do not know them, their names are at the top of the list. I hope that in the near future other companies may be able to qualify for membership in this distinguished group.

Fellowships and Awards

I am sure that everyone here is familiar with our two major medal awards, the Acheson Gold Medal and the Palladium Medal. It is appropriate that a learned society have such means of recognizing unusual accomplishment. We could use at least one more. If we had such an award tonight we could dispense with these remarks—surely a step in the right direction.

It is unfortunate that we have not been able to continue a major fellowship, but an amount of money which in the past would have been interesting to a student of stature does not have the same attraction today. Our summer assistance grants have proven to be very much worthwhile and should be continued. We should try to find a source for another major fellowship—your suggestions are solicited.

Local Sections

It seems to be a safe prediction that the Society will continue to grow at its present rate, or more rapidly. With this we can expect larger Local Sections, and no doubt more of them. Very recently the Texas Section, which was established in 1959, has formed two Sections, one in Dallas and one in Houston. We may expect to see similar divisons in other rapidly growing areas. On the other hand, also recently, a Local Sections has suspended operation.

As I stated earlier, each Section is different from each other Section. But in general, I think, the health of a Section is more closely related to the interest and activity of a few individuals who are willing to do quite a bit of work for which no medals and little thanks are given. Here present tonight are a number who worked hard to establish this Local Section which is right now contributing more free (and, I hope, not thankless) labor, that this meeting may be a success. Every man here with me tonight on this dais has contributed most substantially of time and effort to make the Society what it is. We must expect that this number will be small—there are always far more members who come only for the ride and who probably are not at all concerned how this or any other society continues to operate just so long as there are meetings at which to present papers and journals in which to have them published. But when the small hard core is missing from a Local Section it cannot exist very long. I think that we need strong Local Sections. I would like to encourage, especially, the younger members to become personally interested in their Local Section. The future of our Society depends on your activity.

In my visits to Local Sections I have noted two problems that frequently recur—one is the competition of many other meetings, the other is the scattering of membership over a wide area. Probably the solution is different for each Section, but I would like to point out a way by which the Ontario-Quebec Section solved both problems. (The competition of other meetings only affects the less-interesting meeting, so this can be avoided if the meetings can be kept interesting.) Recently I attended a one-day symposium in Montreal. The meeting was held at a local university and speakers were invited. A pertinent round table afforded ample opportunity for discussion. This meeting was attended by at least 150 persons. I suggest consideration of meetings of this kind also as a means of relieving our national meetings of some of the pressure of papers, particularly where the topic may be limited to a smaller number or where it might be geographically concentrated in the local area.

Divisions

Our technical Divisions are all healthy and are evidencing their good condition by well-attended meetings and by well-received Monographs. We should be alert to the possibility of developing new Divisions as new scientific and related areas of interest come into being. We have in the past afforded a meeting place for new interests in the field of metallurgy and electronics. Some of our most flourishing Divisions have come to us as infants. Because we already embrace a variety of scientific and engineering interests we are a more modern Society than many, looking forward to increasing research of an interdisciplinary nature.

Meetings

As we have grown in numbers, so have our general meetings become larger until recently we have had to alert the hotels where we shall meet in the future to the necessity of scheduling five-day meetings. At this meeting we have had to schedule up to eight simultaneous sessions to handle 270 papers. Although this may be one of our larger meetings we can expect that future meetings will be even larger. We are approaching a point where we must decide if we wish to become a paper-presenting Society, severely limiting the discussions, or whether we should find other meeting arrangements such as locally sponsored one-day meetings or possibly a summer meeting at a pleasant university location. I believe that this would be a good topic for consideration by the Technical Committee.

Past Presidents

I have mentioned our presidential training program. An elected Vice-President spends three years becoming acquainted with the operations of the Society by participation (in two cases as Chairman) in the four committees which are advisory to the Board of Directors on Finance, Publication, Technical Affairs, and Ways and Means (in other words legislation). There is quite a bit more work involved in these responsibilities than can be seen from the outside—and the new Vice-President is usually surprised to discover how much time is required of him. After a year as President, which in my case has proven to require about a full day a week—possibly a little more—, the Past-President serves as a member of the Board for two years. At the end of this period he has been in close touch with Society affairs for six years—prior to which he had been active in the affairs of a Section or Division. He has the continuing privilege of attending meetings of the Board of Directors without voting power. I would like to suggest that these experienced and devoted individuals be used more directly to further the interests of our Society. I do not think that oldtimers should run the Society. I think that the Sections and Divisions should be able to develop the younger men who should head these groups and provide new blood for the National Offices. I would sincerely suggest that a Past-President be named as an advisor to each important National Committee. This would promote continuity as well as provide an interested source of information and experience. I think that we could use special study groups in many areas, much as we did to review our Constitution and Bylaws some years ago. Some of the things that could be studied profitably are:

—How can we go about interesting young scientists and engineers while they are in the university? What can we do for them, other than give them awards of money?

—How can we more effectively cooperate with other technical societies in which our members have interests?

—Should we consider summer meetings directed especially to the younger teachers who often are not free at the time of the year when we have our general meetings?

In my preceding comments I have suggested other problems for study. I recommend that these study groups should be appointed by the President annually and that each should report in writing to the Board.

In Conclusion

In the last ten years our Society has seen its greatest prosperity. In numbers we have increased at least threefold. In the esteem of our peers we have never stood higher. Our principal reasons for being—our publications and our meetings—are flourishing. We are in good financial health. (I hope that everyone understands in this connection that this does not mean that we have unlimited funds for publication, but the very general acceptance of a page charge is tending to relieve that situation also.)

We must not take this prosperity for granted. Our future growth should relate to our ability to serve the many interests which we represent—and to our ability to attract new and interested related disciplines and technologies. Our membership should continue to be limited to those who are truly interested in our objectives and who can meet our requirements for membership. We are an international Society—We provide a common meeting place for many scientific and engineering interests—In our meetings the traditional and the very new meet and learn from each other.

In these and in all respects our Society meets the requirements of the presently rapidly moving technology of the world.

In closing I would like to thank all those who have worked with me over many years in Society affairs. For me these have been my best years. I am grateful for them. Thank you.

Current Affairs

Electrochemical Society Awards

Richard E. Westerman

Young Author's Prize for 1964

At the Annual Banquet held on Tuesday May 11, during the San Francisco Meeting of The Electrochemical Society, Richard E. Westerman, a research associate at the Chemical Metallurgy Unit of Battelle-Northwest, Richland, Wash., was announced as the winner of the 1964 Young Author's Prize of $100.

His prize-winning paper "High Temperature Oxidation of Zirconium and Zircaloy-2 in Oxygen and Water Vapor" appeared in the February 1964 issue of the JOURNAL.

Dr. Westerman's current interests include high temperature oxidation of superalloys and refractory metals, and diffusion and solubility of hydrogen in zirconium alloys.

He holds a B.S. degree in Metallurgical Engineering from the Montana School of Mines and a Ph.D. degree (received in 1960) from the Rensselaer Polytechnic Institute.

He is a member of the American Institute of Mining, Metallurgical, and Petroleum Engineers, American Society for Metals, Sigma Xi, and Phi Lambda Upsilon.

Turner Memorial Award for 1964

Roger W. Bartlett of the Sanford Research Institute, Menlo Park, Calif., was announced as the winner of the Francis Mills Turner Memorial Award, sponsored by the Reinhold Publishing Corp., in recognition of his paper "Growth Kinetics of Discontinuous Thermal Oxide Films; Aluminum," which appeared in the August 1964 issue of the JOURNAL.

The award, consisting of $100 worth of scientific and technical publications, was made to Dr. Bartlett at the Society's Annual Banquet on May 11 in San Francisco.

Dr. Bartlett recently joined Stanford Research Institute as a senior materials scientist. He was previously with Aeronutronic Division of Philco Corp., Newport Beach, Calif.

His research interests include oxidation of metals and intermetallic compounds, surface properties, solid state diffusion, chemical kinetics, refractory coatings, vapor deposition, synthesis of composite materials and application of thermodynamic data to materials behavior at high temperatures. He has also studied hypervelocity impact phenomena and two-phase flow behavior in rocket nozzles.

Dr. Bartlett received a B.S. degree in 1953 and a PhD. degree in Metallurgy from the University of Utah in 1961.

He is a member of The Electrochemical Society, The American Institute of Mining, Metallurgical and Petroleum Engineers, the American Society for Metals, the Combustion Institute, and Tau Beta Pi.

Robert W. Bartlett

Abstracts of "Recent News" Papers

Presented at the Electronics Division Semiconductor and Laser Sessions, San Francisco, Calif., May 9-13, 1965

Semiconductors

(111) Faceting in Epitaxy Grown Over Stepped Surfaces

C. E. Benjamin and E. J. Patzner, International Business Machines Corp., Systems Manufacturing Div., East Fishkill, N. Y.

Epitaxial silicon layers grown over surface mesas and recesses exhibit structures that "smear" certain edges and shift patterns laterally. These effects become more pronounced as the wafer surface approaches a (111) plane. Orientation measurements show that these smears are approximately truncations of growing surface steps by this (111) plane. Thus, the smear width is dependent on the step height, and the lateral shift, primarily on epitaxy thickness. Slight deviations observed from this model are discussed.

Heteroepitaxial Growth of Ge on GaP and GaAs Substrates

R. A. Mueller, D. R. Chambers, and J. J. Bordeaux, Sanford Research Institute, Menlo Park, Calif.

Single crystal Ge has been deposited on single crystal substrates of both GaP and GaAs using the hydrogen reduction of $GeCl_4$ in an open tube reaction system. Germanium nucleates and grows much more rapidly on these substrates than on silicon or germanium used in previous work. Junctions produced are uniform and planar, and Laue patterns indicate single crystal growth in the same orientation as the substrate. Diodes made from the heterojunctions are being studied electrically.

The Preparation of Epitaxial Semi-Insulating Gallium Arsenide by Iron Doping

P. L. Hoyt and R. W. Haisty, Texas Instruments Inc., Dallas, Texas

Epitaxial semi-insulating ($\sim 10^5$ ohm-cm at 300°K) GaAs deposits were prepared by doping with iron using an open tube deposition system. Resistance measurements as a function of temperature show a deep acceptor energy level of 0.5 ev. Experimental apparatus and production of n-SI-n sandwich structure are described. [We wish to acknowledge support of the Electronic Technology Lab. of the Research and Technology Div., Air Force Systems Command, U.S. Air Force, Contract AF 33(615)-1275.]

The Epitaxial Growth of CdS on Tetrahedral Faces of GaAs and GaP

Martin Weinstein and A. A. Menna, Tyco Laboratories, Inc., Waltham, Mass.

Vapor phase chemical reaction techniques have been developed for the growth of single crystal CdS films on tetrahedral faces of GaAs and GaP. Smooth, highly polished wurtzite CdS films, 1-100μ thick and 1 cm^2 in area, have been grown on the {111} "Ga-face" of GaAs and GaP using an H_2-HCl mixture as the reactant gas and a substrate temperature of 720°C. Using the HCl-H_2 mixture sphalerite-type CdS films were grown on $\{\bar{1}\bar{1}\bar{1}\}$ "As-face" and "P-face" of GaAs and GaP, respectively. Employing H_2 as the reactant gas, highly polished wurtzite CdS films, containing characteristic hexagonal facets, were grown on both the $\{\bar{1}\bar{1}\bar{1}\}$ and {111} of GaAs and GaP. Electronmicroprobe analyses have shown the junctions to be chemically abrupt. The physical and chemical properties of these films are discussed.

Epitaxial Growth of Silicon on Hexagonal Silicon Carbide

T. L. Chu, G. A. Gruber, J. J. Oberly, and R. L. Tallman, Westinghouse Research Labs., Pittsburgh, Pa.

The epitaxial growth of silicon on the basal plane of hexagonal silicon carbide substrates has been accomplished by using the pyrolysis of silane in a flow system. The effects of deposition variables on the properties of grown films were evaluated using chemical etching and optical microscope techniques as well as reflection electron diffraction examinations. The films were found to be predominately of {111} and {110} orientations, and the relative abundance of these orientations varied with the crystallographic orientation of the substrate surface and the deposition conditions. [The research reported in this paper was sponsored by the Air Force Cambridge Research Laboratories under Contract No. AF19(628)-4220.]

In Situ Etching of Silicon Substrates Prior to Epitaxial Growth

T. L. Chu, G. A. Gruber, and R. Stickler, Westinghouse Research Labs., Pittsburgh, Pa.

The cleanness of the substrate surface is important for the epitaxial growth of silicon, and the *in situ* etching of substrates prior to the growth process has been shown to be capable of reducing structural imperfections in epitaxial silicon films. In this work, epitaxial silicon films were deposited on silicon substrates of high perfection by using different *in situ* etchants, and the substrate-film interface regions in these specimens were examined by transmission electron microscopy. The effects of various etchants on the structural perfection of epitaxial silicon films are discussed. (The research reported in this paper was sponsored by the George C. Marshall Space Flight Center of the National Aeronautics and Space Administration under Contract NAS8-11432.)

Reactivity and Bond Strain of Electron Gun Evaporated SiO_2 Films

W. A. Pliskin, IBM Components, Poughkeepsie, N. Y.

A detailed study has been made on electron gun evaporated SiO_2 films utilizing spectroscopic, optical, and etch rate techniques discussed previously for the evaluation of SiO_2 films. Due to a high degree of bond strain in addition to porosity, electron gun evaporated films exhibit fast etch rates and considerable reactivity with water at relatively low temperatures. Significant changes in film thickness, refractive index, etch rate, and structure are caused by exposure to high humidity.

Macroscopic Defects in Epitaxial Silicon

E. R. Skaw and K. M. Busen, Research Center, Sprague Electric Co., North Adams, Mass.

Macroscopic defects in epitaxial silicon variously labeled hillocks, pips or stars have been studied. It is found that the occurrence of these defects is material dependent. Evidence is presented to show that these defects arise from a microalloy which is liquid at the growth temperature. The shape of the defect is predominantly crystallographically determined. The impurity in the defect has been identified.

Dislocation Reactions in Silicon Web

S. O'Hara, Dept. of Materials Science, Stanford University, Stanford, Calif., and G. H. Schwuttke, Components Div., International Business Machines Corp., Poughkeepsie, N. Y.

The origin of dislocations in silicon web are discussed. Dislocations having $[2\bar{1}\bar{1}]$ axes or $<110>$ type axes have been characterized. In the former case, normal edge and 30° dislocations are seen; however, an apparently new dislocation with a $[2\bar{1}\bar{1}]$ axis and [101] type or [110] type of Burgers vector has also been observed. Dislocations having a $[1\bar{1}0]$ axis and [101] Burgers vector have been identified and associated with the Cottrell-Lomer reaction. The presence of multiple twin planes parallel to the growth direction of the web, accompanied by regions of very high dislocation density near the dendrites, increases the probability of certain dislocation reactions.

Formation of Precipitates in Gold Diffused Silicon

R. Stickler and E. D. Wolley, Westinghouse Research Labs., Pittsburgh, Pa.

Silicon wafers were gold diffused at 1200°C for two hr using a closed tube gaseous diffusion. Highly dislocated and relatively perfect wafers were both fast and slow cooled from the diffusion temperature. After diffusion, the silicon wafers were thinned and examined by transmission electron microscopy. Precipitated particles were observed near the wafer surfaces. In highly dislocated and fast cooled wafers, small particles were found precipitated onto dislocations while in the slowly cooled, dislocation free wafers large cube shaped particles were found near the wafer surface. By comparison of electron diffraction data observed from the large particles with x-ray diffraction data obtained from prepared bulk gold-phosphorus compounds the large precipitated particles in the slow cooled, gold-diffused, silicon wafers have been tentatively identified as Au_2P_3. (The research reported in this paper was sponsored by the George C. Marshall Space Flight Center of the National Aeronautics and Space Administration under Contract NAS8-11432.)

The Structure and Perfection of Thermally-Grown Oxide Films on Silicon

R. Stickler, R&D Center, Westinghouse Research Labs., Pittsburgh, Pa., and A. N. Knopp, Semiconductor Div., Westinghouse Research Labs., Pittsburgh, Pa.

Thermally-grown silicon oxide films are used in many processes required for silicon device and integrated circuit fabrication. The knowledge of perfection, cleanliness, and structure of such films is very desirable. The structure of thermally-grown oxides was studied as a function of various heat treatments. Uniform amorphous and crystalline films can be obtained which may contain gross defects such as cracks resulting from special heat treatments.

Observations on Phosphorus Stabilized SiO_2 Films

M. Yamin, Bell Telephone Labs., Inc., Murray Hill, N. J.

Two experiments with SiO_2 films which have been stabilized against ionic drift effects by phosphorus diffusion are described. In the first experiment the interaction between phosphorus and boron in silicon dioxide films was studied. Diffusion of boron into a phosphorus-stabilized oxide is found to destroy the stabilization, but even a light phosphorus diffusion over a boron-diffused oxide will restore stabilization.

In the second experiment, conduction measurements were performed at 600°C to clarify the difference between phosphorus stabilized and untreated oxide specimens. A slowly varying voltage was applied to an MOS structure formed by evaporating a gold dot over the oxide film, and the current was recorded. Both stabilized and untreated films showed rectifying characteristics at 600°C, the more highly conducting polarity being that with the silicon negative. In the case of the untreated film, a large peak of current is superimposed on this characteristic at —2.5v. This peak is absent in phosphorus-stabilized films. Discharge currents equivalent to the charging currents are not observed on removing voltage from the specimen, as they are at 400°C.

The Effect of Fluorides on the Wettability of Silica Surfaces

M. L. White, Bell Telephone Labs., Inc., Allentown, Pa.

The contact angle of water on silica surfaces is a function of the temperature to which the silica is heated and is also affected by fluoride adsorbed on the silica from aqueous HF solutions. This adsorbed fluoride cannot be rinsed off with water, but is removed by complexing with ferric ion, or by high-temperature steam. From measurements on a porous silica it is estimated that 4% of a monolayer of fluoride is strongly adsorbed.

The Influence of Phosphorus Concentration on the Atmospheric Steam Oxidation of Silicon

R. P. Donovan and M. N. Hobgood, Research Triangle Institute, Durham, N. C.

The influence of phosphorus concentration on the atmospheric steam oxidation of silicon has been investigated by comparing the thicknesses of oxides grown on the surface of phosphorus diffused wafers with those grown simultaneously on a bevelled cross section through the diffused layer. The influence of phosphorus concentration is most pronounced at low temperatures ($\sim$ 700°C) where the growth rate at high phosphorus concentration may exceed that at low concentration by a factor of 4 or more. The correlation between oxidation rate and phosphorus concentrations suggests that this technique may enable one to rapidly and easily establish the impurity profile of heavily-diffused phosphorus layers, since the oxidation of the cross section gives rise to well defined color bands.

Thin Films Grown on Silicon Surfaces by Excess Nitric Acid Process

W. B. Glendinning, Sidney Marshall, and Albert Mark, U.S. Army Electronics Labs., Fort Monmouth, N. J.

Several types of transparent films have been grown on the surface of silicon materials of varying doping levels (ranging from 0.05 ohm-cm to 50 ohm-cm) and both conductivity types. By application of liquid drops of concentrated nitric acid and vapors of concentrated hydrofluoric acid directly to the surface of silicon samples, thin films which are insoluble in HF acid were grown at vertical growth rates of several to hundreds of angstroms per second. A lateral growth mechanism is also present which develops films horizontally at several angstroms per second. Film growth reaction rates are related to doping levels of silicon surfaces.

Enhanced Etching in Electron and Proton Bombarded Silicon Dioxide Layers

T. W. O'Keeffe, Westinghouse Research Labs., Pittsburgh, Pa.

Thermally grown silicon dioxide layers show enhanced etching rates after bombardment with 2-10 kev electrons. The enhancement effect: (1) saturates for bombardments of approximately 1 ampere second/cm^2 for 10 kev electrons; (2) is dependent on the etchant used; (3) can show a three-fold increase in etch rate; (4) provides a means of uniform selective etching. Samples bombarded with 100 kev protons have shown 11 fold increases in etch rate. The effect provides a novel means to study energy-penetration relationships for electrons and protons in the 0-2μ range.

GaAs Prepared from Nonstoichiometric Melts

F. J. Reid, R. D. Baxter, and S. E. Miller, Battelle Memorial Institute, Columbus, Ohio

Gallium antimonide single crystals have been prepared from melts ranging in composition from nearly stoichiometric to Sb/Ga atom ratios of about 3/1. P-type GaSb and, by suitable impurity additions, n-type GaSb have been produced with superior electrical properties. The residual acceptor concentration has been reduced to the order of 2 x $10^{16}/cm^3$ by growing crystals from antimony-rich melts. Hole mobilities at 78°K in excess of 6000 cm^2/v-sec and electron mobilities of over 10,000 cm^2/v-sec have been realized. (Work supported by the Air Force Office of Scientific Research, Grant No. 525-64.)

The Equilibria in the System GaSb-GaAs

Miroslav Miksovsky (Present address: Dept. of Chemical and Metallurgical Engineering, University of Michigan, Ann Arbor, Mich.) and B. M. Kulwicki (Present address: Materials and Controls Div., Texas Instruments, Inc., Attleboro, Mass.) Institute of Solid State Physics, Czechoslovak Academy of Sciences, Prague, Czechoslovakia

The liquidus curve for the pseudobinary system GaAs-GaSb has been obtained by thermal analysis measurements. Samples were prepared by direct fusion of the elements in sealed evacuated ampoules and quenched in air. Each ingot was ground to a fine powder ($<$ 90 micron particle size), analyzed chemically, pressed into pellets, resealed, and annealed for 185 hr and 1720 hr at 695°C before measurement. Chemical analysis indicated that negligible material was lost during processing and the measured sam-

December 1965 Discussion Section

A Discussion Section, covering papers published in the January-June 1965 JOURNALS, is scheduled for publication in the December 1965 issue. Any discussion which did not reach the Editor in time for the June 1965 Discussion Section will be included in the December 1965 issue.

Those who plan to contribute remarks for this Discussion Section should submit their comments or questions in triplicate to the Managing Editor of the JOURNAL, 30 East 42 St., New York, N. Y., 10017, *not later than September 1, 1965*. All discussion will be forwarded to the author(s) for reply before being printed in the JOURNAL.

ples were in fact on the pseudobinary tie-line. X-ray data indicate that both GaAs and GaSb were present in the samples as made and both phases remained in the central region of the diagram after the indicated annealing times. The liquidus curve contains a flex point, and transitions observed in the two-phase liquid region may be associated with changes in curvature of the liquidus and solidus curves. However the existence of a completely isomorphous system is not established by this work.

Structural and Optical Properties of Thin Films of ZnS-CdS

W. M. Kane, J. P. Spratt, L. W. Hershinger, and I. H. Khan, Applied Research Lab., Philco Corp., Blue Bell, Pa.

Films of the alloy system ZnS-CdS have been produced by simultaneous evaporation from two separately controlled sources onto a single substrate. Films of uniform compositions covering the full range from 0% to 100%, ZnS concentration have been evaluated using X-ray diffraction and optical transmission edge measurements. A gradual phase transition from wurtzite to zincblende crystal structure was found to take place between 60% and 85% ZnS. The lattice parameters were found to vary smoothly with composition, and are close to values reported for bulk material. Optical energy gap measurements show a nearly linear variation of gap width with ZnS concentration.

A Novel Crystal Growth Phenomenon: Single Crystal GaAs Overgrowth onto Silicon Dioxide

F. W. Tausch, Jr., and A. G. Lapierre, III, Sylvania Semiconductor Div., General Telephone and Electronics, Inc., Woburn, Mass.

Epitaxial growth of GaAs in windows on SiO_2-masked GaAs substrates has been studied and found to yield smooth-surfaced single-crystal epitaxial layers. Single-crystal overgrowth onto the SiO_2 films, initiating from the windows and growing out laterally over the SiO_2, has also been observed to occur in many instances. Studies of growth habits and patterns, inspection of cleaved sections, x-ray studies, and crystallographic considerations have led to a proposed growth mechanism which is not only consistent with the experimental window growth and overgrowth observations, but also indicates that the processes are highly controllable; it has been shown that overgrowth can be virtually inhibited, and it is concluded that with proper mask geometry single crystal overgrowth can occur over large areas almost without restraint.

Reduction of Surface Charge in SiO_2 by Oxidation Under Bias

A. Goetzberger, Bell Telephone Labs., Inc., Murray Hill, N. J.

Oxidation of silicon was carried out under the influence of an electric field. The field was applied by means of an electrode suspended about 1 cm above the surface. Negative electrode potential resulted in a low surface charge density after steam oxidation. Above several hundred volts, surface charge density saturates at about 4 x 10^{11} states cm^{-2}. No influence of field on surface state density during dry oxidation was found. MOS drift experiments showed greatly improved stability of bias grown wet oxides.

Growth of Drift-Free Silicon-Dioxide

R. Schmidt, Bell Telephone Labs., Inc., Murray Hill, N. J.

Sodium in SiO_2 may result in a change of the surface charge in metal-silicon dioxide-silicon structures. Sodium may originate from the silicon substrate itself, from contamination during cleaning and oxidation, or from handling the sample. To obtain a drift-free SiO_2, it is necessary to begin with a silicon substrate whose sodium content is low, to properly clean the silicon substrate before oxidation, to grow the oxide in a suitable furnace and to keep the sample clean after oxidation. Fabrication under these conditions results in uniform devices and aging in steam at 300°C for 26 hr (silicon negative, $E_{SiO_2} = 10^6$ v/cm) results in a change of less than 10^{11} charges per cm^2.

Threshold of Metal-Oxide-Silicon Field Effect Transistors

G. Cheroff, F. Fang, and D. P. Seraphim, Thomas J. Watson Research Center, International Business Machines Corp., Yorktown Heights, N. Y.

The gate to source potential (V_t) at which drain current first rises in the silicon MOS FET is considered as a function of the applied source to body potential (V_b) and impurity level, N, in the bulk. V_t may be adequately described by including the bulk charge in the depletion region $Q_b = (2\epsilon\epsilon_s qN[\psi_s + V_b])^{1/2}$ and a fixed surface charge Q_{ss} for a range of impurity concentrations. The correlation of channel conductance and capacitance are shown. Some novel techniques for controlling Q_{ss} are described.

Hall Mobility of Electrons on Inverted Surfaces

A. B. Fowler, Thomas J. Watson Research Center, International Business Machines Corp., Yorktown Heights, N. Y.

Measurements of the Hall mobility and density of electrons on the surface of inverted p-type substrates have been made as a function of electric field on substrates with resistivities ranging from 1 ohm-cm to 100 ohm-cm. The mobility has been observed to increase at low fields and to decrease at high fields. Impurity level has a strong effect at low fields. The result of heat treatment was to remove surface traps and to decrease mobility. Substrate bias and increase of temperature also reduced the mobility.

Residual Stress in Epitaxial Silicon Films on Sapphire

C. Y. Ang and H. M. Manasevit, Autronetics, A Division of North American Aviation, Inc., Anaheim, Calif.

Based on the consideration of their thermal expansion coefficients, it is most probable that an epitaxial silicon film growth on sapphire is thermally stressed. Some knowledge of the magnitude and state of stresses in the silicon films should be of value to the study of lattice imperfections as a function of growth conditions and to the development of thin film devices. This paper describes the results obtained in measuring the residual stress in an epitaxial silicon film on sapphire using the cantilever beam technique. A silicon film was grown on a

0°-oriented (basal) sapphire ribbon, and from the deflection of the combination at room temperature, the total residual stress was calculated. The value is considerably less than the estimated yield strength of silicon.

Stabilization of Tantalum Thin Film Resistors

H. A. Waggener and M. T. Morris, Bell Telephone Labs., Inc., Murray Hill, N. J.

Tantalum thin-film resistors which use Al_2O_3 passivation are described. The two systems Ta-Al_2O_3-Ta_2O_5 and Ta-Ta_2O_5-Al_2O_3, produced by anodization of layered metal structures, will be compared to the usual system Ta-Ta_2O_5. Preliminary experiments demonstrate that incorporation of Al_2O_3 can provide an order of magnitude improvement in stability, when the applied stress is either temperature, 550°C—or power, 80 to 120w per in.^{2} film. Discussion of the major factors influencing stability is described.

Dielectrically Isolated Silicon with Sharp Impurity Gradient

V. Y. Doo and D. K. Seto, Systems Development Div., International Business Machines Corp., Poughkeepsie, N. Y.

Sharp impurity gradient at the N-N$^+$ (or P-P$^+$) interface and low collector resistance are required for high-frequency transistors. N-N$^+$ (or P-P$^+$) impurity profiles in the dielectrically isolated silicon produced by using methods known today suffer considerable gradation because of the subsequent heating during the oxidation and polycrystalline silicon growth. A new method which gives sharp impurity gradient and low collector resistance after isolation is described. Techniques which give high yields are presented, and the results are discussed.

Nondiffusion Junction Isolation Scheme

V. Y. Doo and R. E. Jones, Systems Development Div., International Business Machines Corp., Poughkeepsie N. Y.

A nondiffusion junction isolation scheme and its technical requirements are discused. The advanatges of the nondiffusion junction isolation over the conventional diffusion junction isolation are: the simplicity in process, the sharp N-N$^+$ impurity gradient, the low collector resistance, and, above all, the low cost. Photomicrographs of the completed sample wafers are shown, and the electrical data measured on the isolated units are presented.

A Composite Insulator—Junction Isolation Scheme

R. E. Jones and V. Y. Doo, Systems Development Div., International Business Machines Corp., Poughkeepsie, N. Y.

An isolation scheme is described which utilizes biased PN junction isolation at the bottom of an isolated unit and oxide isolation on the side walls of the units. The advantage of this structure is the reduction of the isolation capacitance and leakage current over the well-known diffused junction-isolation structure. Photomicrographs of the structure and electrical data are presented.

Storage Time Control in Silicon pnp Transistors using Gold and Platinum

R. Edwards and A. B. Kuper, Bell Telephone Lab., Inc., Murray Hill, N. J.

When gold is diffused into pnp silicon planar transistors to reduce collector lifetime, severe reduction of lifetime in the base layer can also occur, limiting h_{FE}. By annealing, large increases in h_{FE} (*e.g.*, from 10 to 100) are obtained with only moderate increases in storage time (8-15 nsec.), indicating different rates of gold precipitation in the collector and base. Platinum is also found to act as an effective source of recombination centers. Results are qualitatively similar to those obtained with gold, with some quantitative differences.

Second-Phase Formation in Diffused Transistor Structures

J. M. Fairfield, B. J. Masters, and G. H. Schwuttke, International Business Machines Corp., Poughkeepsie, N. Y.

Recently it has been shown that the Scanning Oscillator Technique (SOT) is capable of detecting failure mechanisms in diffused transistor structures. In this paper, the technique is actually applied to the study of "second phase" formation after the diffusion process. Large-area x-ray topographs of silicon wafers containing diffused transistor structures reveal the presence of crystallographic imperfections and precipitation in the device area. After boron diffusion only the imperfections are observed. A subsequent gold diffusion does not change the imperfection pattern. Si-P and Si-P-Au compound formation is detected after phosphorus diffusion and after phosphorus diffusion followed by a gold diffusion, respectively. The x-ray measurements are verified by autoradiographic analysis. The implications of these findings on device properties are discussed.

A Process to Deposit Uniform Silicon Films for Electrical Isolation

M. Juleff and P. Wang, Semiconductor Div., Sylvania Electric Products, Woburn, Mass.

One technique to achieve improved electrical isolation between the components of silicon microelectronic circuits is oxide isolation. In this technique it is necessary to grow polycrystalline silicon films of several mils thick on oxidized silicon wafers. Standard vapor phase epitaxial growth process usually produces etching and sporadic growth on the bottom surface, which creates a processing problem. In this paper we describe a simple process which produces very flat and uniform polycrystalline growth on oxidized silicon wafers with no etching or growth on the bottom surface. The properties of this Si/SiO_2/poly Si sandwich structure is described.

Page Charge Adopted for the JOURNAL

Increased costs of publication have made it necessary for The Electrochemical Society to institute a per page charge for publication in the JOURNAL.

At the Meeting of the Board of Directors held in New York on September 29, 1963 a charge of $35.00 per printed page was established by the Board of Directors, on recommendation of the Publication and Finance Committees, for papers published in the JOURNAL. This action becomes effective for papers received after February 1, 1964.

A 10% reduction in the page charge will apply to papers authored by one or more members of The Electrochemical Society and/or by one or more employees of Patron or Sustaining Members of the Society.

Papers are accepted for publication on the basis of merit by established practices of review. Acceptance of future papers for publication will not be dependent on payment of this invoice. Where funds are not available for payment of this charge it will be waived by The Electrochemical Society.

The Effects of Gold Diffusion in a Silicon Integrated Block Structure, A Lateral PNP Transistor

Philip Shiota, Westinghouse Molecular Electronics Div., Elkridge, Md.

An extended experiment of gold diffusions in an integrated block structure, a lateral PNP transistor, in a diffusion temperature range from 700°C-900°C has been performed. Little work has been published on gold diffusions into silicon integrated blocks at these lower temperatures. A relationship between the change in gain of a lateral PNP transistor and the density of gold atoms is derived. The change of current gain *vs.* gold density is given. The solubility curve of gold in silicon which is obtained using the above-mentioned relationship between the change in gain of the lateral transistor and the density of gold atoms is compared with published data. A comparative analysis between the results of this paper and published data is discussed.

Silicon Junction Devices Formed by Sodium Ion Bombardment

J. Cohen, R. P. Ruth, Autronetics, A Division of North American Aviation, Inc., Anaheim, Calif., and J. F. Hon and R. L. Steele, Rocketdyne, Autonetics, A Division of North American Aviation, Inc., Anaheim, Calif.

Junction devices have been produced in p-type silicon by injection of sodium ions of 1 to 20 kev energy. Host crystals in several crystallographic orientations and in a wide range of resistivities have been used. Diodes and other structures employing oxide masking techniques have been fabricated. Highly uniform electrical characteristics have been obtained for diodes formed on single wafers. Reverse breakdown voltages up to nearly 200v have been observed.

Metallizing for Beam Lead-Devices

M. P. Lepselter, Bell Telephone Lab., Inc., Murray Hill, N. J.

This talk will describe a process sequence developed to fabricate beam-lead semicondutcor devices and integrated circuits. The basic structure consists of a planar-oxidized silicon chip with diffused junctions, platinum silicide ohmic contacts, titanium and platinum layers bonded to the silicon oxide, and electroformed gold leads. The techniques discussed are metal layer sputtering, glow discharge etching of inert metals, and electroforming high resolution gold patterns.

Light Emission of Gallium-Arsenide Electroluminescent Diodes

T. H. Yeh and M. M. Roy, Components Div., International Business Machines Corp., Poughkeepsie, N. Y.

This paper discusses the spatial origin and appearance of light emitted by electroluminescent gallium-arsenide diodes. Michel, *et al.*, have shown that in high-efficiency stimulated emission diodes the light issues from the P region, and that the emitting region's appearance does not change with increase in current. This Letter shows that for electroluminescent diodes (with spontaneous emission) the light also comes from the P region, but the region does change in appearance as the current changes.

Solution Regrowth of Planar InSb Laser Structures

I. Melngailis and A. R. Calawa, Lincoln Lab., Massachusetts Institute of Technology, Lexington, Mass.

A new technique for growing a thin layer of InSb on an InSb substrate from a melt consisting of In saturated with InSb was used to fabricate large volume lasers, which emit coherent light parallel to the direction of current. The basic process was first developed by Nelson for growing GaAs and Ge junctions. For the lower temperatures required for InSb (about 300°C), we used hot liquid stearic acid to cover the InSb substrate and the melt during the growth process. Uniform planar InSb junctions about 2 cm^2 were obtained by suitably doping the melt. (With support from the U.S. Air Force.)

Lasers

Nonradiative Transitions in Solids Containing Trivalent Erbium Ion

S. A. Pollack, TRW/Space Technology Labs., Redondo Beach, Calif.

Nonradiative energy transfer to $^4S_{3/2}$ state of erbium ion was studied in the following hosts: CaF_2, BaF_2, SrF_2, $CaWO_4$, $CaMoO_4$, and Y_2O_3. The purpose of the study was to determine conditions under which the quantum efficiency of the $^4S_{3/2} \rightarrow {}^4I_{15/2}$ transition in Er^{3+} at 5500Å is a maximum. The above transition is considered to be suitable for laser action. An optical method using a 10 nsec pulsed light source was employed.

Q-Switch Operation of a Continuously Pumped Nd:YAG Laser

R. G. Smith, Bell Telephone Labs., Inc., Murray Hill, N. J.

Q-switched operation of a Nd:YAG laser pumped by a tungsten lamp has been achieved using a rotating mirror. At speeds of 150-400 cps, peak output powers in excess

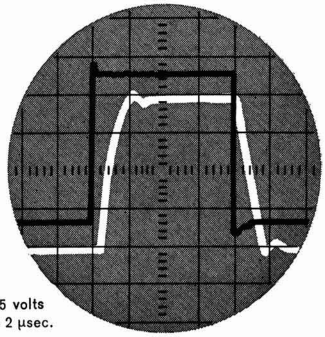

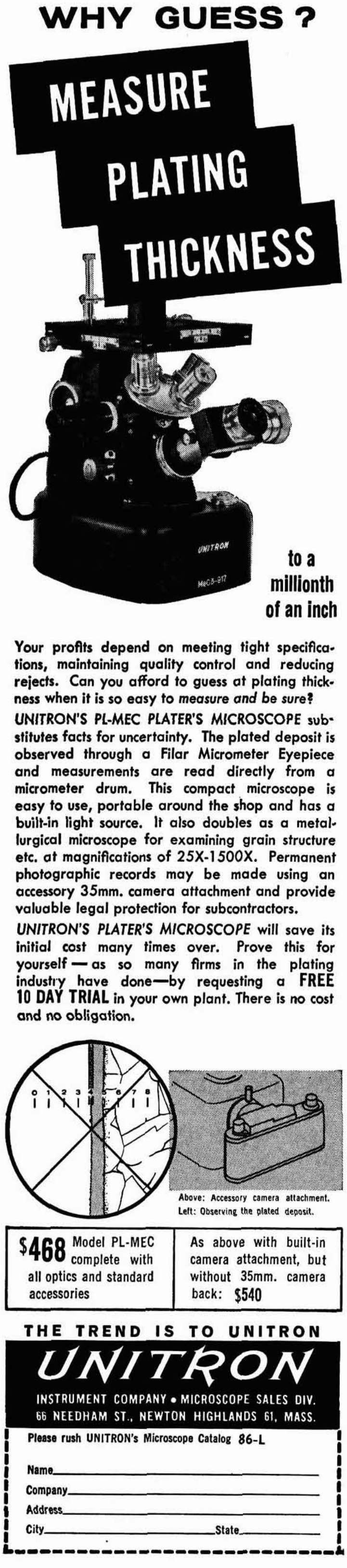

of 250w in the fundamental TEM_{00} mode have been observed; peak powers in the kilowatt range appear possible by optimization of coupling. Details of operation, limitations, and applications are discussed.

Some Characteristics of the Nd^{3+} — Yb^{3+} Calibo Glass Laser

G. E. Peterson and A. D. Pearson, Bell Telephone Labs., Inc., Murray Hill, N. J.

Laser oscillation of Yb^{3+} in Calibo glass utilizing energy exchange from Nd^{3+} has previously been reported by Pearson and Porto. The ions are resonance coupled and the system will oscillate as a three level laser at room temperature. Time resolved spectral studies indicate that the rate of energy exchange from the Nd to the Yb is about $3x10^4$ sec. Estimates of the quantum efficiency of the exchange process from the fluorescence lifetime measurements and from the time resolved spectra yield a value of 0.6.

There is a substantial increase in oscillation threshold with temperature. Measurements have been made on glass rods with varying concentrations over a range from 20°K to room temperature. The increases are probably attributable to two effects: (1) reduction in the Nd→Yb exchange efficiency; (2) changes in the population of the crystal field components of the Yb ground state. We have found no evidence for simultaneous laser oscillation of both ions in the Calibo glass. Gandy and Ginther have reported such in $LiMgAlSiO_3$ glass rods. It would appear that the coupling between the Nd and Yb is very much stronger in our case than in theirs.

The fluorescence lifetime of the Yb in the coupled system is about 1 millisecond. This relatively large value, coupled with the fact that there are substantial absorption bands for the pump light, tend to make this system particularly attractive as a high power laser.

CW PbS Diode Laser

J. S. Butler and A. R. Calawa, Lincoln Lab., Massachusetts Institute of Technology, Lexington, Mass.

Injection luminescence and CW laser action have been observed from PbS diodes at 4°K. Below threshold the spontaneous emission exhibits a main peak at 4.3μ and a lower intensity peak at 4.6μ. Above a threshold current density of 300Å cm^{-2} a laser line at 4.3μ with a half-width less than 15Å and a well defined mode structure are observed. Fabrication methods are based on controlling deviations from stoichiometry in as-grown single crystals.

Laser Induced Luminescence in Biphenyl and Its Derivative

W. L. Peticolas, K. B. Eisenthal, and K. E. Rieckhoff, Research Lab., International Business Machines Corp., San Jose, Calif.

Although the frequency of the first single absorption band of biphenyl is greater than twice the ruby laser frequency, 14,400 cm^{-1}, and the frequency of the first biphenyl triplet is almost twice the laser frequency, we have found that ruby laser light will induce an intense luminescence throughout the visible region in biphenyl molecules in the crystalline or liquid state. The phenomenon has also been observed in most other molecules which we have examined which contain a phenyl-phenyl single bond. These include not only substituted biphenyls, but fluorene, dibenzofuran, dibenzothiophene, and terphenyls. Since other molecules such as benzene, styrene, naphthalene, *etc.*, do not show this effect even under intense giant-pulsed laser beams, it appears that this behavior is probably associated with the phenyl-phenyl single bond.

Section News

Boston Section

The Annual Business Meeting of the Boston Section was held on Thursday, April 29, 1965, at the MIT Faculty Club, Cambridge, Mass. Reports of the Secretary and Treasurer were presented and approved. Councillor H. Homer reported in detail on the activities of the Council of Local Sections.

The following officers were elected for the coming season:

Chairman—John L. Sienczyk, Arthur D. Little, Inc.
Vice-Chairman—Ralph B. Soper, Sylvania Electric Products
Secretary—Mario D. Banus, MIT Lincoln Laboratory
Treasurer—Martin S. Frant, Orion Research, Inc.
Councilor (2 years)—Walter W. Harvey, Kennecott Copper Corp.

After the business portion of the meeting, Dr. Duncan E. Macdonald presented a fascinating talk entitled "Modern Explorations" in which he reviewed the use of photographic techniques to study the surface of the earth and nearby celestial bodies. Photo reconnaissance has extensive commercial as well as military applications. The classic example of the latter was the photo evidence of the missiles in Cuba. The detailed aerial survey of the remote areas of Cuba which were complete, timely, and convincing demonstrations of the major principals of reconnaissance which can help keep peace by preventing "force-level" surprise, technological surprise or accidents of miscalculations.

In space exploration, the use of photographs or direct television particularly with the correction addition of filters and adsorbers permits gathering of much useful scientific data. Using these artificial "eyeballs" without the extensive and expensive life-support systems necessary for direct observation by astronauts would give much more scientific information and give it sooner. As an example, he discussed how to determine the presence of fluorescent minerals on the Moon by photographic methods.

Personals

Eugene P. Cocozza has been promoted to manager, Chemical and Material Lab., International Business Machines Corp., Hopewell Junction, N.Y.

Hill Cross Co. Inc., West New York, N.J., has announced the election of **Herman N. Hammer** as president of the firm. Also announced was the purchase of a significant interest in Hill Cross by **Dr. Dodd S. Carr,** who was elected to the Board of Directors and who will assume the offices of vice-president and secretary previously held by Mr. Hammer. **Donald Wood** will continue as treasurer and **Glenn W. Holland** as vice-president.

Thomas F. Sharpe recently joined the Electrochemistry Department of the General Motors Research Labs., Warren, Mich. He was formerly with Melpar, Inc., of Falls Church, Va.

News Items

ECS Officers for 1966-1967

The report of the Nominating Committee has been approved by the Board of Directors at the San Francisco Meeting. The slate to be voted on this Fall is as follows:

President—Harold J. Read
Vice-President—N. Corey Cahoon, Frederick W. Fink, and Austin E. Hardy.

Photographs and biographies of each candidate will appear in the September 1965 issue of the JOURNAL.

Latest Volume in ECS Series

The Electrochemical Society is pleased to announce the availability of the latest volume in The Electrochemical Society Series:

"First International Conference on Electron and Ion Beam Science and Technology," Edited by R. Bakish. 945 pages $24.50.

This volume contains the papers presented at the First International Conference on Electron and Ion Beam Science and Technology held May 3-7, 1964 in Toronto, Canada. Virtually a single volume library in this field of scientific and technological endeavor, the book represents the most up-to-date material in the field. The conference was under the sponsorship of the Electrothermics and Metallurgy Division of The Electrochemical Society in cooperation with the Metallurgical Society of the AIME.

The volume is available from the publisher, John Wiley & Sons, Inc., 605 Third Ave., New York, N. Y., 10016. A 33 1/3% discount is offered to ECS members only and can be obtained by ordering through Society Headquarters, 30 East 42 St., New York, N.Y. 10017.

Third International Congress on Metallic Corrosion

The Third International Congress on Metallic Corrosion will be held in Moscow, May 16-25, 1966. Professor Y. M. Kolotyrkin of the Karpov Institute of Physical Chemistry and president of the Congress announces that special sessions will be devoted to presentation of papers in the following areas: basic research, passivity and anodic films, inhibitors, stress corrosion cracking, underground corrosion, salt water corrosion, nonmetallic coatings, metallic coatings, high-temperature oxidation, corrosion in the power industry, and atmospheric corrosion. Invited plenary lectures will be presented by Professor K. Schwabe of the Technical University of Dresden, East Germany, Dr. T. P. Hoar of Cambridge University, Cambridge, England, Professor H. H. Uhlig of Massachusetts Institute of Technology, Cambridge, Mass., Dr. M. Prazak of the Research Institute for Materials Protection, Prague, Czechoslovakia, and Professor N. D. Tomashov of the Academy of Science, U.S.S.R. Dr. E. C. Greco of the United Gas Corp., P.O. Box 1407, Shreveport, La., is one of the honorary vice-presidents of the Moscow meeting and is also chairman of the permanent Council for the International Congress. Inquiries about the Congress should be directed to him or to Mrs. T. V. Victorova, 11 Gorky St., Moscow K-9, U.S.S.R.

Submitted by H. H. Uhlig

Call for Papers for Cleveland Meeting, May 1966

Papers are being solicited for the Spring Meeting of the Society, to be held at the Sheraton-Cleveland Hotel in Cleveland, Ohio, May 1, 2, 3, 4, and 5, 1966. Technical sessions probably will be scheduled on: Electric Insulation, Electronics (including Luminescence and Semiconductors), Electrothermics & Metallurgy, Industrial Electrolytic, and Theoretical Electrochemistry.

To be considered for this meeting, **triplicate copies of the usual 75-word abstract, as well as of an extended abstract of 500-1000 words** (see notice on page 121C of the May issue), must be received at The Electrochemical Society, 30 East 42 St., New York, N. Y., 10017, *not later than December 15, 1965. Please indicate on 75-word abstract for which Division's symposium the paper is to be scheduled, and underline the name of the author who will present the paper.* No paper will be placed on the program unless one of the authors, or a qualified person designated by the authors, has agreed to present it in person. Clearance for presentation of a paper at the meeting should be obtained before the abstract is submitted. An author who wishes his paper considered for publication in the JOURNAL or ELECTROCHEMICAL TECHNOLOGY should send triplicate copies of the manuscript to the Managing Editor of the appropriate publication 30 East 42 St., New York, N. Y., 10017. Concerning papers to be published in the JOURNAL, see notice on per page charge on page 151C of this issue.

Presentation of a paper at a technical meeting of the Society does not guarantee publication in the JOURNAL or ELECTROCHEMICAL TECHNOLOGY. However, all papers so presented become the property of The Electrochemical Society, and may not be published elsewhere, either in whole or in part, unless permission for release is requested of and granted by the Editor. Papers already published elsewhere, or submitted for publication elsewhere, are not acceptable for oral presentation except on invitation by a Divisional program Chairman.

Symposium on Stress Corrosion of High Strength Materials

A Symposium on Stress Corrosion of High Strength Materials sponsored by the National Association of Corrosion Engineers will be held in Miami, Fla., April 18-22, 1966. The purpose of the Symposium is to familiarize engineers and scientists with the peculiar problems of stress corrosion testing, mechanisms, and evaluation of high strength materials.

Papers for this Symposium are invited. Approximately 100 word abstracts should be submitted by July 31, 1965, to either the Chairman or Co-Chairman of the Symposium. The Chairman is Dr. L. R. Scharfstein, The Carpenter Steel Co., Front & Bern Sts., Reading, Pa., and the Co-Chairman is Mr. W. K. Boyd, Battelle Memorial Institute, 505 King Ave., Columbus, Ohio.

New Members

It is a pleasure to announce the following new members to The Electrochemical Society as recommended by the Admissions Committee and approved by the Board of Directors for February 1965.

Active Members

Bard, A. J., Austin, Texas
Bender, S. L., Andover, Mass.
Bennion, D. N., Van Nuys, Calif.
Brixey, Jr., J. C., Richardson, Texas
Burkhardt, P. J., Poughkeepsie, N.Y.
Carini, F. F., Scotia, N.Y.
Chao, P.-Y., Torrance, Calif.
Chapman, J. R., Pittsburgh, Pa.
Chotkevys, G. P., Berea, Ohio
Cioffi, F. J., Iselin, N.J.
Clifton, J. K., Indianapolis, Ind.
Conrad, R. W., Dallas, Texas
Cowen, Arthur, Detroit, Mich.
Cuomo, J. J., Yorktown Heights, N.Y.
Dallas, N. S., Oak Park, Ill.
Darland, Jr., W. G., Parma, Ohio
Durham, H. B., Southfield, Mich.
Evans, E. B., South Euclid, Ohio
Finnie, L. N., Little Falls, N.J.
Frank, W. B., New Kensington, Pa.
Greef, Robert, Cleveland, Ohio
Hadley, R. L., Gainesville, Fla.
Hasler, M. F., Goleta, Calif.
Healy, J. H., Lexington, Ky.
L'Heureux, R. C., Fort Wayne, Ind.
Hillenbrand, L. J., Columbus, Ohio
Hodge, F. G., Poland, Ohio
Hooton, K. A. H., Tempe, Ariz.
Horak, F. A., Pasadena, Calif.
Kerr, D. R., Poughkeepsie, N.Y.
Kesler, G. H., Coraopolis, Pa.
Kestigan, Michael, Sudbury, Mass.
Krauss, C. J., Trail, B. C., Canada
LaBrie, J. J., Mountain View, Calif.
Lacksonen, J. W., Columbus, Ohio
Lambermont, Hank, Ogallala, Nebr.
Levine, C. A., Concord, Calif.
Littlewood, Roy, Hamilton, Ont., Canada
Lord, D. E., Greensburg, Pa.
MacKenzie, J. S., Arvida, P. Q., Canada
Marek, R. W., Tonawanda, N.Y.
Moyle, K. J., Palo Alto, Calif.
Naiditch, Sam, Pasadena, Calif.
Nicolliam, E. H., Murray Hill, N.J.
Poling, G. W., Beacon, N. Y.
Reed, Jr., M. W., Fort Wayne, Ind.
Reyer, Greg, Danbury, Conn.
Rigopulos, P. N., Melrose, Mass.
Rychlewski, T. V., Seneca Falls, N.Y.
Sagal, M. W., Murray Hill, N.J.
Sanders, Daniel, Glastonbury, Conn.
Skouson, G. W., Severna Park, Md.
Steele, Raymond, West Chester, Pa.
Taylor, H. L., Austin, Texas
Tuwiner, S. B., New York, N.Y.
Van Gelder, D. W., Roermond, The Netherlands
Wagner, Jr., J. B., Evanston, Ill.
Wakefield, Gene, Richardson, Texas
Weinstock, I. B., Gainesville, Fla.
Whyte, D. D., Pittsburgh, Pa.
Wynn, J. E., Neptune, N.J.
Young, J. P., Washington, D.C.
Youngquist, J. A., Madison, Wis.

Associate Member

Schreier, L. A., Lansdowne, Pa.

Student Associate Member

Akiyama, Akitane, Los Angeles, Calif.

Transfers from Student Associate to Active Membership

Kovac, Zlata, Yorktown Heights, N.Y.
Phillips, S. L., Poughkeepsie, N.Y.
Plambeck, J. A., Arlington Heights, Ill.
Schaer, M. J., Bozeman, Mont.
Venkatachalam, S., Montreal, P.Q., Canada

Transfer from Active Membership to Student Associate

Carbone, S. P., Lynnfield, Mass.

Announcements from Publishers

"Electronically Functional Organic Materials," Report AD 609 831N,* $2.00.

"Tables of Ideal Gas Thermodynamic Functions for 73 Atoms and Their First and Second Ions to 10,000°K," Report AD 606 163N,* $7.55.

"Corrosion of Metallic Materials by Uranium Hexafluoride at High Temperatures," Report AEC-TR-6504N,* $4.00.

"Investigation of Power Sources for Man-Pack Equipment," Report AD 610 104N,* $6.00.

"Morphology of PbO_2 in The Positive Plates of Lead Acid Cells," Report AD 609 986N,* $1.00.

"Solar Cell Performance at High-Temperatures," Report N65-11904N,* 50 cents.

"A Review of Metal Cleaning by Ion Bombardment," Report RFP-433N,* $2.00.

"The Ion Exchange Properties of Cerium (IV) Compounds," Report AD 610 108N,* $3.00.

---

* Order from Office of Technical Services, U. S. Department of Commerce, Springfield, Va. 22151.

ATTENTION, MEMBERS AND SUBSCRIBERS

Whenever you write to The Electrochemical Society about your membership or subscription, please include your Magazine address label to ensure prompt service.

ATTACH LABEL HERE

Change of Address

To change your address, please give us five weeks' advance notice. Place magazine address label here. Print your NEW address below. If you have any question about your subscription or membership, place your magazine label here and clip this form to your letter.

Mail to the Circulation Department, The Electrochemical Society, Inc., 30 East 42 St., New York, N. Y., 10017.

name ______________________

address ______________________

city ______________ state ______________ zip code ______________

Advertiser's Index

Patron and Sustaining Members
of
THE ELECTROCHEMICAL SOCIETY

Patron Members

Aluminum Co. of Canada, Ltd., Montreal, Que., Canada

Dow Chemical Co.
Chemicals Dept., Midland, Mich.
Metals Dept., Midland, Mich.

International Nickel Co., Inc., New York, N. Y.

General Electric Co.
Capacitor Dept., Hudson Falls, N. Y.
Chemical Laboratory, Knolls Atomic Power Laboratory, Schenectady, N. Y.
Chemical and Materials Engineering Laboratory, Advanced Technology Laboratories, Schenectady, N. Y.
Chemistry Research Dept., Schenectady, N. Y.
Direct Energy Conversion Operation, West Lynn, Mass.
Lamp Division, Cleveland, Ohio
Materials & Processes Laboratory, Large Steam Turbine-Generator Dept., Schenectady, N. Y.
Metallurgy and Ceramics Research Dept., Schenectady, N. Y.

Olin Mathieson Chemical Corp.
Chemicals Division, Research Dept., New Haven, Conn.

Union Carbide Corp.
Divisions:
Carbon Products Division, New York, N. Y.
Consumer Products Division, New York, N. Y.

Westinghouse Electric Corp.
Electronic Tube Division, Elmira, N. Y.
Lamp Division, Bloomfield, N. J.
Molecular Electronics Division, Elkridge, Md.
Semiconductor Division, Youngwood, Pa.
Research Laboratories, Pittsburgh, Pa.

Sustaining Members

Air Reduction Co., Inc., New York, N. Y.

Allen-Bradley Co., Milwaukee, Wis.

Allied Chemical Corp.
General Chemical Div., Morristown, N. J.

Alloy Steel Products Co., Inc., Linden, N. J.

Aluminum Co. of America, New Kensington, Pa.

American Metal Climax, Inc., New York, N. Y.

American Potash & Chemical Corp., Los Angeles, Calif.

American Smelting and Refining Co., South Plainfield, N. J.

American Zinc Co. of Illinois, East St. Louis, Ill.

American Zinc, Lead & Smelting Co., St. Louis, Mo.

M. Ames Chemical Works, Inc., Glens Falls, N. Y.

Ampex Corp., Redwood City, Calif.

Armco Steel Corp., Middletown, Ohio

Basic Inc., Bettsville, Ohio

Bell Telephone Laboratories, Inc., New York, N. Y. (2 memberships)

Bethlehem Steel Co., Bethlehem, Pa. (2 memberships)

Boeing Co., Seattle, Wash.

Burgess Battery Co., Freeport, Ill. (2 memberships)

Burndy Corp., Norwalk, Conn.

Canadian Industries Ltd., Montreal, Que., Canada

Carborundum Co., Niagara Falls, N. Y.

Chrysler Corp., Detroit, Mich.

Consolidated Mining & Smelting Co. of Canada, Ltd., Trail, B. C., Canada (2 memberships)

Continental Can Co., Inc., Chicago, Ill.

Corning Glass Works, Corning, N. Y.

Diamond Alkali Co., Painesville, Ohio

Wilbur B. Driver Co., Newark, N. J. (2 memberships)

E. I. du Pont de Nemours & Co., Inc., Wilmington, Del.

Eagle-Picher Co., Chemical and Metals Div., Joplin, Mo.

Eastman Kodak Co., Rochester, N. Y.

Eltra Corp.
Prestolite Div., Toledo, Ohio
C&D Batteries, Conshohocken, Pa.

Electric Storage Battery Co., Philadelphia, Pa. (2 memberships)

Engelhard Industries, Inc., Newark, N. J. (2 memberships)

The Eppley Laboratory, Inc., Newport, R. I.

Exmet Corp., Bridgeport, Conn.

Fairchild Semiconductor Corp., Palo Alto, Calif.

FMC Corp.
Inorganic Chemical Div., Buffalo, N. Y.
Inorganic Chemicals Div., South Charleston, W. Va.

Foote Mineral Co., Exton, Pa.

Ford Motor Co., Dearborn, Mich.

General Motors Corp.
Allison Div., Indianapolis, Ind.
Delco-Remy Div., Anderson, Ind.
Research Laboratories Div., Warren, Mich.

General Telephone & Electronics Laboratories, Inc., Bayside, N. Y. (2 memberships)

Globe-Union, Inc., Milwaukee, Wis.

Sustaining Members (Cont.)

B. F. Goodrich Chemical Co., Cleveland, Ohio

Gould-National Batteries, Inc., Minneapolis, Minn.

Great Lakes Carbon Corp., New York, N. Y.

Hanson-Van Winkle-Munning Co., Matawan, N. J. (2 memberships)

Harshaw Chemical Co., Clevleand, Ohio (2 memberships)

Hercules Powder Co., Wilmington, Del.

Hill Cross Co., Inc., West New York, N. J.

Hoffman Electronics Corp., Semiconductor Division, El Monte, Calif.

Honeywell, Inc, Minneapolis, Minn.

Hooker Chemical Corp., Niagara Falls, N. Y. (3 memberships)

HP Associates, Palo Alto, Calif.

Hughes Research Laboratories, Div. of Hughes Aircraft Co., Malibu, Calif.

International Business Machines Corp., New York, N. Y.

International Minerals & Chemical Corp., Skokie, Ill.

International Resistance Co., Philadelphia, Pa.

ITT Federal Laboratories, Div. of International Telephone & Telegraph Corp., Nutley, N. J.

Jones & Laughlin Steel Corp., Pittsburgh, Pa.

K. W. Battery Co., Skokie, Ill.

Kaiser Aluminum & Chemical Corp.
Div. of Chemical Research, Permanente, Calif.
Div. of Metallurgical Research, Spokane, Wash.

Kawecki Chemical Co., Boyertown, Pa.

Kennecott Copper Corp., New York, N. Y.

Leesona Moos Laboratories, Div. of Leesona Corp., Jamaica, N. Y.

Arthur D. Little, Inc., Cambridge, Mass.

Lockheed Aircraft Corp., Missiles & Space Div., Sunnyvale, Calif.

Mallinckrodt Chemical Works, St. Louis, Mo.

P. R. Mallory & Co., Indianapolis, Ind.

Melpar, Inc., Falls Church, Va.

Metal Pumping Services, Inc., Cleveland, Ohio

Miles Chemical Co., Div. of Miles Laboratories, Inc., Elkhart, Ind.

Monsanto Chemical Co., St. Louis, Mo.

M&T Chemicals Inc., Detroit, Mich.

National Cash Register Co., Dayton, Ohio

National Lead Co., New York, N. Y.

National Steel Corp., Weirton, W. Va.

North American Aviation, Inc., El Segundo, Calif.

Northern Electric Co., Montreal, Que., Canada

Norton Co., Worcester, Mass.

Owens-Illinois Glass Co., Toledo, Ohio

Pennsalt Chemicals Corp., Philadelphia, Pa.

Phelps Dodge Refining Corp., Maspeth, N. Y.

Philco Corp., Research Div., Blue Bell, Pa.

Philips Laboratories, Inc., Briarcliff Manor, N. Y.

Pittsburgh Plate Glass Co., Chemical Div., Pittsburgh, Pa.

Potash Co. of America, Carlsbad, N. Mex.

Radio Corp. of America
Electronic Components and Devices, Lancaster, Pa.
RCA Victor Record Div., Indianapolis, Ind.

Ray-O-Vac Co., Madison, Wis.

Republic Foil Inc., Danbury, Conn.

Reynolds Metals Co., Richmond, Va.

Shawinigan Chemicals Ltd., Montreal, Que., Canada

Socony Mobil Oil Co., Inc., Dallas, Texas

Speer Carbon Co.
International Graphite & Electrode Div.,
St. Marys, Pa.

Sprague Electric Co., North Adams, Mass.

Stackpole Carbon Co., St. Marys, Pa.

Stauffer Chemical Co., Dobbs Ferry, N. Y.

Texas Instruments, Inc., Dallas, Texas
Metals and Controls Corp., Attleboro, Mass.

3M Company, St. Paul, Minn.

Titanium Metals Corp. of America, Henderson, Nev.

Tyco Laboratories, Inc., Waltham, Mass.

Udylite Corp., Detroit, Mich. (4 memberships)

United States Borax & Chemical Corp., Los Angeles, Calif.

United States Steel Corp., Pittsburgh, Pa.

Univac, Div. of Sperry Rand Corp., New York, N. Y.

Universal-Cyclops Steel Corp., Bridgeville, Pa.

Upjohn Co., Kalamazoo, Mich.

Western Electric Co., Inc., Chicago, Ill.

Wyandotte Chemicals Corp., Wyandotte, Mich.

Yardney Electric Corp., New York, N. Y.